Electrooxidation of carbon monoxide and formic acid on polycrystalline palladium

by

Robert Lee Sacci
B.S., University of Tennessee, 2006

A Dissertation Submitted in Partial Fulf llment of the

Requirements for the Degree of

DOCTOR OF PHILOSOPHY

in the Department of Chemistry

University of Victoria

Electrooxidation of carbon monoxide and formic acid on polycrystalline palladium

by

Robert Lee Sacci
B.S., University of Tennessee, 2006

Supervisory Committee

Dr. David A. Harrington, Supervisor

(Department of Chemistry)

Dr. Alexandre Brolo, Departmental Member

(Department of Chemistry)

Dr. Lisa Rosenberg, Departmental Member

(Department of Chemistry)

Dr. Rustom Bhiladvala, Outside Member

(Department of Engineering)

Supervisory Committee

Dr. David A. Harrington, Supervisor
(Department of Chemistry)

Dr. Alexandre Brolo, Departmental Member
(Department of Chemistry)

Dr. Lisa Rosenberg, Departmental Member
(Department of Chemistry)

Dr. Rustom Bhiladvala, Outside Member
(Department of Engineering)

ABSTRACT

A systematic study of formic acid electrooxidation on polycrystalline palladium is presented. The study begins with a discussion on the oxide growth process on platinum and palladium. CO electrooxidation under controlled mass transport is studied in order to elucidate the manner in which Pd interacts with CO, a proposed poisoning species in formic acid oxidation. The mechanism of formic acid oxidation is studied using various potentiodynamic techniques, including dynamic electrochemical impedance spectroscopy, which provides impedance measurements during a voltammogram. Through kinetic analysis, a model for the oxidation was developed. The impedance measurements support both the dc measurements as well as the results of the oxidation model. It was determined that CO formation was slow on Pd within the time scale of the experiments. The chief cause of

surface deactivate was then determined to be the Pd surface interaction with the (bi)sulfate adsorption in the double layer region.

Table of Contents

List of Tables

List of Figures

Nomenclature

Symbol	Meaning	Units
A	Surface area	cm^2
C	Capacitance	$\mathrm{F\,cm}^{-2}$
C_{dl}	Double layer capacitance	$\mathrm{F\,cm}^{-2}$
c	Concentration	$\mathrm{mol\,L}^{-1}$
c^*	Bulk concentration	$\mathrm{mol\,L}^{-1}$
D	Diffusion coeff cient	$\mathrm{cm}^2\,\mathrm{s}^{-1}$
f	Frequency	s^{-1}
F_{χ^2}	F-ratio of χ^2	1
g	Interaction parameter	1
I	Current	A
j	Current density	$\mathrm{A\,cm}^{-2}$
j_{ac}	Ac current density	$\mathrm{A\,cm}^{-2}$
j_{dc}	Dc current density	$\mathrm{A\,cm}^{-2}$
E	Applied potential	V
E^{o}	Standard potential	V
$E_{\mathrm{a}}^{\mathrm{p}}$	Anodic peak potential	V
$E_{\mathrm{c}}^{\mathrm{p}}$	Cathodic peak potential	V

Symbol	Meaning	Units
E_{ac}	Applied ac potential	V
E_{dc}	Applied dc potential	V
E_{L}	Potential sweep limit	V
E_{r}	Reference potential	V
I	Current	A
j	Current density	$\mathrm{A\,cm^{-2}}$
j_{ac}	Ac current density	$\mathrm{A\,cm^{-2}}$
j_{dc}	Dc current density	$\mathrm{A\,cm^{-2}}$
K	Equilibrium Constant	various
k	Rate constant	various
k^{o}	Standard rate constant	various
L	Inductance	$\mathrm{H\,cm^2}$
n	Number of electrons	1
Q	Charge	C
Q_{CPE}	Constant phase element	$\mathrm{F\,cm^{-2}\,s^{-\alpha}}$
R	Resistance	$\Omega\,\mathrm{cm^2}$
R_{ct}	Charge transfer resistance	$\Omega\,\mathrm{cm^2}$
$R_{\|\|}$	Parallel combination resistance	$\Omega\,\mathrm{cm^2}$
r	Radius	cm
r_i	Net rate of production of i	$\mathrm{mol\,cm^2\,s^{-1}}$
t	Time	s
v	Potential sweep rate	$\mathrm{V\,s^{-1}}$
v_i	Rate expression of reaction i	$\mathrm{mol\,cm^2\,s^{-1}}$
v_r	Radial velocity	$\mathrm{cm\,s^{-1}}$
v_z	Axial velocity	$\mathrm{cm\,s^{-1}}$

Symbol	Meaning	Units
v_ϕ	Angular velocity	$\mathrm{cm\,s^{-1}}$
W	Walburg constant	$\mathrm{F\,cm^{-2}\,s^{-1/2}}$
X	Mole fraction	1
Y	Admittance	$\mathrm{S\,cm^{-2}}$
Z	Impedance	$\Omega\,\mathrm{cm^2}$
z	Distance from electrode surface	cm
GREEK		
α	Constant phase element phase	1
α	Transfer coeff cient	1
β	Symmetry factor	1
Γ_m	Surface saturation concentration	$\mathrm{mol\,cm^{-2}}$
δ	Diffusion layer thickness	cm
δ_H	Hydrodynamic layer thickness	cm
θ	Surface coverage	1
ν	Kinematic viscosity	$\mathrm{cm^2\,s^{-1}}$
ρ	Density	$\mathrm{g\,cm^{-3}}$
σ	Charge density	$\mathrm{C\,cm^{-2}}$
τ	time constant	s
ϕ	Phase angle	$^\circ$
φ	Phase angle	$^\circ$
χ^2	Chi square	1
ω	Angular frequency	$\mathrm{rad\,s^{-1}}$

ACKNOWLEDGMENTS

As I was staring at the computer screen thinking of those whom I ought to and even *had* to acknowledge for enabling me to be able to complete this thesis I was humbled. The shear number of people that have molded my mind to what it is today and what it can be tomorrow is simply staggering. This is not an extensive list of those craftsmen, for that would be impractical if not impossible to achieve. This section will focus on the brightest stars in my life.

I begin with my wife, Danielle. She keeps me honest and humble. She brings more joys then I could ever have hoped for and she has given me a beautiful daughter. Antonia is just like her mother, but more ferocious in every respect. She violently loves her father and I love her much the same.

I thank my parents for their support over the years. I have had a number of friends that I am sad to say meant more to me than what I probably meant to them. Josh Roop will always be my brother. Keith Abel and Simon Birne-Lecovich are now my Canadian brothers and without them and their crazy antics graduate life would have been dull.

I, of course, could not do this without the help and guidance of David Harrington. I give special thanks to my lab-mates, Jakub Drnec for the interesting conversations we had. I also thank Gabi Haber for letting me rant about the ills of the world. It was very therapeutic.

Lastly, I thank the Natural Sciences and Engineering Research Council of Canada the University of Victoria and Tekion for support of the research. Thanks to the University of Victoria for the Nora and Mark DeGroutier Memorial Scholarship.

DEDICATION

This work is dedicated to my two girls: Danielle and Antonia.

SDG

Chapter 1

Introduction

The oxidation of single carbon molecules such as carbon monoxide, formic acid, formaldehyde, and methanol are of substantial importance to emerging energy economies. Palladium has long been known to be an eff cient catalyst for CO oxidation in the gas phase, which explains the automotive industry's heavy dependence upon it in catalytic converters to oxidize combustion by-products to CO_2. There has yet to be a systematic study of carbon monoxide and formic acid electrooxidation on bare palladium surfaces. Also absent from the literature are the effects of mass transport upon the mechanism of the oxidations. Lastly, electrochemical impedance spectroscopy (EIS) has not been used in a thorough manner to study the systems. This technique can provide more detailed information on system kinetics and number of adsorbed species. In this work we seek to rectify the above shortcomings by presenting a detailed electrochemical study of CO and HCOOH electrooxidation on Pd using various potentiostatic techniques.

In this thesis, Chapters 3–6 were written as a seperate publication. In Chapter 2 the explanation of experimental methods used in this study is given. Of particular focus is electrochemical impedance spectroscopy, which was used extensively in this work. The technique has been around for more than half a century [1] and there are still different

schools of thought pertaining to its use in obtaining kinetic information [2]. We demonstrate how an equivalent circuit represents a simple electrochemical reactions and how EIS can be used to extract kinetic information. Afterward we discuss dynamic electrochemical impedance spectroscopy (dEIS) which was described by Smith [3–5] only a decade after EIS came into use. There are various ways in which dynamic impedance can be conducted, but we describe an unique setup which allows for high data density and frequency span that to our knowledge is unmatched in the literature. We describe the experiment in detail and its limitations using dummy cells. We used both EIS and dEIS in Chapter 3, 4, and 6. We then turn our attention to the rotating disk electrode (RDE) which was used in our CO oxidation study (Chapter 4). Here we provide a brief description of the principles and derivations behind the technique as well as describe its use.

We use the dEIS system to study oxide growth and reduction in acidic media on platinum and palladium in Chapter 3. Two acidic solutions were used: $HClO_4$ and H_2SO_4. With dEIS we were able to obtain a high density of points when f tting equivalent circuits at changing potentials. We show how these acids affect the oxide growth and reduction of Pd and Pt. In addition to that we look into how sweep rate affects the impedance—a previously unused parameter. We show that care should be taken when using mechanistic analysis in conjunction with equivalent circuits as subtle differences in mechanisms are not always manifested in equivalent circuits. We review new spectroscopic data and provide a ref nement to the place exchange mechanism.

Chapter 4 focuses on carbon monoxide oxidation in sulfuric acid on palladium. The RDE is utilized extensively in this study as the main focus of the study is the effect of mass transport upon the electrooxidation. The CO oxidation peak is delayed by an increase in rotation suggesting that increasing the f ux of CO at the surface can inhibit oxide growth. dEIS provided further support by probing the double layer capacitance as a function of potential. The results show that the coverage of CO increases with rotation rate and that

there is a strong relation between the anodic current and the coverage of CO. We show that the reaction kinetics are not stable during the formation of the anodic peak. We explain this result in terms of a nucleation-growth-collision mechanism.

Chapter 5 begins the detailed study of formic acid oxidation on Pd. Here a series of potentiostatic experiments were used to obtain information on the reaction mechanism. Tafel analysis is used to obtained information on the reaction order with respect to formic acid as well as information on the rate-determining step. We show that the rate-determining step changes as the potential is swept. At potentials lower than 0.4 V the rds is an electrochemical step, while at higher potentials it is a chemical step. This was used as an explanation for the change in the Tafel slope and formic acid reaction order. We spike the formic acid solution with various organic contaminants in order to produce a poisoning effect. It is shown that small organic molecules that form CO as an intermediate were effective poisons. Since there were no indicators of CO formation in the voltammograms, an additional process had to be added to the mechanism in order to explain the passivation in the region where the current-potential slope is negative. After review of the literature, interaction between adsorbed formate and adsorbed (bi)sulfate anion was used to model the passivation process.

The study of formic acid electrooxidation continues into Chapter 6 with the addition of dEIS. Here the effect of concentration and sweep rate on the impedance data is investigated. Two time constants were used to f t the impedance data in the region where the current is increasing. In the region where the current decreases with potential, the impedance needed three time constants to be f tted. All the time constants involving adsorption were positive and independent of sweep rate. We related the number of time constants to the number of adsorbed species on the surface and found good agreement with spectroscopy data. The dEIS data provides support to the mechanism given in the previous chapter. The impedance further suggests that CO is not readily formed on the Pd surface and that the

potential-driven passivation process is linked to a decreased reactivity of the Pd surface and not solely a site-blocking mechanism.

Finally, conclusions from this thesis on the reactivity of electrooxidations on Pd and suggestions for further work are given in Chapter 8.

Chapter 2

Techniques

2.1 Abstract

This chapter discusses the two primary tools of this work, **e**lectrochemical **i**mpedance **s**pectroscopy (EIS) and the rotating disk electrode. It gives both an introduction to their theory, and the experimental details that are common to the other chapters.

2.2 Electrochemical Impedance Spectroscopy

There are many different schools of thought on how to best extract information from electrochemical impedance spectroscopy [2]. One may begin with the formulation of a mechanism and from that derive an equivalent circuit (EC). This circuit models the electrochemical system by connecting kinetic and mechanistic information to a particular construction of electrical elements. Another way to use EIS is to f t arbitrary equivalent circuits to the data in order to acquire the best f t with the fewest elements. In this work we use a semi-empirical method in which a basic model was developed and circuits with element values that were most easily related to kinetic information were used. This method minimizes the

tendency to overinterpret the f tted elements.

There are two books in particular that provide an in depth look into the ability of EIS to provide information on electrochemical systems [1, 6], though most books with a focus on electrochemistry provide some detail of EIS. Instead of a lengthy formal treatment of EIS, we will walk through a simple system with brief pauses along the way to further elucidate concepts.

The essence of EIS is a periodic perturbation that is applied to the electrochemical system. There are three external variables in an electrochemical experiment: time (t), potential (E), and current (I). Controlling time is not within the capacity of the electrochemist, but we can choose which of the other two variables we can control and use as our stimulus. All of the EIS experiments done in this work were under potentiostatic control and so we will describe basic impedance concepts assuming potential-controlled conditions.

We def ne the applied potential as

$$E = E_{\mathrm{dc}} + E_{\mathrm{ac}} = E_{\mathrm{dc}} + |E| \sin(\omega t) \tag{2.1}$$

where E_{dc} is the constant potential that the impedance is measured at, $|E|$ is the amplitude, and $\omega = 2\pi f$, where f is the frequency of the perturbation. If $|E|$ is kept small ($\leq 5\,\mathrm{mV}$) the ac current response is proportional to $|E|$ and the system can be approximated as linear. Assuming linearity, we expect the current response to be of the form

$$j = j_{\mathrm{dc}} + j_{\mathrm{ac}} = j_{\mathrm{dc}} + |j| \sin(\omega t + \phi) \tag{2.2}$$

where ϕ is the shift in the phase in radians. We now represent the ac current by the complex

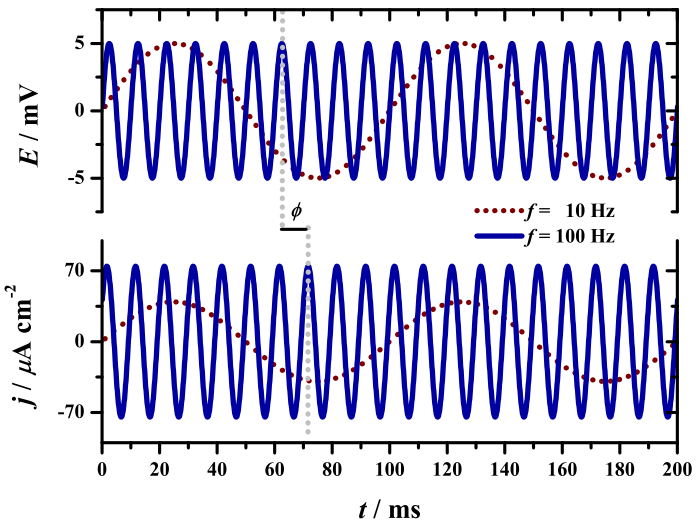

Figure 2.1: Example of two potential sine waves applied in an EIS experiment (top) with their respective current response (bottom).

number

$$\tilde{j} \;=\; |j|\exp(\mathrm{i}\phi) \tag{2.3}$$

and similarly for the potential whose phase is zero by def nition. The impedance is obtained from the ratio between the potential waveform and the current response,

$$Z \;=\; \frac{\tilde{E}}{\tilde{j}} = \frac{|E|}{|j|\exp(\mathrm{i}\phi)} = |Z|\exp(-\mathrm{i}\phi) \tag{2.4}$$

Figure 2.1 depicts the type of stimulus and response commonly found in EIS experiments. Therefore an EIS experiment gives the impedance amplitude, $|Z|$, and phase, ϕ, as functions of frequency. By changing the potential of measurement, E_{dc}, these two qualities then become functions of ω and E, that is $Z(\omega, E_{\mathrm{dc}})$.

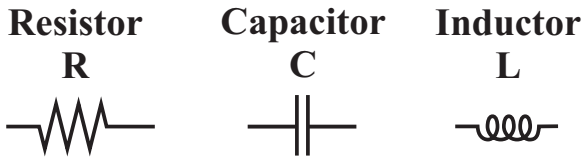

Figure 2.2: Electronic symbols of the circuit elements used to form equivalent circuits for f tting EIS data.

2.2.1 Equivalent circuits and elements

In this study we use three basic circuit elements in our impedance analysis: resistor, capacitor, and inductor (shown in Fig. 2.2). The derivation of the impedance of each circuit is given below starting with the resistor. Since the current will be normalized to the surface area (that is we use current density, j) the values of the elements are also normalized to surface area, i.e., a resistor will have the unit of $\Omega\,\mathrm{cm}^2$; capacitor: $\mathrm{F\,cm}^{-2}$; inductor: $\mathrm{H\,cm}^2$, etc.

2.2.1.1 Resistor

The impedance of R is obtain by beginning with Ohm's law.

$$dj = \frac{1}{R}\,dE \tag{2.5}$$

Substituting Eq. (2.1) and (2.2) into Eq. (2.5) gives

$$\omega|j|\cos(\omega t)\,dt = \frac{1}{R}\,\omega|E|\cos(\omega t)\,dt \tag{2.6}$$

Recognizing the fact that $\cos(\omega t) = \sin(\omega t + \pi/2)$ and the fact that the signal $|A|\sin(\omega t + \pi/2)$ is associated with the phasor (complex number) $\tilde{A} = |A|\exp(\mathrm{i}\pi/2)$ which leads to the rela-

tionship between the two phasors

$$\omega|j|\exp\left(\mathrm{i}\pi/2\right) = \frac{1}{R}\omega|E|\exp\left(\mathrm{i}\pi/2\right) \tag{2.7}$$

Combining Eqs. (2.3), (2.4), and (2.7), and rearranging gives the impedance of a resistor.

$$Z_{\mathrm{R}} = \frac{\tilde{E}}{\tilde{j}} = \frac{|E|}{|j|} = R \tag{2.8}$$

Therefore, the impedance of a resistor is the ratio of the amplitudes with no phase shift between the potential and current waveforms.

2.2.1.2 Capacitor

A capacitor is def ned by

$$j = C\frac{dE}{dt} \tag{2.9}$$

Again, substituting Eq. (2.1) into this form and converting to complex notation gives

$$j = \omega C|E|\cos\left(\omega t\right) \tag{2.10}$$

$$= \omega C|E|\sin\left(\omega t + \pi/2\right) \tag{2.11}$$

In terms of phasors, this is

$$\tilde{j} = \mathrm{i}\omega C\tilde{E} \tag{2.12}$$

Rearrangement gives the impedance form of a capacitor

$$Z_{\mathrm{C}} = \frac{\tilde{E}}{\tilde{j}} = \frac{1}{\mathrm{i}\omega C} \tag{2.13}$$

Thus a capacitor produces an impedance that is inversely proportional to ω with a 90$^{\mathrm{o}}$ ($\pi/2$) phase shift. This means that Z_{C} approaches zero as the frequency increases to inf nity and it approaches inf nity as the frequency decreases to zero. In other words, a capacitor behaves as a wire at high frequencies and as an open circuit at low frequencies.

2.2.1.3 Inductor

An inductor is def ned as

$$E = L\frac{dj}{dt} \tag{2.14}$$

Following a similar procedure to that shown for the capacitor we get

$$E = \omega L|j|\cos(\omega t) \tag{2.15}$$

$$= \omega L|j|\sin(\omega t + \pi/2) \tag{2.16}$$

In terms of phasors, this is

$$\tilde{E} = \mathrm{i}\omega L\tilde{j} \tag{2.17}$$

Rearrangement gives the impedance form of an inductor

$$Z_{\mathrm{L}} = \frac{\tilde{E}}{\tilde{j}} = \mathrm{i}\omega L \tag{2.18}$$

An inductor produces an impedance with a -90° (or +270°, $^{3\pi}/_{2}$) phase shift that is directly proportional to ω. That is, Z_{L} approaches inf nity as the frequency increases to inf nity and approaches zero as the frequency decreases to zero. Stated differently, an inductor behaves as a wire at low frequencies and as an open circuit at high frequencies.

2.2.1.4 Combining impedances

The rules for combining impedances in circuits are: 1) impedances in series are additive; 2) reciprocals of impedances in parallel are additive. For example, the *RC*-series circuit has the impedance

$$Z = R + \frac{1}{\mathrm{i}\omega C} \tag{2.19}$$

whereas *RC*-parallel has the impedance

$$Z^{-1} = R^{-1} + \mathrm{i}\omega C \tag{2.20}$$

2.2.2 Using equivalent circuits

All electrochemical systems contain two non-faradaic elements: solution resistance, R_{s}, which is the resistance between the working electrode and the reference electrode, and double-layer capacitance, C_{dl}, which models the charging of the double layer. The cell time-constant is the product of R_{s} and C_{dl}.

$$\tau_{\mathrm{cell}} = R_{\mathrm{s}} C_{\mathrm{dl}} \tag{2.21}$$

This describes the fastest rate at which the potential can change. Therefore, processes that occur faster than τ_{cell} cannot be measured/detected by EIS or other electrochemical methods.

Faradaic processes occur across the double layer and therefore the faradaic impedance, Z_{f}, is parallel to the double layer capacitance (Figure 2.3a). The impedance of an electrochemical process, say electrooxidation of a small organic molecule, can be solved for if the mechanism is known. The impedance for a species undergoing electrosorption is derived in Chapter 3 and is expanded upon in Chapter 6 to include n intermediates. Here, we give an example of a species undergoing a single step oxidation without adsorbing onto the surface, that is

$$\mathrm{A^-(aq)} \quad \rightleftarrows \quad \mathrm{A(aq) + e^-} \tag{2.22}$$

Assuming that mass transport is fast compared to the oxidation rate, mass action kinetics leads to the rate expression for Eq. (2.22) of

$$v \quad = \quad k^{\mathrm{o}}[\mathrm{A^-}] \exp\left[\frac{(1-\beta)F}{RT}(E - E^{\mathrm{o}})\right] - k^{\mathrm{o}}[\mathrm{A}] \exp\left[-\frac{\beta F}{RT}(E - E^{\mathrm{o}})\right] \tag{2.23}$$

Since in this example the rate of electron production is equal to the rate of reaction, v, we can write

$$j \quad = \quad vF \tag{2.24}$$

To find the perturbation in the current at steady state caused by $\tilde{E}$ we use a Taylor series

retaining only the linear terms

$$j(E) \;=\; j(E_{\rm dc}+|E|\sin(\omega t)) = j(E_{\rm dc}) + \left(\frac{dj}{dE}\right)_{E_{\rm dc}} |E|\sin(\omega t) + \cdots \tag{2.25}$$

$$\tilde{j} \;\approx\; \left(\frac{dj}{dE}\right)_{E_{\rm dc}} \tilde{E} \tag{2.26}$$

This then can be used to obtain the faradaic impedance by dividing by $\tilde{E}$

$$Z_{\rm f}^{-1} \;=\; \frac{\tilde{j}}{\tilde{E}} = \left(\frac{dj}{dE}\right)_{E=E_{\rm dc}} \frac{\tilde{E}}{\tilde{E}} = \left(\frac{dj}{dE}\right)_{E=E_{\rm dc}} \tag{2.27}$$

$$\begin{aligned} Z_{\rm f}^{-1} = \quad \left(\frac{dj}{dE}\right)_{E=E_{\rm dc}} = \quad & \left(\frac{(1-\beta)F^2}{RT}\right) k^{\rm o}[{\rm A}^-] \exp\left[\frac{(1-\beta)F}{RT}(E_{\rm dc}-E^{\rm o})\right] \\ & + \left(\frac{\beta F^2}{RT}\right) k^{\rm o}[{\rm A}] \exp\left[-\frac{\beta F}{RT}(E_{\rm dc}-E^{\rm o})\right] \end{aligned} \tag{2.28}$$

The faradaic impedance here is simply the charge transfer resistance, $R_{\rm ct}$, which has a Tafel-like relationship at potentials far from the reversible potential.

$$\ln\left(R_{\rm ct}^{-1}\right) \;=\; \frac{(1-\beta)F}{RT}(E_{\rm dc}-E^{\rm o}) + \ln\left[\left(\frac{(1-\beta)F^2}{RT}\right) k^{\rm o}[{\rm A}^-]\right] \tag{2.29}$$

corresponds to the anodic process and the cathodic process is given as

$$\ln\left(R_{\rm ct}^{-1}\right) \;=\; \frac{\beta F}{RT}(E_{\rm dc}-E^{\rm o}) + \ln\left[\left(\frac{\beta F^2}{RT}\right) k^{\rm o}[{\rm A}]\right] \tag{2.30}$$

A plot of $\ln(R_{\rm ct}^{-1})$ vs E can then be used to gain information on β and the rate constants.

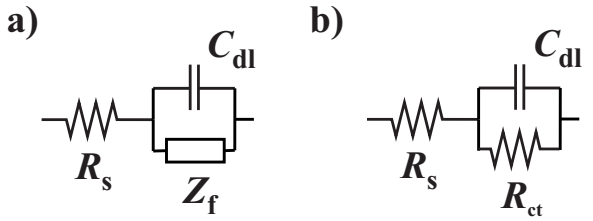

Figure 2.3: Equivalent circuits used to fit impedance results of electrochemical reactions. a) general form for surface reactions; b) specific case for Eq. (2.22).

Since $Z_{\rm f} = R_{\rm ct}$, the equivalent circuit that is predicted from this mechanism is a simple resistor in parallel with the double layer capacitance, Fig. 2.3. The expected impedance of this EC is presented in Fig. 2.4. A single semicircle is present in the Nyquist plot and decreases in size as the applied potential increases; the $j - E$ slope increases with an increased potential. The diameter of the half circle is $R_{\rm ct}$ and the distance between the origin and where low frequency impedance converges is the polarization resistance, $R_{\rm p}$, which is closely related to the steady state polarization curve, that is

$$R_{\rm p} = \frac{dj_{\rm ss}}{dE} = \frac{1}{\lim_{\omega\to 0} Z(\omega)} \tag{2.31}$$

Eq. (2.28) can be used to obtain the Tafel-like relationship between potential and $R_{\rm ct}$ which can be used to find β, $k_1^{\rm o}$, and $k_{-1}^{\rm o}$. This method provides advantages over using the steady state polarization curve since $R_{\rm ct}$ can be separated out from other processes thereby producing a more ideal relationship—Fig. 2.5.

2.3 dEIS[1]

Dynamic electrochemical impedance spectroscopy (dEIS) is a particular class of impedance measurement. It combines the frequency span of regular steady state EIS experiments with that of ac voltammetry's dynamic properties. Smith pioneered the use of fast Fourier

[1]This subsection is a slightly revised version of the paper [7], omitting the conclusions.

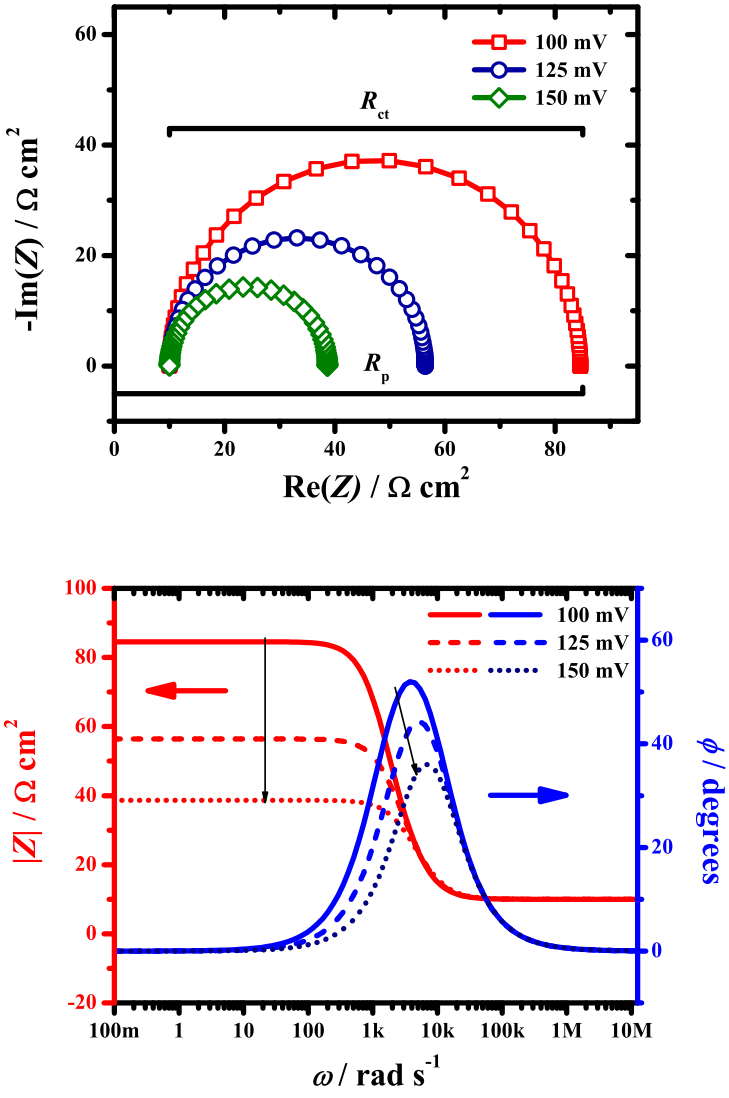

Figure 2.4: Simulated impedance shown in Nyquist (top) and Bode (bottom) plots resulting from varying E_{dc} of the derived electrochemical reaction, Eq. (2.22), and its equivalent circuit (Fig. 2.3b). $k_1^{\mathrm{o}} = k_{-1}^{\mathrm{o}} = 1 \times 10^{-5}\,\mathrm{cm\,s^{-1}}$, $E^{\mathrm{o}} = 0\,\mathrm{V}$ $[\mathrm{A}^-] = [\mathrm{A}] = 1 \times 10^{-5}\,\mathrm{mol\,cm^{-3}}$, $\beta = 0.5$, $R_{\mathrm{s}} = 10\,\Omega\,\mathrm{cm}^2$, $C_{\mathrm{dl}} = 10 \times 10^{-6}\,\mathrm{F\,cm^{-2}}$.

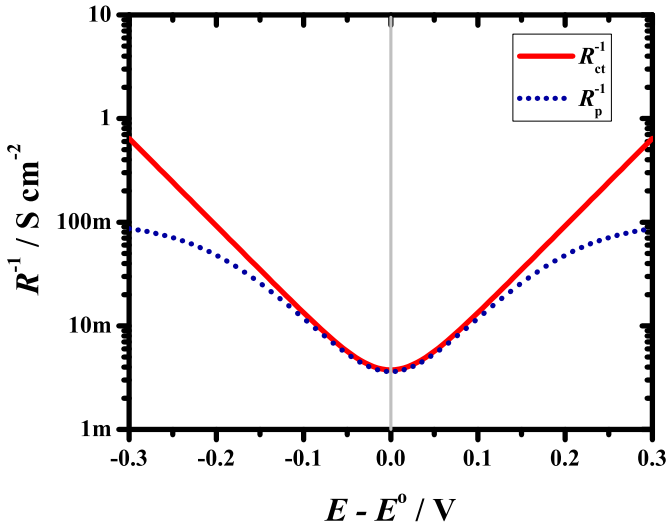

Figure 2.5: Tafel plot of the polarization and charge-transfer resistance obtained from the same simulation as in Fig. 2.4.

transform (FFT) methods in the field of EIS [3, 4, 8]. Over several generations of computer technology, the instrumentation has steadily improved [9, 10]. FFT-EIS has been used to probe a variety of electrochemical processes and has recently been used to study non-stationary processes [4, 11–16]. Some of the theoretical and experimental limitations of dynamic electrochemical impedance spectroscopy (dEIS) have been discussed by Garland et al. [17]. We describe here the hardware and software for a system that applies a multi-sine waveform on top of a potential sweep, and digitizes current and voltage in an instrument controlled over a USB connection, which can be used with any analog potentiostat. We validate its use by demonstrating its capability with dummy cells. A feature of this setup is that impedance spectra can be continuously acquired around a cyclic voltammogram, so that the surface condition studied can be identified as that existing at a given potential, and the evolution of the surface can be studied.

2.3.1 Brief history

In a typical EIS experiment both the dc potential and the dc current response must be stationary, particularly when low frequencies are being analyzed. This allows study of a surface at steady state or equilibrium, but cannot probe a surface undergoing change. Since FFT-EIS can rapidly acquire spectra, it is possibly to dynamically study the impedance of an electrochemical system while it is undergoing change. In essence, dEIS involves continuously applying a multi-sinusoidal potential waveform of small amplitudes to an electrochemical cell while under non-stationary conditions, i.e. a slow ramp voltage as in cyclic voltammetry. In a clever experiment by Popkirov [18], two identical electrochemical cells were placed under the same dc potential, and the ac potential waveform was added to one of the cells. This allowed for separate recording of the dc and ac current responses. Harrington et al. used a series of ac voltammetry experiments to build up the dynamic impedances of various systems [19–21]. Hazi et al. [11] have made great strides in mov-

ing FFT-EIS from being a stationary technique to a dynamic one [13, 17]. Using the ac voltammetry theory and limitations developed by them and Englom et al. [22, 23] have been able to investigate constraints on dEIS and further its development. Roy, in particular, has not only provided an electronic architecture for dEIS but has investigated its experimental constraints [17, 24]. More recently, Darowicki came up with an alternative design for the system and has used it extensively in corrosion experiments [10, 13]. Ragoisha has reported the dEIS spectra of reversible, underpotential deposition and electropolymerization reactions [14], as well as an initial study of surface reactions on clean platinum [25]. Since then, there have been a number of dynamic impedance systems described [26–28], though there has not been a lot done to harness its most powerful feature – the effects of the changing surface composition on the impedance. In particular no other method of dEIS applies the waveform and records the current response f uidly as is the case with our setup.

2.3.2 Methodology

2.3.2.1 Instrumentation

In principle, an FFT-EIS data generation and acquisition system requires a single digital-to-analog converter (DAC) to output the potential ramp and multi-sine waveform into a potentiostat, and two analog to digital converters (ADC) to sample the potential actually applied to the cell and the current f owing through it. Our system (block diagram shown in Figure 2.6) improves on this in several important ways. To maximize the resolution of the potential waveform, the multi-sine signal (DAC0) is generated with close to 10 V amplitude at 16 bit resolution, and is then divided down (box indicated with $\div$) and added (left-hand box indicated with $+$) to an analog cyclic potential sweep waveform (E_{dc}) with analog circuitry, thus maintaining the f delity of the signal, which the potentiostat then applies to the cell.

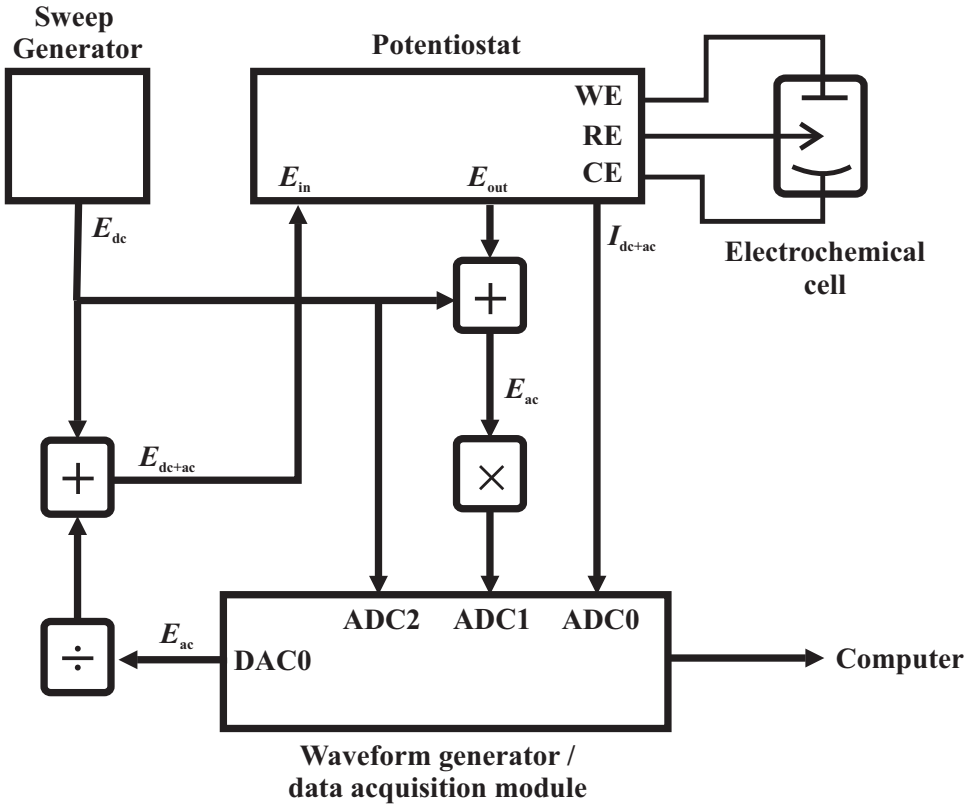

Figure 2.6: General schematic of the dynamic electrochemical impedance spectroscopy system.

The potential actually applied is measured by the potentiostat. Direct digitization of this signal would result in loss of resolution, since the required small ac waveform is on top of a much larger, slowly varying potential sweep, E_{dc}. Therefore the known large component E_{dc} is subtracted off to leave the ac component, which is then amplified (box with $\times$) to near the full scale of the ADC (ADC1 in Figure 2.6). The subtraction is actually an addition (right-hand box containing $+$) since the potentiostat outputs an inverted potential signal. This subtraction leaves the system without knowledge of the dc component of the potential, so that this needs to be separately recorded (ADC2). For the current, the dc component cannot be subtracted off before digitization because it is not known, so the dc and ac components are not separated but are recorded together by ADC0. Suitable filtering might give an approximate dc current to subtract, but this subtraction was much less critical for the current than for the potential so was not implemented in the present design.

The actual implementation of this is shown in Figure 2.7. The central generator/data acquisition module is a Keithley Instruments model KUSB-3116. This has a maximum sampling speed on a single channel of 500 kHz, has 16 bit ADC and DAC that are clocked synchronously by an 18 MHz master clock. Communication with the computer is *via* a USB port. We use the mode in which the multi-sine waveform is preloaded into the KUSB-3116 and then output repeatedly on DAC0 without further interaction with the computer. Use of this mode much simplifies the software, but limits the waveform period to 122 880 samples, although this is not a serious limitation in practice. The three ADC channels continuously sample while the waveform is output, and are sent to the computer. A buffering system ensures that continuous sampling at the maximum rate without any overruns is possible for the half hour or so required for a long experiment. The sampled data are written to a file, which is post-processed to give the impedance.

The analog scaling, summing and amplifying were carried out with small instrument modules (SIM) from Stanford Research Systems, as indicated in the figure. Simple op-

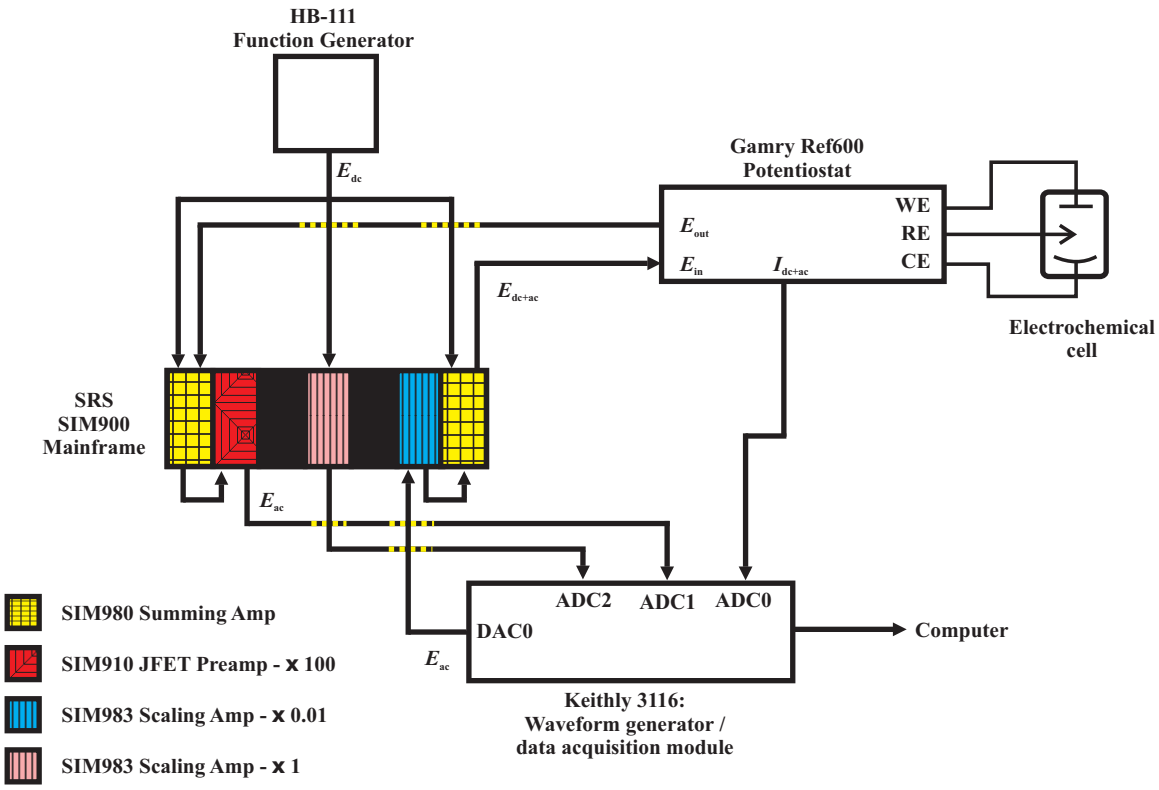

Figure 2.7: Hardware implementation of the dEIS system.

amp circuits could be used for carrying out the same function as the SIM in a more cost effective way. The Keithley module apparently has lower-than-rated input impedance when running in multichannel mode, so the SIM modules also serve the function of buffering the individual ADC inputs. A potential sweep generator (Hokuto Denko, HB-111) produces an analog sweep waveform for cyclic voltammetry. A Gamry REF 600 potentiostat was set up with the Gamry software but was otherwise used as an analog potentiostat. The potentiostat or other instrumentation does not introduce any apparent phase shifts within the frequency rage used here.

In this dissertation the impedance data was fitted using ZsimpWin or ZView using modulus weight fitting.

2.3.2.2 Sampling Strategy and Software

Custom software (written in Visual Basic 6 using the ActiveX controls supplied by Keithley) handled the waveform generation, data acquisition, fast Fourier transformation, impedance calculation, and file management. The waveform used in this chapter is composed of approximately forty sine waves of varying frequencies, phases, and amplitudes. One necessary condition for frequencies is that they have an exact number of sine waves that fit into the period, $T = 1/f_{\min}$. In order to accomplish this, each frequency is a multiple of the minimum one,

$$f_n = n f_{\min} \tag{2.32}$$

where the integer n is the "frequency number". We used frequency numbers similar to those suggested by Popkirov [18], namely 1, 3, 5, 7, 9, 11, 13, 17, 21, 25, 31, 37, 44, 52, 64, 75, 90, 100, 110, ..., with the last one being the first of 13 points for another decade that repeats the earlier 13 frequencies but a factor of 10 higher. Following Roy

[17], the rms amplitudes for the individual sine waves, a_i, are decreased by a factor of two for every decade increase in the frequency. This is done in order to keep the current response for each frequency within similar magnitudes. The amplitudes of all the individual frequencies were kept below 5 mV rms; the higher frequencies had lower amplitudes. The overall amplitude of the multi-sine waveform was kept around 30 mV peak-to-peak. These amplitude restrictions limit the number of simultaneous frequencies that can be used to about f fty, because the power in the individual frequencies becomes too low when too many frequencies are used.

The phases, ψ_i, are given random values between 0 and 2π for each frequency. The waveform is therefore

$$E = E_{\mathrm{dc}} + \sum_{i=1}^{N\,\mathrm{Freq}} \sqrt{2} a_i \sin\left(2\pi f_{n_i} t + \psi_i\right) \tag{2.33}$$

where $a_i = a_{\min} \cdot f_i^{-\log_{10}(2)}$ and E_{dc} is the signal produced from the function generator without the ac component. The current response to the potential waveform is

$$I = I_{\mathrm{dc}} + \sum_{i=1}^{N\,\mathrm{Freq}} \sqrt{2} I_i \sin\left(2\pi f_{n_i} t + \varphi_i\right) \tag{2.34}$$

With the slow dc component, the sampled current waveform is no longer strictly periodic. If a constant slope signal is present in addition to the ac components, then the FFT treats this as though it is periodic, i.e., similar to a sawtooth waveform. This sawtooth has frequency components at the fundamental frequency and at higher frequencies that will introduce errors at these frequencies, even though the FFT signal correctly calculates the dc component of this slope. This baseline effect was corrected for using the dc components of the last two transformed time series to estimate the slope in the next time series and subtract it before transformation. After baseline correction, the measured current and potential sig-

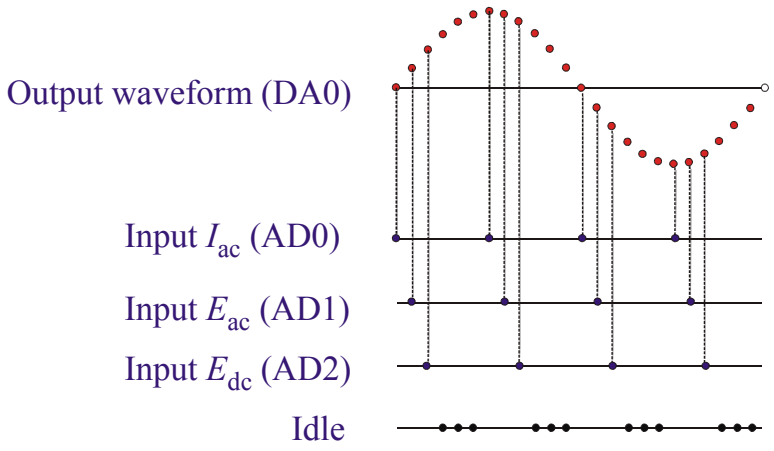

Figure 2.8: Timing diagram for DAC output and ADC sampling.

nals were fast-Fourier transformed, and converted to impedance by division of the complex transformed potential by the complex transformed current.

As indicated in Figure 2.8 (only one sine wave is shown for simplicity), the sampling of the three channels is not simultaneous. These are sampled at equal intervals δt, which introduces an apparent phase shift of $\phi = 2\pi f \delta t$ radians. Since this known for each frequency, it can be corrected for by multiplying the calculated impedance at that frequency by $\exp(-\mathrm{i}\phi t)$ [17]. The idling cycles reduce the amount of data that needs to be written to f le to prevent possible buffer overruns, but idle cycles were not found to be necessary in this work.

Because there are continuous uninterrupted time-series of potential and current available for analysis it is possible to center the period T to be transformed at any desired potential around the voltammogram. Accordingly, the potential intervals at which impedance spectra are calculated are limited only by the sampling rate, and can be chosen to be independent of the period T. Overlapping periods may be transformed, and multiple periods may be transformed in order to signal average. The software handles all these cases with a single pass through the f le of raw sampled data.

There are some constraints on the transform period or its reciprocal, the minimum fre-

quency. As with ac voltammetry, the most basic restriction is that the dc potential should not change too much during one cycle at the lowest frequency:

$$\frac{Fv}{RT} \ll 2\pi f_{\min} \tag{2.35}$$

This relationship was derived for a reversible solution reaction by Bond et al. [5] and by Harrington [29] for a surface reaction. At a practical slow sweep rate of $10\,\mathrm{mV\,s^{-1}}$, this limits to minimum frequency to about 1 Hz. Garland et al. [17] has also discussed the condition that the dc current should not change much during a period,

$$\left|\frac{d\tilde{j}}{dt}\right| \ll \left|\tilde{j}_{\min}\right| 2\pi f_{\min} \tag{2.36}$$

where $\left|\tilde{j}_{\min}\right|$ is the rms amplitude of the lowest frequency current component. In our work these restrictions were satisf ed by maintaining the following relationship between sweep rate and minimum frequency

$$f_{\min} = 200\,\mathrm{V^{-1}}\,v \tag{2.37}$$

2.3.2.3 Experimental conditions

All the dummy cells used in this study were constructed using standard resistors and capacitors. Standard EIS experiments (at constant dc potential) were conducted for comparison to the dEIS results. The frequency range used in the EIS experiments was 0.1 Hz to 80 kHz with a perturbation of 5 mV rms. Unless noted otherwise, the dc potential was kept at 0 V for every EIS experiment. Both experiments were run using the Gamry potentiostat's built-in functions and slightly augmented software scripts. Note, in order to avoid confusion, $\mathrm{i} = \sqrt{-1}$, and j is the current density. Impedance data were f tted to the equivalent circuit

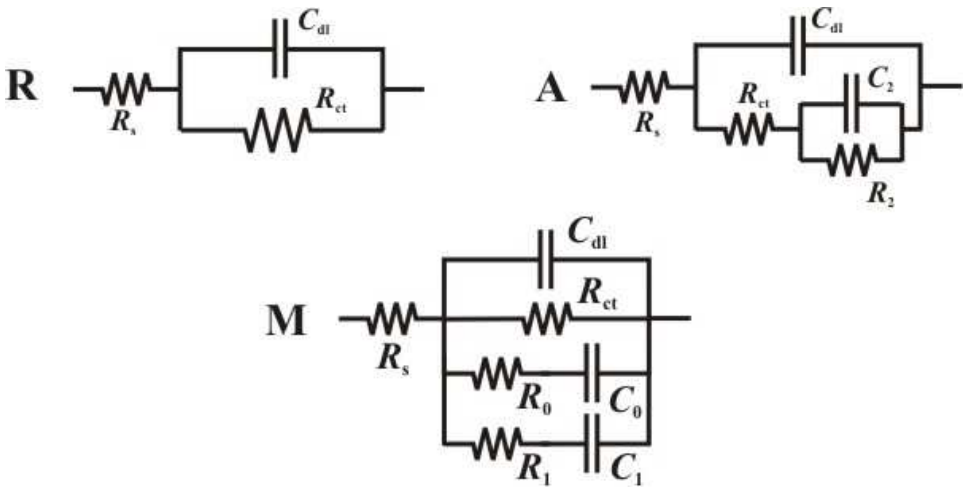

Figure 2.9: Dummy cells used in for testing our dEIS system.

models using ZSimpWin.

2.3.3 Testing and validation of the instrumental setup

2.3.3.1 Comparison between EIS and dEIS experiments

A number of dummy cells were created to test various limits of the dEIS system (Figure 2.9). A series of circuits, **R**, that model a simple electron-transfer process at an interface were used, with varying resistance and capacitance to investigate both scaling and sensitivity limits of the system. In addition, two other circuits were used to show how more complicated circuits with numerous elements, such as a redox reaction with adsorption, **A**, or several competing adsorption processes, **M**, could be solved to a high degree of precision and accuracy at steady and sweeping potentials of various scan rates. The values of the resistors and capacitors used were chosen to be those that might be expected in an electrochemical process.

Potentiostatic EIS using the Gamry REF600 was done in order to obtain accurate impedance data of each of the dummy cells at $E_{\mathrm{dc}} = 0\,\mathrm{V}$. These values were assumed to be correct and the data obtained from dEIS were then compared to them. The EIS fre-

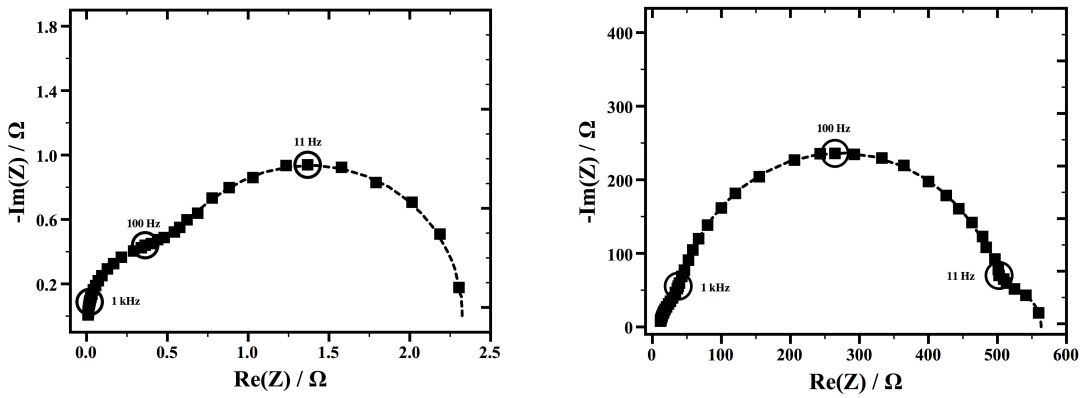

Figure 2.10: Nyquist plots of circuits **A** (left) and **M** (right) as measured by dEIS at a stationary potential of 0 V. The sample period was 1 s, which corresponded to $f_{\min} = 1$ Hz, and was taken after 29 periods were measured. The dash curves are least-squares f ts to the data.

quency range was 80 kHz to 0.1 Hz, with the perturbation amplitude of 5 mV rms. The measurement times for a single low noise EIS scan and a fast EIS scan using the built-in Gamry procedures were found to be 15 min and 5 min, respectively. The experiments had high reproducibility and precision and there were no statistical differences between the low noise and fast scan results.

The dEIS system is capable of both steady-state EIS, chronoamperometric EIS, and potential sweep EIS experiments. The sample period for each experiment is def ned as $T = 1/f_{\min}$; therefore if the minimum frequency is 1 Hz, then the sample period is 1 s. Each of these experiments was done on dummy cells to show whether or not the system could obtain accurate and precise results.

Dummy cells composed of linear elements (Figure 2.9) were used in the characterization of the system. Figure 2.10 shows the obtained impedance spectra measured by the dEIS at 30 s (30^{th} period) system along with the circuit f ttings for circuits **A** and **M**. The values were found to be within 0.5% of the EIS experimental values and were within the statistical range of the data f t error.

Circuit **M** was analyzed at $E_{\text{dc}} = 0$ V for 30 s. During this time 30 impedance spectra

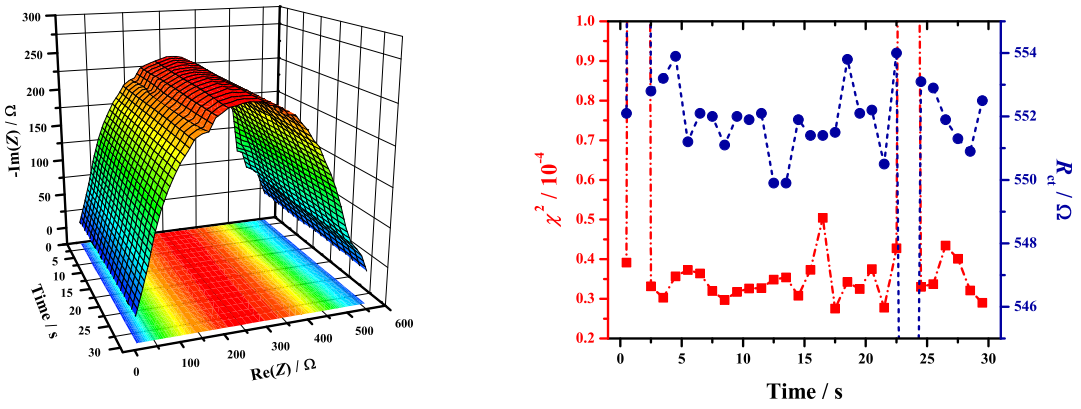

Figure 2.11: The complete time-dependent dEIS scan of circuit **M** at a steady dc potential of 0 V. The right plot shows the R_{ct} and χ^2 values from the calculated f t (outliers are outside the plot range).

were acquired, one for every 1 s waveform period, shown in Figure 2.11. The f rst couple of spectra showed some randomness in the lowest frequency data points. Both the f tted χ^2 and R_{ct} values are given for each period to show the consistency of the impedance spectra. The average R_{ct} value was calculated to be 556.0±4.2 Ω even including the two outliers at 2.5 and 23.5 s. Each element had a standard deviation of lower than 1.5% throughout the 30 s of acquisition, which was within the calculated error of the data f t.

In addition to the constant potential experiments, potential sweep experiments were conducted. The potential was scanned from -0.4 to 0.4 V with a scan rate of 5 mV s^{-1} so that the conditions in Equation 2.37 could be met. Again, the waveform period was of a length 1 s, which corresponds to a spectrum every 5 mV. Circuit **A** was used to test any error associated with changing the dc potential. Figure 2.12 shows similar errors to that of the constant potential experiments meaning that scanning the potential does not produce any signif cant errors. The plot of R_{s} is given as to show the stability of the high frequency impedance across the varying potential. The precision and accuracy with which R_{s} can be obtained is important as it is used to solve for C_{dl} when using CPEs in a real electrochemical cell. Here, R_{s} has a standard deviation of 0.02 Ω, which is well within the f tting error.

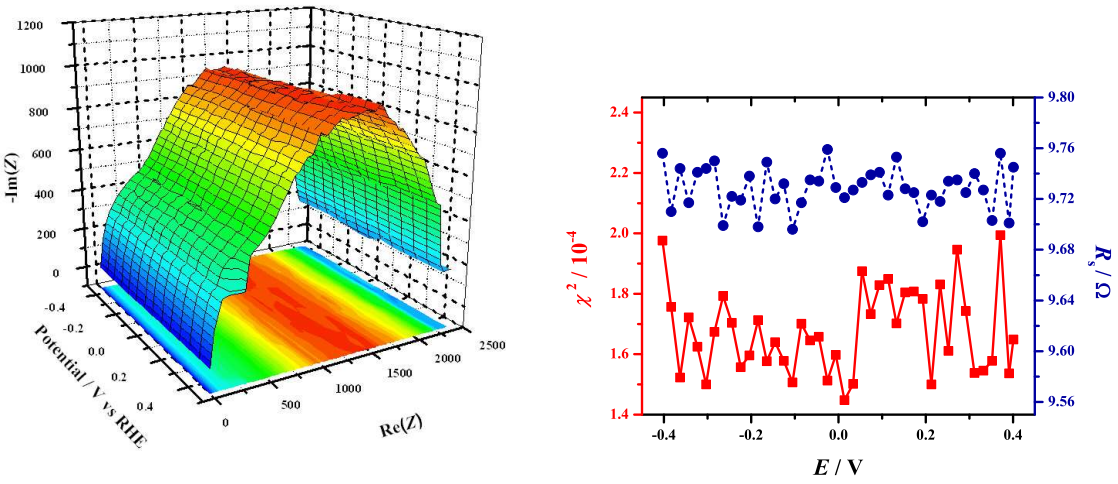

Figure 2.12: The complete dEIS scan of circuit **A** from -0.4 V to 0.4 V at 5 mV s^{-1} is shown on the left. The right plot shows the R_s and χ^2 values from the calculated f t.

Table 2.1: Summary of the f tting results to circuit **A** at various sweep rates. Impedance spectra from -0.4 V to 0.4 V were used to provide the average values of the elements.

v / mV s^{-1}	R_s/Ω	$C_{dl}/\mu F$	R_{ct}/Ω	$C_2/\mu F$	$R_2/k\Omega$	$\chi^2/10^{-4}$
EIS	10.07	1.75	825	8.22	1.50	0.3
5	9.73	1.78	818	8.16	1.49	1.7
10	9.83	1.77	820	8.17	1.49	1.0
20	10.08	1.74	823	8.28	1.51	0.9
50	10.25	1.71	821	8.23	1.49	2.2

Scan rates of 5, 10, 20 and 50 mV s^{-1} were used and the impedance were calculated between -0.4 V and 0.4 V at intervals of 5 mV. The minimum frequency was kept constant at 1 Hz. Table 2.1 shows the summarized data of the fitted elements at various scan rates. There was no statistical effect of the sweep rate between the obtained values at these scan rates and the stationary result. The 50 mV s^{-1} scan does seem to manifest more error around the potential limits, though that could be an artifact from switching directions.

Equation 2.35 suggests that as the scan rate increased, the results might show artifacts from the dc potential changing on the timescale of the minimum frequency. However, these equivalent circuits are linear and will not show this effect. Because of this, the speed at which potentials are reached has no bearing on the measurement of the low frequency responses other than to increase the error.

2.3.3.2 Time-constant dependence

The sensitivity of the system was tested by changing the resistor and the capacitor value of circuit **R**. Keeping the capacitor constant at 10 μF, the resistor was systematically changed from 100 Ω to 100 kΩ. R_{s} was kept constant at 10 Ω so the scale of the current AD converted in the dEIS module could also be kept constant between experiments.

As the resistance increases, the current response due to f_{min} decreases according to Ohm's law $(E = IR)$ and the time constant of the parallel combination capacitor and resistor, and so the limit of detection of the current response of the lower frequencies may be obtained. A summary of the data obtained from both EIS and dEIS is given in Table 2.2. From this, it can be seen that for resistor values under 50 kΩ, the dEIS system was able to measure the lower frequency responses to a high degree of accuracy and precision. For the higher resistance circuits, the error in R_{ct} is likely due to the lack of sufficiently low frequencies to define a complete semicircle. This potentially could be solved by going to lower frequencies, but a test using a waveform from 0.1 Hz to 1.3 kHz worsened the higher

Table 2.2: Set of the circuits of the form **R** used for testing the effects of resistor values on dEIS system's response.

R_{s}/Ω		$C_{\mathrm{dl}}/\mu\mathrm{F}$		$R_{\mathrm{ct}}/k\Omega$		$\chi^2/10^{-5}$	
EIS	dEIS	EIS	dEIS	EIS	dEIS	EIS	dEIS
10.04	10.06	9.88	9.87	0.0990	0.0988	0.35	5.47
10.04	10.00	9.88	9.91	0.827	0.832	0.54	3.39
10.03	10.01	9.89	9.89	5.50	5.43	3.33	4.23
10.03	10.04	9.88	9.87	10.05	9.91	8.61	8.41
10.04	9.97	9.88	9.86	47.02	46.29	2.14	13.51
9.91	9.98	9.88	9.94	98.99	98.29	1.51	7.41
	8.2*		10.*		90.03*		7.7*

* Frequency range of the waveform is 0.1 Hz to 1.3 kHz

frequencies' accuracy.

One strategy is to measure low and high frequency ranges separately. There was not perfect agreement between 0.1 Hz to 1.3 kHz and 10 Hz to 54 kHz scans, but combining only the lower frequency measurements (0.1 Hz–0.9 Hz) with the 10 Hz to 54 kHz scan gave accurate f ts to the impedance.

A second series of circuit **R** was made for testing the effects of the capacitors. Keeping the resistor constant at 5 kΩ, the capacitor values ranged from 0.5 μF to 20 μF. The table below gives results from f tting the exact circuit parameters to the plot obtained from dEIS at 30 s and standard EIS. The values obtained from the dEIS experiment are in close agreement with their EIS counterparts. The R_{ct} and C_{dl}values obtained by dEIS are within the experimental errors of EIS. As in all other cases, there was no statistical benef t in adding an inductor in series with R_{s} in the f tted circuit to compensate for phase shifts due to cabling and instrumentation.

From Table 2.3 one can see as C_{dl} increases, the f tted R_{ct} value decreases for the dEIS data. The higher error in the parallel resistor, in reference to the standard EIS experiment, is due to the fact that the lowest measured frequency in dEIS was 1 Hz while that in EIS was 0.1 Hz. Also, the density of points in the f rst decade for dEIS is limited to f ve frequencies, thereby giving fewer data points on the right-hand side of the semicircle. A dEIS scan was done on the circuit with the 18 μF capacitor with $f_{\mathrm{min}} = 0.1$ Hz. The resulting R_{ct} was found to be 5.45 kΩ, while R_{s} was found to be between 5-50 Ω. This shows that value of the capacitor does not limit the ability of the FFT to resolve the response signal; rather the frequency range is the limiting factor. Again, a low frequency scan was used to test the range of the usable frequencies and to ascertain if data from a high and low frequency scan could be added together to produce a complete spectrum. It was found that the data could be summed together to produce a valid impedance spectrum with extended frequency range and density. The f tting error did not improve signif cantly as a result of combining the two

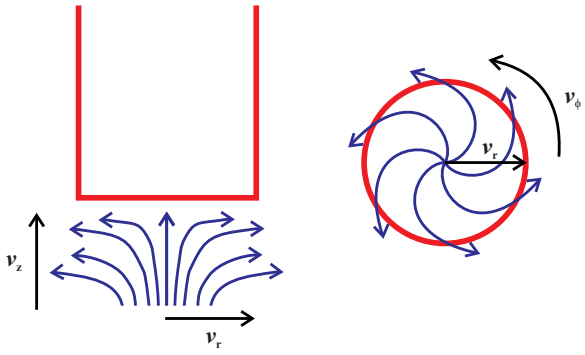

Figure 2.13: Flow profile of a rotating disk electrode.

spectra.

2.4 Rotating disk electrode

There exist several books on the hydrodynamics and electrochemistry of the rotating disk electrode (RDE) [30–32]. Essentially, rotation of the disk (rate given as ω having units of rad s^{-1}) causes drag in the solution which then causes solution near the disk to flow parallel to the disk from the center to the perimeter (Fig. 2.13). This flow in turns creates a flow towards the electrode surface.

Controlling the mass transport has advantages in that the kinetics of the system can be studied in more detail. If a reaction rate occurs along the same time scale as mass transport then the current is a complicated function of mass transport (time) and potential. The deconvolution of these two variables is difficult without a way of controlling the mass transport. Figure 2.14 shows the concentration profile during a potential step experiment with and without mass transport control. When the electrode is not rotating, the flux of the species at the surface deceases with time (as it is related to the slope of the C-z curve at $z = 0$), and with it, the current. However, upon disk rotation the concentration profile is quickly established and becomes independent of time.

Table 2.3: Set of the circuits of the form **R** used for testing the effects of capacitor values on dEIS system's response.

R_s/Ω		C_{dl}/μF		$R_{ct}/k\Omega$		$\chi^2/10^{-5}$	
EIS	dEIS	EIS	dEIS	EIS	dEIS	EIS	dEIS
9.98	9.91	0.69	0.69	5.507	5.521	5.0	12.1
10.05	9.87	1.59	1.61	5.511	5.483	5.5	34.7
9.92	9.89	5.72	5.73	5.504	5.436	2.3	15.3
10.04	10.04	9.89	9.87	5.501	5.434	3.3	4.2
9.87	9.86	18.09	18.18	5.496	5.443	7.5	10.6
	8.7*		20.7*		5.45*		20.4*

* Frequency range of the waveform is 0.1 Hz to 1.3 kHz

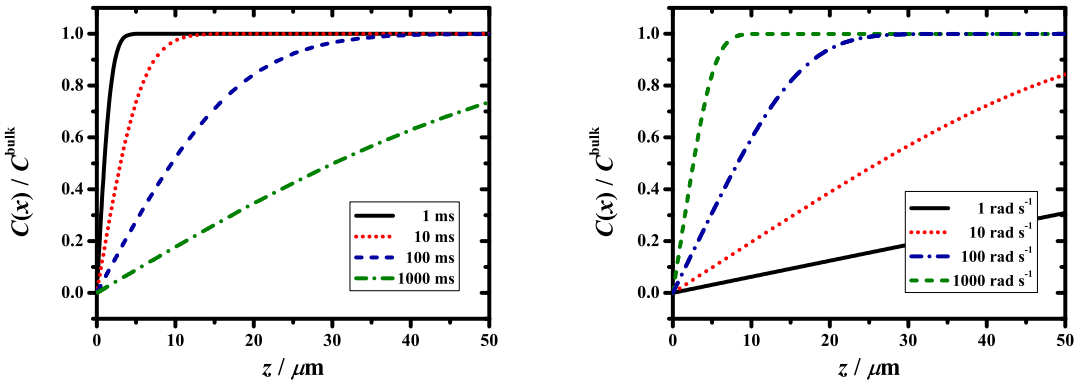

Figure 2.14: Concentration prof les of a diffusion controlled ($\omega = 0$) reaction at different times (left) and at different electrode rotation rates at steady state (right).

The derivation of the concentration prof le and thereby the f ux of species in solution toward the surface begins with solving the f ow f eld caused by rotating a disk. The Navier-Stokes equations for cylindrical coordinates (r, ϕ, z)–assuming no edge effects and taking into account axial symmetry–have the form

$$\frac{\partial v_r}{\partial r} + \frac{v_r}{r} + \frac{\partial v_z}{\partial z} = 0 \tag{2.38}$$

$$v_r \frac{\partial v_r}{\partial r} - \frac{v_\phi^2}{r} + v_z \frac{\partial v_r}{\partial z} = -\frac{1}{\rho}\frac{\partial p}{\partial r} + \nu \left[\frac{\partial^2 v_r}{\partial r^2} + \frac{\partial}{\partial r}\left(\frac{v_r}{r}\right) + \frac{\partial^2 v_r}{\partial z^2} \right] \tag{2.39}$$

$$v_r \frac{\partial v_\phi}{\partial r} - \frac{v_\phi v_r}{r} + v_z \frac{\partial v_\phi}{\partial z} = \nu \left[\frac{\partial^2 v_\phi}{\partial r^2} + \frac{\partial}{\partial r}\left(\frac{v_\phi}{r}\right) + \frac{\partial^2 v_\phi}{\partial z^2} \right] \tag{2.40}$$

The no-slip boundary condition gives the velocity components (shown in Fig. 2.13) at the surface

$$v_r = 0 \tag{2.41}$$

$$v_\phi = r\omega \tag{2.42}$$

$$v_z = 0 \tag{2.43}$$

Far away from the surface there is only f ow toward the disk, i.e.

$$v_r = 0 \tag{2.44}$$

$$v_\phi = 0 \tag{2.45}$$

von Karman showed that the slow equations are separable, and can be written in terms of

three functions of the non-dimensionalized distance from the surface, ζ [32].

$$\zeta = z\sqrt{\frac{\omega}{\nu}} \tag{2.46}$$

$$v_r = r\omega F(\zeta) \tag{2.47}$$

$$v_\phi = r\omega G(\zeta) \tag{2.48}$$

$$v_z = -\sqrt{\nu\omega}H(\zeta) \tag{2.49}$$

where v is the kinematic viscosity (for water $v \approx 0.01$ cm^2 s^{-1}) and ω is the angular velocity or electrode rotation speed. Substituting the above equations and boundary conditions into the Navier-Stokes equations and solving the differential system provides solutions for $F(\zeta)$, $G(\zeta)$, and $H(\zeta)$.

$$F(\zeta) = a\zeta - \frac{\zeta^2}{2} - \frac{b\zeta^3}{3} + \ldots \tag{2.50}$$

$$G(\zeta) = 1 + b\zeta + \frac{a\zeta^3}{3} + \ldots \tag{2.51}$$

$$H(\zeta) = -a\zeta^2 + \frac{\zeta^3}{3} + \ldots \tag{2.52}$$

$$a = 0.510233;\ b = -0.61592 \tag{2.53}$$

The hydrodynamic boundary thickness layer, $\delta_H = \sqrt{v/\omega}$, is about ten times greater than the diffusion layer thickness, δ

$$\delta \sim \left(\frac{D}{\nu}\right)^{1/3} \delta_H \tag{2.54}$$

where D is the diffusion coeff cient of the species of interest. Over this distance the velocity components can be approximated by using only the f rst term in the series (2.50)–(2.52) to

give

$$v_r = r\omega F(\zeta) \approx a\omega^{3/2}\nu^{-1/2}rz \tag{2.55}$$

$$v_\phi = r\omega G(\zeta) \approx r\omega \tag{2.56}$$

$$v_z = \sqrt{\nu\omega}H(\zeta) \approx -a\omega^{3/2}\nu^{-1/2}z^2 = -Bz^2 \tag{2.57}$$

The flux of a solute with concentration c towards to the disk is given by

$$\boldsymbol{J} = D\nabla^2 c - \boldsymbol{v}\cdot\mathrm{grad}\, c \tag{2.58}$$

Substituting this into the continuity equation, which describes conservation of solute, using the approximation in Eq. (2.57), and noting that the concentration depends on neither ϕ (symmetry) nor r (uniform accessibility), gives the convective diffusion equation

$$\frac{\partial c}{\partial t} = D\frac{\partial^2 c}{\partial z^2} - v_z\frac{\partial c}{\partial z} \approx D\frac{\partial^2 c}{\partial z^2} + Bz^2\frac{\partial c}{\partial z} \tag{2.59}$$

This result means that we need only the axial component of the flow field, Eq. (2.57), to solve for the mass transport. The concentration profile can be solved for at steady state ($\frac{\partial c}{\partial t} = 0$) and the diffusion layer thickness can be obtained as

$$\delta = 1.6117D^{1/3}\omega^{-1/2}\nu^{1/6} \tag{2.60}$$

meaning that the diffusion layer thickness is a function of rotation rate.

For an anodic reaction, the current and the flux at the surface are proportional (but of opposite signs) and so when mass transport is slow compared to the reaction rate ($c(0) = 0$)

the limiting current is

$$j_{\mathrm{L}} = -nFD\left.\frac{\partial c}{\partial z}\right|_{z=0} = nFD\frac{c(\infty)-c(0)}{\delta} = nFD\frac{c^*}{\delta} \tag{2.61}$$

where n is the total number of electrons produced in the oxidation. The Levich equation is obtained by substituting Eq. (2.60) into Eq. (2.61)

$$j_{\mathrm{L}} = 0.620nFc^*D^{2/3}v^{-1/6}\omega^{1/2} \tag{2.62}$$

If the kinetics of the reaction are along the same time scale as mass transport then the current for a reaction that is f rst order in concentration can be described by

$$j = nFkc(0) = -nFD\left.\frac{\partial c}{\partial z}\right|_{z=0} = nFD\frac{c(\infty)-c(0)}{\delta} \tag{2.63}$$

where k represents the overall reaction rate. Solving for $c(0)$ and then substituting back into Eq. (2.63) gives the Koutecky-Levich equation.

$$j_{\mathrm{KL}} = \frac{nFkDc^*}{(D+\delta k)} \tag{2.64}$$

We used the rotating disk electrode (RDE) technique in our studies of carbon monoxide oxidation on palladium in Chapter 4. The experiment was carried out in a typical glass cell for RDE experiments. The glass cell accommodated the RDE, reference electrode cell, and Pd counter electrode, as well as one or two gas bubblers. The rotating disk tip (Pine Instrumentation, E8) was a polytetraf uoroethylene (PTFE or Tef on©) rod with a Pd disk embedded in the end. The RDE tip was polished by a series of diamond/alumina compound pastes, with particle size from 5 μm to 0.05 μm and then rinsed thoroughly before

sonication for 10 min in Millipore water. The RDE was then placed in the cell in a hanging meniscus conf guration with the meniscus forming at the edge of the PTFE rod unless noted otherwise. The RDE was driven by the Modulated Speed Rotator (Pine Instrumentation, AF-MSRX), with the rotating speed controlled over a wide range from 100 to 5000 rpm (or 10.5 to 523.6 rad s^{-1}). The reactions we investigated involved adsorption and were kinetically slow with regards to mass transport, therefore we normalized the current to the electrochemical surface area and not the geometric area.

Chapter 3

Dynamic impedance study of oxide growth on Pd and Pt in acid

3.1 Abstract

Dynamic electrochemical impedance spectroscopy (dEIS) is used to elucidate the kinetics and mechanism of oxide growth at palladium and platinum polycrystalline electrodes. This method enables a high density of points when f tting equivalent circuits at slowly changing potentials. The faradaic impedance is shown to be affected by sweep rate. Care should be taken when using mechanistic analysis in conjunction with equivalent circuits as subtle differences in mechanisms are not always manifest in equivalent circuits. We review existing spectroscopic data and provide a ref nement to the mechanism of oxide growth.

3.2 Introduction

There has been extensive research on oxide growth at platinum and palladium surfaces in acidic media, and several reviews exist [33–35]. The kinetics of thin anodic oxide f lms

(referred to as α-oxide) have been studied using various types of electrochemical techniques: chronoamperometry, cyclic voltammetry, and differential capacitance measurements. However, there have been slight disagreements in the potential dependence of the components of the rate law. The literature has yet to settle on the precise mechanism of the anodic process, though schemes have been developed and tested. Studying the mechanism is diff cult because there are a limited number of *in situ* spectroscopic techniques that allow for precise study and characterization of oxide formation and reduction on Pt and Pd. A number of *ex situ* techniques have been utilized, namely low energy electron diffraction (LEED) [36] and scanning tunneling microscopy (STM) [37–39]. They have given insight into the structural reconstruction that occurs during oxidation-reduction cycles. X-ray photoelectron spectroscopy (XPS) has been used to investigate the chemical composition of the thin oxide f lms [40], and it has been shown that the α-oxide is composed primarily of Pt(II) species (or Pd(II)). Electrochemical quartz crystal microbalance (EQCM) [41, 42] provided an *in situ* technique for analyzing the change in mass due to oxide growth.

There have been a number of mechanisms proposed to explain both the kinetic data and the spectroscopic data. In the 60's, Böld and Breiter [43] used a simple electrosorption model with a Temkin exponential factor to explain the voltammogram shape and transient currents. Later, Vetter and Schultze [44, 45] introduced the place exchange model where the metal oxide "f ips" after oxygen electrosorption. Macdonald's group has introduced a point defect model, though it is primarily used for thicker f lms [40, 46]. Van der Geest and Harrington [21] chose to explain the oxidation-reduction mechanism in terms of surface reconstruction due to metal atoms popping out of the lattice after oxygen electrosorption and undergoing surface diffusion. Since new spectroscopic data has emerged we provide an updated model to that presented in [21]. We also critique the place exchange model.

Dynamic electrochemical impedance spectroscopy (dEIS) is unique in that while it can be used routinely, similarly to cyclic voltammetry, it is powerful enough to allow for

studying electrochemical processes as it has the ability to characterize the surface though impedance. Furthermore, it can be used while the system is undergoing classical electrochemical experiments both stationary and dynamic. Harrington's group has utilized ac voltammetry to collect dynamic impedance spectra, however there are two main shortcomings to this method: 1) long collection time; 2) poor reproducibility. The former comes from the fact that the experiment must be repeated for each frequency desired in the impedance spectra. The system must be identical during the measurement of all the frequencies. Ragoisha et al. [25] have described a dEIS system and used it to analyze the properties of the double layer and oxide growth of Pt, though no mechanistic details were discussed. We here describe a series of experiments where dEIS is used to expand our understanding of the electrode interface and oxide growth on Pt and Pd.

3.3 Experimental

3.3.1 dEIS setup

The instrumentation details and the experimental setup has been described previously [7] and only a brief description is given here. The "dc" voltammetry sweeps and the multisine waveform were synthesized by separate function generators. The signals were added together before being applied to the cell *via* a potentiostat. The potential and current were continuously digitized by an acquisition module and recorded to a data file. After an experiment, the raw data was Fourier transformed and converted into impedance spectra at chosen intervals (here 5 mV) and ac voltammograms. The multisine ac waveform consisted of 46 frequencies from 25 kHz to 2 Hz and followed the rules as developed by Popkirov and Schindler [9], Roy's group [12, 17], and Sacci [7]: 1) each frequency in the waveform had an integer number of periods in the waveform period, $T = 1/f_{\text{min}}$; 2) the rms amplitude for the individual sine waves decreased by a half for every decade increase in the frequency; 3)

the phases of the individual sine waves were randomized; 4) the maximum amplitude of the ac waveform was 30–35 mV which corresponded to a maximum amplitude of 4.5 mV rms for the lowest frequency and a minimum of 0.5 mV rms for the highest frequency. The sampling was done on a Keithley-3116 module with a sampling speed of 80 kHz.

3.3.2 Electrochemistry

The electrolyte used was 0.5 M H_2SO_4 (Fluka, puriss) or 0.5 M $HClO_4$ (Fluka, puriss) and the platinum working electrodes (WE) were made by sealing Pt wire (Johnson-Matthey, 99.999%) in a soda glass tube. The counter electrode was a Pt mesh attached to a platinum wire sealed in glass. The palladium WE was spot welded to a copper wire and was degreased in boiling acetone. It was then sealed in FEP/PTFE Dual-Shrink tubing (Zeus, Inc.). All Pt electrodes were first conditioned in fresh piranha solution (7:3 H_2SO_4 to H_2O_2) for 5 min and rinsed prior to being placed in the cell. Pd electrodes were placed in a warm H_2SO_4 bath for 5 min so as to not damage the heat-shrink tubing. While bubbling the electrolyte with ultrapure Ar gas (Praxair, 99.999%) for 10 min, the WE was further conditioned by applying a 100 mV s^{-1} cyclic voltage sweep between 0 and 1.6 V (0.2 and 1.5 V for Pd) for 30 min until the corresponding clean voltammogram at 5 mV s^{-1} could be obtained. All experiments were conducted in a grounded faraday cage. All potentials are given against the reversible hydrogen electrode (RHE), which consisted of a Pt electrode placed in a small glass compartment filled with 0.5 M electrolyte while hydrogen gas was bubbled past the wire. The compartment was separated from the main cell by a Vycor glass joint. There was negligible phase shift throughout the frequency range due to the instrumentation and cell setup.

3.3.3 Normalization to electrochemical surface area

It has been well established that the charge for hydrogen underpotential deposition (H-UPD) on polycrystalline Pt is approx. $220\mu C\,cm^{-2}$ in sulfuric acid. The same smooth Pt wire was used for all the experiments in this report and therefore it was expected that the electrochemical surface area (ESA) should not have changed signif cantly. The H-UPD charge was found to be 29 μC, 30 μC, in $HClO_4$ and H_2SO_4, respectively. This gives the ESA as 0.13 cm^2, which corresponds to a roughness factor of 1.6.

The surface area of the Pd wire was obtained (i) from the double layer capacitance at 0.5 V assuming 25 $\mu F\,cm^{-2}$ (in 0.5 M sulfuric acid) [47] and (ii) by calculating the charge due to oxide reduction grown by sweeping to a positive potential limit of 1.4 V (in 0.5 M perchloric acid). Fresh palladium wires of different lengths were used in this study for each electrolyte. It is diff cult to use the H-UPD charge to obtain the ESA of Pd. This is because the rate of hydrogen absorption into the metal lattice is fast. It has been suggested that the double layer capacitance or the charge from oxide growth (or the oxide reduction) could be used for Pd [34]. The anodic charge for oxide growth is problematic as Pd dissolution is prevalent [34, 48]. We therefore used the oxide reduction charge, $Q_{\mathrm{red}}^{\mathrm{ox}}$, to f nd the ESA of Pd in perchloric acid. The double layer capacitance at 0.5 V in sulfuric acid is thought to be 25 $\mu F\,cm^{-2}$ [47]. We used this to obtain an oxide reduction charge of 360 $\mu C\,cm^{-2}$ when the potential is swept to 1.4 V (50 $mV\,s^{-1}$) in sulfuric acid. This reduction charge was then used to f nd the ESA of the Pd wire used in perchloric acid under the assumption that the amount of oxide grown is independent of electrolyte. A roughness factor of 2.1 was found independently of electrolyte and wire length.

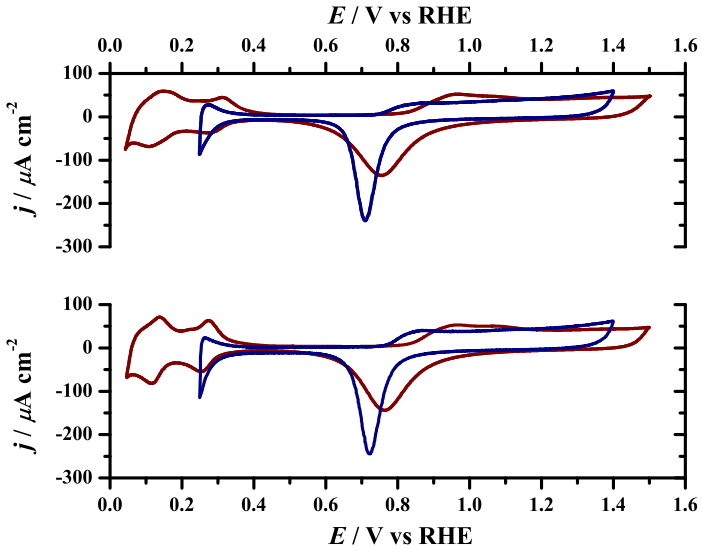

Figure 3.1: Representative voltammograms of platinum (**red**) and palladium (**blue**) in 0.5 M $HClO_4$ (top) and H_2SO_4 (bottom). Sweep rate 50 mV s^{-1}.

3.4 Results

After a general explanation of the cyclic voltammograms, we describe ac voltammograms from the dEIS experiments and then impedance measurements. These experiments will be further discussed by regions in the cyclic voltammograms (Figure 3.1): double layer, oxide growth, and oxide reduction. The H-UPD and H(abs) regions are outside the scope of this chapter, and are not discussed.

3.4.1 Dc voltammetry

Representative voltammograms of palladium and platinum in 0.5 M $HClO_4$ and H_2SO_4 are shown in Figure 3.1. The anodic current beginning near 0.75 V is due to the growth of oxide on the metal surface. In the negative-going sweep a sharp cathodic peak is formed (0.73 V for Pd and 0.78 V for Pt) due to the reduction of the oxide f lm. The difference in the shapes of the anodic and cathodic current suggest that the two possess dramatically different mechanisms. The different electrolytes produce only small differences in the voltammograms

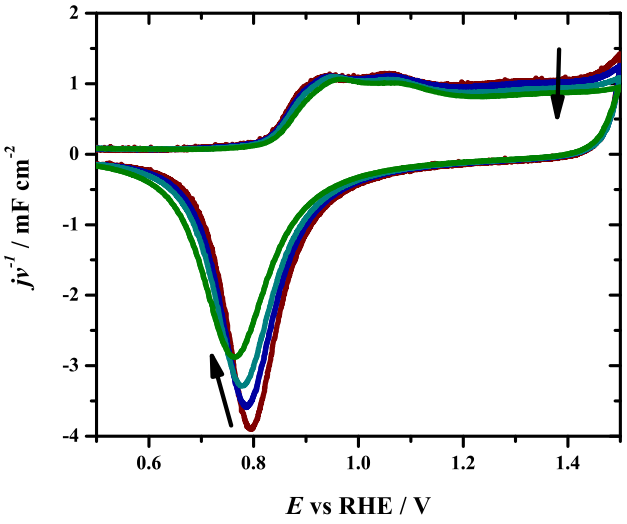

Figure 3.2: Voltammogram of Pt in sulfuric acid normalized to sweep rate. Arrows show the direction of increasing sweep rate: (**red**) 5, (**blue**) 10, (**cyan**) 20, and (**green**) 50 mV s^{-1}.

except for the hydrogen adsorption ($E < 0.3$ V) and onset of surface oxidation (0.75 V for Pd and 0.85 V for Pt). All voltammograms show a clear plateau throughout most of the oxide region (0.9–1.4 V). Pd shows a more level plateau than Pt. The plateau in the current has been described as originating from a zero-order reaction [33, 43, 49].

Subtle differences in surface-dominated processes can be enhanced by normalizing the voltammograms to the sweep rate as in Figure 3.2. The oxide region shows a slight dependence on sweep rate, with more oxide being grown at slower sweep rates. Figure 3.3 shows that the oxide charge decreases as $\log(v)$ increases. The amount of oxide grown is a function of the amount of time spent in the oxide region for both metals.

The reduction peak charge, height, and position are dependent on the amount of oxide grown in the positive going sweep (Figs. 3.2 and 3.3). The peak current for a surface-controlled process is expected to be proportional to the sweep rate, but Figure 3.3 shows signif cant deviations from linearity, likely due to the fact that different amounts of oxide are being reduced (Fig. 3.2). The cathodic peak current, $j_{\mathrm{p}}^{\mathrm{c}}$, and the peak potential, $E_{\mathrm{p}}^{\mathrm{c}}$, are

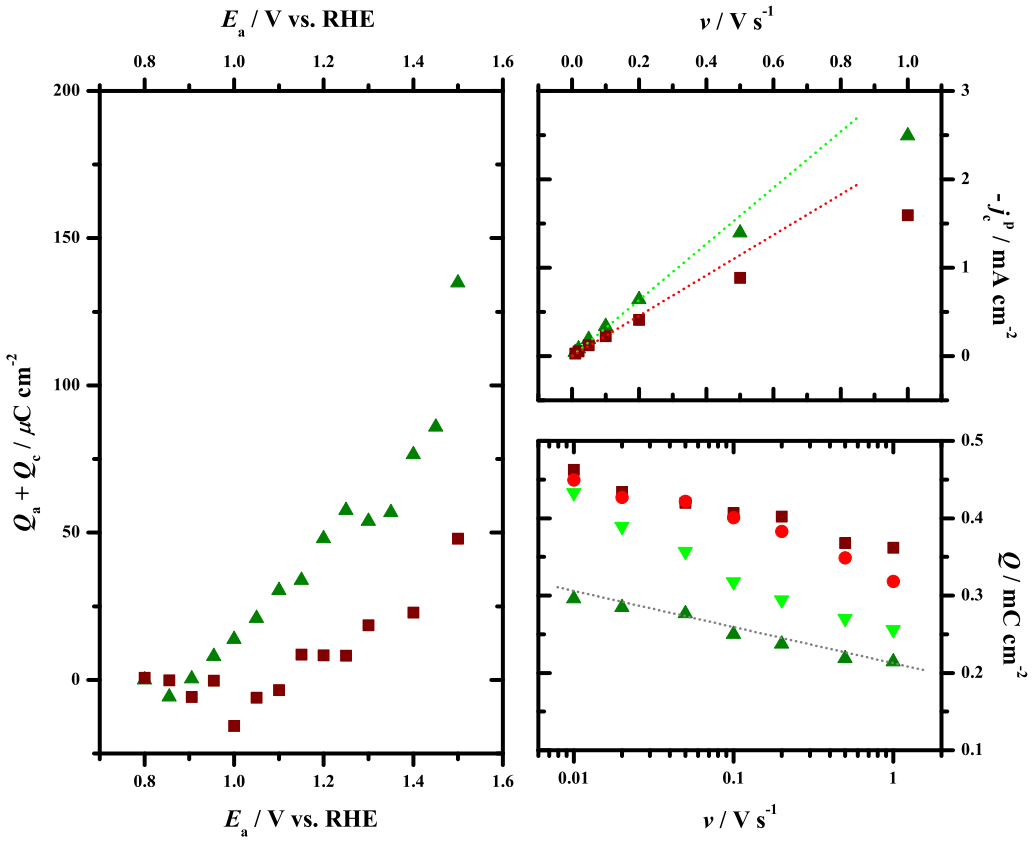

Figure 3.3: Sweep rate dependence oxide growth and reduction. Left: difference in anodic and cathodic charges with sweep reversal potential, E_a, at 50 mV s^{-1}; right top: reduction peak current vs sweep rate; right bottom: anodic charge vs sweep rate. In all plots: **green triangles** (upward and downward), Pd; **red squares** and **circles**, Pt; electrolyte, H_2SO_4. In bottom left plot: lighter shade (circle and downward triangle), $HClO_4$.

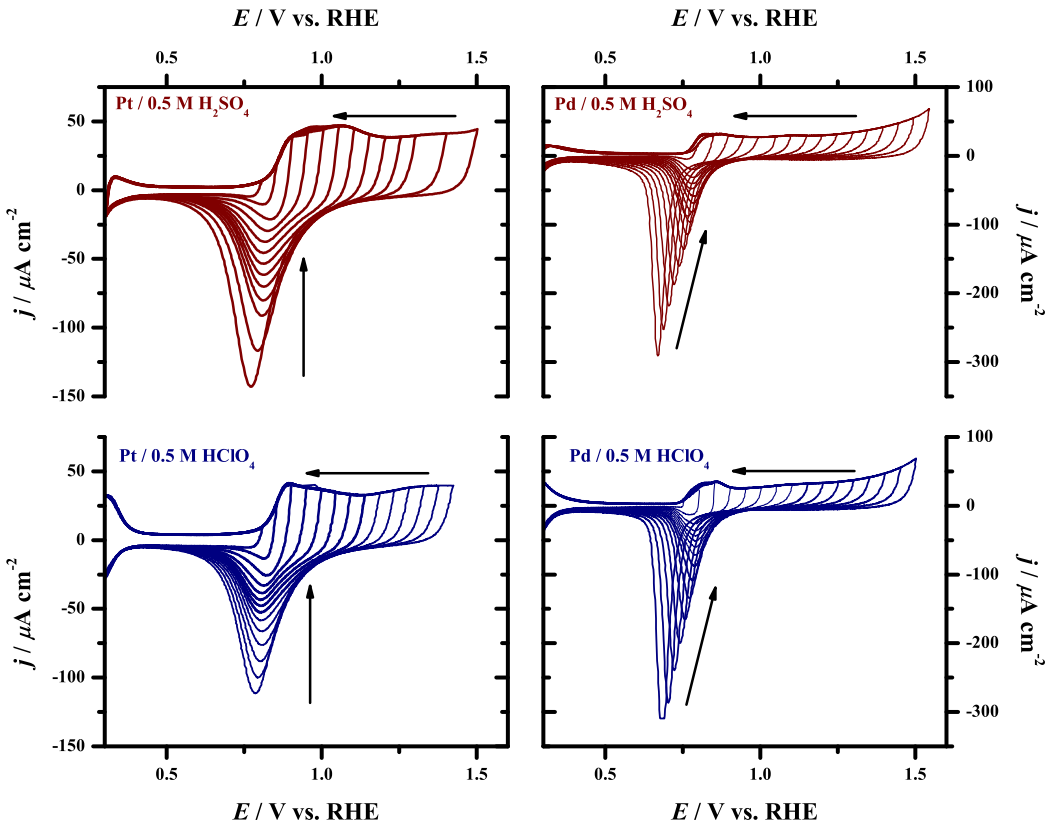

Figure 3.4: Potential limit variations for voltammograms of Pd (right) and Pt (left). Sweep rate of 50 mV s^{-1}.

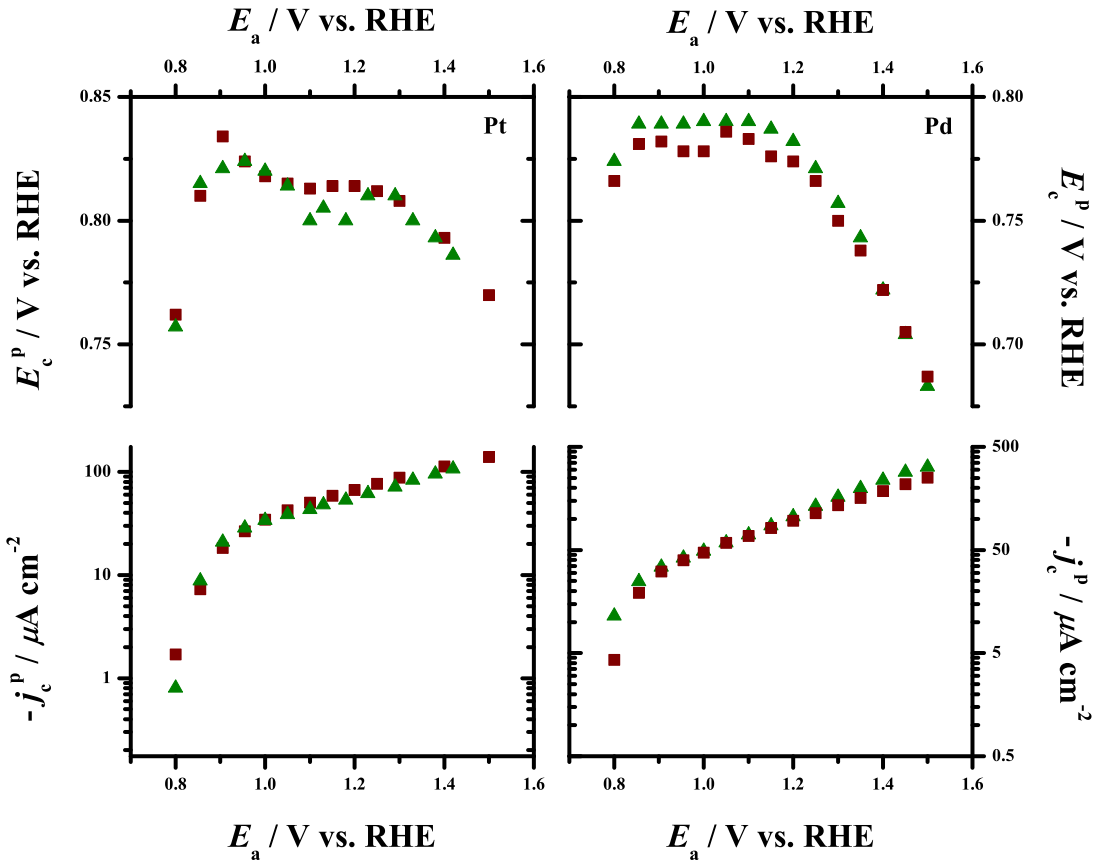

Figure 3.5: Dependence of the oxide reduction peak on the upper potential limit of the cyclic voltammogram. Top plots: peak potential; bottom plots: peak current. **Red squares**, H_2SO_4; **green triangles**, $HClO_4$.

dependent upon the reversal potential, Figs. 3.4 and 3.5. Increasing the amount of oxide grown causes an increase in j_p^c and a decrease in E_p^c at reversal potentials greater than 1.2 V, i.e. the oxide layer becomes more diff cult to reduce as more is formed.

For a reproducible voltammetry cycle to occur the anodic and cathodic charges must be equal. For Pt signif cant deviation from this occurs at reversal potentials greater than 1.4 V while deviation at Pd occurs as low as 1.0 V (Figure 3.3). Higher anodic than cathodic charges implies dissolution of the surface or oxygen evolution. Since there is negligible oxygen evolution below 1.55 V, we can ignore this process for most of the experiments here. We also ignore oxygen reduction as we purged the system of oxygen though Ar-

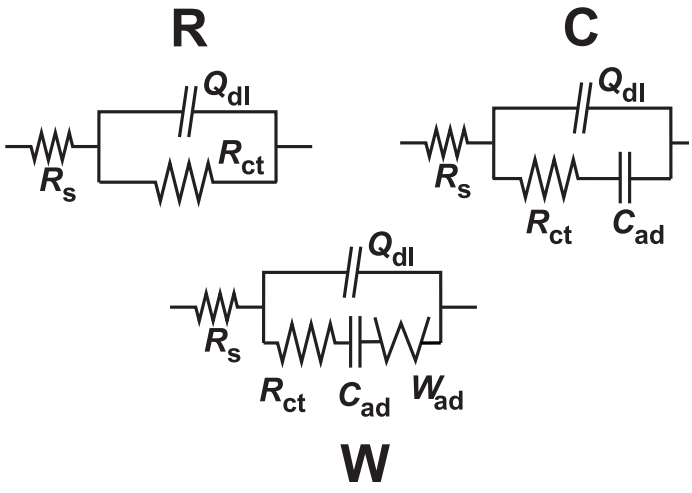

Figure 3.6: Equivalent circuits for double layer and oxide growth regions.

bubbling.

3.4.2 Equivalent Circuits

An equivalent circuit (EC) describing adsorption accompanied by electron transfer has the form of **C** in Fig. 3.6 [21]. Pell et al. [50] used a similar circuit to describe the oxide growth and chloride adsorption on platinum, but used CPEs (symbol Q) in the place of capacitors. CPEs are used instead of capacitors since it has been well established that metal surfaces do not produce perfect capacitive behavior. However, replacement of a capacitor by a CPE introduces an extra fitting parameter, which, in addition to increasing the fit quality, may increase the error of other circuit elements. Pajkossy and Kolb [51–53] and Silbert et al. [54, 55] used **W** to describe adsorption of anions on noble metals in the hydrogen adsorption and double layer regions. In all the models R_{s} describes the uncompensated resistance of the electrolyte and metal wires. Q_{dl} relates to the high frequency capacitance that has classically been converted to the double layer capacitance (Fig. 3.6), C_{dl}, by using

the expression

$$C_{\mathrm{dl}} = (Q_{\mathrm{dl}} R_{||}^{1/\alpha})^{1-\alpha} \tag{3.1}$$

[56] where $R_{||}$ is the parallel combination of R_{s} and R_{ct}, that is $R_{||} = \frac{R_{\mathrm{s}} R_{\mathrm{ct}}}{R_{\mathrm{s}} + R_{\mathrm{ct}}}$. R_{ct} is related to the kinetics of the charge transfer and C_{ad} relates to the change in coverage of the adsorbed species. In model **W**, W_{ad} is said to describe the diffusion of the adsorbed species within the diffusion layer [51].

3.4.3 F-Test statistics

The F-test is used to decide the statistical benef t of adding more parameters into a model. An elementary use of the F-test would be to ask the question, "does the data f t better to a higher order polynomial such as a quadratic than a linear equation?" This is a different question than does a quadratic f t the data more closely, since it is expected that adding more parameters produces better f ts. In other words, the F-test works to remove the bias produced by adding more parameters to arrive at a better model.

The goodness of an equivalent circuit f t to impedance data is calculated in terms of χ^2. The F-ratio is

$$F_{\chi^2} = \frac{\chi^2_{\mathrm{old}} - \chi^2_{\mathrm{new}}}{\chi^2_{\mathrm{new}}} \frac{v_{\mathrm{new}}}{\alpha} \tag{3.2}$$

where v is the degrees of freedom given by $v = 2N_{\mathrm{freq}} + N_{\mathrm{parameters}} - 1$ [57], α is the number of parameters added between "old" and "new" models, and χ^2 is proportional to the sum of squared deviations of the f t.

A larger F_{χ^2} corresponds to a better f t. A statistical test is available to decide if the increase in F_{χ^2} could have arise by chance. The value is compared with a tabulated F value

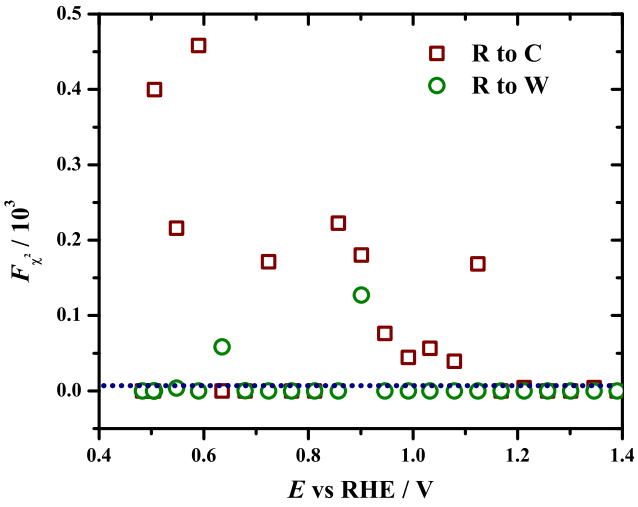

Figure 3.7: F_{χ^2} values obtained from Eq. (3.2) of equivalent circuit fits given as a function of potential of Pt in sulfuric acid. The ECs were compared against circuit **R**, meaning $\alpha = 1$ and $v_{\text{new}} = 94$. Legend given in plot. **Blue** dashed line corresponds to $F_{\chi^2} = 7$. Sweep rate: 5 mV s^{-1}.

using Maple's `Fratio` function for a given v_{new} and α and a confidence value between 0 and 1 is produced. A confidence value of 0.01 means that there is a 1 % chance that the improved fit could have arisen by chance. In other words, a smaller the value equates to more confidence in accepting the new model. For the conditions of this chapter a decrease of 10 % in χ^2 corresponds to a 1 % level, and decreases of 10 % or more were accepted as statistically valid. The F-test is not able to decide between models with the same number of parameters. In this case we looked at the errors of the fitted parameters to see if any were nonsensical. That is, if a fit produced a parameter that had an estimated error of over 50% then that model was considered unacceptable.

Figure 3.7 shows the F_{χ^2} obtain from comparing the fits of circuits **R** to **C** and **R** to **W** as a function of potential. When a data point is above the horizontal line at $F_{\chi^2} = 7$ the new model is statistically valid at the 1 % level. We found that fitting the Pajkossy model, **W**, to our impedance data was not statistically better than fitting circuit **R** and

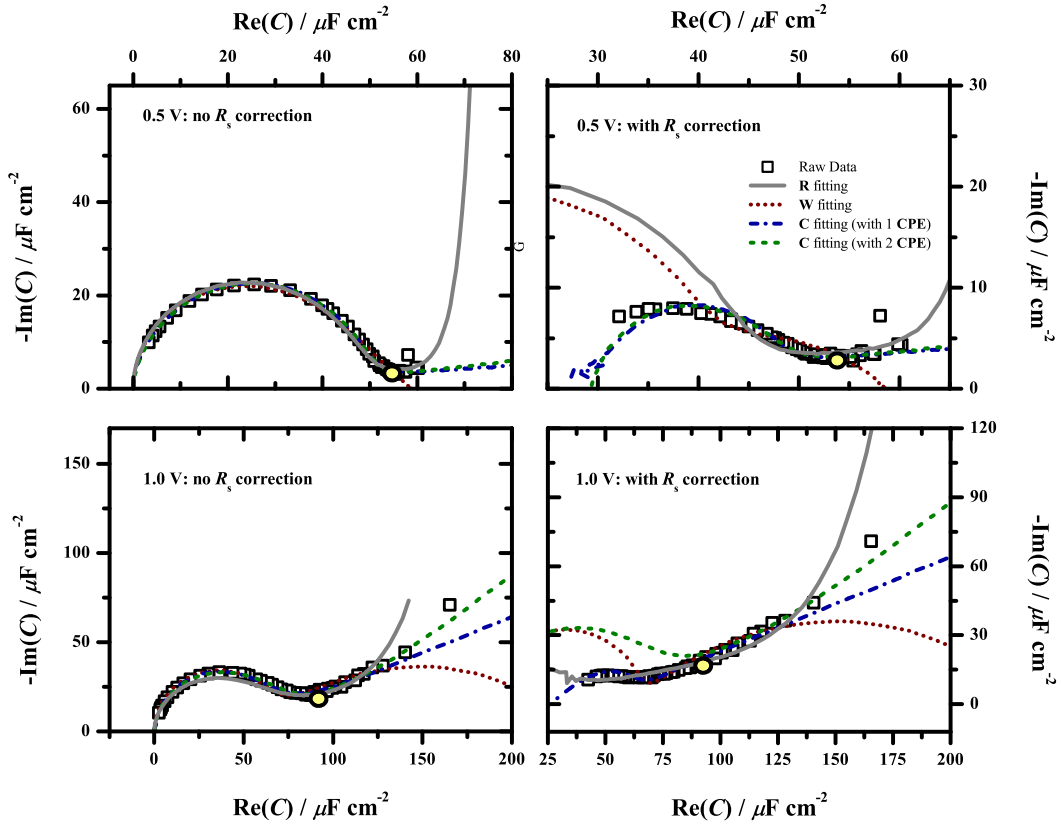

Figure 3.8: Complex capacitance plots from the dEIS experiment of Pt in H_2SO_4 along with f ts of equivalent circuits given in Fig. 3.6. R_s was estimated by linear extrapolation of the high frequency impedance data (5–25 kHz). The value was then subtracted from Re(Z) before the complex capacitance was calculated. Legend given in plot; 150 Hz given by yellow circle. Sweep rate: 5 mV s^{-1}.

the individual elements had high errors. R_{ad} consistently had errors near 100 % thereby making its signif cance dubious. **C** produced higher F_{χ^2} values up to 1.1 V, though "C_{ad}" was found to match the value of C_{dl}, the sum of which was equivalent to the double layer capacitance found from f tting **R**.

Figure 3.8 shows the quality of the f ts in the double layer and oxide growth regions. The impedance data is plotted in the complex capacitance as suggested by Pajkossy and Kolb [58], since representation in the impedance plane is featureless. We show the difference between plotting the complex capacitance plane with and without R_s correction to

highlight the fittings at higher frequencies. In the double layer region (0.5 V), all the fittings converge to the raw data closely throughout the frequency range. After R_{s}-correction, the EC **C** converges to the high frequency data more closely. In the oxide growth region the fittings shows some divergence at frequencies lower than 15 Hz. When R_{s} is compensated for, circuits **R** and **C** converge throughout the frequency range. The F-test does not validate the use of **C** (Fig. 3.7) as the difference between the two plots relies too much on the two frequencies: 6 and 2 Hz.

C convergence was significantly better than **R** in the double layer region but not in the oxide growth region, which suggests that **C** was not modeling the oxide growth, rather it was providing a better model for the non-faradaic impedance. We thus chose to not overinterpret our impedance data and used the **R** circuit for our analysis. The average χ^2 value for fitting **R** to the Pt dEIS data was approximately 9×10^{-4} and that of Pd was 3×10^{-4}. The reason for the absence of C_{ad} from our analysis will be discussed later.

3.4.4 CPE analysis

A particular problem with all of the models is that if R_{ct} is comparable to R_{s} then the fitting routine has difficulty converging. i.e. the relative error becomes near 100%. Given that Conway's group and Pajkossy's group recorded R_{ct} comparable to R_{s} (using circuits **C** and **W**, respectively), that is both were 0.1–10 $\Omega\,\mathrm{cm}^{-2}$ [50, 52, 53], we expect difficulties in batch fitting the impedance spectra to the **W** and **C** circuits. However, if we take the first order approximation that the sum of the faradaic admittance of **W** can be written as a CPE, e.g.

$$Q_{\mathrm{CPE}}(\mathrm{i}\omega)^{\alpha} \approx Q_{\mathrm{R}} + Q_{\mathrm{W}}(\mathrm{i}\omega)^{0.5} + Q_{\mathrm{C}}(\mathrm{i}\omega) \tag{3.3}$$

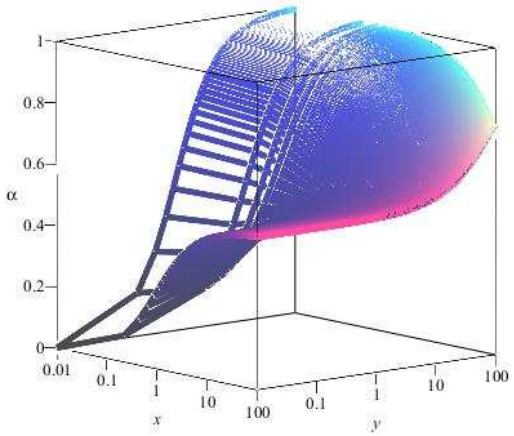

Figure 3.9: Plot of Equation (3.5) with varying x and y.

then we can analyze which (if any) of the terms are dominant. We do this by rearranging Eq. (3.3) and solving for α

$$\alpha \approx \frac{\ln\left(\frac{Q_{\mathrm{R}}+Q_{\mathrm{W}}(\mathrm{i}\omega)^{0.5}+Q_{\mathrm{C}}(\mathrm{i}\omega)}{Q_{\mathrm{CPE}}}\right)}{\ln(\mathrm{i}\omega)} \tag{3.4}$$

or, using dimensionless quantities, α at $\omega = 1$ Hz becomes

$$\alpha \approx \frac{\ln\left(1+\sqrt{\mathrm{i}}x+\mathrm{i}y\right)}{\ln(\mathrm{i})} \tag{3.5}$$

where $x = Q_{\mathrm{W}}/Q_{\mathrm{R}}$ and $y = Q_{\mathrm{C}}/Q_{\mathrm{R}}$. Figure 3.9 shows how the parameter α changes with the ratios of x and y. When Q_{R}, Q_{W}, or Q_{C} dominates, α approaches 0, 0.5, or 1, respectively. However, looking at the region α =0.2–0.8, no term can be said to dominate as the inverse of Eq. (3.5) is not a one-to-one function.

We can plot α as a function of potential and look at regions where the EC can reduce

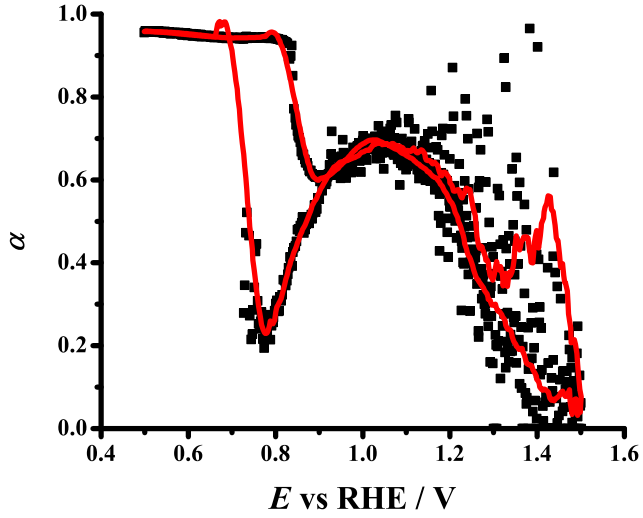

Figure 3.10: α obtained by f tting the dEIS data from Pt by f tting to EC **Q**. **Black** points are the f tting results and the **red** curve is smoothed data. Sweep rate, 5 mV s^{-1}.

down to simpler circuits. Figure 3.10 shows that in the double layer region the faradaic impedance collapses nearly to a pure capacitor. That is, there is no faradaic process in this region. At the onset of oxide growth until 1.2 V we see α converge to 0.6 signifying that there is no dominant element. After 1.2 V, α decreases to near 0 signifying that R_{ct} becomes the dominant term. The reverse sweep follows the same trend with the addition of a drop in α to 0.2 in the oxide reduction region.

3.4.5 Ac voltammetry

Anion effects are demonstrated in the ac voltammograms for Pt and Pd given in Figs. 3.11 and 3.12, respectively. The real admittance voltammograms at 10 Hz are analogous to the dc voltammograms in Figure 3.1, in that the admittance in the oxide formation and reduction resemble the current. For both metals there is little difference in Re(Y) between the electrolytes. The admittance in the double layer region is f at and featureless in the real domain, ref ecting the absence of faradaic processes in this region.

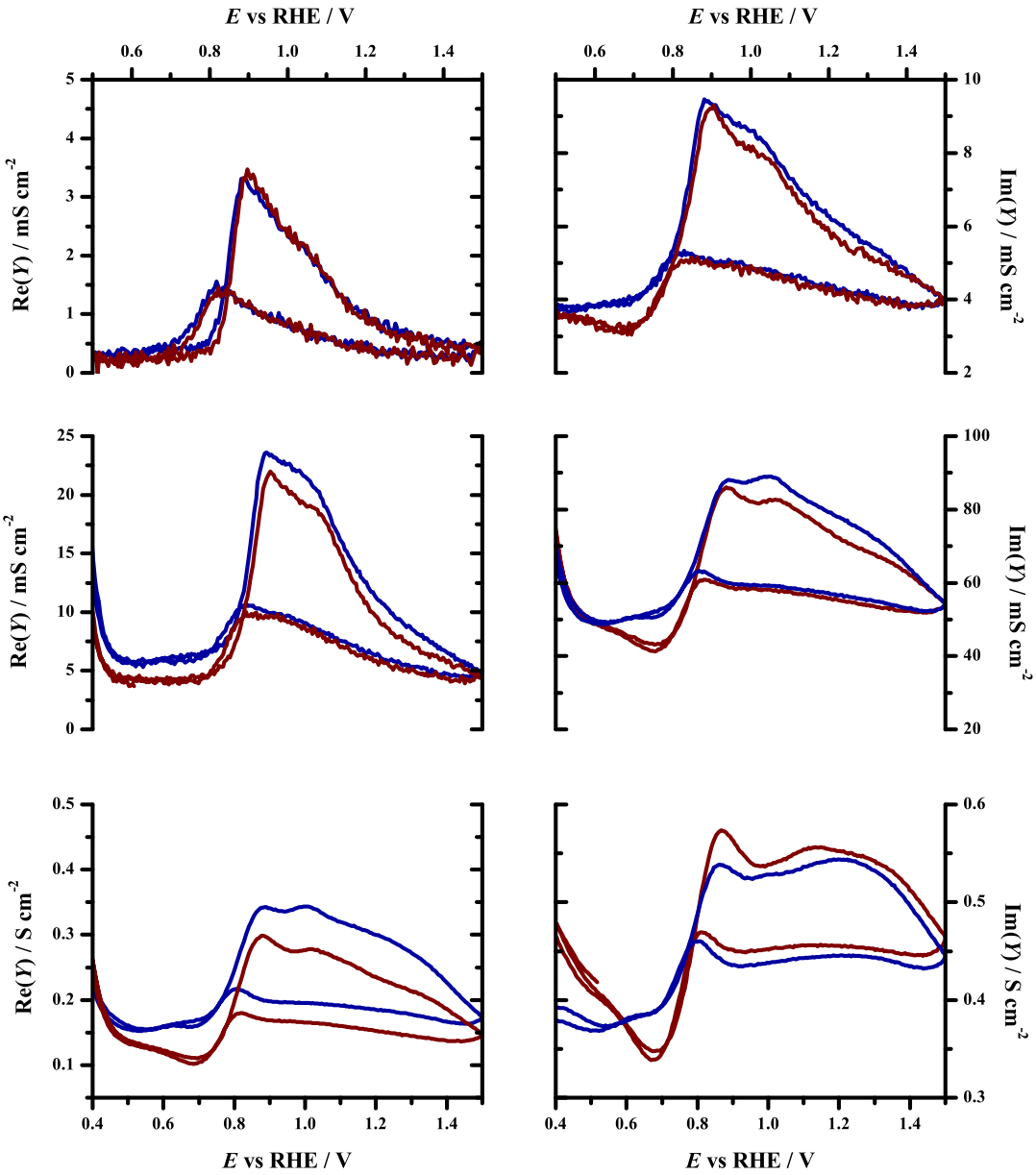

Figure 3.11: Ac voltammograms of Pt in H_2SO_4 (**red**) and $HClO_4$ (**blue**) at a sweep rate of 5 mV s^{-1}: top, 10 Hz; middle, 150 Hz; bottom, 1500 Hz.

At the onset of the oxide growth, the admittance rises sharply and peaks at 0.9 V for Pt and 0.82 V for Pd before slowly decreasing. The rise in the imaginary admittance due to oxide growth begins 0.1 V prior to the rise in the real part. At 1500 Hz $\mathrm{Im}(Y)$ shows a minimum at 0.6 V at Pd before a sharp increase leading up to the oxide growth regions. Pt shows similar results though the admittance peak is greater and the anion effects are less obvious. Since the high frequency impedance is more closely related to the differential capacitance, it shows that the surface condition undergoes dramatic change prior to the formation of the oxide layer.

3.4.6 dEIS

We have previously shown that the faradaic impedance may depend upon sweep rate [19, 21]. R_{ct}^{-1} values throughout the potential range are linearly proportional to the sweep rate, which is indicative of a surface-controlled process (Fig. 3.13). We do not expect the non-faradaic elements, R_{s}, Q_{dl}, and α, to depend on sweep rate as these do not depend upon surface kinetics. Figure 3.13 shows that Q_{dl} and α are independent of sweep rate in the double layer region and throughout most of the oxide region. At the onset of oxide growth there is a slight increase in Q_{dl} with sweep rate. This increase is statistically signif cant as shown by the small error bars. When using Eq. (3.1), C_{dl} sweep rate dependence is seen (Fig. 3.14). Since Q_{dl} and α did not change much with increasing sweep rate, R_{s} must be. Figure 3.14 shows that is this true: the R_{s} values are not constant throughout the potential range as expected. The minimum value is $0.483\,\Omega\,\mathrm{cm}^{-2}$ at 0.9 V and the maximum value is $0.557\,\Omega\,\mathrm{cm}^{-2}$ giving a difference of $0.055\,\Omega\,\mathrm{cm}^{-2}$. This difference is above the f t error (1%), and therefore it is reasonable to assume that this element is contaminated by a fast faradaic process. This explains the apparent sweep rate dependence of C_{dl}.

The anions have little effect on R_{ct}^{-1} of palladium, as shown by the ac voltammograms (Fig. 3.15). As for Pt, the double layer region is featureless in R_{ct}^{-1} but a large peak forms

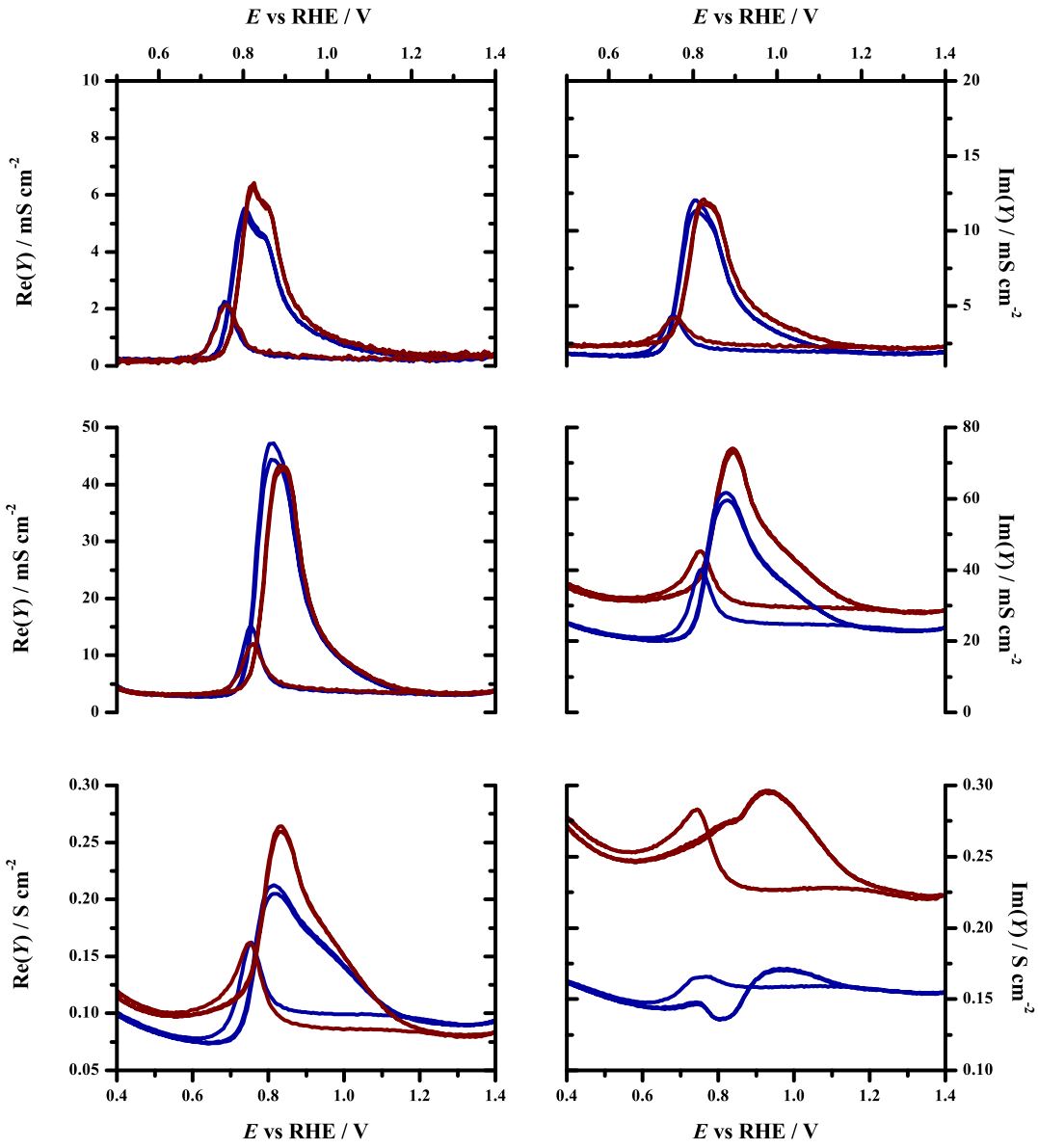

Figure 3.12: Ac voltammograms of Pd in H_2SO_4 (**red**) and $HClO_4$ (**blue**) at a sweep rate of 5 mV s^{-1}: top, 10 Hz; middle, 150 Hz; bottom, 1500 Hz.

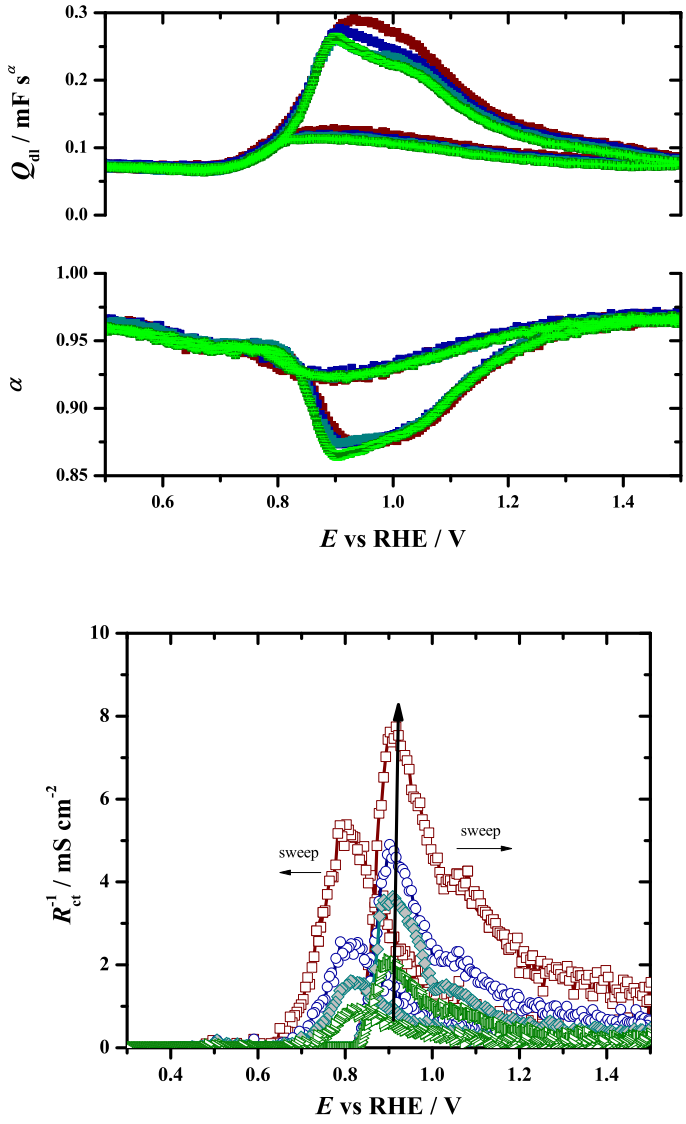

Figure 3.13: Q_{dl}, α and R_{ct}^{-1} for Pt in sulfuric acid at different sweep rates. Elements were obtained by f tting dEIS data to EC **R**. Error bars are given for 5 mV s^{-1}. Arrow shows trend of increasing sweep rate.

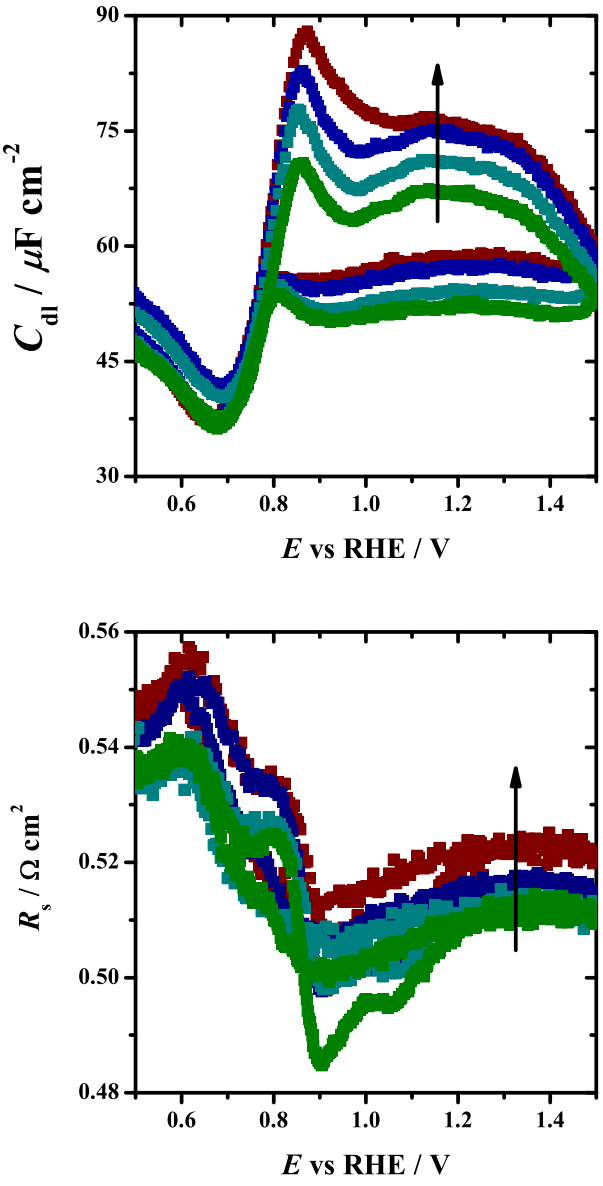

Figure 3.14: C_{dl} and R_{s} for Pt in sulfuric acid at different sweep rates. Elements were obtained by f tting dEIS data to EC **R**. Arrow shows trend of increasing sweep rate.

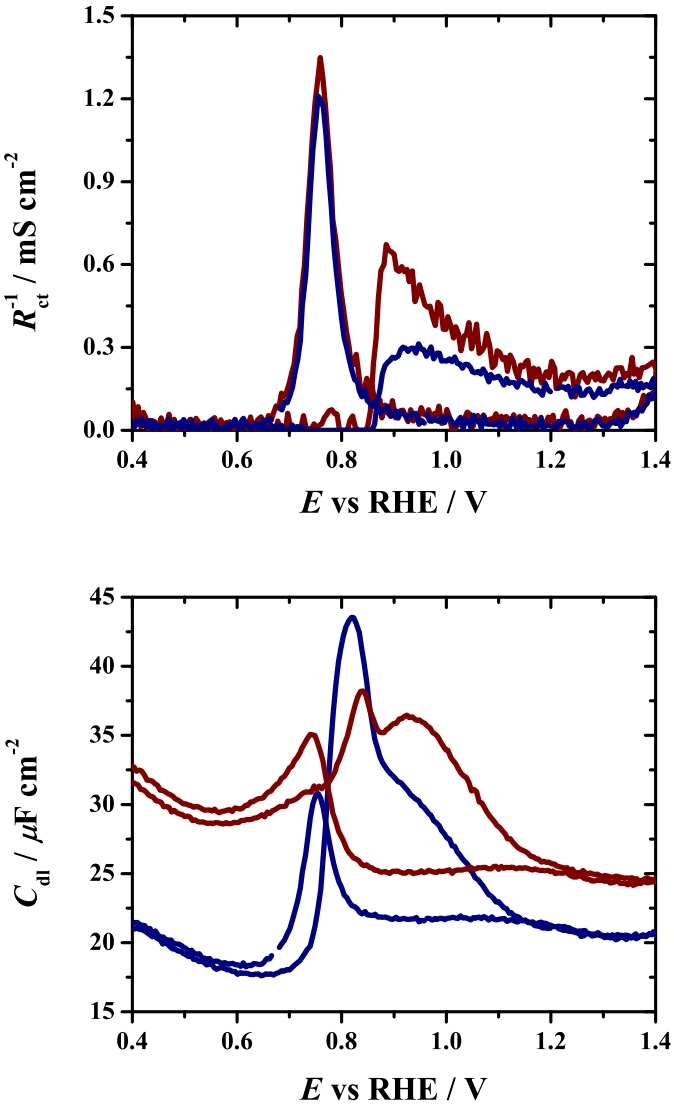

Figure 3.15: Fitted elements from EC **R** for palladium in H_2SO_4 (**red**) and $HClO_4$ (**blue**). Sweep rate, 5 mV s^{-1}.

at the onset of surface oxidation. The peak is greater for H_2SO_4 than for $HClO_4$. During the oxide reduction, a large sharp peak forms at 0.75 V. This peak is signif cantly larger than the oxide growth peak, which is in contrast to Pt (Fig. 3.13b). This parallels the fact that on Pd the oxide reduction produces a much larger peak in the CV than on Pt (Fig. 3.1). A dramatic difference between the electrolytes is seen in the capacitance voltammograms (Fig. 3.15b). H_2SO_4 produces a higher capacitance throughout the potential region than $HClO_4$.

Plotting the complex capacitance shows the change of the interface as a function of potential, Figure 3.16. Here, the diameter of the semi-circle is related to the capacitances in the equivalent circuit [58]. In the top plots we can see one clear semi-circle at 0.6 V with a downward 45 degree line at low frequencies. This was seen on Pt in steady state EIS experiments by Pajkossy and Kolb [53, 58, 59] and was attributed to interactions with the anion in the solution. The semi-circles increase in size with potential until the onset of surface oxidation (0.8 V for Pt) where a second semi-circle starts to form. This may correspond to a second time constant associated with a large capacitance (over 300 μF cm^{-2}). On Pd the second time constant appears sooner, presumably caused by the earlier oxidation potential. On the reverse sweep, Pt and Pd show similar capacitance trends, though the values are lower for Pd. As stated before, there is no statistical benef t in f tting a second time constant (as in **C**) to the data.

3.4.7 Potential limits

The impedance data shows hysteresis after the onset of surface oxidation, as seen in the C_{dl} and the R_{ct}^{-1} plots in Figs. 3.17 and 3.18 for Pt and Pd, respectively. Anion effects are strong in R_{ct}^{-1} plots, though they are present in the C_{dl} plots. In H_2SO_4, two peaks in R_{ct}^{-1} (at 0.95 and 1.05 V) develop due to consistently sweeping the potential past 1.5 V (both metals). These peaks correspond to the two small plateau regions centered at 0.95

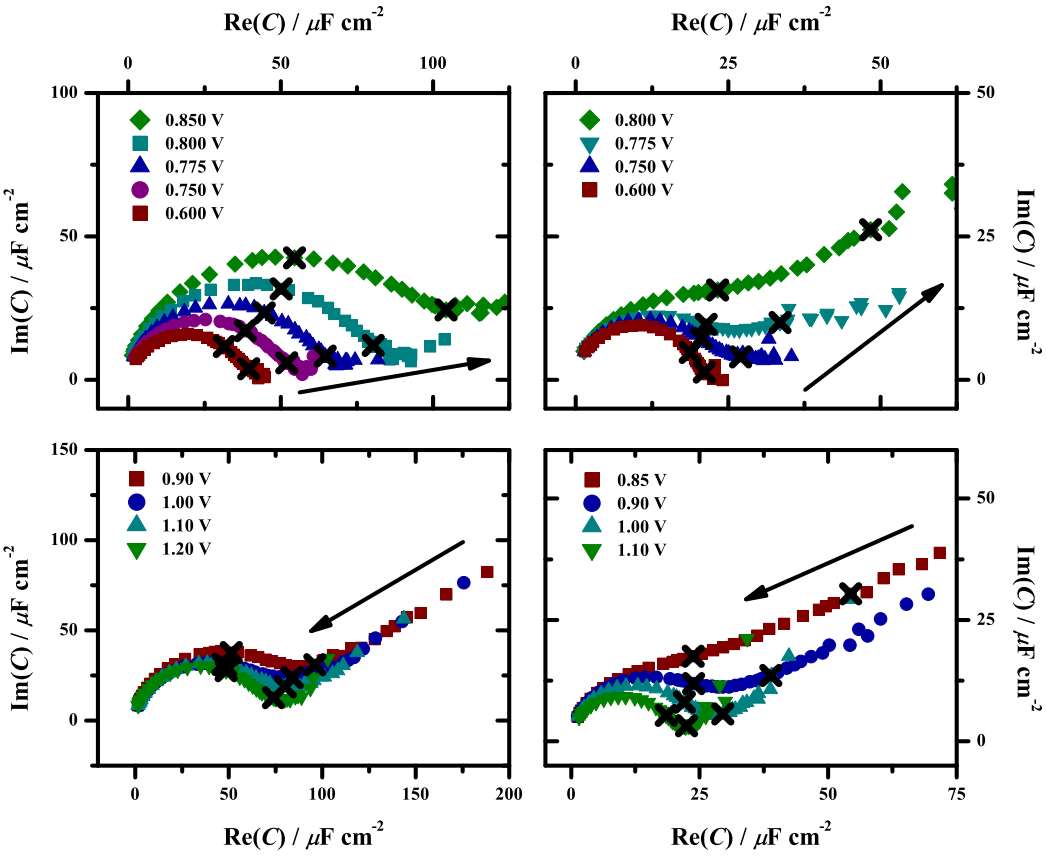

Figure 3.16: Complex capacitance data from a potential sweep at 5 mV s^{-1} in perchloric acid at select potentials. Top plots, positive-going sweep. Bottom plots, negative-going sweep. Arrows show the direction of the potential sweep. Left plots, Pt; right plots, Pd. 1500 Hz and 150 Hz frequencies are marked, with the latter being to the right.

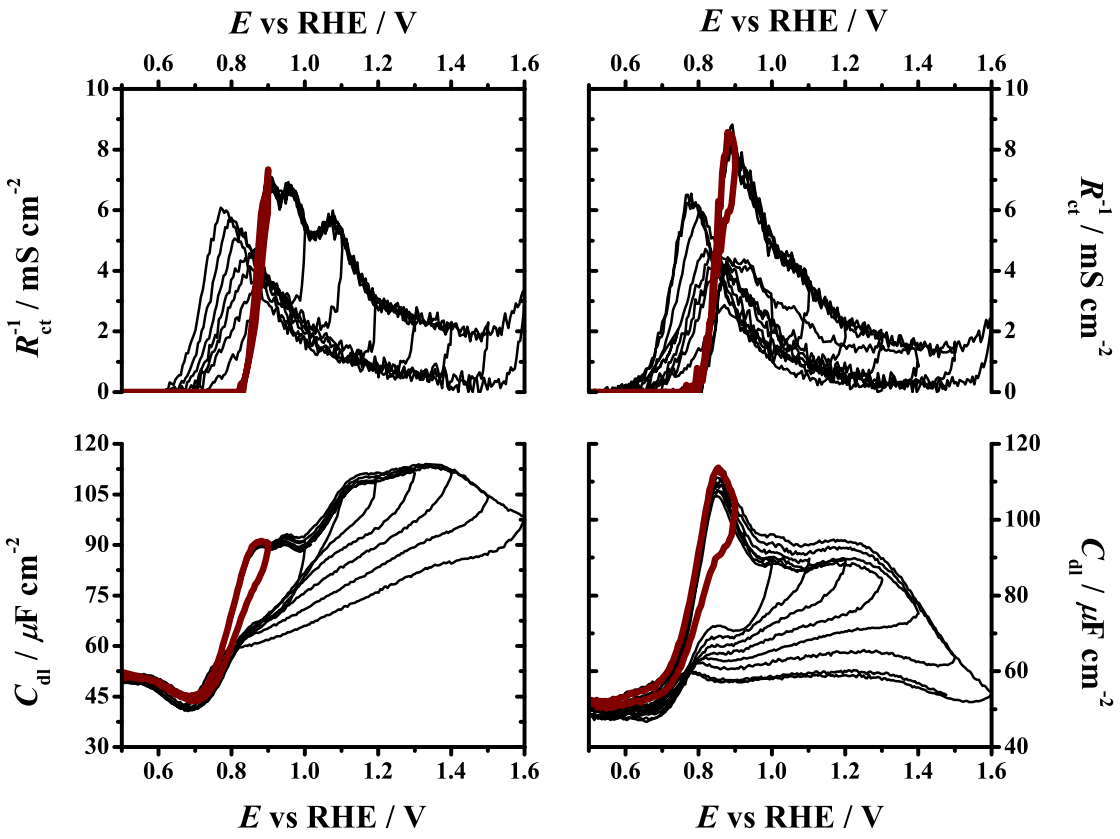

Figure 3.17: Potential-limit C_{dl} and R_{ct}^{-1} plots obtained from f tting the impedance data to **R** of Pt in H_2SO_4 (left) and $HClO_4$ (right). The 0.9 V potential limit plot is highlighted in **red** for added clarity.

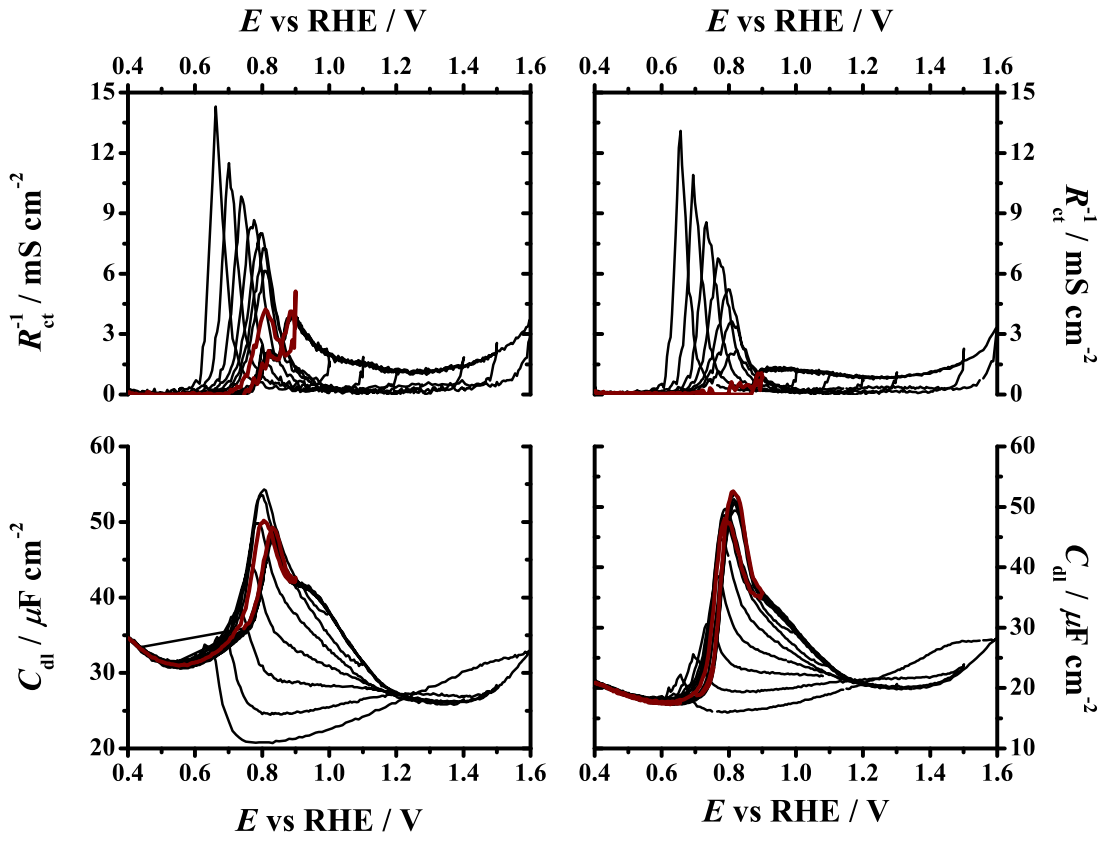

Figure 3.18: Potential-limit C_{dl} and R_{ct}^{-1} plots obtained from f tting the impedance data to **R** of Pd in H_2SO_4 (left) and $HClO_4$ (right). The 0.9 V potential limit plot is highlighted in **red** for added clarity.

and 1.05 V in Fig. 3.1, suggesting that the onset of oxidation is dependent upon the state of the surface. However, only one peak is present in perchloric acid, suggesting that the (bi)sulfate ion interacts with the oxide growth more than the perchlorate ion. The reverse sweeps show a large peak that increases as E_{L} increases. The peak increases more rapidly for Pd than Pt. These peaks mirror the reduction peaks in Fig. 3.4 closely.

The shape of the positive-going capacitance sweeps are similar, though perchloric acid gives lower capacitance in the double layer and oxide regions. The minimum C_{dl} value for Pt is 45 μF cm^{-2} in both electrolytes. For Pd, the minimum C_{dl} values were 30 μF cm^{-2} and 20 μF cm^{-2} in H_2SO_4 and $HClO_4$, respectively. The capacitance plot resembles the

dc voltammogram though the increase precedes the onset of oxide growth. This suggests the desorption of anions and reordering of the surface occurs prior to surface oxidation. A clear difference between the two metals is the nature of the hysteresis in the capacitance plots. For Pd, the capacitance of the reverse sweep closely tracks that of the forward sweep when the potential limit is less than 1.2 V. After 1.2 V, C_{dl} stays near 25 μF cm^{-2} during the reverse sweep, suggesting a dramatic restructuring of the surface at that potential. However, Pt shows hysteresis shortly after the onset of oxidation (0.9 V).

3.5 Discussion

3.5.1 dEIS

Dynamic electrochemical impedance spectroscopy (dEIS) utilizes FFT-EIS developed by Smith et al. [4, 15] in order to measure impedance on-the-fly. In a previous study of Pt oxide growth in our laboratory, 20 ac voltammetry cycles were used to acquire impedance information throughout the oxide region, with one frequency per cycle [21]. At a sweep rate of 10 mV s^{-1}, the entire experiment took over 1 h to complete. dEIS allows us to measure impedance with more frequencies (45) significantly faster (one potential cycle), and the same experiment was done in minutes. Since data is collected continuously, a full impedance spectra at intervals of a few mV are easily obtained. Having a greater density of points in the frequency and potential domains allows for more accurate fitting of EC and mechanistic models.

Perhaps the greatest advantage to this technique is its ability to be coupled with dynamic potentiostatic experiments such as cyclic voltammetry. We used this to investigate a previously inaccessible dimension of oxide growth: sweep rate effects on the impedance. We were able to acquire more detail in the potential and coverage dependence of C_{dl} and R_{ct}^{-1}. Since dEIS is able to measure impedance while the system is undergoing change, it

can capture information about the system in non-steady-state conditions.

3.5.2 Faradaic Impedance

To obtain the equivalent circuit that describes the oxide growth, we begin with a simple adsorption process coupled with an electron transfer such as in Eq. (3.28) where mass transport is fast, e.g.

$$\mathrm{M} + \mathrm{H_2O(l)} \quad \rightleftarrows \quad \mathrm{MO(oxide)} + 2\,\mathrm{H^+(aq)} + 2\,\mathrm{e^-} \tag{3.6}$$

We assume (i) the amount and state of the oxide is characterized by a single parameter, the charge density, σ; (ii) the current (proportional to reaction rate) can be written as a function of charge density and potential.

$$j \quad = \quad \frac{d\sigma}{dt} = f(\sigma, E) \tag{3.7}$$

Harrington has previously shown how j may be approximated as a first order Taylor series [19],

$$\Delta j \quad = \quad j - j_{ss} = \left(\frac{\partial j}{\partial \sigma}\right)_E \Delta\sigma + \left(\frac{\partial j}{\partial E}\right)_\sigma \Delta E \tag{3.8}$$

where $\Delta\sigma = \tilde{\sigma}\exp(\mathrm{i}\omega t)$ and $\Delta E = \tilde{E}\exp(\mathrm{i}\omega t)$. Differentiating $\Delta\sigma$ gives the expression for the current response

$$\Delta j \quad = \quad \frac{d\Delta\sigma}{dt} = \mathrm{i}\omega\tilde{\sigma}\exp(\mathrm{i}\omega t) \tag{3.9}$$

Equating Eq. (3.8) and (3.9) gives

$$\mathrm{i}\omega\tilde{\sigma}\exp\left(\mathrm{i}\omega t\right) = \tilde{\sigma}\exp\left(\mathrm{i}\omega t\right)\left(\frac{\partial j}{\partial\sigma}\right)_E + \tilde{E}\exp\left(\mathrm{i}\omega t\right)\left(\frac{\partial j}{\partial E}\right)_\sigma \tag{3.10}$$

which then may be simplif ed by dividing both sides by $\tilde{E}\exp\left(\mathrm{i}\omega t\right)$.

$$\mathrm{i}\omega\frac{\tilde{\sigma}}{\tilde{E}} = \frac{\tilde{\sigma}}{\tilde{E}}\left(\frac{\partial j}{\partial\sigma}\right)_E + \left(\frac{\partial j}{\partial E}\right)_\sigma \tag{3.11}$$

Rearranging the above expression in terms of $\mathrm{i}\omega\tilde{\sigma}/\tilde{E}$ gives the faradaic admittance

$$Y_\mathrm{f} = \frac{\tilde{j}}{\tilde{E}} = \frac{\mathrm{i}\omega\left(\frac{\partial j}{\partial E}\right)_\sigma}{\mathrm{i}\omega - \left(\frac{\partial j}{\partial\sigma}\right)_E} \tag{3.12}$$

The faradaic impedance is then

$$Z_\mathrm{f} = \left(\frac{\partial j}{\partial E}\right)_\sigma^{-1} - \frac{\left(\frac{\partial j}{\partial\sigma}\right)_E}{\mathrm{i}\omega\left(\frac{\partial j}{\partial E}\right)_\sigma} \tag{3.13}$$

This predicts that the faradaic impedance of the oxide growth may be modeled by an *RC* circuit of the form **C** (Figure 3.6) where

$$R_\mathrm{ct} = \left(\frac{\partial j}{\partial E}\right)_\sigma^{-1} \tag{3.14}$$

and

$$C_\mathrm{ad} = -\left(\frac{\partial j}{\partial E}\right)_\sigma\left(\frac{\partial\sigma}{\partial j}\right)_E \tag{3.15}$$

Given that the current in the oxide region is relatively constant, the oxide charge-

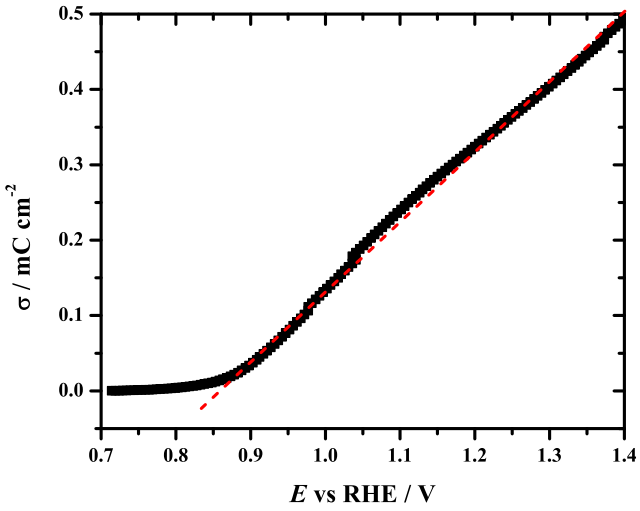

Figure 3.19: Charge density vs potential of Pt in sulfuric acid. Sweep rate: 50 mV s^{-1}.

potential curve is linear, Fig. 3.19. We can estimate the value for C_{ad} throughout the region using $C_{\mathrm{ad}} = \left(\frac{\partial j}{\partial E}\right)_\sigma \left(\frac{\partial \sigma}{\partial j}\right)_E = \left(\frac{\partial \sigma}{\partial E}\right)_j \approx \frac{d\sigma}{dE}$, which is equivalent to j_{plateau}/v. Therefore the estimated value for C_{ad} is 880 μF cm^{-2}. Taking our measurement of $R_{\mathrm{ct}} \approx 4\,\mathrm{k\Omega\,cm^2}$ at 1.1 V and the double layer capacitance of $Z_{\mathrm{dl}} = Q_{\mathrm{dl}}^{-1}(\mathrm{i}w)^{-\alpha}$, where Q_{dl} =65 μF cm^{-2} $\mathrm{s}^{-\alpha}$ and $\alpha = 0.95$, our minimum frequency of 2 Hz would yield an impedance of

$$Z(2\,\mathrm{Hz}) = \frac{1}{Z_{\mathrm{dl}}^{-1} + \frac{1}{R_{\mathrm{ct}} + \frac{1}{\mathrm{i}\omega C_{\mathrm{ad}}}}} = 497\,\Omega\,\mathrm{cm}^2 - 1172\,\Omega\,\mathrm{cm}^2\mathrm{i} \tag{3.16}$$

However, the predicted impedance in the absence of C_{ad} is $Z(2\,\mathrm{Hz}) = 503\,\Omega\,\mathrm{cm}^2 - 1179\,\Omega\,\mathrm{cm}^2\mathrm{i}$. This gives a difference of about 1%, which our experiment is unable to distinguish. This means that while circuit **C** is expected on mechanistic grounds, the measurement of C_{ad} will be diff cult and so EC **R** may be statistically equivalent. Even though C_{ad} can not be extracted from our data, R_{ct} may be.

We note that Ragoisha et al. [25] have used a different dEIS system to study oxide growth on Pt in acidic solutions. They report results that are qualitatively similar to the

ones here as well as the effects of chloride adsorption. However, they chose to f t their data (with chloride and without) to a circuit similar to **C**, with the CPE describing the double layer capacitance being replaced by an ideal capacitor. Pell et al. [50] showed that EC **C** provides good f ts for chloride adsorption but they did not use it for impedance data in the absence of chloride. The values for $R_{\rm ct}$ reported by Ragoisha et al. [25] are two orders of magnitude lower than those reported here, i.e. $10\,\Omega\,{\rm cm}^2$ (theirs) vs $1000\,\Omega\,{\rm cm}^2$ (ours). They do express doubt over the meaning of their CPE element and its effects on $R_{\rm ct}$ as its value is far from the expected value of $C_{\rm ad}$ (given below). Fitting our data to the same ECs as used by Ragoisha et al. produced results for $R_{\rm ct}$ of the same magnitude. Given that fact and that the $R_{\rm s}$-corrected complex capacitance plots shows no evidence for a $C_{\rm ad}$ value of less than $300\,\mu{\rm F\,cm}^{-2}$ (Fig. 3.8), it is reasonable to assume that the f tting of $C_{\rm ad}$ adversely affected their $R_{\rm ct}$.

3.5.3 Analysis of rate law

There is general agreement that the oxide growth rate law assumes the form

$$j_{\rm a} \;=\; \frac{d\sigma}{dt} = k^{\rm ref}\exp\left(cE\right)\exp\left(-b\sigma\right) \tag{3.17}$$

The origin of the $\exp\left(-b\sigma\right)$ term is controversial as is the reason why the rate law is zero-order with respect to M(sites), i.e., has no $(1-\theta)$ factor. The standard way to obtain both c and b is by a potential step experiment where the potential is held in the oxide region and the charge is recorded as a function of time [49, 60, 61]. An expression for the transient growth of the oxide at constant potential found by integrating the above equation (Eqs.

(3.18) and (3.19)).

$$\int_{\sigma_0}^{\sigma} \exp(b\sigma)\ d\sigma \quad = \quad \int_0^t k\exp(cE)\ dt \tag{3.18}$$

$$b^{-1}\left[\exp(b\sigma) - \exp(b\sigma_0)\right] \quad = \quad k\exp(cE)\,t \tag{3.19}$$

Rearrangement gives the transient growth law expression.

$$\sigma \quad = \quad b^{-1}\ln(t+\tau) + b^{-1}\ln\left(\frac{k}{b}\right) + \frac{cE}{b} \tag{3.20}$$

where $\tau = \exp(b\sigma_0)/bk\exp(cE)$. The above expression allows for the determination of b and c by calculation from the slope and intercept, respectively, of a σ–$\ln(t)$ curve.

Studies of transient oxide growth at constant potential at Pt do not all agree. Conway et al. suggested that b is independent of potential in the potential range of 1.2–1.6 V [33, 61]. Conway and Jerkiewicz found similar results on Pt(111) and Pt(100) [62] and found that b is affected by surface orientation. Gilman describes b as linearly dependent on E in the early oxide region (E < 1.1 V) but independent afterwards [49]. Heyd and Harrington suggested that b is a linear function of E throughout the oxide region from sweep hold experiments [63]. Alsabet et al. [64] showed evidence that b is constant throughout the potential range (0.9–1.4 V) at $\sigma < 440\ \mu\text{C cm}^{-2}$, after which it is a function of both E and σ. Because there are differing results from similar experiments a new method to extract information of b is needed.

Harrington suggested obtaining information about the growth law though the use of impedance spectroscopy Harrington [19], van der Geest et al. [65]. Equation (3.14) shows that R_{ct}^{-1} is a measurement of the partial differential of the current with respect to E. We

proceed by assuming a very general form of the rate law, assuming only that it is a product of two separate functions of potential and coverage (given here as charge), that is

$$j = g(E)f(\sigma) \tag{3.21}$$

This covers the case of Eq. (3.17) provided that b is independent of potential and c is independent of σ. If $\theta \propto \sigma$ it also covers a range of common rate laws for adsorption species. R_{ct}^{-1} then assumes the following form

$$R_{\mathrm{ct}}^{-1} = \left(\frac{\partial j}{\partial E}\right)_{\sigma} = g'(E)f(\sigma) \tag{3.22}$$

$f(\sigma)$ can be removed by dividing by Eq. (3.21), that is

$$\frac{1}{jR_{\mathrm{ct}}} = \frac{g'(E)}{g(E)} = h(E) \tag{3.23}$$

A similar analysis can be done for C_{ad} which gives

$$C_{\mathrm{ad}} = -\left(\frac{\partial j}{\partial E}\right)_{\sigma}\left(\frac{\partial \sigma}{\partial j}\right)_{E} = -\frac{g'(E)}{g(E)}\,\frac{f(\sigma)}{f'(\sigma)} \tag{3.24}$$

Substituting Eq. (3.23) and rearranging gives

$$\frac{1}{jR_{\mathrm{ct}}C_{\mathrm{ad}}} = \frac{f'(\sigma)}{f(\sigma)} = l(\sigma) \tag{3.25}$$

If C_{ad} could be accurately determined, the above expression could be used to obtain $f(\sigma)$.

Figure 3.2 shows that the normalized current is dependent on sweep rate, and therefore different σ values are accessible by varying v. Therefore a test for the product form of

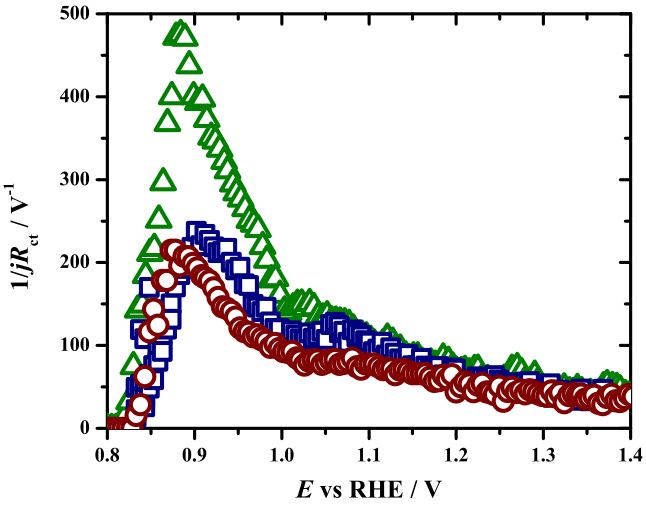

Figure 3.20: $1/jR_{\mathrm{ct}}$ vs E at varying sweep rates: (**green triangles**) 10 mV s^{-1}; (**blue squares**) 20 mV s^{-1}; and (**red circles**) 50 mV s^{-1}.

the rate law is that $1/jR_{\mathrm{ct}}$ depends only on potential independently of charge (Eq. 3.23). For example, $1/jR_{\mathrm{ct}}$ vs E at different sweep rates should fall on a common curve. If true, integration can be used to find $g(E)$. Therefore $1/jR_{\mathrm{ct}}$ should show no sweep rate dependence. Figure 3.20 shows the dependence of $1/jR_{\mathrm{ct}}$ on v, suggesting that $1/jR_{\mathrm{ct}}$ is not solely a function of potential in the potential range 0.85–1.2 V, after which all the curves converge. Past 1.0 V, $1/jR_{\mathrm{ct}}$ is linear with E with a negative slope until 1.3 V where it plateaus at 35 V^{-1}. Palladium shows a similar result (Fig. 3.21) though the slope is less and the plateau is 55 V^{-1}. Therefore, for $E >$ 1.0 V the product form of the rate law in Eq. 3.21 applies.

If we further assume $g(E) = \exp(cE)$ as in Eq. (3.17) then Eq. (3.23) predicts a constant value of c from $1/jR_{\mathrm{ct}}$. This applies at $E >$ 1.2 V and the value for Pt agrees with the value obtained by Heyd and Harrington [63]. In the region 1.0–1.2 V we have convergence of the curves but they are not constant, suggesting that the product forms holds, but that $g(E)$ is not strictly exponential. This may suggest some potential dependence of c. This analysis does not give any information about $f(\sigma)$, since C_{ad} was not accessible.

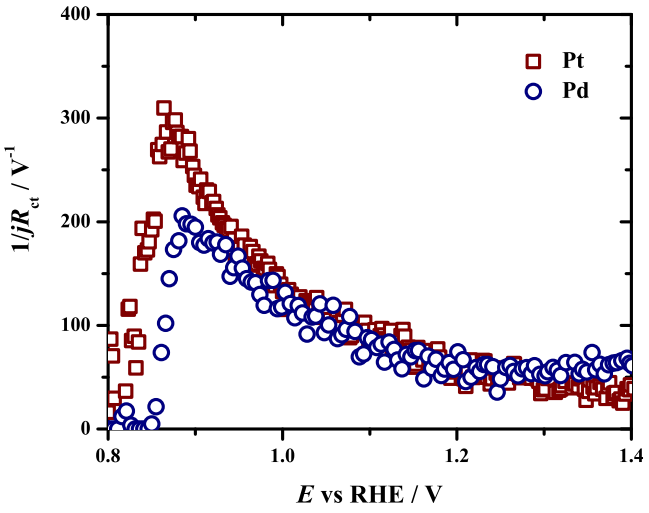

Figure 3.21: Plot of $1/jR_{\mathrm{ct}}$ vs E at (**red squares**) Pt and (**blue circles**) Pd in sulfuric acid.

Explaining the sweep rate effects on $1/jR_{\mathrm{ct}}$ requires that b be a function of E. The precise function cannot be determined as it requires access to C_{ad} in order that $(\partial j/\partial\sigma)_E$ may be known. Our results support the findings that the slopes of the σ-$\ln(t)$ plots change with potential and so we conclude that b is a function of potential below 1.2 V [63, 66]. However, below 1.0 V the plot shows a more complicated relationship to sweep rate implying a need for a more complicated rate law.

3.5.4 Microscopic mechanisms

We will give briefly survey the microscopic theories of oxide growth; we refer the reader to Conway's [33] and Gilman's [35] reviews of the subject and an review by Grden et al. [34] that focuses on Pd. The oxide growth was originally treated as oxygen adsorption. Böld and Breiter [43] provided the first kinetic treatment, and focused on providing an explanation for the plateau in the current during the linear sweep. They suggested the following reaction scheme

$$\mathrm{M(site)} + \mathrm{H_2O} \quad \rightleftarrows \quad \mathrm{MOH(ads)} + \mathrm{H^+(aq)} + \mathrm{e^-} \tag{3.26}$$

$$\mathrm{MOH(ads)} \quad \rightleftarrows \quad \mathrm{MO(ads)} + \mathrm{H^+(aq)} + \mathrm{e^-} \tag{3.27}$$

They incorporated the Temkin term $\exp(-b\sigma)$ to account for the energy of adsorption increasing with coverage of oxygen. The selection of a rate determining step was problematic as there existed little evidence to fully support either step. However, Breiter's capacitance measurements suggested that Eq. (3.26) was reversible [67], and there was no evidence from transient currents for two adsorbed species [49]. Gilman took these facts to imply that the coverage of OH(ads) was small and therefore Eq. (3.26) was fast [35].

Conway and Gottesfeld [68] found hysteresis at $E > 1.1$ V between the positive-going and negative-going potential scans using ellipsometry and ac voltammetry. In the early stages ($E < 1.1$ V) both scans were superimposable. They interpreted the hysteresis as kinetic irreversibility, though there was no measurement of the frequency dispersion. Reversible later became synonymous with fast, and Eq. (3.26) was treated as being both fast and reversible [33, 61].

The rate law derived for the two step electrosorption (and desorption) such as in Eq. (3.26) (fast) and (3.27) (rate determining) was

$$v_{\text{ads}} = k_1(1-\theta_{\text{ox}})\exp(cE)\exp(-b\sigma) \tag{3.28}$$

where v_{ads} is the rate of adsorption and θ_{ox} is the coverage of MO(ads). It has been noted that the growth law shows no change when the charge reaches a monolayer, which seems incompatible with the presence of a $(1-\theta_{\text{ox}})$ factor. Gilman assumed that θ_{ox} remained small and therefore the factor was disregarded [35].

Visscher and Devanathan [69] gave one of the first treatments of oxide growth based upon film growth theory. They suggested that the rate determining step was the migration of cations under the influence of an electric field not unlike that of a Mott and Cabrera mechanism [70]. Damjanovic et al. [71] also interpreted the logarithmic growth law in terms of a high-field mechanism. The rate of the growth of the oxide film was said to be controlled by a potential drop across the film. It is typically assumed that the initial potential drop at the metal-film and film-metal interface remains constant during film growth. As the film increases, the ion transport through the film slows down since the slope of the potential gradient decreases, Fig. 3.22. The high-field model takes ion transport as the rate limiting process and therefore the rate oxide growth decreases as its thickness increases.

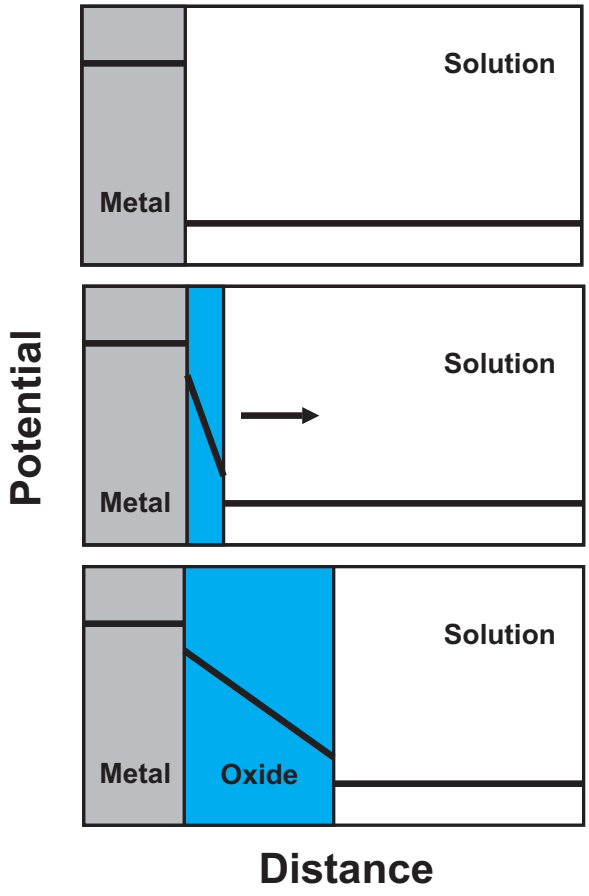

Figure 3.22: Depiction of the potential prof le across an oxide f lm during growth at constant potentials.

Thus, the rate law assumed a form similar to

$$\frac{dL}{dt} = k\exp(cE - gL)) \tag{3.29}$$

where L is the film thickness. Given that $L \propto \sigma$, Eq. (3.29) can assume the form of Eq. (3.17). Vetter and Schultze noted that a film model was unlikely due to the fact that the oxide layer was less than 0.7 nm which does not seem to be within the film regime [45]. In other words a film model based on a continuum picture as in Fig. 3.22 is hard to imagine unless the film is many monolayers thick. Reddy et al. [72] and later Gilroy [73] also criticized the use of film theory as the rate law does not change during the transitions between submonolayer and multilayer.

Vetter and Schultze proposed reconstruction of the surface as an explanation for the "Temkin" factor [44, 45]. The reconstruction of the surface was suggested to originate from a place-exchange mechanism. Reddy et al. [72] and later Gilroy [73] suggested that the Temkin parameter, b, relates to the repulsive forces between OH(ads). Conway et al. [61] further developed the place exchange mechanism and provided a microscopic explanation suggesting that the electrosorbed oxygen, MO(ads), formed in Eq. (3.27) creates a dipole which when placed under an electric field can "flip".

$$\mathrm{MO(ads)} \rightleftarrows \mathrm{OM(lattice)} \tag{3.30}$$

The drive for place exchange is dependent not only upon the applied potential but also the extent to which the surface has been oxidized, that is σ. As shown in Fig. 3.22, as σ increases, the film thickness increases which then decreases the potential gradient throughout the oxide. Since the slope of the potential gradient is related to the electric field strength, as the film grows the electric field drops, and with it the drive for the MO(ads) dipoles to

"f ip". Thus, parameters c and b were related to physical quantities

$$c = -\frac{2\beta\mu}{RT}\frac{(\Delta\phi - \chi_o)}{d} \tag{3.31}$$

$$b = \frac{8\pi N_{\mathrm{A}}\beta\mu^2}{dFRT} \tag{3.32}$$

where μ is the dipole moment of MO, d is the thickness of the f lm, and β is a symmetry factor. Dall'Antonia et al. [74] used this model to explain oxide growth on Pd. Later, Alsabet et al. [64] commented that the units for b as obtained from Eq. (3.32) are not correct and numbers obtained from it are nonsensical and so N_{A} was squared to correct this problem. This mechanism has been criticized by Sun et al. [40] who suggested that spontaneous dipole f ipping seems unlikely from an entropic point of view.

The electrochemical quartz crystal microbalance (EQCM) was used to study the mass change of the electrode during oxide growth. Birss et al. [42] saw no evidence for OH(ads) though they only studied larger anodic charges at Pt. EQCM studies on Pd oxide growth in acid are not easy due to the propensity for Pd dissolution [48, 75]. Jerkiewicz et al. [41] also saw no evidence for OH(ads) precursor when they reported the change in mass and charge gives $8\,\mathrm{g\,mol^{-1}\,e^-}$ (they gave the number as $16\,\mathrm{g\,mol^{-1}}$ in terms of grams per mole O). This was calculated by taking the difference in mass between the potential of zero total charge (pztc) and 1.4 V under the assumption that water is bound to the surface in the double layer region and therefore must be corrected for. It was then concluded that the surface species was O(ads) and not OH(ads), though like Birss et al. [42], the change in mass at the onset of oxide growth was not studied.

Van der Geest and Harrington [21] collected ac voltammograms at 20 different frequencies spanning four decades. After f tting the impedance data to a number of equivalent

circuits it was determined that only a single time constant was present, though they noted that processes faster than double layer charging would not be seen. They also noted that the value for c as obtained by a number of groups [33, 61, 63, 64, 74] was the same magnitude as $\frac{\alpha F}{RT}$. The value of $\alpha = 1$ suggested a concerted 2-electron transfer process. Combining their results with those from the EQCM, they concluded that there was only a single process. That is, Eq. (3.26) and (3.27) could be combined into a single step, Eq. (3.33).

$$\mathrm{M} + \mathrm{H_2O} \quad \rightleftarrows \quad \mathrm{MO} + 2\,\mathrm{H^+(aq)} + 2\,\mathrm{e^-} \tag{3.33}$$

If c can be treated as a typical electrochemical electron transfer factor, the plateaus in the $1/jR_{\mathrm{ct}}$ plot provide information on α. The α values obtained were 0.90 at Pt and 1.4 at Pd in sulfuric acid. In perchloric acid the α values were 0.90 and 0.77 for Pt and Pd, respectively. These results agree with previously determined values for c [63] and suggest a concerted 2-electron transfer process. As usual, the activation to the transition state is by some type of bond-breaking process, and the motion of Pt out of the metal lattice into the growth oxide was suggested to fulf ll this role.

Since only one time constant was seen throughout the potential range, the result was a "pop-out" mechanism where the M atom leaves the lattice and surface-diffuses until it reaches a cluser of oxide. This replaced the place-exchange of Eq. (3.30) with the rate determining step followed by fast surface diffusion.

$$\mathrm{M(lattice)} + \mathrm{H_2O} \quad \rightleftarrows \quad \mathrm{MO(surf)} + 2\,\mathrm{H^+(aq)} + 2\,\mathrm{e^-} \tag{3.34}$$

This mechanism was supported by prior STM and XPS data, which showed surface reconstruction after oxidation-reduction cycles. Low energy electron diffraction measurements suggested that an ordered Pt surface reconstructs to give random steps and terraces

[36]. STM by Itaya et al. [37] showed that after a single oxidation-reduction cycle small clusters form. After multiple cycles they reported a “rolling hills” surface structure. Monte Carlo simulations of the pop-out mechanism were able to reproduce some features of the STM results [76].

The reduction follows Eq. (3.35) well.

$$j_{\mathrm{c}} \;=\; k_{-1}\sigma_{\mathrm{ox}} \exp\left(-\frac{\alpha_{\mathrm{c}} F}{RT} E\right) \tag{3.35}$$

Therefore the rate determining step is an electrochemical one. This would suggest that oxide growth and its reduction proceed via two different mechanisms. However, it is known that when the potential is swept past 1.2 V irreversible structural changes occur [60, 68]. This is consistent with the pop-out model if we take the reduction of the metal oxide to be faster than surface diffusion. In order for a metal atom to be stabilized after popping out of its lattice it must be strongly bound to oxygen. However, when the oxygen is removed during reduction, the metal atoms reform bonds to the surface and adjacent metal atoms. Conway et al. [33, 60, 68] and Grden et al. [34] have discussed the apparent reversible nature of oxide grown at lower potentials for Pt and Pd, respectively. Since STM and X-ray data show only slight displacement at low coverages and potentials, the apparent reversibility comes from the fact that the metal atoms can drop back into place.

New spectroscopic evidence f nds metal atoms that are out of the surface plane as opposed to place-exchanged. Allen et al. [77] used x-ray absorption f ne structure (XAFS) to study the change in Pt charge and bonding of O and Pt during surface oxidation and reduction at Pt nanoparticles. They saw only a single process during oxide growth. Since the logarithmic growth law applied to the structural changes over a wide range of oxide thicknesses (that is, there is no lag between the formation of Pt–O bonds and Pt restructuring), they suggested that the surface rearrangement was local. They explained this with

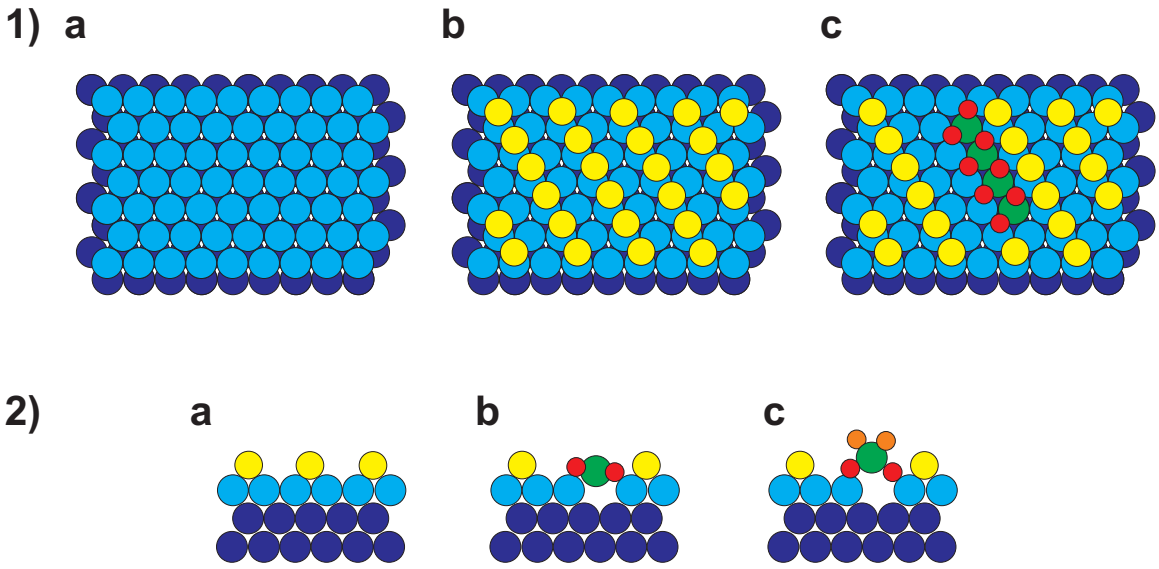

Figure 3.23: Sequential growth of the Pt oxide chain structure that forms on the Pt(111) based upon Fig. 6 in Ref. [39]. Large **blue**, **cyan**, and **green** circles represent subsurface, surface, and "lifted" Pt atoms, respectively. **Yellow** and **red** circles represent oxygen atoms in the p(2 × 1)-O position and the oxide chain, respectively. The orange circles are oxygen atoms from water molecules that provide additional coordination to the displaced Pt atoms. The atomic sizes and positions are not to scale.

migration of Pt atoms to sites that produce lower Pt coordination which would then be sites for preferential electrosorption of oxygen. Devarajan et al. [39] studied oxygen adsorption from dosing NO_2 under ultrahigh vacuum on Pt(111) using STM. At coverages less than 0.4 ML, adsorbed oxygen atoms are arranged in a p(2 × 1) structure. However, upon further NO_2 dosing, oxygen addition into p(2 × 1)-O ordered regions produced a raised Pt oxide chain compound. This means that the Pt atoms leave the metal lattice forming Pt oxide on the surface. Fig. 3.23 depicts an oxygen covered Pt(111) surface before and after PtO chains are formed. The STM images show protrusions and chains which were attributed to the addition of oxygen atoms to these chains to give branched "Y" structures and hexagons. Further evidence for these chain-like Pt oxide structures was found on Pt(110) using STM by Li et al. [38] whose work was supported by DFT calculations by Helveg et al. [78]. Li et al. suggested that the O-O repulsive interactions are fully compensated by distortions in the Pt lattice. In other words, addition of oxygen into a compact surface

structure is favorable upon the weakening of Pt–Pt bonds. Wang et al. [79] saw evidence for the preferential formation of Pt oxide along steps on Pt(332) thereby giving Pt oxide chains. Using XAS, Friebel [80] concluded that the chemical species of the oxide formed on the surface was square-planar PtO. X-ray ref ectivity, hard X-ray diffraction, and X-ray absorption spectroscopy [80, 81] measurements suggest the Pt surface becomes slightly lifted upon oxidation forming a 3D oxide layer as depicted in 2b of Fig. 3.23. After the initial oxide formation a large structural rearrangement is seen, akin to bulk PtO (2c of Fig. 3.23), presumably because of the large lattice mismatch between PtO and Pt [39, 78].

Given that (i) electrosorption of oxide preferentially occurs at low-coordination sites; (ii) electrosorption at these sites causes Pt atoms to be slightly lifted off the surface; (iii) chains grow from these sites; and that (iv) the surface is reconstructed during this process, a pop out mechanism is supported. However, whether chain growth is due to weakening of adjacent metal–metal bonds or capturing diffusing metal surface atoms by providing extra coordination is unclear. At low O(ads) coverage, minimal surface reconstruction occurs given that O(ads) is well distributed across the surface (1b in Fig. 3.23). However, at greater coverages, reconstruction must occur to support the additional oxygen and metal-metal bond breaking due to oxo-coordination from oxygen electrosorption (1c in Fig. 3.23). Oxide reduction at these chains allows the metal atoms to conglomerate which causes drastic reconstruction of the surface.

Using this model we can provide an explanation of the apparent zero-order rate law. First, the $(1 - \theta_{\mathrm{ox}})$ term in Eq. (3.28) is equivalent to the coverage of surface sites, θ_{site}, that can accept oxygen. As stated before, Gilman suggested that the coverage of oxide remained small therefore $(1 - \theta_{\mathrm{ox}})$ could be taken as constant [35]. Since the oxide is well distributed across the surface, θ_{ox} being small cannot be accurate. If we think in terms of θ_{site} we can rationalize that it remains near constant as long as the metal atoms can pop-out of the lattice thereby creating more sites for oxygen electrosorption. This would occur if

the rate of Eq. (3.34) remains fast. Under these conditions the number of sites that can undergo further oxidation will be relatively unchanged, leading to the apparent zero-order rate law in surface sites.

While there are similarities in the growth of Pt and Pd oxide, it has been shown that electrooxidation of formic acid [82] and carbon monoxide [83] show different reactivity at Pt and Pd. Pt shows activity in the oxide region while Pd shows no activity towards formic acid oxidation, and only slight activity towards CO. A possible explanation is that the oxide layer on Pd is more uniformly spread over the surface [84]. We have discussed the evidence of the growth of oxide chains on Pt. Therefore we can say that on Pt the oxide grows in multilayers before having the surface fully covered, whereas for Pd the coverage of the oxide is more uniform.

Given the facts presented above, a film model does not properly explain growth of the oxide up to 2 ML. Alsabet et al. [64] used place exchange to explain sub-monolayer oxide growth and suggested that a film model similar to Cabrera and Mott [70] be used after a few monolayers form. However, the erratum showed that the point where the place exchange mechanism gives way to the film model is around 2 ML. Reddy et al. [72] as well as Gilroy [73] have emphasized that film models are not appropriate. Thus, the Cabrera-Mott model as utilized by Jerkiewicz's group for both palladium [74] and platinum [41, 64] does not seem likely. One of the primary pieces of evidence against a film model for a growing oxide layer is the fact that an ideal Tafel slope of 30 mV dec^{-1} is measured for the oxygen evolution reaction [72, 73]. If the oxide was indeed a film then the Tafel slope of oxygen evolution at high potentials would be affected by the potential drop across the growing oxide film—but this is not seen. The subtle change in different growth behavior after 2 ML seen by Alsabet et al. [64] can be explained by taking $b = f(E, \sigma)$ and not just a change in mechanism. The physical meaning of c and b would then involve bond breaking and formation as opposed to dipole flipping in an electric field. The fact that both

metals exhibit c values of 25–35 V^{-1} is a strong indication of an electron transfer process. The Temkin coeff cient can arise from the increased diff culty of electrosorption of oxygen onto more coordinated metal atoms.

In light of new STM and X-ray spectroscopic information we need a new microscopic explanation of the rate law. To use terminology that is consistent with the literature, "place exchange" need not mean a f ipping of the MO dipole due to the applied electric f eld. We also do not require a high-f eld mechanism that requires a potential to drop across an oxide "f lm" because the thickness of the oxide layer (submonolayer to a few monolayers) cannot account for a substantial drop in potential. Instead, place exchange can mean that the metal atom comes out of the lattice and forms an oxide on the surface. This has the advantage of not needing oxygen to move between metal atoms in a lattice, as such diffusion is unlikely due to the differences in atomic size. More spectroscopic and theoretical studies are needed to give more detailed microscopic explanations for the Temkin coeff cient, b, and the electron transfer coeff cient, c.

3.6 Conclusions

This report uses dynamic electrochemical impedance spectroscopy to study oxide growth of platinum and palladium in sulfuric and perchloric acids. This technique allows for rapid acquisition of the impedance prof le of a system. Because it can be used in conjunction with standard potential-controlled experiments, e.g. cyclic voltammetry, chronoamperometry, etc., it enables us to measure the impedance of a system undergoing change. We show how the impedance of the oxide growth changes as a function of potential and sweep rate. The effect of the latter is novel to impedance measurements as it is only possible when using dEIS. Changing the sweep rate allows for the measurement of the impedance at different oxide coverages at the same potential.

By f tting the impedance results to equivalent circuits, we extract some qualitative information from the double layer capacitance and the oxide growth region. We show that the measured capacitance depends on oxide coverage in a complicated way. This seems to be due to anion effects and possible surface reconstruction. The charge transfer resistance showed a dependence on sweep rate which we attributed to a change in coverage. This suggests that b is a function of potential and oxide coverage at potentials lower than 1.2 V. The convergence of R_{ct}^{-1} at all sweep rates at $E > 1.2\,\mathrm{V}$ supports Conway et al. [61] and Gilman's [35] f nding that b has a region where it is independent of potential.

We ref ne a previous oxide growth mechanism given by van der Geest et al. [21] in light of recent spectroscopic results. We suggest a pop-out type model where a surface metal atom is drawn out from its lattice by coordination with electrosorbed oxygen. In this model, less coordinated sites such as kinks and steps, act as seeds for oxide growth. This is the reason for oxide growth reversibility at the start. However, after these sites are used up, oxide growth occurs at terraces and the metal atoms become displaced and significant surface reconstruction occurs. As more information is obtained from more powerful spectroscopic techniques such as synchrotron and neutron sources, a new microscopic explanation of the rate law is needed. We maintain that place-exchange need not mean a f ipping of the dipole of the metal oxide, rather it seems more reasonable that the electrosorbed oxygen weakens the adjacent metal-metal bonds which allows the metal atom to leave the lattice and form metal oxide at the surface.

Chapter 4

Rotating disk electrode study of CO electrooxidation on Pd

4.1 Abstract

The electrooxidation of carbon monoxide is studied on polycrystalline palladium in CO saturated sulfuric acid solution. We utilized rotating disk and potentiostatic methods to study the kinetics of CO oxidation. A comparison of CO stripping voltammograms with those conducted in CO-saturated electrolyte is given to show the inf uence of mass transport. We discuss the current response at the onset of CO oxidation within the frame work of a nucleation-growth-collision mechanism involving competition between OH(ads) and CO(ads).

4.2 Introduction

While the oxidation of carbon monoxide on platinum has been and continues to be extensively studied [85, 86], much less work has been done for CO oxidation on palladium.

There has been increased interest in CO studies on Pd as Pd has been investigated as a potential catalyst for formic acid oxidation in direct formic acid fuel cells. It may be expected that the mechanism of CO electrooxidation on Pd would be similar to that on Pt, given that they are both group 10 elements. However, there are signif cant differences. The saturation coverage of CO on Pt is near one monolayer [87, 88], but there are indications that the saturation coverage is less on Pd [89]. The effects of mass transport on CO electrooxidation on Pt have been studied [90–92], but much less is known about the effects on Pd. Here we focus on the effects of mass transport upon the adsorption and electrooxidation of CO on polycrystalline Pd.

Recently, CO adsorption and electrooxidation has been studied on various forms of Pd, such as nanoparticles and alloys [93, 94]. Gas phase adsorption studies have been performed on Pd(111) and thin f lms [95–97]. Single crystal studies have been conducted in acidic [98] and alkaline [99] solutions. Various techniques have been used to study CO adsorption and oxidation on Pd: stripping voltammetry [47, 100], infrared ref ectance spectroscopy [101], surface-enhanced raman spectroscopy [102], and electrochemical quartz crystal microbalance [103], to name a few. Most studies have been "stripping" studies, in which the CO is pre-adsorbed and then the oxidation is studied without CO present in the solution. However, some studies have been conducted in CO-saturated solutions [101–104], giving evidence that there are surface sites whose reactivity is dependent upon in-solution CO concentration. These sites are more reactive and thus are thought to be defect sites [47, 92].

In this work we investigate mass transfer effects in carbon monoxide oxidation at a rotating disk electrode (RDE) using cyclic voltammetry and chronoamperometry experiments. The low constant current region prior to the main oxidation peak is shown to have a faradaic component, and the CO coverage in this region is inf uenced by mass transport of dissolved CO. More importantly, we focus on how mass transport affects CO oxidation

during the main anodic peak and the oxide growth and reduction. We discuss our results within the framework of a nucleation-growth-collision (NGC) mechanism, using a simplified reaction scheme, reactions (4.1)–(4.3). Note that while the adsorbed oxygen species is specified as OH(ads), its exact identity is uncertain, and other possibilities are not excluded. We will show evidence of a second form of adsorbed oxo-species that does not participate in CO oxidation.

$$\mathrm{Pd(site) + CO} \underset{k_{-1}}{\overset{k_1}{\rightleftharpoons}} \mathrm{PdCO(ads)} \tag{4.1}$$

$$\mathrm{Pd(site) + H_2O} \underset{k_{-2}}{\overset{k_2}{\rightleftharpoons}} \mathrm{PdOH(ads) + H^+(aq) + e^-} \tag{4.2}$$

$$\mathrm{PdCO(ads) + PdOH(ads)} \xrightarrow{k_3} \mathrm{2\,Pd(site) + CO_2(aq) + H^+(aq) + e^-} \tag{4.3}$$

4.3 Experimental

Carbon monoxide in sulfuric acid was studied at a polycrystalline palladium disk in a rotating disk electrode configuration (E5, Pine Instruments, 99.99 %). The reference and the counter electrodes were polycrystalline platinum and palladium wires (Johnson-Matthey, 99.998 %) sealed in glass or PTFE heat-shrink tubing (Zeus Inc.), respectively. All potentials were measured and are quoted against the reversible hydrogen reference electrode, RHE, in the same electrolyte separated from the main cell by a vycor or wetted ground glass joint. All experiments were carried out at ambient temperature, ca. 21 °C and the normal fluctuations in temperature were found to not affect the results. Potential was controlled with either a custom-built potentiostat or a Gamry Ref 600 potentiostat; the latter was used for the electrochemical impedance spectroscopy (EIS) experiments. For sweep rates lower than 10 mV s^{-1} the RDE was repositioned to have a small meniscus to diminish

the effects of leaking seals [105].

All glassware was thoroughly cleaned by soaking in fresh piranha solution (two parts concentrated H_2SO_4 and one part 30% w/w H_2O_2 by volume) for 10 min. It was then placed in hot concentrated H_2SO_4 overnight to oxidize remaining contaminants and to decompose any peroxide remaining. The glass was then rinsed with Millipore water (18 MΩ cm), the cell was assembled, and the electrolyte was added immediately afterwards. The 0.5 M H_2SO_4 solution was prepared using the Millipore water and sulfuric acid (Fluka, puriss). After impedance and CV experiments were conducted in electrolyte saturated with Ar (Praxair, 5.0), the solution was bubbled with CO (Praxair, 2.5) for 30 minutes.

The working electrode was first conditioned by running a cyclic voltammogram between 0.2 and 1.5 V at 200 mV s^{-1} for 30 min, and then from 0.25 to 1.4 V at 50 mV s^{-1} until the representative voltammogram was obtained. The double-layer capacitance at 0.5 V was measured using an impedance spectrum before CO was bubbled into the solution, and was used to obtain the true surface area, assuming 25 μF cm^{-2} for an ideally flat surface [47]. After the CO was bubbled into the solution for 30 min the potential was cycled from 0.25 to 1.4 V at 50 mV s^{-1} until a reproducible voltammogram was obtained.

Slow changes in electroactivity have been observed in similar reactions on Pt [106] and Pd [107], and so we were careful to standardize the conditions before experiments: the potential was cycled from 0.3 V to 1.4 V at 50 mV s^{-1} for 1 h while CO was bubbled into the solution. For every recorded voltammogram, unless otherwise noted, the potential was cycled under a specific set of conditions at least three times, with the last one being shown. For voltammograms in which the reversal (limit) potential was varied, the potential was cycled at least twice between 0.3 V and 1.6 V before the potential limit was adjusted. Voltammograms conducted with a CO-covered surface in the absence of CO in the solution will be referred to as CO stripping experiments (CO-strip). Voltammograms conducted in a CO-saturated solution will be referred to as CO-sat.

We used two particular cyclic voltammetry experiments: (1) potential-reversal experiments in which the upper potential limit was systematically changed, and (2) sweep-hold experiments in which the potential scan was halted and the potential held for a period of time before the sweep was resumed. These experiments had multiple conditioning potential cycles immediately before the recorded sweep. Sweep-hold experiments used a $10\,\mathrm{mV\,s^{-1}}$ scan rate before holding the potential for 120 s. Afterwards the sweep direction was reversed and the potential was swept down to 0.4 V. The potential at which holding and/or reversing occurred will be referred to as the limit potential, E_{L}. All voltammograms were carried out with a sweep rate of $10\,\mathrm{mV\,s^{-1}}$ unless noted otherwise.

4.4 Results and Discussion

The results and discussion is divided into parts according to potential regions in the general CO-sat voltammogram: the double-layer region, the anodic peak(s), the oxide region, and the oxide reduction region. It concludes with discussion of a specific kinetic model for reactions (4.1)–(4.3) that explains these results in a consolidated fashion.

4.4.1 General comments

Although most of our work is in CO-saturated solutions, we conducted comparison CO-strip voltammograms, similar to those described in [47]. The CO-strip and CO-sat voltammograms are compared with the voltammogram of clean Pd in Fig. 4.1. On clean Pd, an oxide layer starts to form at 0.75 V, grows irreversibly at a nearly constant rate until the potential limit at 1.4 V, and is then reduced in a peak at 0.72 V [108]. The precise form of the oxide is uncertain, though it is generally described as PdO. When CO is adsorbed on Pd, the oxide growth is delayed and significant anodic current is not obtained until 0.9 V. During the CO-strip voltammogram the current converges with that of bare Pd at 1.2 V.

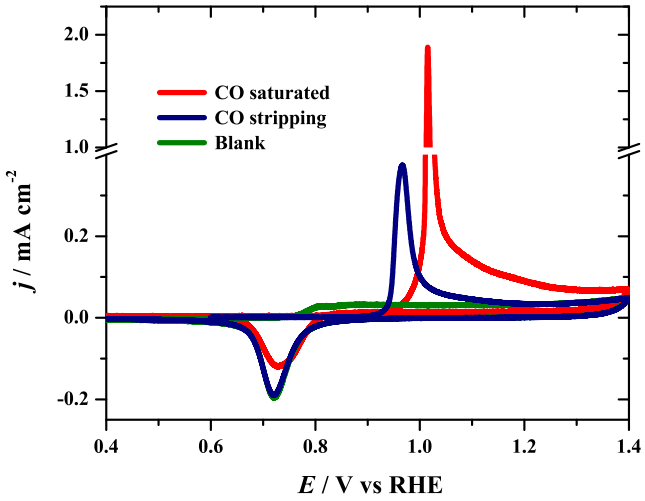

Figure 4.1: Cyclic voltammograms of palladium in sulfuric acid at 50 mV s^{-1}: (**blue**) CO stripping, (**green**) second cycle after CO stripping, and (**red**) CO-saturated electrolyte.

The oxide reduction peak after CO-strip oxidation traces that of bare Pd, implying that all the adsorbed CO is oxidized during the linear sweep to 1.4 V. Because the oxide reduction peaks of the two voltammograms overlap, the amount of oxide grown in the CO-strip experiment was the same as that on bare Pd, even after the initial delay in growth.

In the case of the CO-sat experiment, the anodic current does not converge with the bare Pd, but shows further current due to oxidation of CO from the solution. After the sweep is reversed, the current stabilizes at $+13\,\mu$A cm^{-2} and this value is maintained until 0.8 V, where the oxide is reduced. While the oxide reduction peak in the CO-sat experiment does not match that in the CO-strip nor bare Pd experiments, it is assumed that the same amount of oxide is grown in each case. That is, the smaller reduction peak is attributed to presence of CO oxidation current occurring simultaneously with oxide reduction.

When the solution is quiescent, there is a small amount of anodic current, ca. $+5.5\,\mu$A cm^{-2}**,** on the forward sweep in the double-layer region (< 0.75 V), which is reduced when the electrode is rotating ($+1.0\,\mu$A cm^{-2}). The double layer capacitance measured by EIS also decreases from 9 μF cm^{-2} to 7 μF cm^{-2} when rotating, but the decrease in capacitance and current quickly saturate and show no dependence on rotation rate above the lowest rotation rate used, 11 rad s^{-1}. The current and capacitance responses have been attributed to mass transport affecting CO adsorption near defect sites [47, 92].

CO oxidation at defect sites can occur in the double layer region due to stronger adsorption of water [109] and/or weaker adsorption of CO at the defect sites [92]. A depiction of this is presented in Fig. 4.2. Due to the oxidation, there will be no CO near these sites during CO-strip experiments without CO being present in solution. The oxidation occurs until a limiting coverage is reached, after which no faradaic current will be present (Fig. 4.2a). By saturating the solution with CO, the surface can maintain a higher CO coverage as CO can irreversibly adsorb onto the surface (Eq. 4.4). The higher coverage and flux of CO towards the surface allows for replenishment of CO at defect sites thus causing an increase

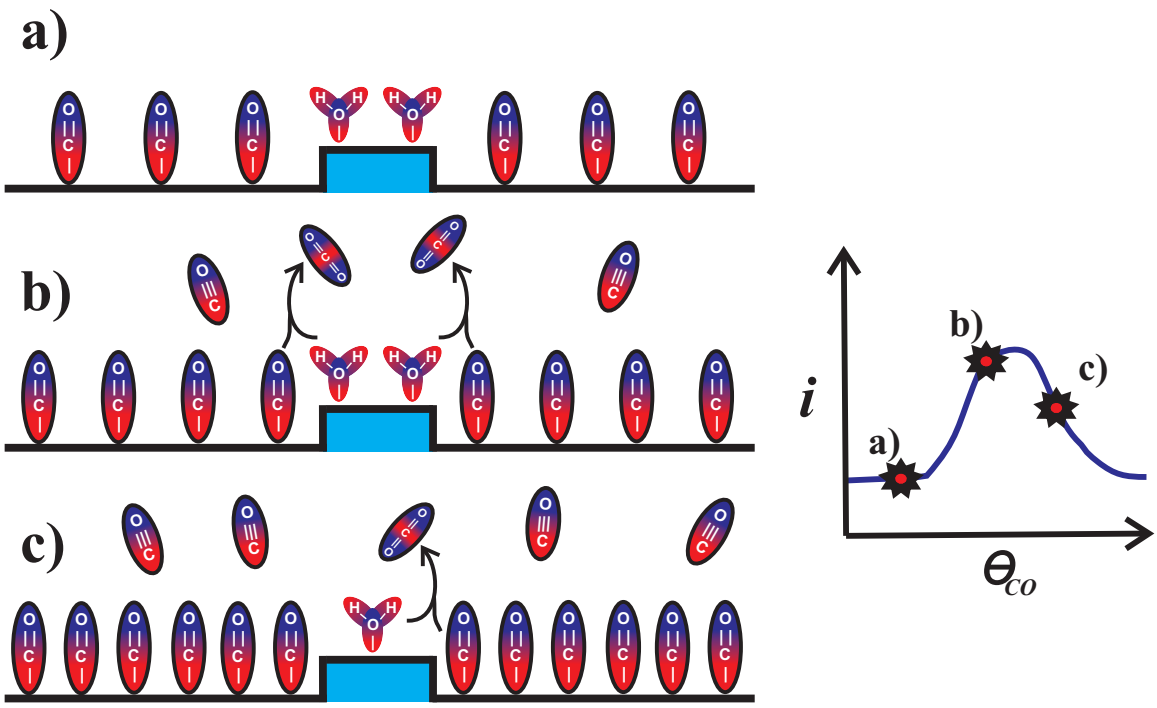

Figure 4.2: Model of CO oxidation during the double layer region (0.3–0.7 V) under different solution conditions at active sites (shown in **blue**): a) shows a surface in a CO-free solution; b) having CO in the solution allows for the replacement of CO(ads) loss due to oxidation with H_2O(ads); c) Increasing the f ux of CO towards the surface saturates the surface with CO(ads) and displaces H_2O(ads). The model predicts a bell-shaped current-θ_{CO} plot.

in current, as shown in Fig. 4.2b. If the rate of CO adsorption becomes greater than the oxidation rate at defect sites ($K_{\mathrm{ads}} > k_{\mathrm{rds}}$) then the coverage of CO saturates. This may displace the adsorbed water (or other reactive oxo-species) and decrease the faradaic current (Figure 4.2c). The faradaic current in the double layer region can then be viewed as a function of CO coverage, which depends upon CO concentration and pressure in addition to the mass transport of CO to the surface.

$$\mathrm{CO(aq)} \underset{}{\overset{K_{\mathrm{ads}}}{\rightleftharpoons}} \underset{\theta_{\mathrm{CO}}}{\mathrm{CO(ads)}} \tag{4.4}$$

$$\underset{\theta_{\mathrm{CO}}}{\mathrm{CO(ads)}} + \underset{\theta_{\mathrm{H_2O(defect)}}}{\mathrm{H_2O(ads)}} \overset{\text{slow}}{\underset{k_{\mathrm{rds}}}{\longrightarrow}} \mathrm{COOH_2(ads)} \tag{4.5}$$

$$\mathrm{COOH_2(ads)} \overset{\text{fast}}{\longrightarrow} \mathrm{CO_2(aq)} + 2\mathrm{H^+(aq)} + 2\mathrm{e^-} \tag{4.6}$$

This coincides with the current being independent of potential during the double layer region. This implies that the rate determining step (rds) is a chemical process occurring before an electrochemical step such as the one given in Eq. 4.5. The slow chemical step is in agreement with DFT calculations pertaining to the high energy of activation required for CO(ads) and H_2O(ads) bond making on Pt [110]. The resulting rate expression would then be

$$\mathrm{rate} = K_{\mathrm{ads}} k_{\mathrm{rds}} \theta_{\mathrm{CO}} \theta_{\mathrm{H_2O(defect)}} \tag{4.7}$$

where k_{rds} is the rate constant of the rds chemical step of CO oxidation.

4.4.2 Anodic peak

The shapes of the forward-going sweeps are typical for CO oxidation on palladium in CO-saturated sulfuric acid (see Fig. 4.3) [104]. Oxidation of CO commences near 0.95 V

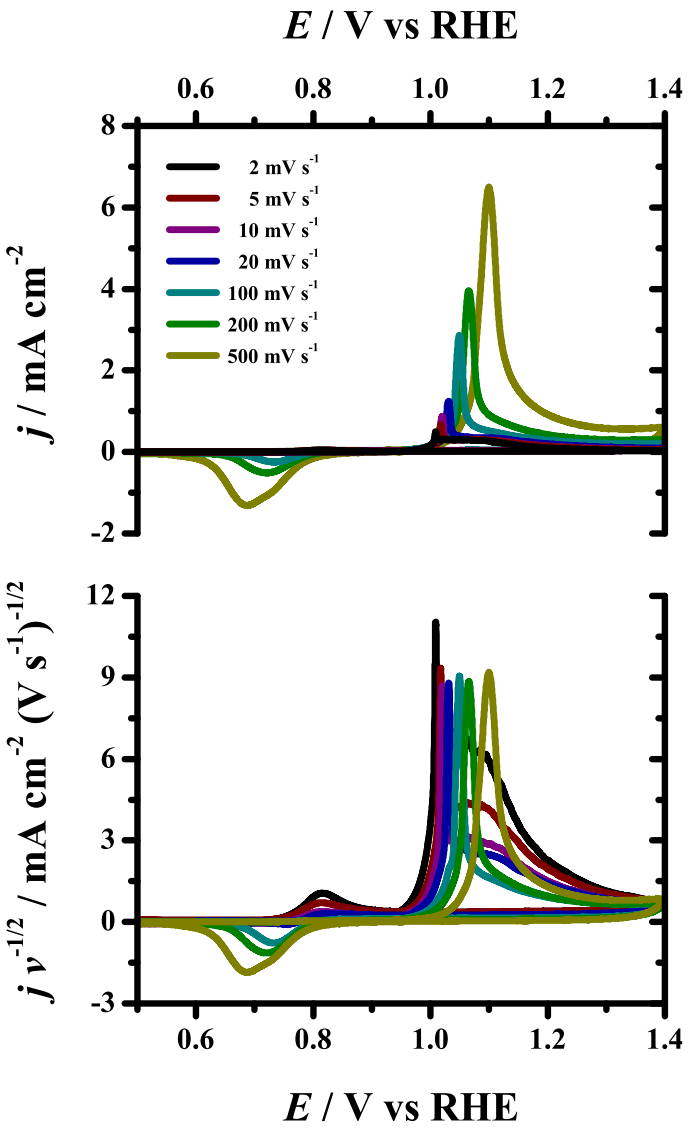

Figure 4.3: Cyclic voltammograms in CO-saturated solution at varying sweep rates, v. The sweep rates of the corresponding curves are given in the f gure. The bottom plot is current density normalized by $v^{1/2}$.

and leads up to a sharp peak at 1.02 V. The peak becomes broader as the scan rate, v, is increased. While it was reported that the peak current of CO-strip experiments on Pd is proportional to v [47], Fig. 4.4 shows that j_{p}, is proportional to $v^{1/2}$ for CO-sat experiments. This proportionality suggests that the current is inf uenced by diffusion. But the slope is larger than predicted by irreversible diffusion limited Randles-Sevik equation

$$j_{\mathrm{p}} = 0.4958nFc^{*}\left(\frac{\alpha F}{RT}Dv\right)^{1/2} \tag{4.8}$$

The reason why the obtained slope is over 3 times that of the predicted value is that CO is present on the surface and participates in the oxidation. This is not allowed under the above model which assumes all reaction steps are fast compared to the f ux of CO to the surface. This is clearly not the case, therefore CO f ux is not limiting.

The peak potential, E_{p}, is linearly dependent upon $\ln\left(v^{1/2}\right)$ (Fig. 4.4) The broadening of the anodic peak and the logarithmic increase of the peak potential with respect to the sweep rate implies an irreversible electrochemical process. Interpreting the Tafel slope as $RT/\alpha F$, we extract an apparent transfer coeff cient, α, of 1.06±0.09 which is in agreement with CO oxidation on Pt [111–114]. The well known description of the anodic transfer coeff cient is

$$\alpha_{\mathrm{a}} = n_{\mathrm{prior}} + n_{\mathrm{rds}}(1-\beta) \tag{4.9}$$

where n_{prior} and n_{rds} are the number of electrons transferred prior to and during the rds, respectively; β is the symmetry factor of the rds transition state. Assuming $\beta = 0.5$, there are two ways of obtaining $\alpha = 1$: having a fast electron transfer occur prior to a slow chemical step ($n_{\mathrm{prior}} = 1$ and $n_{\mathrm{rds}} = 0$); or having a slow concerted 2 e^{-} transfer step ($n_{\mathrm{prior}} = 0$ and $n_{\mathrm{rds}} = 2$). The latter process is rare and no evidence has been seen to support it for CO oxidation. To the contrary, it is more reasonable to assume that combination of OH(ads)

and CO(ads) is the slow step since the energy of activation of this chemical step has been calculated to be quite high [115]. And so the oxidation scheme differs in this peak region from the double layer region since OH(ads) becomes the prevailing adsorbed oxo-species that CO(ads) reacts with.

$$\mathrm{Pd(site) + CO(aq)} \overset{K_{\mathrm{CO,\,ads}}}{\rightleftharpoons} \mathrm{PdCO(ads)} \tag{4.10}$$

$$\mathrm{Pd(site) + H_2O(l)} \overset{K_{\mathrm{OH,\,ads}}}{\rightleftharpoons} \mathrm{PdOH(ads) + H^+(aq) + e^-} \tag{4.11}$$

$$\mathrm{PdCO(ads) + PdOH(ads)} \overset{\text{slow}}{\underset{k_{\mathrm{rds}}}{\longrightarrow}} \mathrm{Pd_{(2)}COOH(ads)\,(+Pd(site))} \tag{4.12}$$

$$\mathrm{Pd_{(2)}COOH(ads)} \rightarrow \mathrm{CO_2(aq) + (2)\,Pd(site) + H^+(aq) + e^-} \tag{4.13}$$

Sweep-hold and potential-reversal experiments were conducted within the region of the anodic peak (0.95 V–1.00 V), Figs. 4.5 and 4.6 respectively. Setting the reversal potential, E_{L}, near 0.95 V, causes the reverse scan to retrace the forward one (yellow curve in Figure 4.6). The fact that the current in this region appears to be a function only of potential is rather surprising.

Most mechanisms for simple desorption predict either an opposite current on reversal as the reverse reaction takes place or—as the case for irreversible NGC—an increased current as islands continue to grow. However, the measured response implies pseudo-steady-state behavior in which the surface condition depends only on potential. We can extend the defect model utilized for the double-layer region by allowing OH(ads) formation at defect sites as in Eq. **(4.11)**. This occurs at specif c nucleation defect sites but the rate of OH(ads) island growth is not able to overcome the rate of CO transport (by surface diffusion or from solution) to adjacent sites; therefore the coverage of OH(ads) is tied directly with the applied potential. When the potential sweep is reversed in this region, the coverage of OH(ads) decreases, and with it the current.

At higher potentials up to the peak maximum at 1.0 V, the current response continues to

increase even after the sweep is reversed, a classic signal of an NGC mechanism. Similar behavior is seen in the sweep-hold experiments. When the potential sweep is halted along the peak before the maximum, (0.97 V–1.00 V), a time-delayed anodic peak forms after which the current decays to a steady value. Figure 4.5 shows that the time difference between halting the potential and the peak maximum, $\log(t_{\mathrm{p}})$, decreases as E_{L} approaches the peak maximum with a slope of 20 mV dec^{-1}.

This type of Tafel behavior has been seen on Pt (though potential steps were used) and attributed to NGC of OH(ads) islands by [116]. These results imply an NGC-based mechanism for CO oxidation on Pd, assuming that reaction 4.3 is rate determining and occurs at the perimeter of islands of OH(ads) in a sea of CO(ads) [117]. More recently, Koper et al. [118] have simulated potential step experiments on CO stripping oxidation on Pt using Monte Carlo methods. They showed that Tafel relations between t_{p} and E_{L} can be obtained from Langmuir kinetics (also referred to as mean-f eld theory or MFT). In this regard, MFT kinetics can often give similar results to those of NGC mechanisms [119, 120] for potential step experiments. The Tafel slopes of $-\log(t_{\mathrm{p}})$ vs E_{L} on Pt were measured to be between 60 and 120 mV dec^{-1} [113, 114] and the simulations predict two limiting slope values, 40 and 120 mV dec^{-1} [111].

Direct comparison between our results and the mentioned simulations is diff cult given that there is an absence of simulations comparing the response of NGC and MFT to potential reversal, sweep-hold, and even linear sweep voltammograms. The values for t_{p} in our sweep hold experiments are nearer to those predicted by NGC, yet the current values and the sharpness of the peaks are closer to those predicted by MFT. Clearly a model incorporating elements from NGC and MFT is needed to explain the current response of the sweep-hold and potential-reversal voltammograms.

Figure 4.7 conf rms in a dramatic way that mass transport affects the oxidation of carbon monoxide on palladium. On the forward sweep, increasing the rotation rate, ω, delays

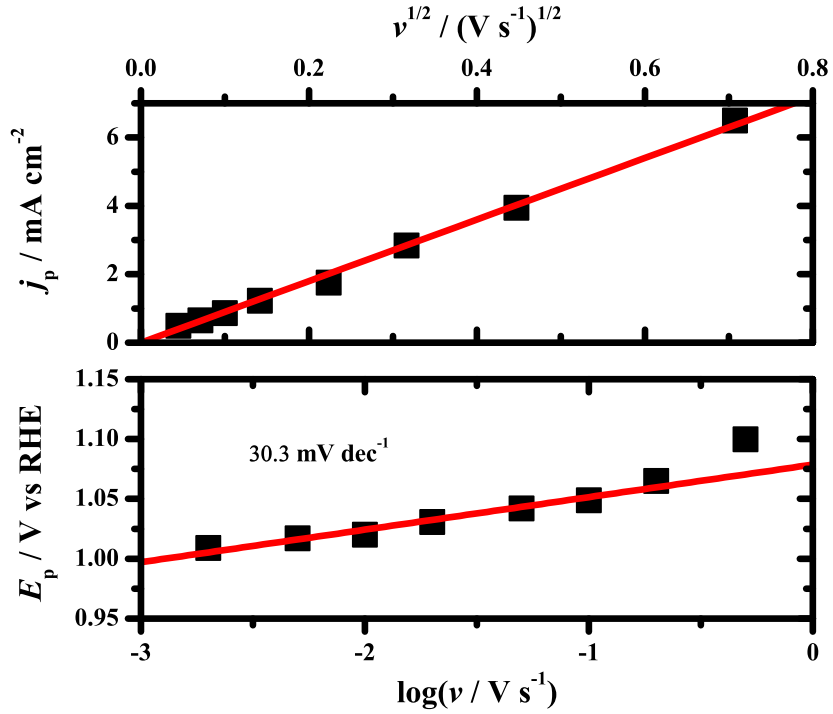

Figure 4.4: Anodic peak potentials and currents as a function of sweep rate. Data taken from plots shown in Figure 4.3.

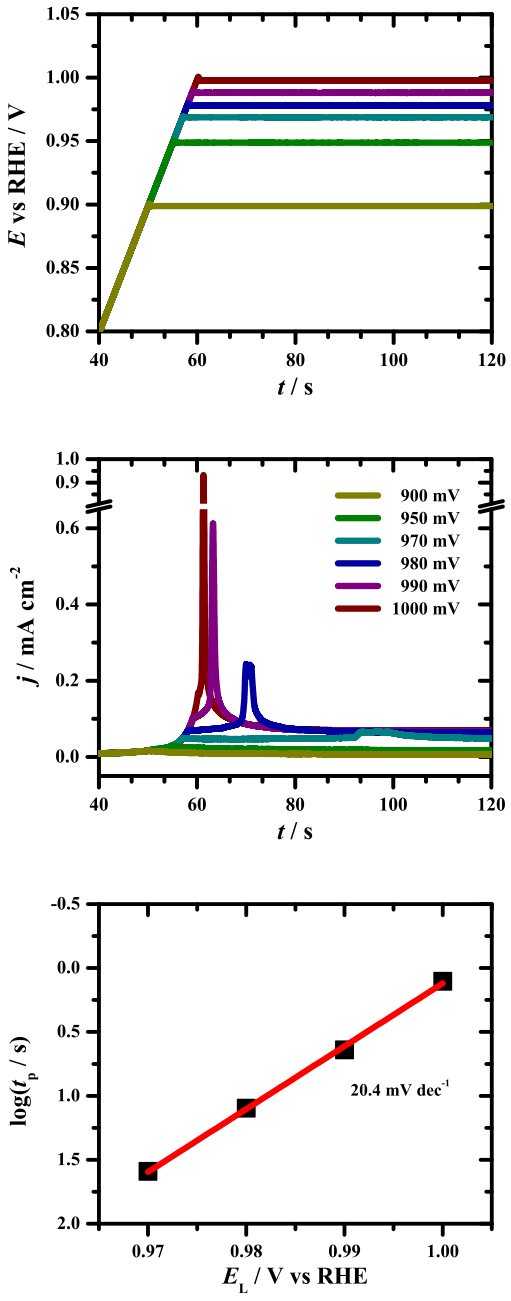

Figure 4.5: Sweep-hold voltammograms of Pd in CO-saturated electrolyte with CO bubbling. Rotation rate: $0\,\mathrm{rad\,s^{-1}}$; sweep rate: $10\,\mathrm{mV\,s^{-1}}$. Top: transient current. Holding potentials given in the legend; all are before the peak maximum. Bottom: Dependence of time at peak maximum on holding potential.

the oxidation of CO. Since H_2O is the prevalent species in solution, it is unlikely that its adsorption and subsequent reaction to give OH(ads) is affected by its transport. The delay in CO oxidation is caused by the increased flux of CO towards the surface. As described in Section 4.4.1 and illustrated by Fig. 4.2, increasing the rate of mass transport of CO causes the surface to be saturated with CO. This in turn displaces adsorbed water thereby impeding the nucleation of OH(ads) islands at defect sites. And so, a greater potential is needed for the rate of OH adsorption to overcome that of CO adsorption which increases with rotation rate. The rate of CO oxidation can then be written as

$$\text{rate} \quad = \quad k_{\text{rds}} K(\omega, E) \theta_{\text{CO}} \theta_{\text{OH(defect)}} \tag{4.14}$$

where $K(\omega, E)$ describes the pseudo-steady state equilibrium constant of the steps prior to the rds.

The oxidation peak current increases with ω and a second peak develops at higher potentials for rotation rates greater than 84 rad s^{-1}. The two peaks will hereafter be referred to as the α-peak (lower potential) and the β-peak (higher potential). Two CO oxidation peaks have been reported by [121] in CO-stripping experiments on Pd thin films on Au(111) surfaces. They attributed the lower-potential peak as being due to oxidation at defect sites, and the second as oxidation on ordered terrace sites. The potential difference between the two peaks is 55 mV while the difference found in [121] was 200 mV. Polycrystalline surfaces are highly defective, with few well-ordered terraces and so it would follow that the two peaks originate from sites of different forms. [122] have suggested that OH(ads) at defect sites and OH(ads) adjacent to defect sites have different reactivities and thus can produce two peaks.

The current increases with ω, with a log-log plot giving slopes of 0.15 ± 0.01 and 0.52 ± 0.06, corresponding to the α-peak and the β-peak respectively, Fig. 4.7. The typical

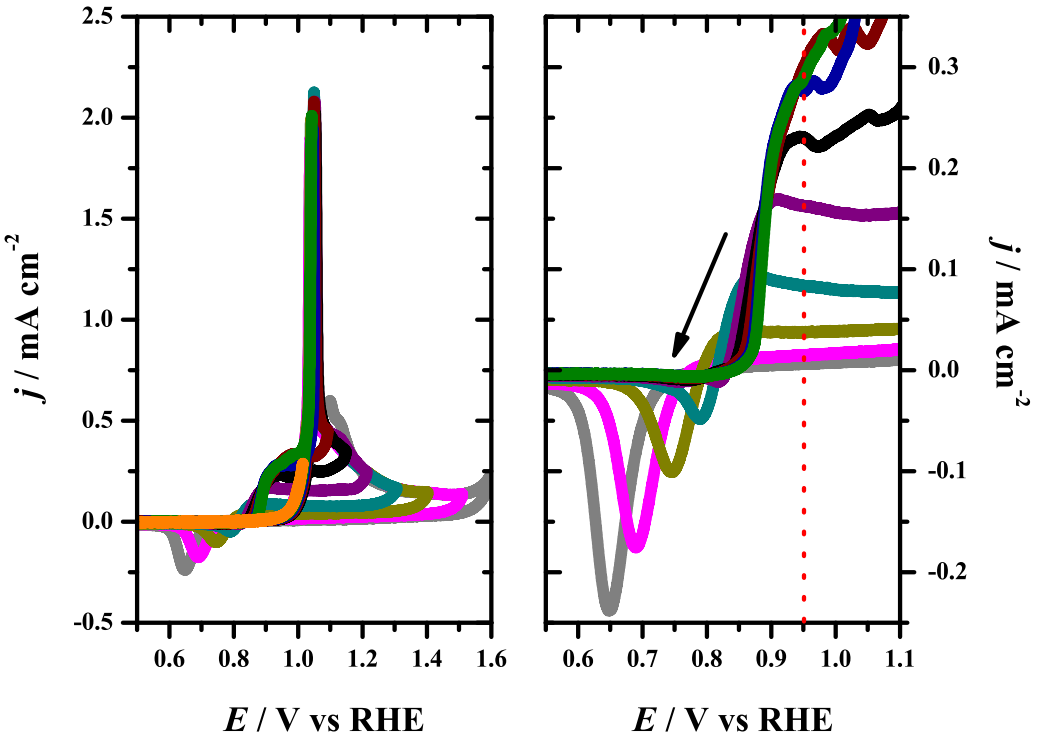

Figure 4.6: Potential-reversal CVs for Pd in CO-saturated 0.5 M H_2SO_4 at 50 mV s^{-1} and a rotation rate of 11 rad s^{-1}. The plot on the right is an expanded view highlighting the anodic current on the reverse sweep and the oxide reduction peak.

$j - \omega$ slope in log-log of a mass-transport limited processes is 0.5, which originates from $\omega^{1/2}$ dependence in the Koutecky-Levich equation (Eq. 4.16). However, a slope less than 0.5 describes a kinetically influenced or limiting process. The peak current of the α-peak begins to decrease when $\omega > 1.57\,\mathrm{rad\,s^{-1}}$. The slopes of E_p-$\ln(\omega^{1/2})$ for the two peak are similar, $72 \pm 2\,\mathrm{mV\,dec^{-1}}$ and $85 \pm 3\,\mathrm{mV\,dec^{-1}}$ (α and β, respectively).

These results further suggest two reaction sites with one being more influence by the reaction kinetics than the other. If we think of the former peak being from the NGC of OH(ads) in the active region then the kinetic influence would come about by the rate of OH(ads) islands growth. When the reactive region is saturated with OH(ads) the rate of the rds is increased (Eq. 4.14). This then causes CO(ads) diffusion towards the perimeter of these regions to have a greater influence on the current. It is not obvious whether the transport of CO to the edge of the islands is from surface diffusion or from the solution. The most likely explanation involves surface diffusion and solution diffusion working in conjunction to increase the oxidation rate.

4.4.3 Oxide growth region

CO electrooxidation in the oxide region after the main anodic peak depends on sweep rate. The charge associated with CO oxidation was calculated by integrating the current response from the forward-going sweeps after correcting for charge due to oxide growth [123]. The CO-strip charge was $0.32\,\mathrm{mC\,cm^{-2}}$, in close agreement with Losiewicz et al. [47]. The same charge in CO saturated solution was found to be $1.15\,\mathrm{mC\,cm^{-2}}$, indicating oxidation of CO from the solution. The difference between the anodic charge for CO-strip and CO-sat experiments decreases as the sweep rate increases. This is expected given that slower scans allow for more CO to be oxidized from the solution. In sweep-hold experiments, holding the potential after the peak produces a slowly decaying current that reaches steady-state in about 10 s (Fig. 4.10). However, holding at potentials over 1.3 V leads to decaying curves

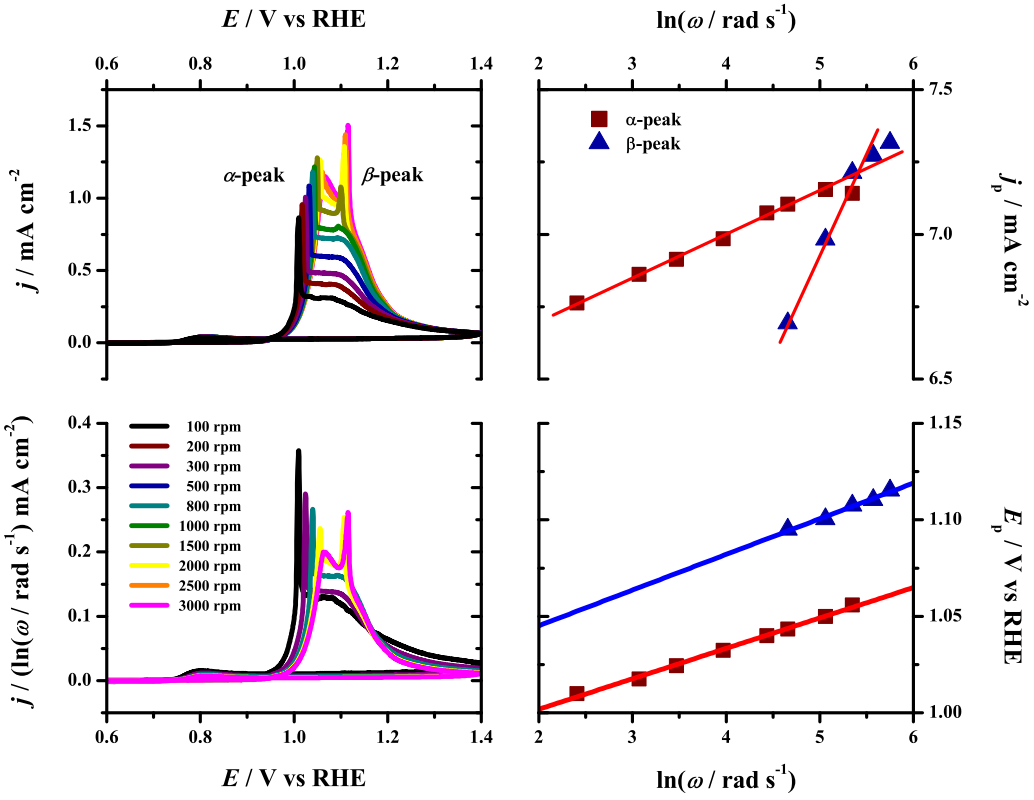

Figure 4.7: Cyclic voltammograms of Pd in CO saturated 0.5 M H_2SO_4 at 10 mV s^{-1} at various rotation rates (top left). Bottom left plot shows current normalized to $\ln(\omega)$, and at the right, the dependency of the peak current and peak potential of the two anodic peaks to $\ln(\omega)$ (top and bottom, respectively).

that do not reach steady state even after 60 s.

Continued CO oxidation at higher potentials where the surface is oxide covered may occur by direct reaction with the oxide, or may occur on oxide-free regions of the surface. The estimated charge of formation of a complete monolayer of O(ads) on polycrystalline palladium is 420 μC cm^{-2} [47, 124], assuming two electrons per Pd**.** However, oxide growth may not occur uniformly, and may grow topotaxially, i.e., 3-D growth may commence when there are still oxide-free regions on the surface [124]. Auger spectroscopy experiments suggest that Pt$_x$O(ads) reaches a coverage of ca. 0.5 monolayers before lattice place exchange takes place [125]. Assuming that oxide growth on Pd is similar, there would exist free sites for CO adsorption at high potentials. The normalized plot (Figure 4.3) shows a convergence point at 1.2 V, so that the CO oxidation current is proportional to $v^{1/2}$ at this potential, implying the inf uence of diffusion. We assume that the current is diffusion-controlled, but on the small fraction of the surface that is not covered by oxide. The active surface area will decrease as the coverage of oxide increases. The sweep-hold data supports this conclusion as the currents at 90 s decrease as the potential is increased (green curve in Figure 4.8).

Since the oxide region shows diffusion-inf uenced kinetics, it is expected that rotation rate will have an effect upon the oxidation within the region. This has been shown to be true for platinum [90–92] and it is clear from our results (Figure 4.7) that the same is true for palladium. When the electrode is rotating, the current plateaus from 1.05 V to 1.10 V before it decreases rapidly. Near 1.2 V all the RDE voltammograms converge to a common curve. On Pt, the same convergence is not seen until 1.6 V [126]. The normalized plot in Figure 4.7 highlights this convergence by displaying an intersection point at 1.15 V.

In order to gather quantitative information of the effects of mass transport on CO oxidation in the oxide region, we f tted the current responses to Levich (L) and Koutecky-Levich (KL) kinetics. The Levich equation (Eq. 4.15) is used to describe a system at steady-state

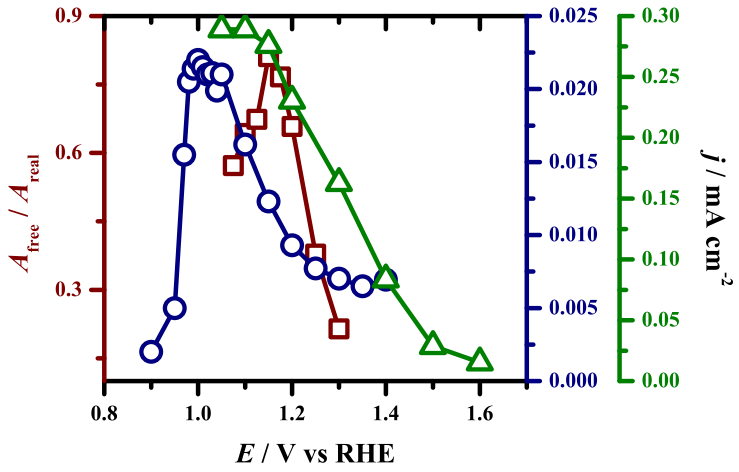

Figure 4.8: Summary of potential dependencies upon (**red squares**) $(1 - \theta_{\mathrm{OH}})$ (reproduced from Figure 4.9), (**blue circles**) sweep-hold currents taken at 90 s (Figure 4.10), and (**green triangles**) currents taken at 0.95 V from potential-reversal experiments (Figure 4.6). For the latter, the potential refers to the reversal potential.

where mass transport is slow compared to the electron-transfer process(es). This model shows no dependency of the current response to applied potential. Eq. 4.16 describes KL kinetics on a reactive surface which includes a potential-dependent kinetic term and the mass-transport term. The Levich and Koutecky-Levich plots shown in Figure 4.9 were obtained by utilizing data from Figure 4.7.

$$j_{\mathrm{L}} = 0.620nFc^{\star}D^{2/3}v^{-1/6}\omega^{1/2} = K_{\mathrm{L}}\omega^{1/2} \tag{4.15}$$

$$j_{\mathrm{KL}}^{-1} = \frac{j_{\mathrm{L}} + j_{\mathrm{k}}}{j_{\mathrm{L}}\, j_{\mathrm{k}}} = j_{\mathrm{k}}^{-1} + j_{\mathrm{mt}}^{-1} \tag{4.16}$$

$$j_{\mathrm{k}} = nFc^{\star}k_{\mathrm{app}} \exp\left(\frac{\alpha_{\mathrm{app}}F}{RT}\left(E - E_{\mathrm{RHE}}\right)\right)\Theta_{\mathrm{active}} \tag{4.17}$$

$$j_{\mathrm{mt}} = K_{\mathrm{L}}\Theta_{\mathrm{active}}\omega^{1/2} \tag{4.18}$$

The small potential region immediately after the α-peak (1.07 V - 1.10 V) adheres more closely to Levich kinetics as the current is proportional to $\omega^{1/2}$. After that, the system follows KL kinetics as shown in Figure 4.9. The kinetic term, j_{k}, shows an exponential dependence on potential as expected from Equation 4.17. A break in this linear relationship occurs near 1.2 V; consistent with the convergence point of the RDE voltammograms. However, in true KL kinetics $j_{\mathrm{mt}}\omega^{-1/2}$ is potential independent, as j_{L} would equal j_{mt}. This would appear in the KL plot as the curves being parallel (i.e., having the same slopes). This is clearly not the case: see bottom right plot in Figure 4.9. $j_{\mathrm{mt}}\omega^{-1/2}$ slowly decreases until 1.15 V where it increases sharply. This potential dependency of the mass-transport coeff cient supports the changing active surface area argument given above. An active surface area correction term, Θ_{active}, can be calculated given that the concentration of CO in solution and the diffusion coeff cient are 0.999 mM and $2.1 \times 10^{-5}\,\mathrm{cm^{-2}\,s^{-1}}$, respectively [127]. Assuming an overall $2\,\mathrm{e^-}$ transfer process, the mass transport constant, K_{L}, then becomes $1.94 \times 10^{-4}\,\mathrm{C\,cm^{-2}\,s^{-1/2}}$. The kinetic current term can then be corrected for the

change in the active surface area by dividing j_{k} by Θ_{active} giving $j_{\mathrm{k}}^{'}$.

$$j_{\mathrm{k}}^{'} = nFc^{\star}k_{\mathrm{app}} \exp\left(\frac{\alpha_{\mathrm{app}}F}{RT}\left(E - E_{\mathrm{RHE}}\right)\right) \tag{4.19}$$

The obtained apparent transfer coeff cient, α, prior to the peak in $\ln(j_{\mathrm{k}}^{'})$ and after is 0.65 and -0.68, respectively. Throughout most of the oxide region α is negative which agrees with the negative slope of a slow linear potential sweep. Negative slopes on polarization curves have been measured with reference to formic acid on palladium (double layer region) [128] and CO oxidation on platinum (oxide region) [83, 104]. However, the change in reactive surface area due to oxide formation cannot account for the exponential decrease in current, since this factor was corrected for. Rather, increasing the potential must inversely affect the rate of a particular reaction or facilitate alternative reaction scheme which in turn inhibits the reaction. [129] have demonstrated how inhibition and site blocking causes a negative Tafel slope. In particular cases where adsorbed species inhibit surface reactions by increasing the energy of activation the positive and negative Tafel slopes are symmetric, e.g. $\pm RT/\alpha F$. This kinetic inhibition theory supports our f ndings for CO oxidation in the oxide region.

It has been detected that the formate intermediate in formic acid oxidation on Pd is more prevalent in the oxide region [130]. This means that its removal is slowed down signif cantly as the potential increases, which causes a negative $j - E$ slope. The cause of this may be due to the change in nature of the oxo-species. Here OH(ads) undergoes a second electron transfer to give O(ads). The nature of surface PdO is complicated (as is that of PtO) but it follows from our results that its reaction with CO(ads) is slower than that of OH(ads). The reaction scheme then becomes

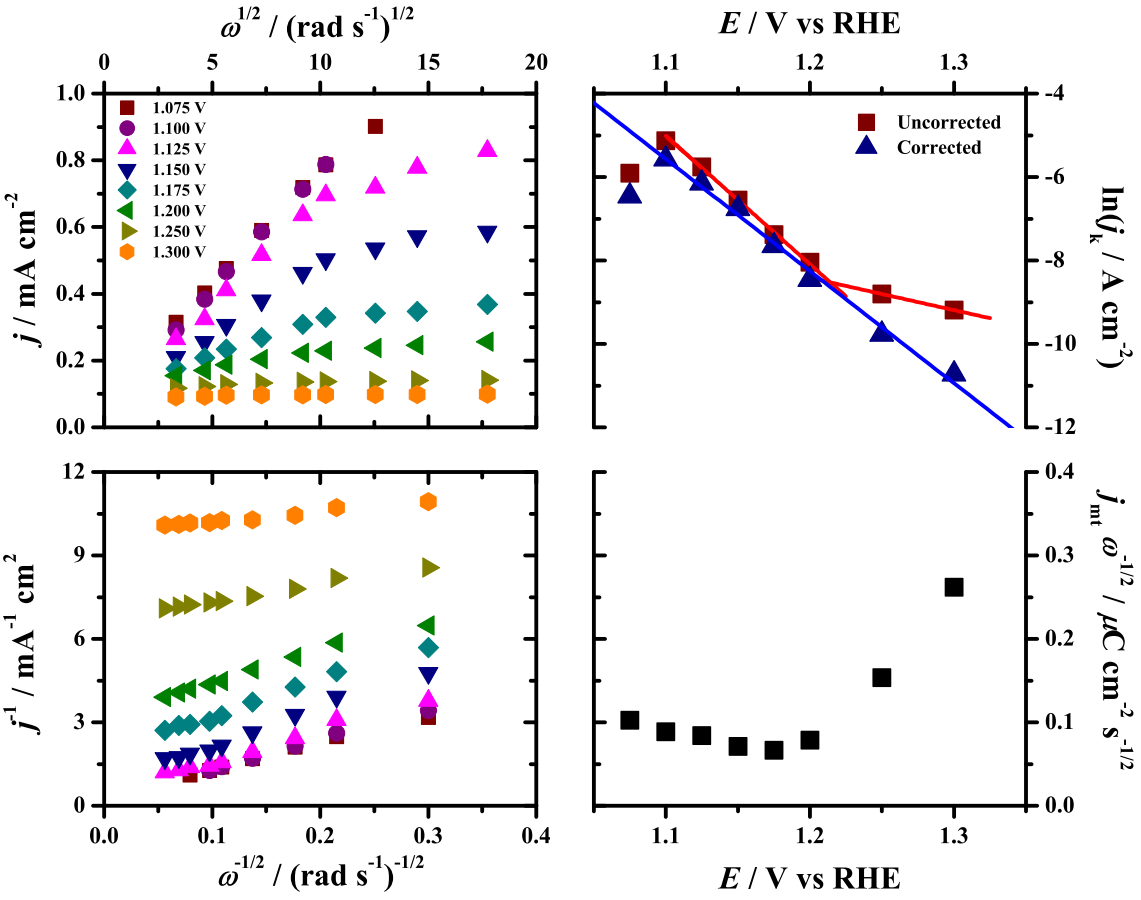

Figure 4.9: Levich plot at varying potentials (top left) and Koutecky-Levich plots at those same potentials (bottom left). The dependency of the Koutecky-Levich terms obtained through f tting of Eq. 4.16 are shown on the right. Legend is given in the f gure and the data are taken from curves shown in Figure 4.7.

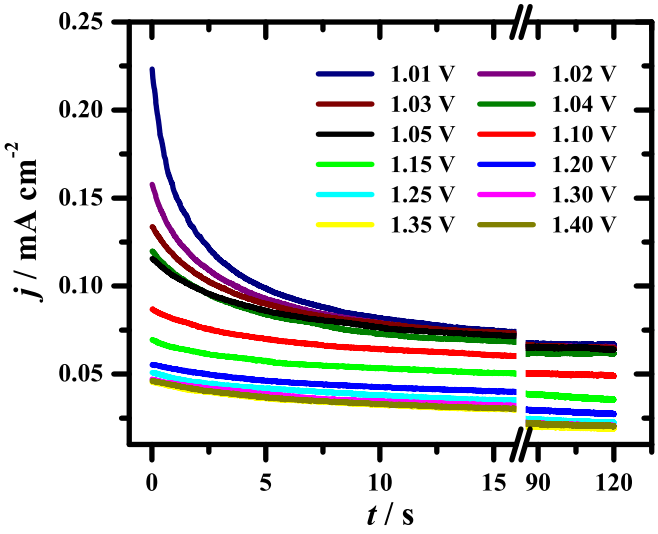

Figure 4.10: Sweep-hold voltammograms of Pd in CO-sat electrolyte at no rotation with CO bubbling, after the anodic peak. The holding potentials are given in the legend.

$$\mathrm{Pd(site) + CO(aq)} \overset{K_{\mathrm{CO,\,ads}}}{\rightleftharpoons} \mathrm{PdCO(ads)} \tag{4.20}$$

$$\mathrm{PdOH(ads)} \overset{K_{\mathrm{O,\,ads}}}{\rightleftharpoons} \mathrm{PdO(ads) + H^{+}(aq) + e^{-}} \tag{4.21}$$

$$\mathrm{PdCO(ads) + PdO(ads)} \overset{k_{\mathrm{rds}}}{\longrightarrow} \mathrm{CO_2(aq) + 2\,Pd(site)} \tag{4.22}$$

4.4.4 Oxide reduction region

As mentioned before, the current response on the negative-going sweep maintains a near constant anodic value until the oxide reduction region. Sweeping the potential below 0.85 V results in a small increase in the anodic current before the formation of an oxide reduction peak. The cathodic peak is dependent upon the sweep rate: a faster sweep rate increases the peak current and shifts the peak more negative. At sweep rates smaller than $20\,\mathrm{mV\,s^{-1}}$ there is no detectable amount of charge due to oxide reduction. At greater than $80\,\mathrm{mV\,s^{-1}}$, the reduction peak develops a shoulder at a potential more positive than the main peak. This shoulder appears to be connected to the same processes that causes the small anodic peak in the reverse sweeping direction at slower scan rates. A small peak in the opposite direction superimposed upon a larger peak would cause this shoulder.

The opposing effects that manifest themselves in the reverse peak are the oxide reduction and CO oxidation. This also explains why the charge of the oxide reduction is less for the CO-sat experiments than it is for the CO-strip. When the potential is swept past 0.8 V in the negative direction the competition between the reduction of the oxide and the oxidation of CO increases due to a greater number of active sites. At slower sweep rates, the rate of CO oxidation is along the time scale of the potential sweep, which allows for removal of OH(ads) more so by CO oxidation than OH(ads) reduction; thereby resulting in net anodic currents.

The sweep reversal potential, E_{L}, was varied to measure the effect of OH(ads) coverage upon CO oxidation, and from Figure 4.6, it is clear that it has an effect upon the reverse

scan. When the potential limit was set higher than 1.2 V the reverse current quickly stabilized to a particular value and minimized the effects of sweep rate. On the other hand, the cathodic peak near 0.8 V becomes more pronounced. The reduction peak current increases and shifts more negatively with an increase in E_{L}. The peak is absent at low E_{L} (<1.15 V); instead, an anodic current is measured. This implies that a change in the nature of OH(ads) occurs at 1.15 V. Studies on oxide growth on platinum have produced evidence for a type of adsorbed oxo-species formed near 1.15 V that is different in either composition or in bonding [125, 131]. This species has been referred to as lattice or place-exchanged oxide. We give the place exchange reaction in terms of its OH(ads) precursor.

$$\mathrm{PdOH(ads)} \underset{k_{\mathrm{red}}}{\overset{k_{\mathrm{ox}}}{\rightleftharpoons}} \mathrm{PdO(lattice)} + \mathrm{H^+(aq)} + \mathrm{e^-} \tag{4.23}$$

The current at 0.95 V on the negative-going scan decreases with an increase in reversal potential, as shown in Figure 4.6. It is worth noting that this current has a similar dependency to potential as Θ_{active} (see Figure 4.8). When E_{L} is increased, the oxide reduction peak increases, which conf rms an increase in O(ads) coverage, Θ_{ox} (or decrease in Θ_{active}). This effect on the oxide reduction peak is the same for bare Pd, indicating formation of a stable form of PdO during the forward-going scan after 1.15 V that is resistant towards CO oxidation [104, 107]. Note that Pd oxide has been shown to be resistant towards numerous oxidations that proceed through adsorption and proton transfer [107].

As seen from Figure 4.7, the negative-going potential scans show minimal mass-transport effects until 0.9 V where the anodic peak forms. While the current does not appreciably change in the peak's region, it does shift toward more positive potentials as ω increases. After the peak, the current decreases to the double layer value. Increasing the mass transport to the electrode allows for free sites to be consumed by CO adsorption. This in turn would increase the rate of CO oxidation and decrease the coverage of O(ads) (or OH(ads)).

As the amount of O(ads) decreases the reduction charge would decrease as well.

4.4.5 Dynamic electrochemical impedance spectroscopy

The dynamic impedance technique described in Chapter 2 and used in Chapter 3 was used to further investigate the effects of mass transport on CO oxidation. The obtained ac voltammograms, Fig. 4.11, showed features similar to those in the dc voltammogram, Fig. 4.1. Potentials lower than 0.6 V are featureless in all admittance plots, meaning that the resulting impedance plots are featureless. At all frequencies, the admittances converge to a constant value after sweeping past 1.2 V and remains unchanged until 0.8 V in the negative direction where oxide reduction occurs. A sharp peak is seen in the forward sweep beginning at 0.9 V which corresponds with the anodic peak in the dc voltammogram (low frequencies). The peak increases linearly with sweep rate as well as shifts in the positive direction. This supports the dc voltammogram results of the reaction being an irreversible surface process. The low frequency imaginary admittance becomes negative right before the peak in the real admittance. This means that the impedance is expected to cross into the fourth quadrant ($\mathrm{Re}(Z) > 0$, $-\mathrm{Im}(Z) < 0$) and show inductive behavior. There is no indication of the real admittance becoming negative even in the negative Tafel slope region after the anodic peak. The only effect of increasing the sweep rate on the high frequency admittance is a slight positive shift of the curve. This is expected since the high frequencies probe the non-faradaic processes, solution resistance and charging of the double layer. The oscillations in the high frequency imaginary admittance are caused by the slow rotation of the electrode.

The effects of rotation can also be seen in the ac voltammograms, Fig. 4.12. Here the admittance peaks shift in the positive direction with increasing rotation. The peak in the low frequency real admittance increases with rotation and shows the formation of a broad second peak in the oxide region at higher rotation rates. The imaginary admittance shows

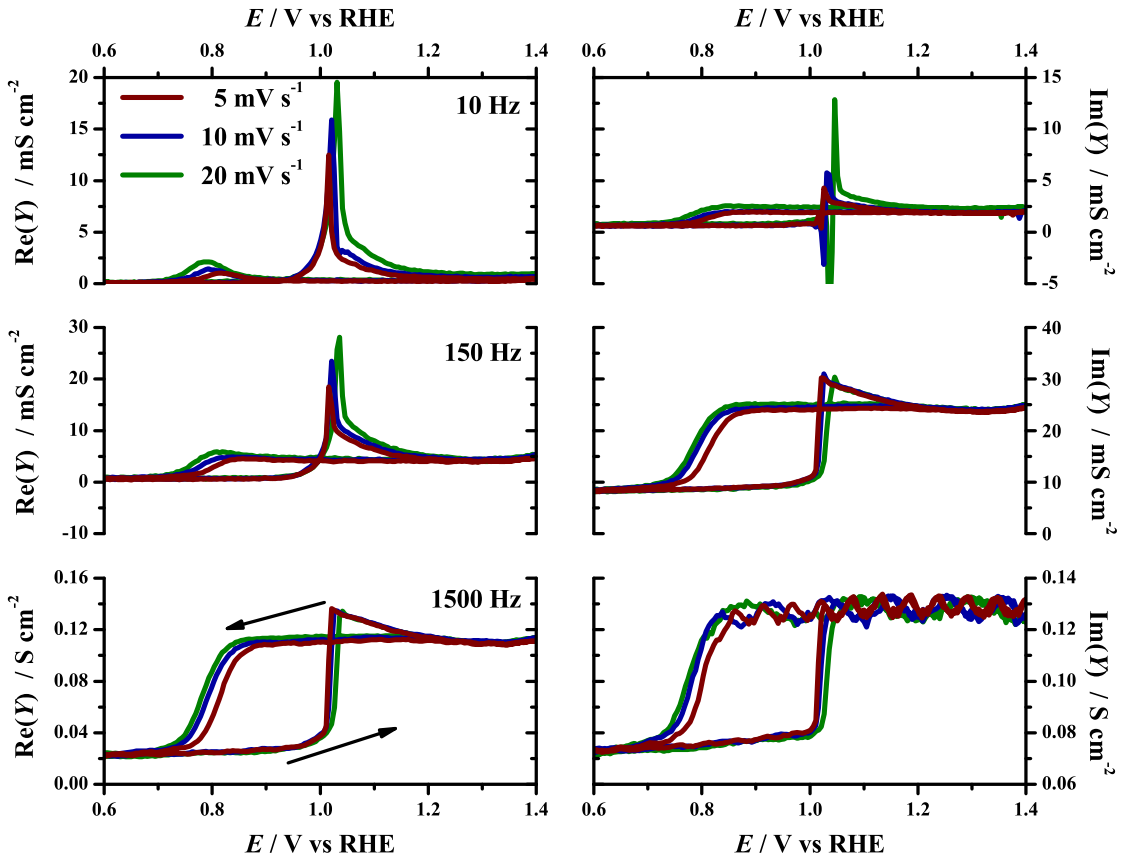

Figure 4.11: Ac voltammograms at varying sweep rates and frequencies. Arrows in direction of potential sweep. Rotation rate: 10 rpm.

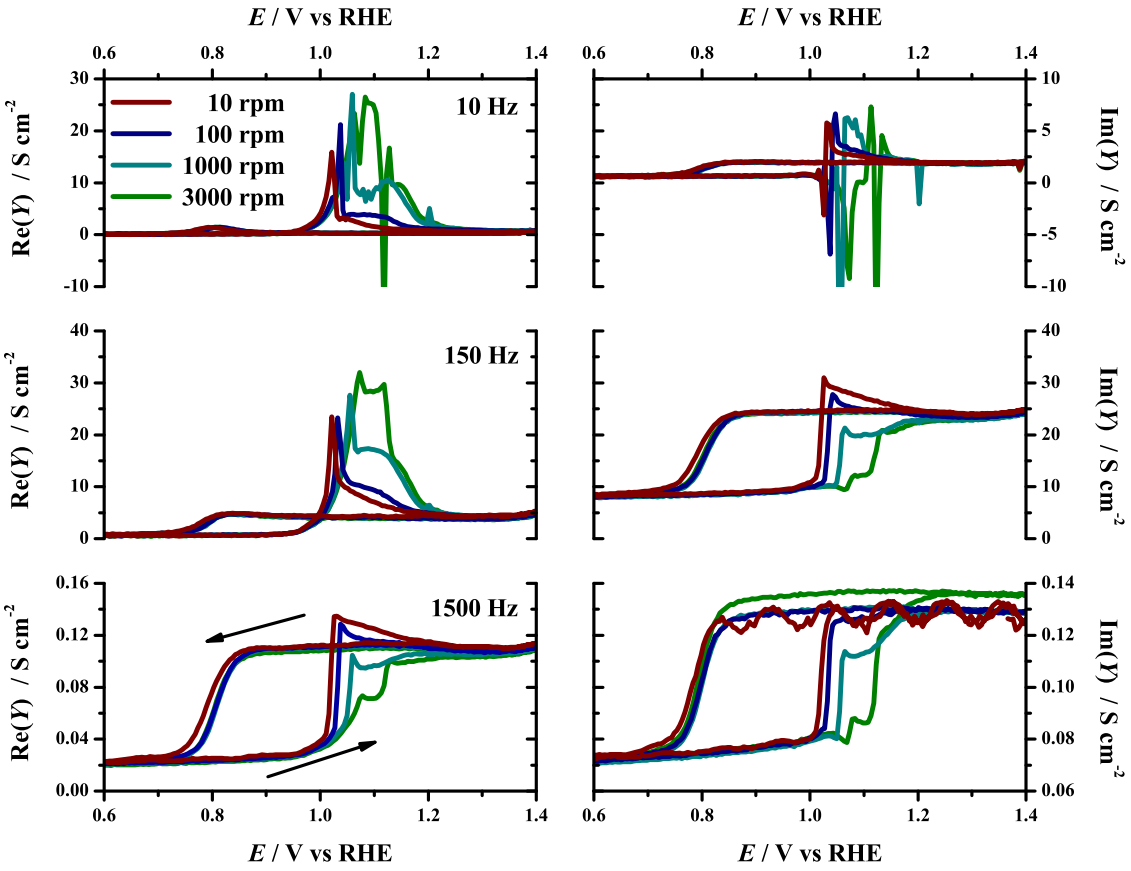

Figure 4.12: Ac voltammograms at varying rotation rates and frequencies. Arrows in direction of potential sweep. Sweep rate: 10 mV s^{-1}.

sporadic behavior in the peak region at high rotation rates which suggests unstable behavior. At high frequencies the admittance in the anodic peak region decreases with rotation rate. This suggests that with the increase of f ux of CO to the electrode surface CO can outcompete oxide growth for free sites that form during CO oxidation. This means that CO is able to maintain its coverage at a high potential. The plateau regions in the high frequency admittance at 3000 rpm correspond to the two peaks found in the dc voltammogram.

Compiling the ac voltammogram data at all frequencies at a particular potential produces an impedance plot. The impedance plots at potentials less than 0.6 V show a large semi-circle that is independent of potential. Near the anodic peak (ca. 0.9 V), the size of the semicircle rapidly decreases as expected from the $\mathrm{Re}(Y)$ plots, Fig. 4.13. In addition

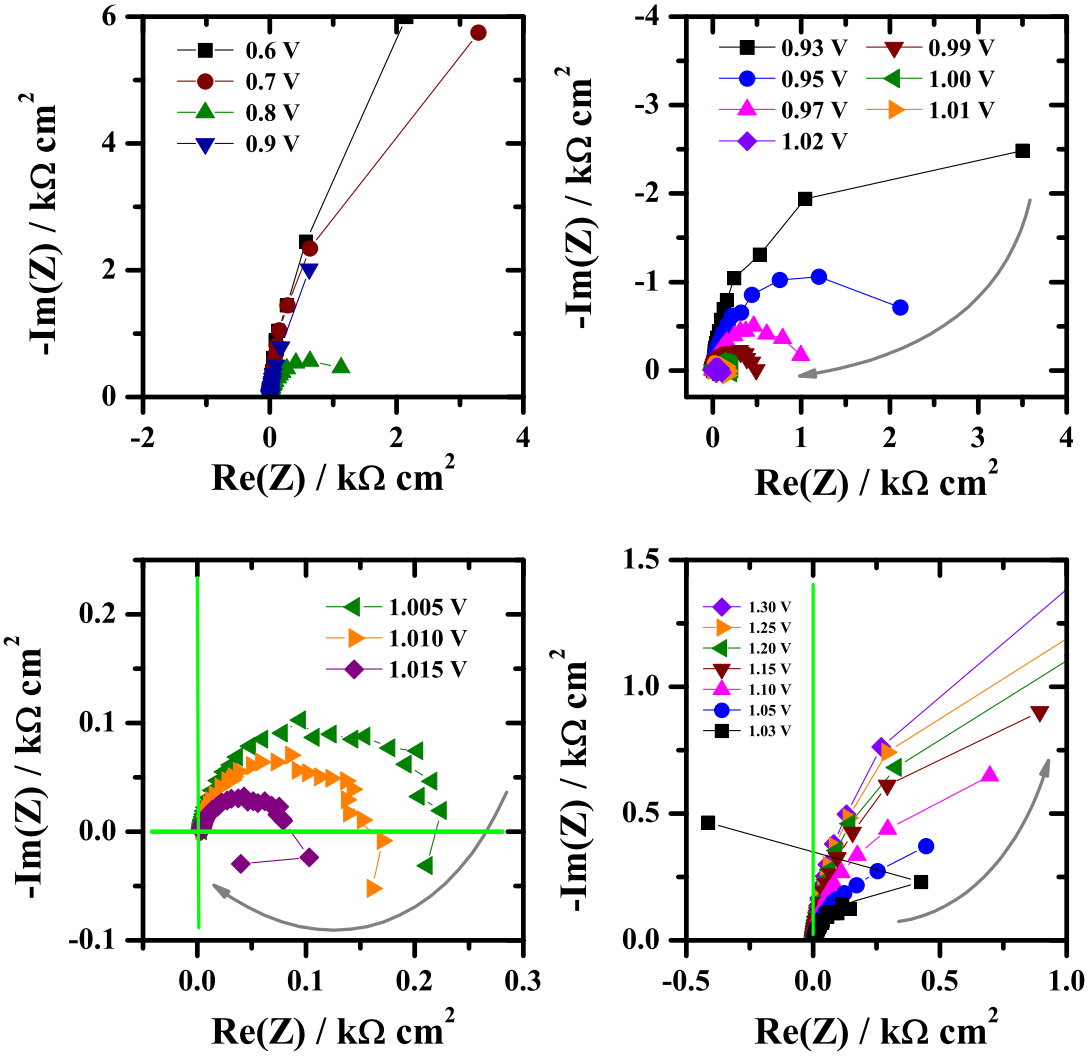

Figure 4.13: Nyquist plots obtained during the dEIS scan (10 rpm, 5 mV s^{-1}). Top left, double-layer region; top right, pre-peak; bottom left, during peak; bottom right, post peak. Arrows in direction of increasing potential.

to decreasing in diameter, a second semicircle forms in the fourth quadrant (bottom left, Fig. 4.13). This means that a second time constant is observed in the region of 0.95–1.1 V. Immediately after the peak maximum the second semicircle flips into the second quadrant (Re(Z) < 0, -Im(Z) > 0), which still produces a positive time constant. Between 1.015 and 1.03 V the spectrum is sporadic due to noise, but by 1.03 V is back into the first quadrant, with the exception of the lowest frequency point, which is likely a noise artifact (bottom right, Fig. 4.13). The second semi-circle disappears as the diameter of the first semi-circle increases with potential.

We fitted the two-time-constant impedance near the peak to an *LR* series circuit (this circuit is discussed in more detail in Chapter 6) in order to test for nucleation and growth characteristics. As shown in Figure 4.14 both R_0 and L_1 are positive throughout this potential region. The fact that R_0 and L_1 show a clear trend suggests that the crossing into the fourth quadrant by a few frequencies in Fig. 4.13 is not caused by random noise. The time constant is given as

$$\tau^{-1} = \frac{R_0}{L_1} = -\Gamma_{\mathrm{m}} \left(\frac{\partial r_\theta}{\partial \theta} \right)_E \tag{4.24}$$

where r_θ is the net production of surface oxo-species, θ, that reacts with CO (e.g., OH(ads)) which from kinetic impedance theory is positive [2, 106, 132]. This means that the system is stable. Both the elements showed Tafel-like relationship to potential. R_0 has a Tafel slope of -45 mV dec^{-1} and L_1 a slope of -60 mV dec^{-1} which are of similar magnitude to the dc current Tafel slope. However, the time constant being positive throughout the peak is inconsistent with the unstable behavior we see in the sweep hold experiments in this potential region.

A NGC process is expected to have a time constant that is negative [106, 133] when the islands are small and growing, and a positive time constant when the islands are large

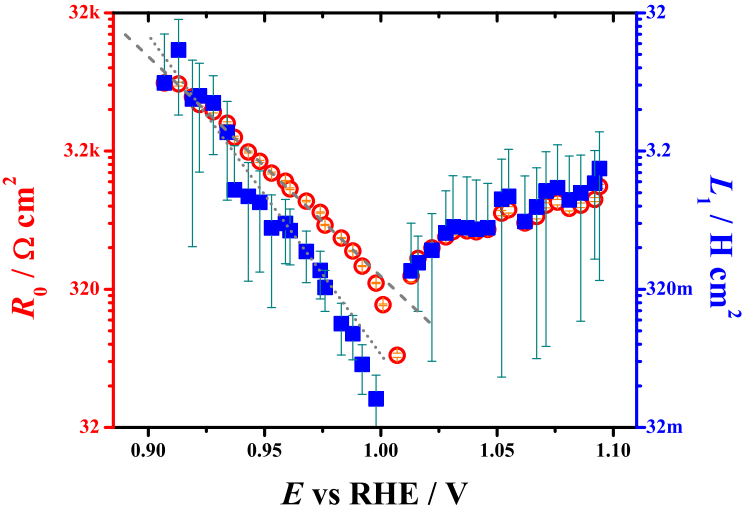

Figure 4.14: Plot of R_0 (**red circles**) and L_1 (**blue squares**) obtained by f tting the dEIS sweep (10 rpm, 5 mV s^{-1}).

and coalescing. Holding the potential during island growth holds the rate constant of island growth constant, but the perimeter of the island (reactive region) will continue to increase, as well as θ. Since the reaction rate is proportional to the perimeter, r_θ will increase as θ increases. Therefore the partial derivative $\left(\frac{\partial r_\theta}{\partial \theta}\right)_E$ will be positive, which in turn causes the time constant to be negative. After the islands become large and begin to collide, the reactive perimeter begins to decrease, and with it r_θ, which then makes $\left(\frac{\partial r_\theta}{\partial \theta}\right)_E < 0$, or $\tau > 0$.

We do not see a change in the sign of the time constant from negative to positive in the impedance data or fits. Such a change in the sign has been seen in methanol and formic acid oxidation on Pt using dEIS [106, 133] and was attributed to the competition between CO and oxide. This competition was regarded as the origin of the unstable behavior. The absence of the the negative time constant at lower frequencies are due to the low frequency limitations of dEIS, in that the change in the dc current must be significantly less than the change in current due to the slowest perturbation. Since the current rises quickly during the peak, this affects the calculation of the low frequency components. Therefore it is possible that the negative time constant features are hidden.

We chose to fit the majority of the impedance data to circuit **R** (see Chapter 2) since only a single semi-circle was detected except during the anodic peak, Fig 4.15. $R_{\rm ct}$ and $C_{\rm dl}$ are featureless and approximately constant for potentials less than 0.8 V (not shown). $R_{\rm ct}^{-1}$ increases with potential prior to the peak in the voltammogram and the sudden change in $C_{\rm dl}$. The slope of $R_{\rm ct}^{-1}$ during the peak is independent of mass transport and has the value of 60 mV dec^{-1} which agrees with the cyclic voltammetry results, that is a chemical step after an electron transfer is rate-determining. After the peak $R_{\rm ct}^{-1}$ increases with rotation and decreases with potential. The $C_{\rm dl}$ plot shows that the amount of CO on the surface (related to the lower limit of capacitance) is affected by rotation. In other words, the coverage of CO increases as the flux of CO toward the surface increases. This agrees with the fact

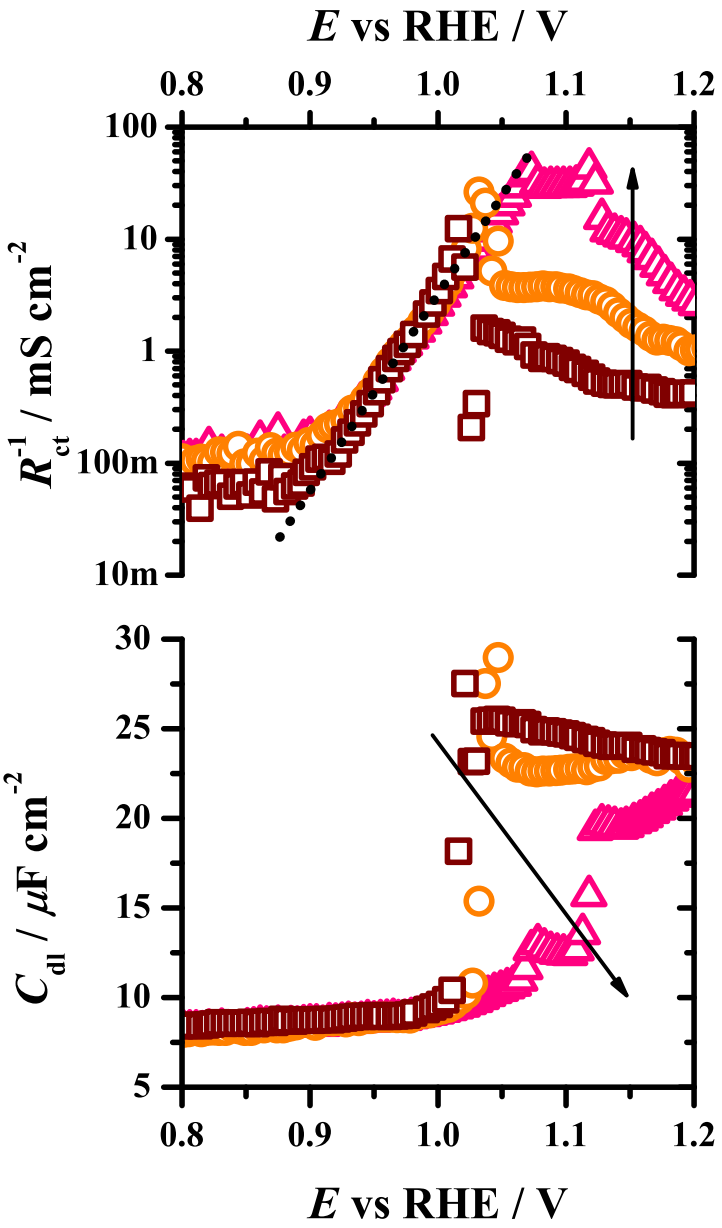

Figure 4.15: Plot of R_{ct}^{-1} and C_{dl} near anodic peak obtained though impedance f ts of circuit **R** to the positive-going sweeps with rotation rate of 0 rad s^{-1} (**red squares**), 10.1 rad s^{-1} (**orange circles**), and 303 rad s^{-1} (**pink triangles**). Sweep rate: 10 mV s^{-1}.

that the reaction has become affected by mass transport while the surface is slowly being passivated by the growth of nonreactive oxide.

In the oxide region ($E > 1.1$ V) rotation rate continues affecting R_{ct} and C_{dl} in that increasing ω causes the charge transfer resistance and capacitance to decrease, Fig. 4.16. Since C_{dl} is related to coverage of CO(ads), the lower capacitance at 3000 rpm suggests that increasing the rotation rate causes θ_{CO} to increase. A similar effect was seen in the current response in the double layer region where increasing the rotation rate delayed CO oxidation since it made the surface more diff cult to oxidize. This means that the CO adsorption equilibrium is affected by electrode rotation. In the oxide region this effect originates from the fact that the CO near the surface is constantly replenished due to convection. Even though the current and R_{ct}^{-1} values generally increase with ω within the oxide region, the $j - E$ and R_{ct}^{-1}- E slopes become more negative as ω is increased. In other words, the rate of passivation increases with ω. The C_{dl} plot suggests that the surface is mostly covered by oxide when $E > 1.15$ V and $\omega = 0$ rad s^{-1} since its value is similar to C_{dl} in bare electrolyte, ca. 25 μF cm^{-2}. The C_{dl} at high ω increases with potential to the value corresponding full oxide coverage. This then means that at no electrode rotation, the passivation rate is small since the electrode has already been passivated by the oxide at $E = 1.15$ V, in other words passivation is independent of potential. At high rotation rate, the oxide growth rate is decrease since the rate of CO adsorption is increased. Therefore, the applied potential has a greater effect on the passivation at higher mass transport rates. It is clear then that the current and R_{ct}^{-1} are related to the amount of CO on the surface: as θ_{CO} decreases j and R_{ct}^{-1} decrease.

The entire negative sweep can be f tted using the simple RC circuit, Fig. 4.17. As with the oxide reduction in bare electrolyte, extrapolation of the impedance to $\omega = 0$ gives a positive resistance. The R_{ct}^{-1} and C_{dl} plots are relatively featureless throughout the scan with the exception of the oxide reduction region. Here R_{ct}^{-1} peaks with Tafel slopes of

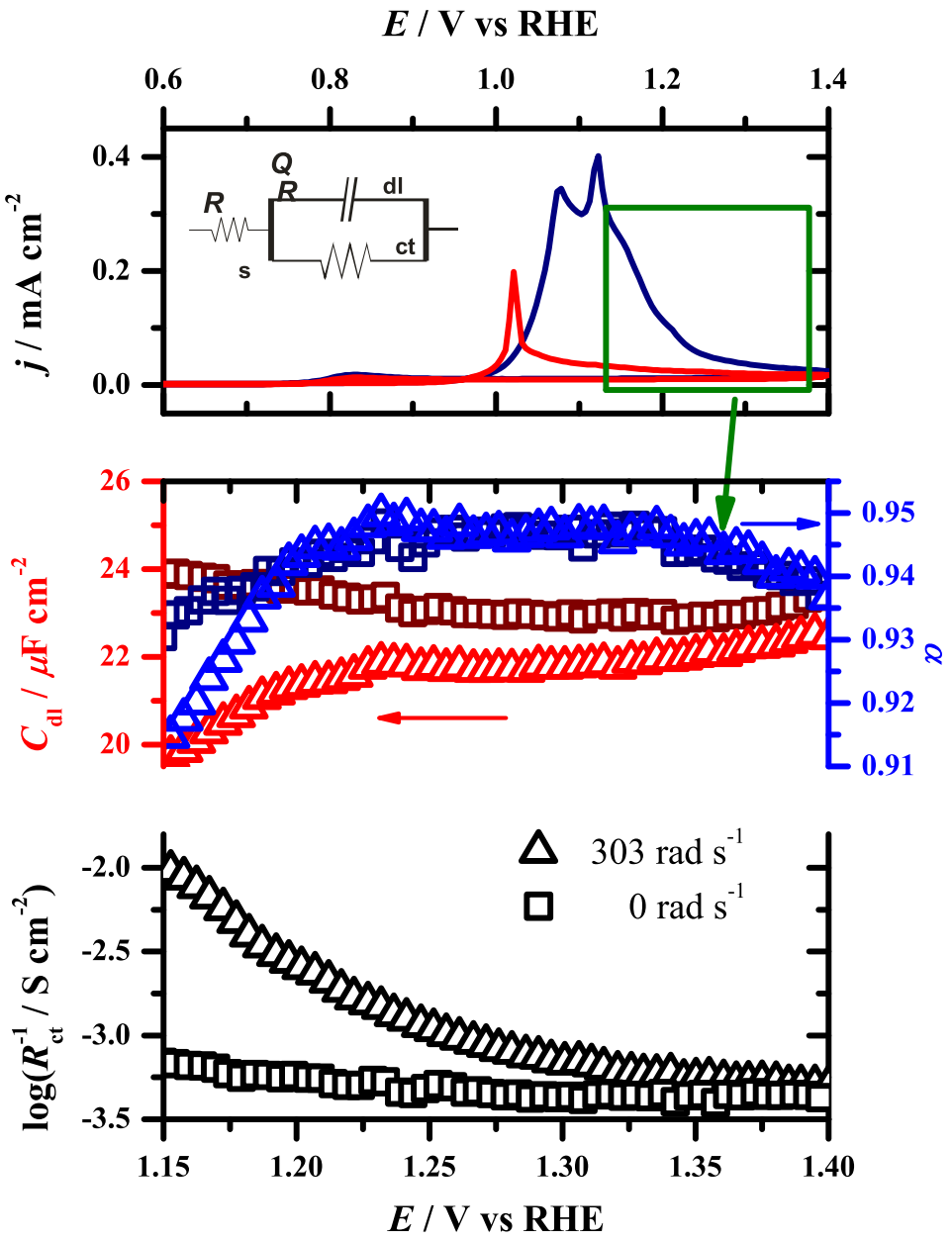

Figure 4.16: Plot of R_{ct}^{-1} and C_{dl} obtained though impedance f ts of circuit **R** to the positive-going sweeps with rotation rate of 0 rad s^{-1} (squares) and 303 rad s^{-1} (triangles). Sweep rate: 10 mV s^{-1}.

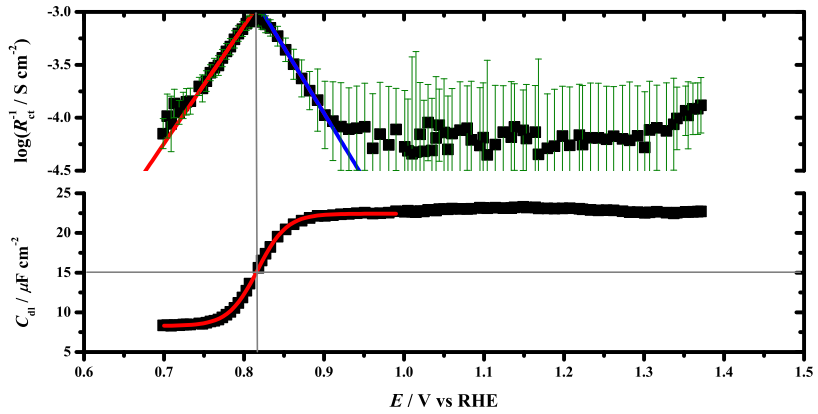

Figure 4.17: Fitted double layer capacitance and charge transfer resistance on the negative-going 5 mV s^{-1} sweep. Solid lines are f tted curves.

+90 mV dec^{-1} and -81 mV dec^{-1} on opposite sides.

The oxide-covered region ($E > 0.9$ V) and the CO covered region ($E < 0.7$ V) have signif cantly different C_{dl} values. Since only two surface species are expected in the negative scan (O(ads) and CO(ads)) the capacitance can be used to approximate the change in CO(ads) coverage during the sweep.

Assuming no free sites the coverages are related by

$$1 = \theta_{\mathrm{CO}} + \theta_{\mathrm{O}} \tag{4.25}$$

The capacitances of the two regions can be considered to be in parallel, leading to

$$C_{\mathrm{dl}} = \theta_{\mathrm{O}} C^*_{\mathrm{O}} + \theta_{\mathrm{CO}} C^*_{\mathrm{CO}} \tag{4.26}$$

$$= (1 - \theta_{\mathrm{CO}}) C^*_{\mathrm{O}} + \theta_{\mathrm{CO}} C^*_{\mathrm{CO}} \tag{4.27}$$

where C_i^* represents the capacitance for a monolayer of species i. Collecting θ_{CO} gives

$$\theta_{\mathrm{CO}} = \frac{C_{\mathrm{dl}} - C_{\mathrm{O}}^*}{C_{\mathrm{CO}}^* - C_{\mathrm{O}}^*} \tag{4.28}$$

We now assume that the potential dependence of coverage follows a Langmuir isotherm

$$K \exp\left(\frac{\alpha F}{RT} E\right) = \frac{\theta_{\mathrm{O}}}{\theta_{\mathrm{CO}}} = \frac{1 - \theta_{\mathrm{CO}}}{\theta_{\mathrm{CO}}} \tag{4.29}$$

Substituting Eq. (4.28) into Eq. (4.29) and rearranging gives the equilibrium expression in terms of measured double layer capacitance.

$$C_{\mathrm{dl}} = C_{\mathrm{O}} + \frac{C_{\mathrm{CO}} - C_{\mathrm{O}}}{1 + K \exp\left(\frac{\alpha F}{RT} E\right)}$$

The above equation was used to fit the capacitance data in Fig. 4.17, from which we obtained the exponential factor, $\frac{\alpha F}{RT}$, to be $55\,\mathrm{V}^{-1}$ which corresponds to $\alpha = 1.4$. The fact that a simple Langmuir isotherm could fit the capacitance data suggests that there is little interaction between the oxide and CO. That is, there is no evidence of a Frumkin-type interaction. This supports the fact that the negative slopes of the kinetic current from the Koutecky-Levich plots are due to the passivation of the surface by nonreactive oxide. Thus only oxide formed at lower potentials provides good reactivity towards CO oxidation.

4.5 Conclusions

Mass transport effects in electrooxidation of carbon monoxide from CO saturated electrolyte were effectively studied by the RDE. It was found that the competition between CO(ads) and the oxo-species over free sites changes with potential. In the double layer

region (c.a. 0.4 V–0.9 V), the presence of CO in solution increases the coverage of CO on the surface. The coverage of CO(ads) can be further increased by raising the mass transport rate CO(aq) to the surface. It was found that the faradaic current has a bell-shaped dependency on CO(ads) coverage. This result was explained by taking the reaction between H_2O(ads) and CO(ads) at defect sites to be the rate determining step (Eq. 4.4). Here, increasing CO(ads) coverage causes an increase in the current until H_2O(ads) displacement occurs at or near defect sites, thereby causing a lower anodic current in the double layer region. Therefore, raising the rate of CO mass transport shifts the dynamic competition between strongly adsorbed water and CO towards CO(ads) on or near defect sites.

During the onset of CO oxidation (0.95 V) the competition occurs at the perimeter of newly formed OH(ads) "islands" at defect sites. These sites were most likely formed by the oxidation of H_2O(ads) but were delayed due to displacement by increased CO mass transport. The results suggest that the same chemical step is the rds though the oxo-species is now OH(ads) which would imply a fast electron transfer prior to the rds. And so the rate of CO oxidation is interconnected with the coverage of OH(ads) and the perimeter of the OH(ads) islands. Mass transport shifts the pre-rds equilibrium to the left thereby resulting in a delaying of oxidation with regard to potential (causes a positive potential shift). After the anodic peak the reaction occurs at defect sites and terrances, though at different rates. Within this region (1.0-1.2 V) increasing mass transport increases the rate of CO oxidation in a manner predicted by the Koutecky-Levich equation.

The state of the palladium surface changes around 1.2 V. Potential reversal experiments show an increase in the oxide reduction peak when the potential limit is set higher than 1.2 V. There is a decrease in mass transport effects at potentials greater than 1.25 V. This is evidence for two types of oxo-species on the surface: one that participates in CO oxidation and one that does not. From what is known about the oxide growth process on palladium we ascribe the latter oxo-species as being O(ads) that has undergone lattice exchange, but

the exact form of this passivating species is unclear. Assuming that O(ads) is the catalyst that facilitates the removal of the COOH(ads) intermediate in this potential region by depotonating the adsorbed carboxyl then one can say that the oxophilicity of palladium discourages the proton transfer to the coordinated oxo-species. Stated differently, O(ads) not only acts as a site-blocking species but also inhibits the oxidation by reacting more slowly with CO(ads) than OH(ads).

We were able to qualitatively explain our results within the framework of nucleation-growth-collision at defect sites on the palladium surface with CO mass transport to the island perimeter. This model has the benef t of supporting experimental results of site-selective reactions and CO(ads) surface diffusion. It is also able to explain the potential reversal and sweep hold results. We invoke a changing adsorbed oxo-species that reacts with CO(ads). In the double layer region we ascribe this species as H_2O(ads), during the anodic peak it is OH(ads), and afterwards O(ads). The inhibition of CO oxidation during the oxide region agrees with previously observed facts that palladium oxide passivates the surface to most electron transfer processes. [107] have suggested that the formation of this oxo-species occurs predominantly at defect sites prior to spreading to the bulk surface. In future work, we will develop a quantitative model for the ideas presented here, that will be tested against dEIS and RDE data.

Chapter 5

Mechanistic study of HCOOH electrooxidation on Pd - Part 1: dc voltammetry

5.1 Abstract

The electrooxidation of formic acid on polycrystalline palladium electrodes in sulfuric acid is studied by potentiodynamic methods. Herein we discuss possible mechanisms of formic acid electrooxidation on Pd throughout the potential range spanning from the hydrogen absorption region to the oxide region. Additions of CO, formaldehyde, methanol, methyl formate, and oxalate were made to investigate the nature of the poisoning species. The kinetics depend on the coadsorbed species: that is, anions and oxo-species. A strategy for eff cient removal of the poisoning species is proposed.

5.2 Introduction

The use of formic acid as a source of electrical energy in a fuel cell has been a "hot" topic in the electrocatalysis f eld [134–136]. There are many studies on formic acid electrooxidation at different electrode materials, most notably platinum and palladium. Most of the mechanistic studies of formic acid oxidation have been conducted on Pt, which is surprising given the benef ts of Pd: lower cost, higher power density, and greater longevity and stability [137]. This report adds to the understanding of the electrocatalytic activity of palladium towards formic acid by providing an in-depth kinetic and mechanistic study throughout the potential range suitable for fuel cell use.

While formic acid has a simple structure and its oxidation only requires two protons and two electrons to be transferred (Eq. (1)), the reaction mechanism is more complicated than expected.

$$\mathrm{HCOOH} \rightarrow \mathrm{CO_2} + 2\mathrm{H^+} + 2\mathrm{e^-} \tag{5.1}$$

The accepted mechanism for formic acid oxidation is a dual-pathway mechanism, whereby the oxidation occurs through a CO(ads) intermediate or proceeds directly to CO_2 [128, 138].

$$\mathrm{Pd(site)} + \mathrm{HCOOH(aq)} \rightarrow \mathrm{PdHCOO(ads)} + \mathrm{H^+(aq)} + \mathrm{e^-} \tag{5.2}$$

$$\mathrm{PdHCOO(ads)} \rightarrow \mathrm{CO_2(aq)} + \mathrm{Pd(site)} + \mathrm{H^+(aq)} + \mathrm{e^-} \tag{5.3}$$

The direct pathway, written for Pd, is described by Eqs. (5.2)–(5.3) and the indirect path-

way is given by (5.4)–(5.6).

$$\mathrm{Pd(site) + HCOOH} \rightarrow \mathrm{PdCO(ads) + H_2O(l)} \tag{5.4}$$

$$\mathrm{Pd(site) + H_2O(l)} \rightarrow \mathrm{PdOH(ads) + H^+(aq) + e^-} \tag{5.5}$$

$$\mathrm{PdCO(ads) + PdOH(ads)} \rightarrow \mathrm{2\,Pd(site) + CO_2(aq) + H^+(aq) + e^-} \tag{5.6}$$

Fig. 5.1 summarizes the main reaction pathways for FA oxidation.

One complication with studying surface reactions on Pd is its tendency to absorb hydrogen. While this property is of great benef t in hydrogen storage [139], it is not desirable for interfacial studies since the current response due to absorbing and desorbing hydrogen can mask surface processes. Losiewicz et al. [47] have used thin-f lm Pd to study CO passivation—a possible component process in formic acid electrooxidation. Recently, there have been a few studies on the kinetics of formic acid electrooxidation on palladium [140–142]. The majority of these studies were conducted on Pd-based alloys and nanoparticles. An early report of the electrocatalytic effect of Pd/C on formic acid was given by Takasu's group [141] where the activity was seen as a function of particle size and possibly morphology. This has been conf rmed by Zhou and Lee [138]. It has been determined that surface morphology plays an important role in the oxidation process on Pd [143–146]. Several spectroscopic studies have indicated that CO(ads) formation is minimal on Pd [144, 145, 147]. These studies have noted that the role of anions in the oxidation process is an important factor as it affects not only the current but also the adsorbed species.

Presented here is a systematic voltammetric study of palladium as an electrocatalytic substrate for formic acid oxidation. We report the effects of scan rate, concentration, and electrode condition on the current response, and discuss them in the context of the above mechanism. We use pure Pd electrodes and show that absorbed hydrogen has a dramatic effect on the oxidation. The decay of activity with time implicates the presence of a poi-

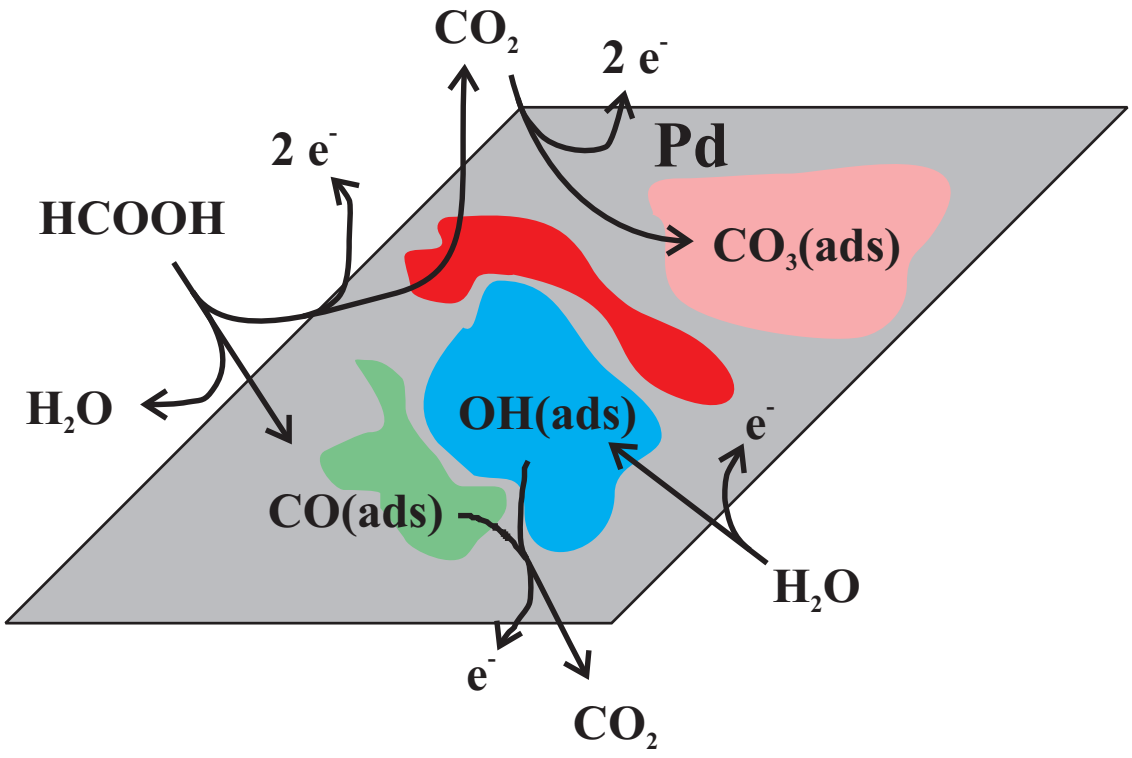

Figure 5.1: Reaction scheme of formic acid electrooxidation on palladium.

soning species whose identity has been controversial [137, 140, 147]. We use deliberate additions of possible poisoning agents to investigate this, and show that CO is not the active poison, at least within the f rst hour of activity. We show that the deactivation of the surface is strongly dependent upon potential.

5.3 Experimental

Formic acid electrooxidation in sulfuric acid was studied at a polycrystalline palladium wire (Johnson-Matthey, 99.998 %) spot welded to a copper wire with the joint covered by PTFE heat-shrink (Zeus, Inc.). The reference and the counter electrodes were polycrystalline platinum and palladium wires (Johnson-Matthey, 99.998 %) sealed in glass or PTFE heat-shrink tubing, respectively. All potentials were measured and are quoted against the reversible hydrogen reference electrode, RHE, in the same electrolyte separated from the main cell by a Vycor®. (BAS) or ground glass joint. All experiments were carried out at ambient temperature, 21 °C. Potential was controlled with either a custom-built or Gamry REF600 potentiostat.

All glassware was thoroughly cleaned by soaking in fresh piranha solution (two parts concentrated H_2SO_4 and one part 30% w/w H_2O_2 by volume) for 10 min. It was then placed in hot concentrated H_2SO_4 overnight to remove remaining contaminants and to decompose any remaining peroxide. The glass was rinsed with Millipore water (18 MΩ cm), and then the cell was assembled. The electrolyte was added immediately afterwards. The 0.5 M H_2SO_4 electrolyte was prepared using the Millipore water and conc. sulfuric acid (Fluka, puriss).

Slow changes in electroactivity have been observed in similar reactions on Pt [106] and Pd [107], and so we were careful to standardize the conditions before recording a voltammogram at a particular formic acid concentration. The working electrode was con-

ditioned by cycling between 0.2 and 1.5 V at 200 mV s^{-1} for 30 min, and then from 0.25 to 1.4 V at 50 mV s^{-1} until the representative voltammogram was obtained in sulfuric acid. The double-layer capacitance at 0.5 V was measured prior to the addition of formic acid using impedance, and was used to obtain the true surface area for palladium, assuming 25 μF cm^{-2} for an ideally smooth surface [47]. Concentrated formic acid (98% Fluka, puriss) was then added to the electrolyte to obtain the desired concentration. For every recorded voltammogram, unless otherwise noted, the potential was cycled under the conditions given in the f gures at least three times, with the last one being shown. For voltammograms in which the reversal (limit) potential was varied, the potential was cycled at least twice between 0.3 V and 1.4 V before the potential limit was adjusted.

We used two nonstandard cyclic voltammetry experiments: (1) potential-reversal experiments in which the upper potential limit was systematically changed, and (2) sweep-hold experiments in which the potential scan was halted and the potential held for a period of time before the sweep was resumed. These experiments had multiple conditioning potential cycles immediately before the recorded sweep. Sweep-hold experiments were cycled at 50 mV s^{-1} before holding the potential for 120 s. The potential at which holding or reversing took place will be referred as the limit potential, E_{L}. All voltammograms were carried out with a sweep rate of 10 mV s^{-1} unless noted otherwise.

5.4 Results

We f rst give a basic summary of the cyclic voltammetry of formic acid on palladium and compare it with that of platinum. We then focus on the effects of solution concentration and sweep rate on the oxidation. Subsequently, we describe some potential reversal experiments where we change not only the positive potential limit but also the negative one. Sweep-hold experiments were conducted in the oxide reduction region as well as the hydrogen

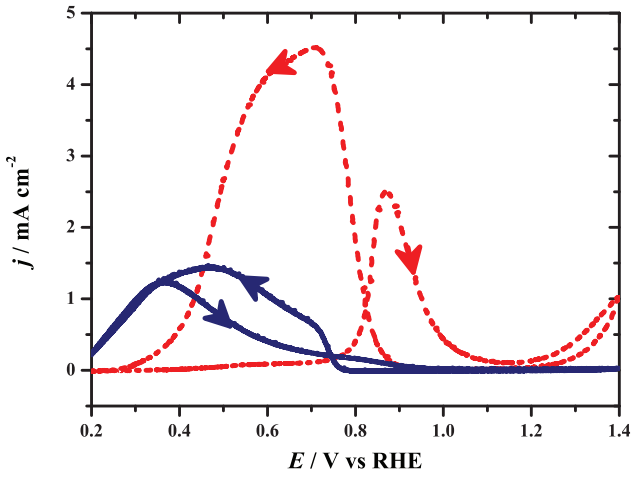

Figure 5.2: Voltammograms for formic acid oxidation at a palladium (**blue solid**) and platinum (**red dash**) electrode. Formic acid concentration 0.25 M; sweep rate 50 mV s^{-1}.

adsorption region. Finally we discuss some poisoning experiments in which the analyte was spiked with foreign organic compounds and CVs were measured and compared. In this chapter the hydrogen absorption region, **A**, refers to potentials below 0.4 V; the double-layer region, **B**, refers to potentials 0.4–0.75 V; and the oxide region, **C**, refers to potentials greater than 0.75 V.

5.4.1 General comments

Figure 5.2 shows that formic acid oxidation on Pd and Pt are signif cantly different, as mentioned by Capon and Parsons [128]. The most notable difference is on the positive-going sweep where the anodic current at Pd forms a broad peak in the double-layer region while on Pt a sharper peak forms in the oxide region. The Pd peak current is 1.3 mA cm^{-2} at 0.35 V as compared to the Pt peak current of 2.6 mA cm^{-2} at 0.87 V. There is signif cant anodic current in the oxide region on Pt due to FA oxidation, but for Pd the current is solely due to the growth of the oxide layer. This indicates that the Pd oxide completely passivates

the surface while on Pt either there are holes in the oxide or the oxide reacts with FA.

On the reverse sweep, the reduction of the oxide leads to a dramatic increase in current as free metal sites are produced, on both Pt and Pd. On Pt the broad peak is signif cantly larger than on Pd though it decreases rapidly at potentials lower than 0.7 V. This supports the dual-pathway mechanism on Pt where CO is produced as an intermediate and passivates the surface from oxidizing FA at lower potentials. The passivation on Pd seems to be closely related to the applied potential. This is not predicted by the dual-pathway mechanism since passivation is a transient effect of the production of CO(ads) and is independent of potential.

5.4.2 Concentration effects

The broad anodic peaks that form in both the positive- and negative-going scans increase with FA concentration (Figure 5.3). In the hydrogen absorption region (**A**) the current decreases with potential. The rate of proton reduction to adsorbed hydrogen and/or dihydrogen exceeds that of HCOOH oxidation at potentials below 0.15 V, producing cathodic current. Above 0.8 V, the current quickly decreases to converge with the current prof le of the blank electrolyte regardless of the concentration. This decrease in the current correlates with the passivation of the surface by the growth of the oxide layer. On the reverse sweep, reduction of the oxide at 0.75 V reactivates the surface at all concentrations. Note that the forward and reverse anodic currents in regions **A** and **B** are nearly identical at concentrations greater than 100 mM. This suggests that the current is at near steady-state and is determined mainly by potential.

We highlight two sweep rates to show the effects of concentration on the anodic peaks in Figure 5.4 . The negative potential limit was maintained at 0.25 V to diminish the effects of hydrogen absorption into the palladium electrode. The peak potential, E_{p}, and $\log(j_{\mathrm{p}})$ increased exponentially with the change in concentration. The slope of $\log(c^{*})$-$\log(j_{\mathrm{p}})$ is

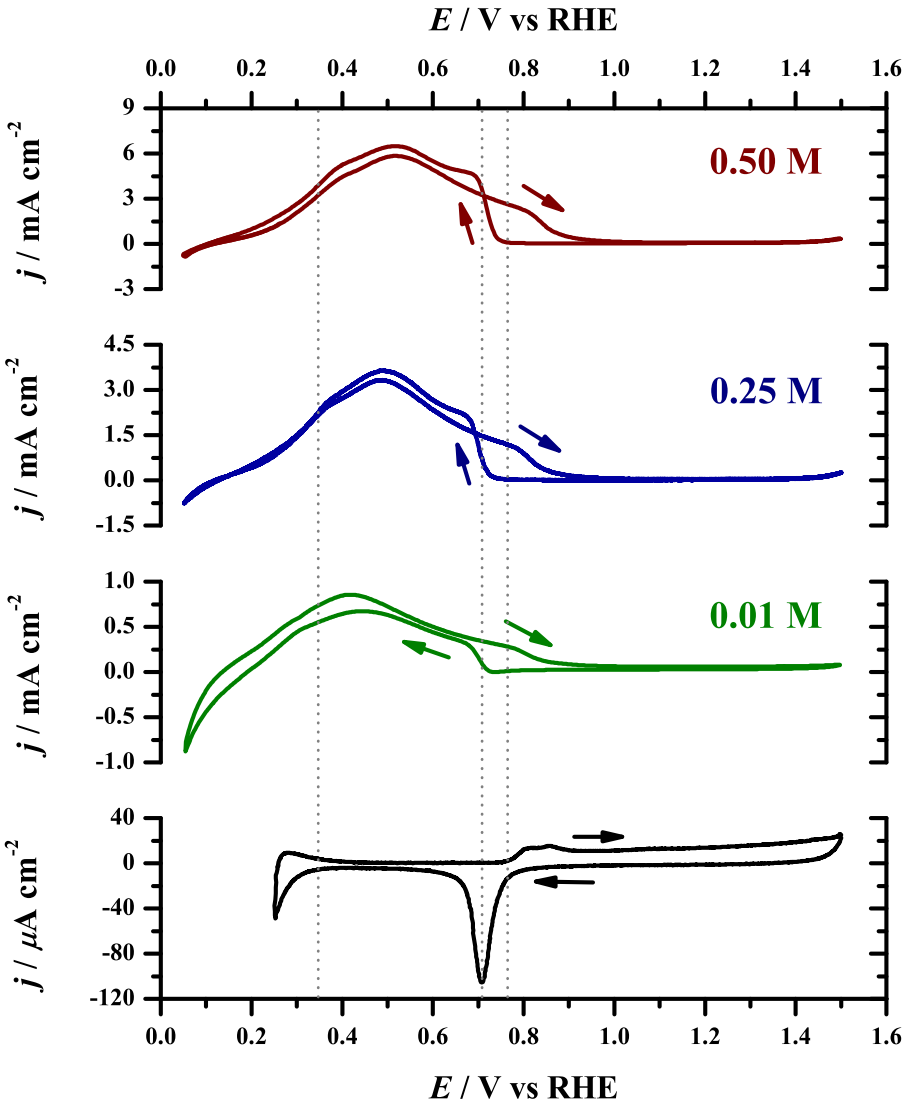

Figure 5.3: Voltammograms of palladium in 0.5 M H_2SO_4 with varying concentrations of formic acid. All at 10 mV s^{-1}: (**red**) 0.50 M; (**blue**) 0.25 M; (**green**) 0.01 M; (**black**) 0 M.

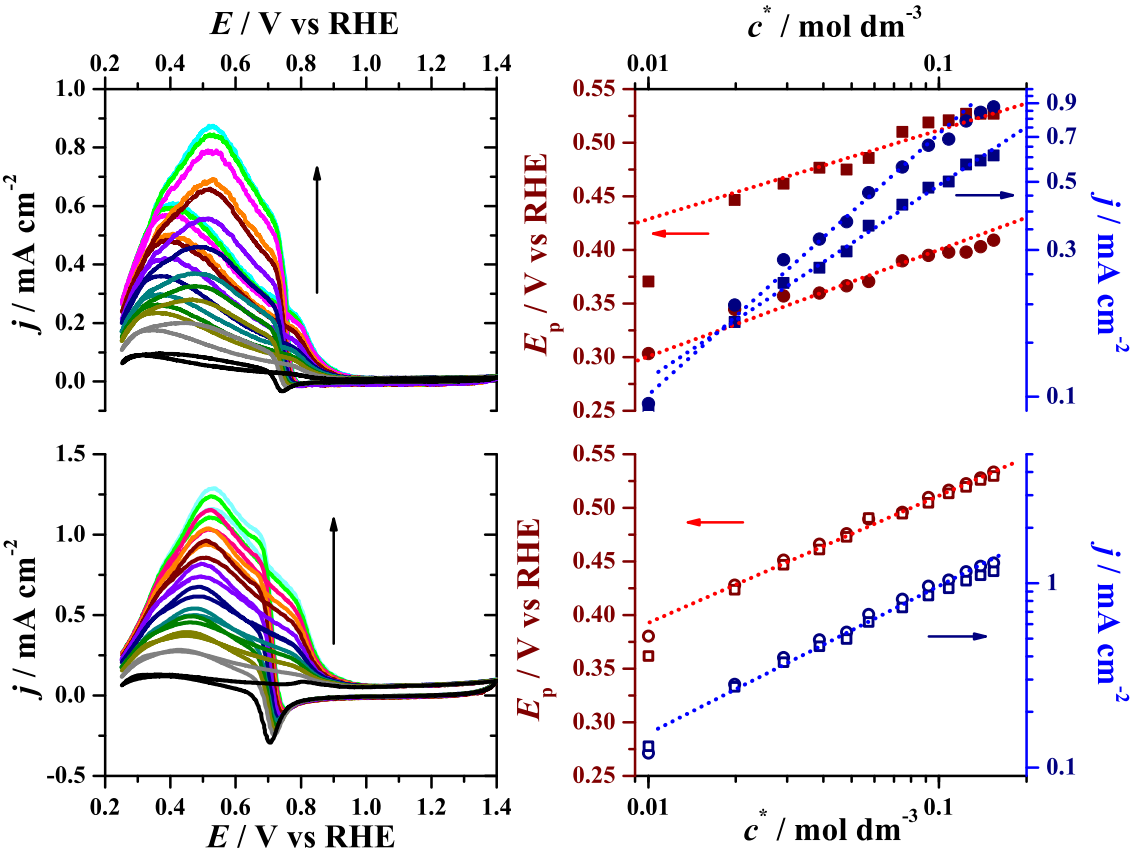

Figure 5.4: Left plots: voltammograms of HCOOH oxidation on palladium at concentrations 10–160 mM; sweep rate: 10 mV s^{-1} (**top**) and 100 mV s^{-1} (**bottom**). Right plots: summary of E_p (**filled red**) and j_p (**open blue**) dependence upon concentration from leftmost plots; **Circles**: positive-going sweeps; **Squares**: negative-going sweeps.

related to the rate order of HCOOH and is 0.75 and 0.9 for the 10 and 100 mV s^{-1} sweeps, respectively. A slope of one shows that the reaction is first order in HCOOH, i.e., that c^* and j_p are proportional. Figure 5.3 shows that at high concentrations j_p is proportional to c^*. In the 10 mV s^{-1} scans, E_p for the positive-going and negative-going scans were offset by 0.125 V, though they showed similar slopes in the plot. j_p increases more rapidly for the negative sweep than the positive-going one, suggesting that the deactivation process present in the positive-going sweep affects the reaction order. For the 100 mV s^{-1} scans, there is little difference between the two E_p from the positive- and negative-going scans. Likewise, there is little difference in j_p, though the positive-going scan is slightly less than the negative-going one. Lastly, Figure 5.4 clearly shows that the oxide reduction region is unaffected by the formic acid at all concentrations at both sweep rates.

5.4.3 Sweep rate effects

We chose two concentrations to highlight to effects of the sweep rate on the peak current and potential, Figure 5.5. Plotting $\log(j_p v^{-1})$ against $\log(v)$ gives a linear plot whose slope provides information about the kinetics of the system. For 10 mM and 100 mM, there is a linear relationship between $\log(j_p v^{-1})$ and $\log(v)$ with the slope$= -0.8$. There are three standard values expected from this plot: $\text{slope} = -1/2$ for a diffusion-limiting process (surface processes are fast); $\text{slope} = 0$ for a surface limited electron-transfer process or a chemical step that occurs after a fast electron-transfer; and $\text{slope} = -1$ for a process in which the peak current is independent of potential, that is, the rate determining step is a chemical step that occurs prior to electrochemical steps. The obtained slope is between the diffusion-limiting and chemical-limiting cases, but is closer to the latter. The relationship between peak potential and sweep rate depends on concentration. For 100 mM, E_p decreases as the sweep rate increases. On the other hand, at 10 mM it increases with v for $v > 100$ mV s^{-1}.

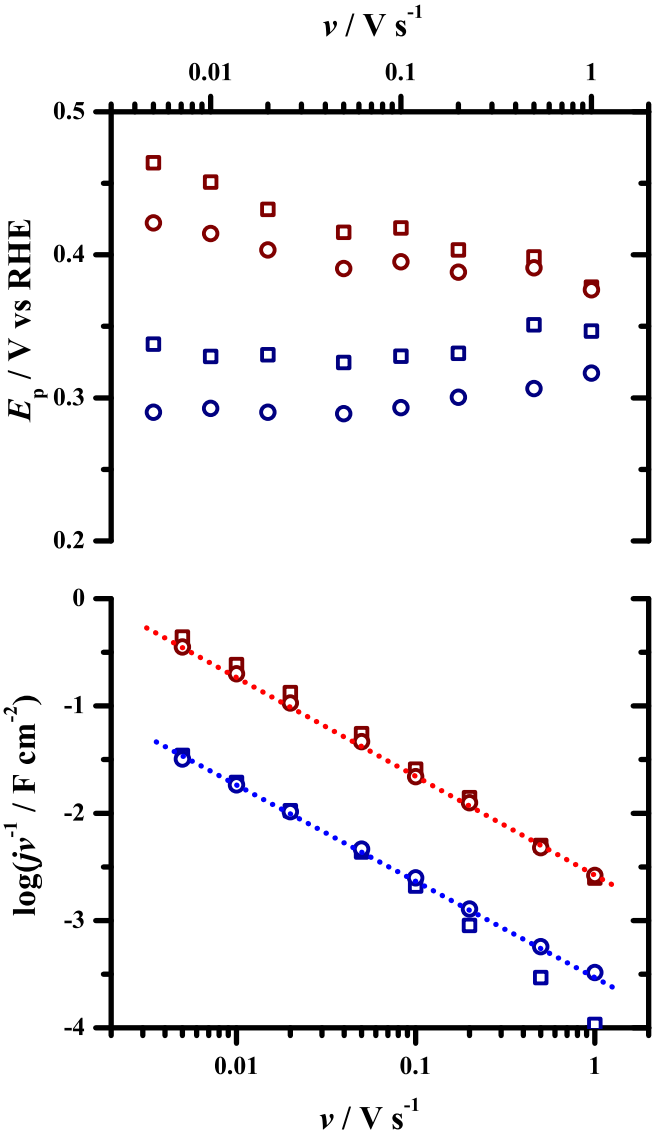

Figure 5.5: Dependence of E_p and j_p on sweep rates for HCOOH concentrations of 100 mM (**filled red**) and 10 mM (**open blue**). Circles correspond to positive-going sweeps and squares to negative-going sweeps.

5.4.4 Tafel plots

A Tafel analysis was carried out for the slowest sweep rate, Fig. 5.6. The first region, $\mathbf{A}_\mathrm{f}$ and $\mathbf{A}_\mathrm{b}$, has positive Tafel slopes, which is typical of oxidation processes. The slopes of the positive- and negative-going sweeps are the same and increase with an increasing concentration, that is the slopes increase from 120 mV dec^{-1} to 360 mV dec^{-1} when FA concentration increases from 10 mM to 250 mM. The Tafel slopes in regions **B** and **C** are negative suggesting a deactivation process. The curves are parallel in these regions, meaning that the slopes are independent of concentration. The apex between regions **B** and **C** correlates with the onset of oxide growth (positive-going) and the endings of oxide reduction (negative-going). The Tafel slopes for **B** are different for the forward going (-540 mV dec^{-1}) and negative-going sweeps (-800 mV dec^{-1}), though both suggest minimal change in the oxidation rate due to potential. Region **C** shows a strong dependence on sweep direction as the slope of $\mathbf{C}_\mathrm{f}$ is -240 mV dec^{-1} and that of $\mathbf{C}_\mathrm{b}$ is -30 mV dec^{-1}. The smaller value in $\mathbf{C}_\mathrm{b}$ means that the rate of surface reactivation has a stronger dependency on potential than the passivation process in $\mathbf{C}_\mathrm{f}$. This agrees with the overall nature of oxide growth and reduction as given in Fig. 5.3 where the rate of oxide growth remains constant after 0.85 V while the reduction shows a sharp peak versus potential.

As stated before, comparing the change in log(j) to FA concentration gives information on the apparent reaction order with regards to FA. This comes from the standard Tafel equation for the rate, Eq. (5.8).

$$j = k[\mathrm{HCOOH}]^n \exp\left(\frac{\alpha F}{RT}E\right) \tag{5.7}$$

where n is the apparent reaction order with respect to FA.

$$\log(j) = \frac{\alpha F}{RT}E + \log(k) + n\log([\mathrm{HCOOH}]) \tag{5.8}$$

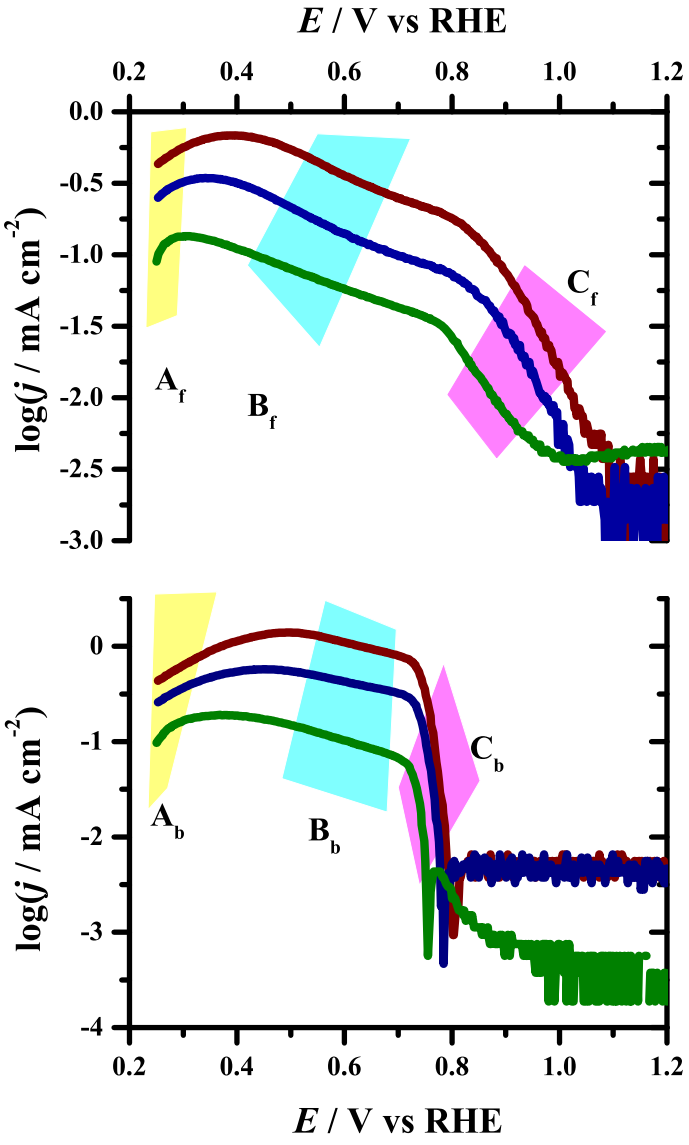

Figure 5.6: Tafel plots obtained from 5 mV s^{-1} cyclic voltammograms of 0.01 M (**green**), 0.1 M (**blue**), and 0.25 M (**red**) formic acid in sulfuric acid. Top plot for positive-going sweep; bottom plot for negative-going sweep.

From this n can be obtained from the slope of $\log(j)$-$\log([\mathrm{HCOOH}])$ curve. Throughout the potential range, n depends on concentration. At low concentrations, n was of the order of 0.5 and at concentrations greater than 100 mM, it was near 0.95. This agrees with the results from Fig. 5.4 which followed concentration's effect on the peak current.

If we assume that the passivation in regions **B** and **C** is due to build up of a spectator species, either a by-product, slow reactive intermediate, or a co-adsorbed species, then we can write the Tafel expression as $j_{\mathrm{a}} = kc^{*}\theta_{\mathrm{active}}$. Figure 5.6 shows that the rate of passivation increases with potential, though this effect can be explained by the fact that oxide formation is potential dependent. Region **B** before the oxide growth region shows less potential dependence. The passivation in this region can be due to either mass transport limitations, that is a concentration gradient is being developed, or a chemical step is becoming more pronounced. Given that on the time scale of the experiment (380 s), the mass transport-limited peak current value would be 1.7 mA cm^{-2} at 10 mM—a order of magnitude greater than the measured current—the former case can be neglected. Therefore a chemical step is becoming more dominant and is adversely affecting FA oxidation.

5.4.5 Sweep-hold and potential-reversal experiments

As stated above, oxide growth on palladium passivates the surface towards HCOOH oxidation. Reversing the potential in the oxide region demonstrates this effect. We know from previous reports that as more oxide is formed on the surface, the harder it is to remove [108]. As the potential limit, E_{L}, increases, more oxide is formed and the reduction of the oxide shifts to more negative potentials. Figure 5.7 shows that re-initiation of formic acid oxidation on the negative-going sweep is delayed as E_{L} increases, i.e., until oxide reduction begins. In addition to the dependence of the commencement of HCOOH oxidation on the amount of oxide, the current prof le has subtle changes. While the peak current in the negative-going sweep does not signif cantly change, the current leading up to it does. This

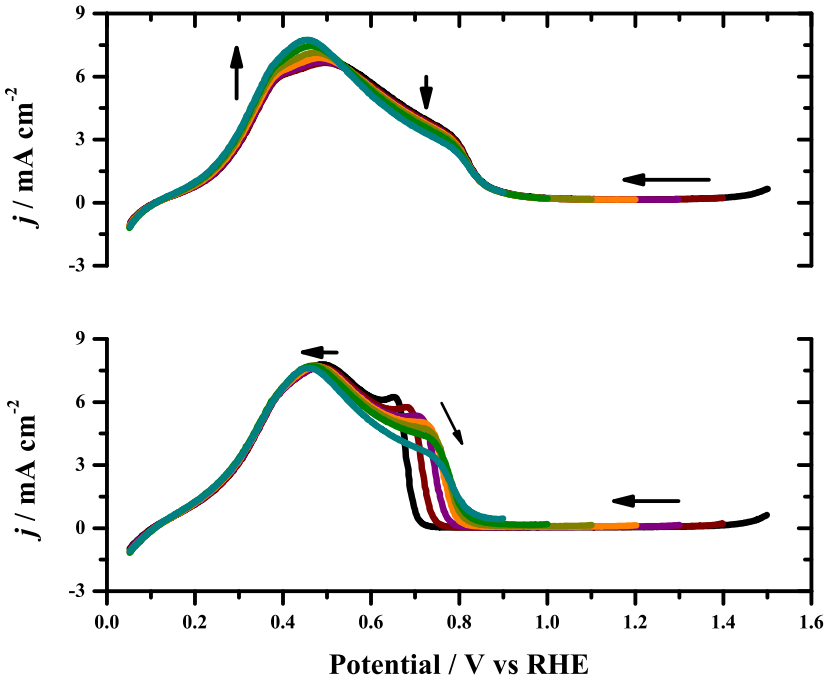

Figure 5.7: Potential reversal experiment for 0.5 M HCOOH in 0.5 M H_2SO_4 at 50 mV s^{-1}. Arrows show the direction of the changing potential limit, i.e. they follow the changes of the current due to the particular positive potential limit.

seems to suggests that cycling to potentials as low as 1.0 V is sufficient to reactivate the surface.

A subtle effect is seen in the current peak on the positive-going sweep. As the positive potential limit is decreased the peak current increases. This can be explained by the fact that the potential in the experiment is swept down to 0.05 V which is well into the hydrogen adsorption region. The sweep rate is relatively fast at 50 mV s^{-1}, which means that there is insufficient time for the complete removal of absorbed hydrogen. Therefore the increase in current comes from a delayed oxidation of H(abs).

Sweep hold experiments, holding the potential during the forward and reverse sweeps, typically produce current decays to a steady-state—red curve in Figure 5.8. There is a slow decrease at longer times, presumably due to slow surface passivation. However, there are two interesting regions that show different behavior: the oxide reduction (0.65–0.75 V) and hydrogen absorption (<0.3 V) regions. In the former region, shown in Figure 5.8, the current increases to a maximum value before decreasing slowly. The current at the maximum increases with decreasing holding potential, which follows the general trend of the current in that region (that is, a negative Tafel slope). The time it takes for the current to reach its maximum value decreases with decreasing potential. This can be taken to mean that the rate of reactivation is controlled by potential and it may involve a reduction process given that a more negative potential better promotes the process. This is reasonable given that the reduction of the oxide frees up surface sites which reactivates the surface. The general shapes of the transient curves follow what is expected for an electro-desorption process that frees up surface sites for an electrocatalysis process to occur. That is, the transient currents provide an indirect measurement of the change in oxide coverage during its reduction. Figure 5.9 shows a similar sweep-hold experiment but at a lower concentration where the oxide reduction current is more pronounced. It can been seen that the pseudo-steady state current value that the transient curves reach is the same as that obtained from a slow sweep

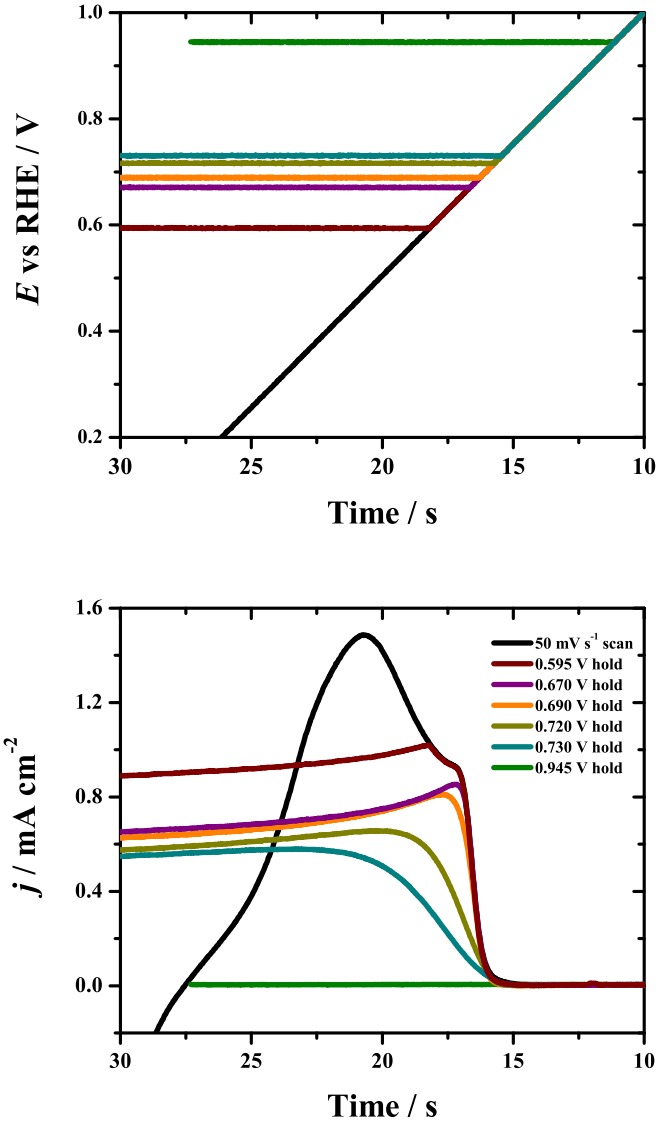

Figure 5.8: Sweep-hold experiment of the negative-going scan during the oxide reduction region (0.65–0.75 V) in 0.25 M HCOOH + 0.5 M H_2SO_4. The complete linear sweep at 50 mV s^{-1} (**black** curve) is also plotted vs time. The reversal potential, 1.4 V corresponds to $t = 0$. Holding potentials are given in the legend.

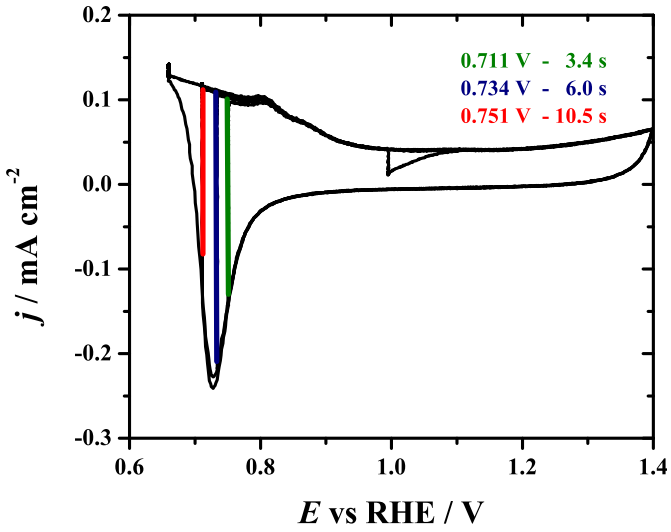

Figure 5.9: Sweep-hold experiment in the negative-going scan during the oxide reduction region in 0.01 M HCOOH and 0.5 M H_2SO_4. The CV at 10 mV s^{-1} (**black curve**) is also plotted vs potential. Time differences between holding the potential and the transient peak are given. The moment of potential holding corresponds to $t = 0$.

in the forward direction. That is, the current increases as the oxide is removed and reaches the same value as an oxide-free surface at that potential.

At low formic acid concentrations, the hydrogen absorption region shows similar behavior. Sweeping to a more negative potential produces a transient current that rises at a greater rate and gives a higher peak current value, see Figure 5.10 . This means that holding the potential deeper into the hydrogen absorption region allows the surface to reach a pseudo-equilibrium state where the transient current, j_t, is higher than that obtained from a linear sweep, j_0. This is signif cant because: 1) it occurs at potentials more negative than the current peak (0.4 V) and so the "drive" towards oxidation is small; 2) hydrogen absorption, a cathodic process, is substantial in this region. Also, the j-t slope increases with a decreasing potential, which again suggests that a cathodic process *promotes* the overall oxidation until an equilibrium is established. Together with the potential reversal experiments, this suggests that either the rate of formic acid oxidation increases or the rate of proton

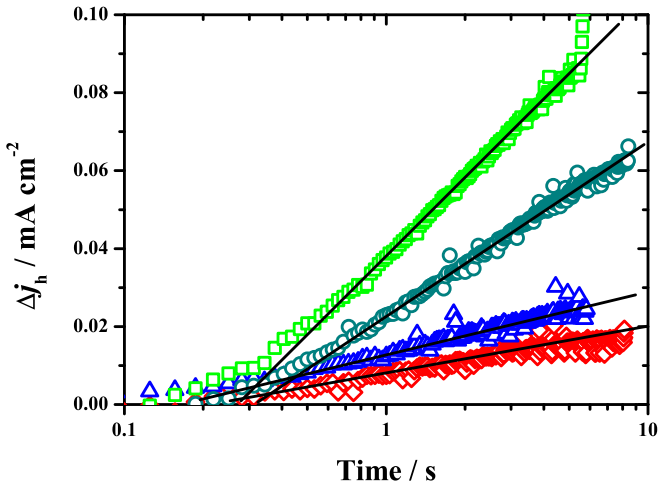

Figure 5.10: Summary of the transient current rise during the sweep-hold experiment in the hydrogen absorption region in 0.01 M HCOOH + 0.5 M H_2SO_4. The moment of potential holding corresponds to $t = 0$ and $\Delta j_{\mathrm{h}} = j_{\mathrm{t}} - j_0$. Holding potentials: (**green squares**) 0.22 V; (**cyan circles**) 0.24 V; (**blue triangles**) 0.27 V; (**red diamonds**) 0.28 V.

reduction to hydrogen absorption decreases into Pd. This signif cant interaction between absorbed hydrogen and formic acid oxidation is discussed further below.

5.4.6 Surface Poisoning

We conducted a series of experiments to study the poisoning of formic acid oxidation. Sweep-hold experiments were used to measure the time it took for the current at 0.45 V to decrease to 25% of its initial value. It took 75 min for this drop in current to occur when [HCOOH] was 10 mM and 15 min when [HCOOH] was 100 mM. After the experiment, a stripping voltammogram measured the anodic charge in the oxide region of the positive-going sweep before the potential was reversed. Figure 5.11 shows that the current stays near 25% of the initial current until the oxide region for both concentrations. The stripping curve converges with the blank voltammogram at 0.8 V but then increases after 1.0 V, suggesting that the poisoning species is being oxidized in the latter region. The reverse sweep shows that current increases from 25% of the original sweep to 50%. Assuming the

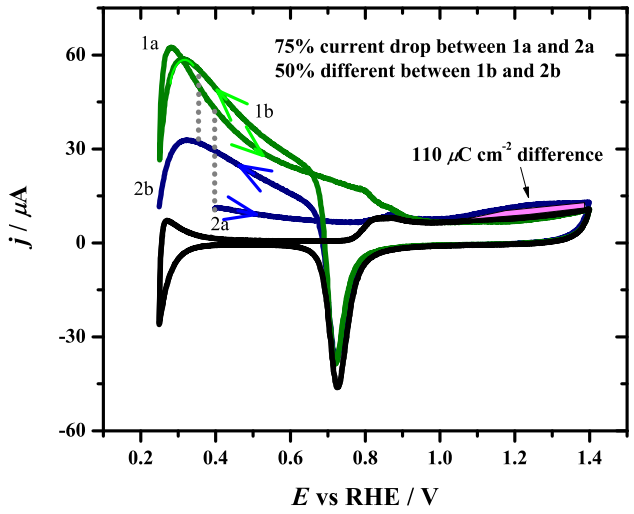

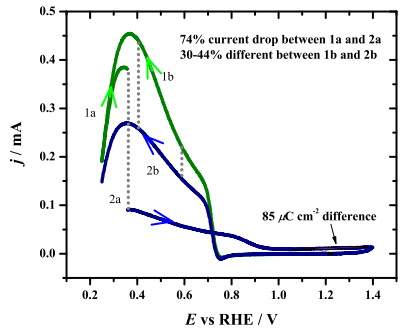

Figure 5.11: Poison stripping voltammograms of palladium in 0.5 M H_2SO_4 at a sweep rate 10 mV s^{-1}. Top plot: HCOOH absent (**black**); (**green**) 0.01 M HCOOH; (**blue**) after potential hold at 0.4 V for 75 min. Bottom plot: (**green**) 0.1 M HCOOH; (**blue**) after potential hold at 0.4 V for 15 min.

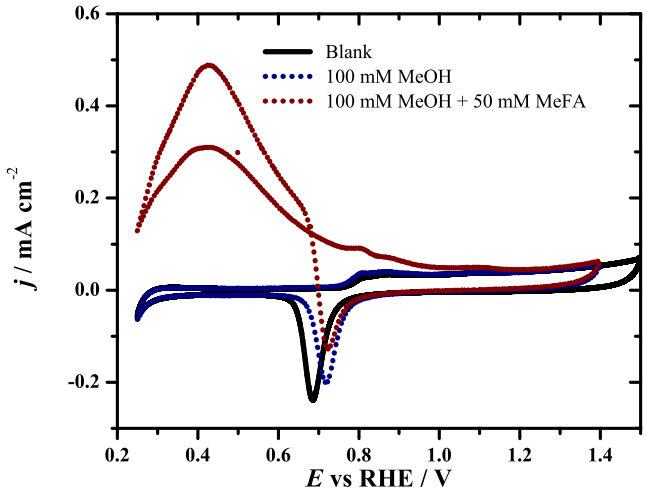

Figure 5.12: Voltammograms of methyl formate and methanol on Pd in H_2SO_4. Legend in plot; sweep rate 50 mV s^{-1}

current drop is due solely to passivation—a decrease in the active surface area—a fourth of the surface was reactivated by sweeping into the oxide region. It follows then that the 110 μC cm^{-2} stripping charge found in the 10 mM experiment corresponds to a saturated charge of 440 μC cm^{-2}. This is the expected charge density of 2 e^- per Pd surface site. At higher concentrations the charge of the blocking species was reduced from 440 μC cm^{-2} to 340 μC cm^{-2}.

We also added aliquots of foreign organic compounds to the system and measured the changes in the voltammogram; Figs 5.12–5.14 summarizes these results. Methanol causes no measurable change, Fig. 5.12. This is consistent with the known lack of catalytic oxidation on palladium [104], and shows that it produces no poisoning species; its initial adsorption is much slower than that of FA. When methyl formate is added the current increases. Under these conditions, methyl formate hydrolyzes to formic acid and methanol (Eq. 5.9).

$$\mathrm{HCOOCH_3(aq) + H_2O(l) \quad \rightleftarrows \quad HCOOH(aq) + CH_3OH(aq)} \tag{5.9}$$

Since methanol has no effect, adding methyl formate to the cell effectively increases the concentration of formic acid, which explains the increase in current. In fact, the amount of methyl formate added increased the current to the value expected if the same molar amount of formic acid was added.

Oxalic acid (added as oxalate) could be potentially produced on the surface by the combination of two adsorbed formates *via*

$$2\,\mathrm{HCOO(ads)} \;\rightleftarrows\; (\mathrm{COO})_2\mathrm{(ads)} + 2\,\mathrm{H^+(aq)} + 2\,\mathrm{e^-} \tag{5.10}$$

In 0.5 M sulfuric acid, oxalic acid exists as both oxalic acid and hydrogen oxalate.

$$\mathrm{HO_2CCO_2H(aq)} \;\rightleftarrows\; \mathrm{HO_2CCO_2^-(aq) + H^+(aq)} \quad \mathrm{pK_a} = 1.38 \tag{5.11}$$

Figure 5.13 shows that the only effect on the voltammogram is in the oxide region where oxalate may oxidize. This suggests that adsorption of oxalic acid or hydrogen oxalate is weak in comparison with FA. Since oxalic acid does not readily adsorb on the Pd surface, controlled formation of co-adsorbed oxalate was not possible.

Addition of formaldehyde or CO gave similar effects: both were able to completely passivate the surface towards HCOOH oxidation, Fig. 5.14. This is not surprising given that CO is a known intermediate in HCHO oxidation [148] that adsorbs strongly on metallic surfaces. The region where oxide reduction occurs showed an increase in anodic current implying that HCOOH and HCHO oxidation occur once holes in the oxide layer are produced in the reduction region. This is because some amount of oxide (or other strongly adsorbed oxo-species) is required in HCHO oxidation, Eq (5.12) and (5.13).

$$\mathrm{HCHO(aq)} \;\rightarrow\; \mathrm{CO(ads)} + 2\,\mathrm{H^+(aq)} + 2\,\mathrm{e^-} \tag{5.12}$$

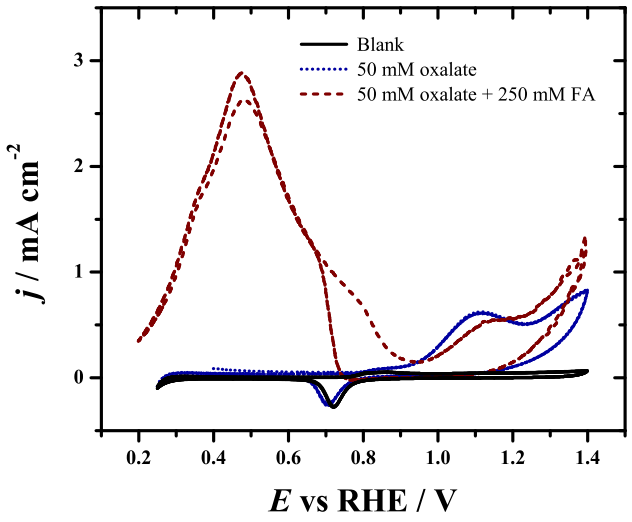

Figure 5.13: Voltammogram of formic acid oxidation in the presence of oxalic acid on Pd in 0.5 M H_2SO_4. Legend in plot; sweep rate 50 mV s^{-1}

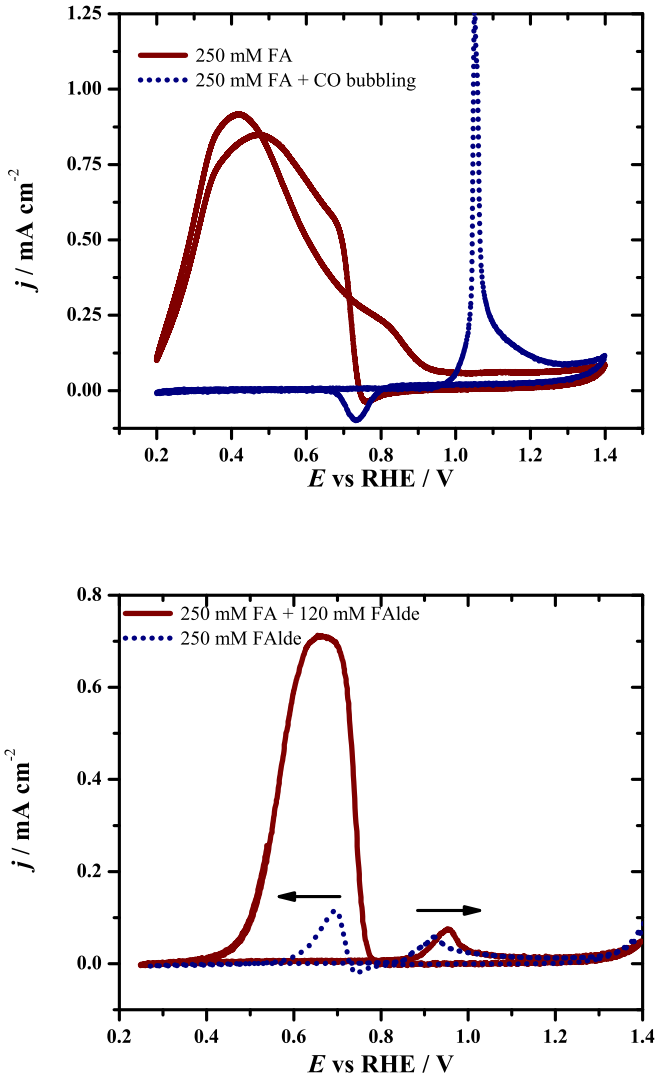

Figure 5.14: Voltammogram of formic acid oxidation in the presence of CO (top) and formaldehyde (bottom) on Pd in 0.5 M H_2SO_4. Legend in plot; sweep rate 50 mV s^{-1}.

$$\mathrm{CO(ads) + OH_2(ads) \;\rightarrow\; CO_2(aq) + 2\,H^+(aq) + 2\,e^-} \tag{5.13}$$

However, when the potential is swept further negative, the surface becomes deactivated due to the build up of adsorbed CO and the absence of oxidants in the form of adsorbed oxo-species.

5.5 Discussion

Formic acid has signif cant advantages for fuel cells that utilize small organics as fuels. This is because it contains two oxygen atoms bonded to a single carbon and it requires only one H–C bond cleavage in order to produce CO_2. Even though this reaction should be a straightforward two-electron transfer process, formic acid may also undergo some dehydration at the surface to give CO(ads). This is problematic given that CO is a stable molecule and the need an additional oxygen requires adsorbed oxygen donor and high potentials. Therefore, for metals such as Pt where this indirect pathway is dominant, high potentials and CO(ads) inhibitors (such as Bi) must be used. Palladium shows a wider potential range of activity towards formic acid oxidation than does platinum (Fig. 5.2) since CO(ads) formation is apparently slow. Because of this, subtle effects in the hydrogen adsorption/absorption region (< 0.3 V) can be detected.

5.5.1 Hydrogen absorption effects

Increasing the potential though this region shows an increase in the anodic current from FA oxidation at all concentrations (Fig. 5.3). In the same region, potential sweep-hold experiments show a transient current increase, Figs. 5.9 and 5.10. Holding at a more negative potential causes both the rate at which the increase occurs, and also the difference between the initial current and the peak current, to increase (Fig. 5.10). In other words,

the current increase is caused by both a potential-driven and a time-dependent process. The increase in the current during the potential sweep can occur from either an increase in the rate of FA oxidation or the decrease in hydrogen absorption, or both. In other words, assuming the total current can be written as $j_{\mathrm{tot}} = j_{\mathrm{FA}} + j_{\mathrm{Hab}}$ (with j_{Hab} being negative), an increase in j_{tot} comes about by either an increase in j_{FA}, a decrease in $|j_{\mathrm{Hab}}|$, or both. Likewise, the transient increase in the current can be due to either of these effects.

Beginning with a reaction scheme suggested by Kuliev et al. [149] where the direct pathway is a series of dehydrogenations, Eqs. (5.14)–(5.16), we can qualitatively model how hydrogen absorption into the palladium affects the current response. This scheme assumes that the energy of activation for the dehydrogenation steps is lower when the hydrogen is transferred to the surface or to weakly bound water rather than to unbound water, as suggested by density function theory (DFT) calculations [115].

$$2\,\mathrm{Pd(site)} + \mathrm{HCOOH(aq)} \;\rightleftarrows\; \mathrm{PdH(ads)} + \mathrm{PdHCOO(ads)} \tag{5.14}$$

$$\mathrm{PdHCOO(ads)} \;\rightleftarrows\; \mathrm{PdH(ads)} + \mathrm{CO_2(aq)} \tag{5.15}$$

$$\mathrm{PdH(ads)} \;\rightleftarrows\; \mathrm{Pd(site)} + \mathrm{H^+(aq)} + \mathrm{e^-} \tag{5.16}$$

We incorporate a simplif ed hydrogen absorption step, Eq. (5.17), as it is prevalent in this potential range.

$$\mathrm{PdH(ads)} \;\rightleftarrows\; \mathrm{Pd(site)} + \mathrm{H(abs)} \tag{5.17}$$

Thus, the electrons from FA oxidation are obtained solely through H(ads) oxidation in Eq. (5.16).

During the positive-going potential sweep, the current of the FA oxidation increases to a maximum (ca. 0.4 V) and after the peak it decreases rapidly. Since our scheme has only one step that possesses an electron transfer, the change in current is from the potential-driven shift of Eq. (5.16) left or right depending on the sweep direction. At potentials lower than 0.3 V, underpotential deposition occurs, i.e., Eq. (5.16) goes in the reverse direction thereby lowering the anodic current. In addition to shifting the equilibrium of Eq. (5.16) to the left, the hydrogen absorption step, Eq. (5.17), acts as a reservoir for hydrogen as the surface concentration of H(ads) increases. This suggests that the consumption rate of FA need not change during the decrease in the measured current. In other words, the rate of FA dehydrogenation or CO_2 production may be unaffected during the drop in current.

The transient effect is explained by treating the subsurface region where H(abs) forms as a f nite volume, which may be characterized by the mole fraction of H(abs) [139], that is

$$X_{\mathrm{H}} = \frac{c_{\mathrm{H}}}{c_{\mathrm{total\,sites}}} \tag{5.18}$$

$$X_{\mathrm{free}} = \frac{c_{\mathrm{free}}}{c_{\mathrm{total\,sites}}} = 1 - X_{\mathrm{H}} \tag{5.19}$$

The kinetic formulation of Eq. (5.17) in terms of H(ads) production is then approximated as

$$\Gamma_{\mathrm{m}} \frac{dX_{\mathrm{H}}}{dt} = k_{\mathrm{abs}} \theta_{\mathrm{H}} (1 - X_{\mathrm{H}}) - k_{\mathrm{eject}} \theta_{\mathrm{Pd}} X_{\mathrm{H}} \tag{5.20}$$

As hydrogen is absorbed into the metal, the rate of absorption, $\Gamma_{\mathrm{m}} \frac{dX_{\mathrm{H}}}{dt}$, decreases, because

the $(1 - X_{\mathrm{H}})$ term decreases and the X_{H} increases. As less hydrogen is absorbed in Eq. (5.17) more of the H(ads) is oxidized in Eq. (5.16), which produces an increase in the current. As noted above, the current increase need not all be associated with the production of CO_2 but can be caused by the slowing down of H-absorption, which in turn slows down the rate of proton reduction (reverse of Eq. (5.16)). Such an equilibrium is not established during a potential sweep as the f lling of the subsurface sites is slow on the time scale of the sweep.

At higher formic acid concentrations this transient current increase is not seen, but sweeping to negative potentials causes a decrease in current similar to that at lower concentrations. At these higher concentrations there is a higher rate of H(ads) formation, because of the general increase of rate with concentration. This has the effect of allowing the subsurface hydrogen sites to be f lled up more quickly and the H(ads) concentration approaches an equilibrium value. Therefore, when the potential-sweep is stopped, there is no transient increase in current. Since the system is nearly at steady-state the current in this region (0.1–0.3 V) is solely a function of potential. This current increase must be from an increased rate of FA oxidation, since the effect of H(abs) (or j_{Habs}) is small. However, at low concentrations the steady-state current becomes independent of potential as it is controlled by the H(ads)-H(abs) equilibrium.

A similar effect of hydrogen absorption has been seen by Yepez and Scharifker [150]. The charging of the Pd with H(abs) made the catalyst less susceptible to passivation; it maintained a higher anodic current than in the absence of H(abs). The increase in current may be due to leaching of H(abs), although Lasia's group have shown that H(abs) can be trapped in the metal by a surface-bound species such as CO(ads) [47, 151]. Figure 5.7 shows that the peak oxidation current increases with a decreasing positive potential sweep limit. It is known that desorption of H(abs) is limited by mass transport [152]. Decreasing the positive sweep limit is equivalent to decreasing the time that H(abs) can

desorb. Therefore the net amount of H(abs) formed per cycle increases as the sweep limit is decreased. This then allows more H(ads) to be oxidized in the forward sweep, which is seen as an increase in the current. The adsorption of formate (or CO_2(ads)) is relatively weak and unlikely to substantially block the movement of H(abs) to the surface. We conclude that Pd that has been charged with H(abs) would enable a DFAFC to access a greater potential range and therefore increase its power density.

5.5.2 Surface Poisoning

While there is general agreement about the direct pathway for formic acid oxidation, the poisoning pathway is less well understood. The dominant theory is that the indirect pathway is still present on Pd, but is signif cantly slower than the direct pathway. The slow rate of CO formation is assumed to poison the surface as on Pt. Pickup [153] have conducted long-term potential-hold experiments—over three hours—followed by a stripping potential sweep into the oxide region. These sweeps were able to remove the surface poison and reactivate the surface. Comparing the poison stripping voltammograms with those of CO stripping showed good agreement, suggesting that CO is the chief poisoning species. However, methanol and ethanol oxidation show similar responses on Pd nanoparticles [154]. In other words, most organic molecules give anodic peaks near the onset of oxide growth on Pd, and the possibility of other poisoning species needs to be investigated.

Our poison stripping experiments showed that the passivation rate and the poison's stripping charge were dependent upon formic acid concentration. The estimated saturation charge of the poison is 440 μC cm^{-2} for 10 mM FA (75 min hold) and 360 μC cm^{-2} for 100 mM FA (15 min hold). This suggests CO is the poisoning species, as similar charges are obtained in CO stripping experiments [47, 140, 155]. A charge of 440 μC cm^{-2} corresponds to CO in the on-top conf guration and 360 μC cm^{-2} corresponds to CO in a mixed conf guration of on-top and bridged bonding [47, 155]. While the formation of CO by the

indirect pathway explains the stripping charge, it cannot account for the fact that the oxide growth is not inhibited.

It is known that CO strongly adsorbs on metal surfaces causing a delay in the growth of oxide [83, 156]. Fig. 5.14 shows that if the CO coverage is high, FA oxidation is suppressed. The passivating effects of formaldehyde and CO contamination are also evidence against CO being the poisoning species. Here, the anodic current is suppressed throughout the active region (0.2–0.9 V) until a large anodic peak forms (typical of bulk CO oxidation). Also unaccounted for is the fact that CO oxidation occurs near 0.95 V on Pd, while the poison is removed at 1.2 V. This suggests that the poison adsorbs more strongly than formate but less strongly than CO and seems to be more diff cult to oxidize than CO.

The potential at which the poison oxidizes is similar to that of oxalate whose chemical structure resembles formic acid. Oxidation of oxalic acid requires two main steps: adsorption and C–C bond cleavage, and the diff culty of the cleavage explains the high potential required to oxidize the compound. The voltammogram in Fig. 5.13 shows that, like formic acid, oxalate does not strongly adsorb as the onset of oxide growth is only slightly affected. The addition of oxalate to the FA electrolyte shows little effect on FA oxidation at shorter timescales, presumably because oxalate only weakly adsorbs.

Law et al. [157] studied the effects of contaminants present in a number of commercially available formic acid solutions. They found that the presence of methyl formate increases the rate of passivization. However, we found that the addition of methyl formate increased the current, which we attribute to the hydrolysis of methyl formate to methanol and formic acid (Eq. (5.9)). The addition of methyl formate causes an increase in the concentration of formic acid and methanol. This was conf rmed by adding methyl formate or methanol in the same molar quantities, and observing near identical passivation rates [157]. Methanol oxidation does not readily occur on polycrystalline palladium [83, 107]. This was conf rmed in Fig. 5.12 when the 100 mM MeOH solution produced no additional

anodic current to the bare electrolyte, suggesting that the adsorption of methanol is negligible or it can be readily displaced by formate. The observation of Law et al. might be due to the presence of impurities in their methyl formate (formaldehyde is a known contaminant), or to the difference in reactivity of Pd nanoparticles and polycrystalline Pd. Nanoparticles shown some reactivity with methanol [154]; the reactive sites on the nanoparticles are capable of reacting with methanol to produce CO(ads), which passivates the oxidation. The presence of methyl formate is equivalent to a slight methanol contamination that will be a source of CO(ads) on Pd(nano) [158, 159]. It follows that methanol does not contribute to poisoning at Pd(poly) because the surface is not reactive enough to oxidize methanol to CO [83]. This explains our positive results and the negative results of Law et al. [157] regarding methyl formate.

The results from our poisoning experiments suggest that the passivation process is affected by many variables, most notably the reactivity of the surface. As the surface becomes more reactive towards organic oxidation (e.g., nanoparticles) it will be more reactive towards the organic contaminants in the solution (or from the catalyst support). This is undesirable as most organic electrooxidations produce CO as a poison. Hence the suggestion by Law et al. [157] for further purif cation of commercial FA sources. The reactivity of the surface is closely related to the applied potential; potentials greater than 0.45 V produce lower anodic currents. It is clear that the formation of surface oxides ($E > 0.75$ V) block the surface from participating in FA oxidation. Haan and Masel [160] and Miyake et al. [147] have suggested that the adsorption of anions and oxide precursor species strongly contribute to the potential-promoted passivation of the surface. However, a brief pulse into the oxide region past 1.2 V reactivates the surface. This suggests that byproduct formation does indeed occur, but at a longer time-scale than the potential-controlled process. Garbarino and Burke [107] have suggested an active-site theory for electrocatalytic processes and site-selective oxidation of CO has been demonstrated [109, 161]. It is therefore likely

that poisoning occurs at more reactive sites on the surface, which form only a small fraction of the total surface. This would explain both the organic poisoning at long time scales and the lack of inhibition of the oxide growth.

5.5.3 Mechanism

To explain the potential-controlled passivation process requires a detailed analysis of the mechanism of FA oxidation. The above discussion shows that CO poisoning is not significant on the time scale of a $5\,\mathrm{mV\,s^{-1}}$ sweep. This is in agreement with spectroscopic data where the intensity of the ν(C=O) stretch of CO(ads) slightly *decreased* throughout the potential sweep in both perchloric and sulfuric acids [147, 162]. Therefore the indirect pathway is considered unimportant in describing the voltammogram and will be ignored in our analysis.

Baldauf and Kolb [143] showed that FA oxidation occurs 0.4 V lower than the start of surface oxidation on Pd(111), (101), and (100). This suggests that strongly bound oxo-species are unnecessary in FA oxidation. The current from FA oxidation is dependent on the surface orientation. Pd(100) shows a steady increase in current with an increase in potential until surface oxidation. On the other hand, Pt(111) showed decreasing activity after 0.3 V until the oxide growth region. Hoshi et al. [145, 163] studied structural effects of formic acid oxidation on palladium using stepped surfaces. It was found that surfaces with large terraces of Pd(100) were more reactive than surfaces with higher step density. DFT was used to determine that HCOO(ads) preferentially adsorbs at step sites if the step density is high (e.g., Pd(311)) [145, 146]. Given that stepped surfaces give lower currents, it was concluded that HCOO(ads) is stabilized at step sites, which in turn decreases the rate of FA oxidation. Hoshi et al. [163] saw a correlation between the charge of (bi)sulfate adsorption-desorption and Pd surface orientation with Pd(100) having the highest adsorption charge. However, Pd(111) showed stronger interactions with (bi)sulfate in the double layer region

(0.3–0.75 V) than Pd(100). This suggests that there is a synergistic effect between the palladium surface structure and adsorbed anions on the oxidation of formic acid, more specif cally the cleavage of the H–C bond.

Surface-enhanced infrared adsorption spectroscopy (SEIRAS) data of FA oxidation on Pd thin f lms in perchloric and sulfuric acids was obtained by Osawa's group [147]. This technique is used to detect species at the surface by assigning IR bands to compounds based upon symmetry rules and bond energies. In perchloric acid, they assigned a signal at 1400 cm^{-1} to adsorbed CO_3(ads) (the identif cation is not certain as it is possible for it to be adsorbed carbonate) and saw that its intensity followed the current prof les. That is, the coverage of CO_3(ads) increases with potential until 0.75 V when it decreases. Formate was detected by a peak at 1330 cm^{-1} at 0.8 V that was near the maximum signal intensity for CO_3(ads) and the onset of oxide growth. In sulfuric acid there was no signal corresponding to CO_3(ads), however HCOO(ads) was seen earlier accompanied by the adsorption of (bi)sulfate anions. The signal for (bi)sulfate appeared at 0.4 V and peaked at 0.75 V, while HCOO(ads) appeared at 0.6 V and peaked at 0.8 V. Three conclusions were made from these results: 1) the strongly bound (bi)sulfate anion deactivates the surface towards the H–C bond cleavage as does surface oxide; 2) CO_3(ads) is able to build up in perchloric acid since it is adsorbed more strongly than perchlorate, but less strongly than (bi)sulfate; 3) having a supporting electrolyte that has little aff nity towards adsorption allows for higher FA oxidation currents. Swamy et al. [164] controlled the amount of sulfate in the acidic electrolyte to study the role of anion adsorption on the current response. They found that passivation rates and the peak currents were dependent upon the concentration of the supporting anions—in $HClO_4$ FA passivation is slower and the peak current is greater than in H_2SO_4. However, small amounts of sulfuric acid in perchloric acid and vice-versa produced *higher* currents and had $slower$ passivation rates than the pure electrolytes. This means that perturbing the anion surface structure promotes FA oxidation, presumably by

freeing up surface sites or changing the hydration energies near the surface.

We explain these results with an extension of the mechanism that we used for the hydrogen absorption region by assuming that Eq (5.16) is fast at potentials greater than 0.3 V. Therefore we can combine it with Eqs. (5.14) and (5.15). We break apart Eq. (5.15) into an electron transfer step and a desorption step since CO_3(ads) was detected in perchloric acid solutions. Note that the precise nature of the CO_3(ads) species is not settled [147]. If the adsorbed species is carbonate anion (CO_3^{-2}(ads)) then a chemical step would follow to give CO_2.

$$\mathrm{PdCO_3^{-2}(ads) + 2\,H^+(aq) \;\rightleftarrows\; Pd(site) + CO_2(aq) + H_2O(l)} \tag{5.21}$$

If it is seen as $PdCO_3$(ads) then it must undergo a two electron reduction to form CO_2, which if it became the rate limiting step (rds), would give a negative Tafel slope, Eq. (5.25). In taking this as the rds, the pre-rds steps would simplify to

$$\mathrm{Pd(site) + HCOOH(aq) \;\rightleftarrows\; PdCO_3^{-2}(ads) + 4\,H^+(aq) + 4\,e^-} \tag{5.22}$$

which has the equilibrium expression

$$\frac{\theta_{\mathrm{CO_3}}}{\theta_{\mathrm{Pd}}} \;=\; K \exp\left[\frac{4F}{RT}\,(E - E_{\mathrm{r}})\right] \tag{5.23}$$

where E_{r} is the measurement reference potential. Coupling this with the rate expression for Eq. (5.22) would seem to give a positive Tafel slope of

$$\mathrm{slope} \;=\; \frac{RT}{2F(2-\beta)} \tag{5.24}$$

However, the removal of $PdCO_3$(ads) would be slow and the surface would become populated with $CO_3(\mathrm{ads})$ thereby causing θ_{CO_3} to be large, which voids the small coverage requirement typically used in Tafel analysis. This can be avoided if we consider the surface to be mostly $CO_3(\mathrm{ads})$ and the coverage of free sites is small. Under this condition the first step in the reaction mechanism would be the removal of $PdCO_3$(ads) in order to create free sites for FA adsorption and oxidation. That is, the first step becomes

$$\mathrm{PdCO_3(ads)} + 2\,\mathrm{H^+} + 2\,\mathrm{e^-} \quad \rightleftarrows \quad \mathrm{Pd(site)} + \mathrm{CO_2(aq)} + \mathrm{H_2O} \tag{5.25}$$

which is a reduction having a Tafel slope of

$$\mathrm{slope} \quad = \quad -\frac{RT}{2\beta} \tag{5.26}$$

While this could be used to explain the negative Tafel region, the experimental values of the slopes are much different from the above prediction and the $CO_3(\mathrm{ads})$ species was not detected by SEIRAS in sulfuric acid. Therefore we simplify the $CO_3(\mathrm{ads})$ desorption step by referring to the adsorbed species as $CO_2(\mathrm{ads})$ and propose the following mechanism

$$\mathrm{Pd(site)} + \mathrm{HCOOH(aq)} \quad \rightleftarrows \quad \mathrm{PdHCOOH(ads)} \tag{5.27}$$

$$\mathrm{PdHCOOH(ads)} \quad \rightleftarrows \quad \mathrm{PdHCOO(ads)} + \mathrm{H^+(aq)} + \mathrm{e^-} \tag{5.28}$$

$$\mathrm{PdHCOO(ads)} \quad \rightleftarrows \quad \mathrm{PdCO_2(ads)} + \mathrm{H^+(aq)} + \mathrm{e^-} \tag{5.29}$$

$$\mathrm{PdCO_2(ads)} \rightleftarrows \mathrm{Pd(site)} + \mathrm{CO_2(aq)} \tag{5.30}$$

The kinetic expressions of the individual steps assume the common mass-action form, that is

$$v_1 = k_1\theta_{\mathrm{Pd}}[\mathrm{HCOOH}] - k_{-1}\theta_{\mathrm{HCOOH}} \tag{5.31}$$

$$\begin{aligned} v_2 = {} & k_2\theta_{\mathrm{HCOOH}} \exp\left[\frac{(1-\beta_2)F}{RT}(E-E_{\mathrm{r}})\right] \\ & -k_{-2}\theta_{\mathrm{HCOO}} \exp\left[-\frac{\beta_2 F}{RT}(E-E_{\mathrm{r}})\right] \end{aligned} \tag{5.32}$$

$$\begin{aligned} v_3 = {} & k_3\theta_{\mathrm{HCOO}} \exp\left[\frac{(1-\beta_3)F}{RT}(E-E_{\mathrm{r}})\right] \\ & -k_{-3}\theta_{\mathrm{CO_2}} \exp\left[-\frac{\beta_3 F}{RT}(E-E_{\mathrm{r}})\right] \end{aligned} \tag{5.33}$$

$$v_4 = k_4\theta_{\mathrm{CO_2}} - k_{-4}[\mathrm{CO_2}] \tag{5.34}$$

where the symbols have their usual meanings. The mechanism predicts that the following results are possible: 1) the reaction order of FA is one—if v_1, v_2, or v_3 are rate-determining; 2) the current will reach a maximum value—if v_1 or v_4 are rate-determining; 3) the experimental charge transfer coeff cient will be between β_2 and 1 + β_3 at low potential values—if v_2 or v_3 are rate-determining; 4) self passivation will occur if HCOO(ads) or CO_2(ads) builds up on the surface—if $v_2 \gg v_3$ or if v_4 is rate-determining.

The experimental reaction order with respect to formic acid at concentrations greater

than 100 mM is near unity. Other groups have reported a similar result at palladium nanoparticles [165–168]. However at lower concentrations, deviation from unity is found. There are a number of reasons for a decrease in reaction order, one of which is if the coverage of any particular species is high, the low coverage condition required in classical Tafel analysis is not met. Under this scenario the rate determining step becomes the reaction and desorption of the species that is blocking the surface. Once a free site is made, then FA may then adsorb. Therefore the reaction would be considered zero order in terms of FA as a slow step occurs prior to FA adsorption. Given that FA does not strongly adsorb on palladium it is reasonable to assume that the rate determining step at low FA concentrations is the removal of a more strongly bound species such as (bi)sulfate or oxo-species.

The current reaches a maximum value that is an order of magnitude lower than the peak current if the oxidation rate were mass transport limited. Also, the peak current increases with sweep rate far more slowly than proportionately (i.e. $^{\Delta \log(j)}/_{\Delta \log(v)} = 0.2$). This suggests that the maximum oxidation rate is determined by a chemical step such as in Eq. (5.27) or (5.30). Two results can be obtained depending on which of the two chemical steps is rate determining. If FA adsorption, (5.27), becomes the rds then the current will plateau and be potential independent as the rates of Eqs. (5.28) and (5.29) increase with potential. However, if CO_2(ads) desorption becomes rate determining, the current will peak and then converge to a lower value. The decrease is caused by the buildup of CO_2(ads), which causes the amount of free Pd sites to decrease thereby causing a decrease in FA adsorption. In perchloric acid there is a relationship between CO_2(ads) (detected as CO_3(ads)) and the current decrease after the peak. However, CO_3(ads) is not detected in (bi)sulfate even though the decay in the current in far more rapid. This suggests that (bi)sulfate can displace CO_3(ads), which effectively increases its desorption rate. Thus the decrease in the current in sulfuric acid comes from the interaction between FA and the adsorbed anions.

The Tafel slopes of FA oxidation on Pd-based surfaces are typically between 100–

180 mV dec^{-1} [165–168]. These Tafel slopes were obtained in the potential region -0.2–0.2 V. Although we used a much smaller potential window, we obtained the consensus value of 120 mV dec^{-1} for lower concentrations of FA. These values suggest that the first electron transfer step in Eq. (5.28) is rate determining in this potential range. At higher potentials the current decreases with a Tafel slope of -540 mV dec^{-1} between 0.5 V and 0.7 V, and -240 mV dec^{-1} between 0.7 V and 0.9 V in the forward-going scan. This negative current slope is potential controlled as opposed to originating from a time-dependent slow passivation process. If the current decay was from the indirect pathway, it would be suppressed at higher sweep rates. This is not the case: the current decreases sharply regardless of the sweep rate.

Negative Tafel slopes are indicative of passivation processes. Gilroy and Conway [129] have described the origins of negative Tafel slopes and their relation to the positive slopes. Self passivation processes were shown to have negative slopes that mirrored the positive ones. However, passivation that involves an adsorbed species not directly related to the reaction will cause a negative Tafel slope of arbitrary value. Since these Tafel slopes are much higher than is sensible for a charge transfer process, they are likely caused by (bi)sulfate adsorption and oxide growth that occurs in these two regions. Therefore, analysis of the Tafel slope in this region does not provide much information and so we will turn our attention toward a qualitative explanation using spectroscopic data.

SEIRAS data shows that there is a correlation between the signal intensity of $(H)SO_4$(ads) and that of HCOO(ads). The rise in the $(H)SO_4$(ads) signal was followed by HCOO(ads) which suggests that the adsorption of (bi)sulfate does more than block sites as the presence of (bi)sulfate causes adsorbed formate to build up on the surface. This suggests that it shifts the equilibrium of Eq. (5.29) to the left, thereby decreasing the rate of HCOO(ads) oxidation. Modeling of FA oxidation requires the adsorption of the supporting anions, as

in

$$\mathrm{Pd(site)} + x\mathrm{HSO_4^-(aq)} \;\rightleftarrows\; \mathrm{Pd(HSO_4)}_x\mathrm{(ads)} + x\,\mathrm{e^-} \tag{5.35}$$

(or equivalent for $\mathrm{SO_4^{-2}}$) where x is the fractional charge transfer that may occur from the anion adsorbing. The interaction between $\mathrm{(H)SO_4^{-(2)}(ads)}$ and HCOO(ads) can be modeled by incorporating a Frumkin-type interaction into Eq. (5.29).

Once the adsorbed oxide layer begins to form, Eq. (5.36), the current decay decreases more rapidly to converge with the current from the blank curve regardless of FA concentration.

$$\mathrm{Pd(site)} + \mathrm{H_2O(l)} \;\rightleftarrows\; \mathrm{PdO(ads)} + 2\,\mathrm{H^+(aq)} + 2\,\mathrm{e^-} \tag{5.36}$$

This occurs because formic acid is easily displaced, the passivation is from electrosorbed oxygen blocking adsorption sites [107, 128, 147]. The growth of the oxide and its reduction can be crudely modeled by

$$\begin{aligned} v_5 \;=\; & k_5\theta_{\mathrm{Pd}} \exp\left[\frac{(1-\beta_5)\,F}{RT}\,(E-E_{\mathrm{r}}) - g_5\theta_{\mathrm{O}}\right] \\ & -k_{-5}\theta_{\mathrm{O}} \exp\left[-\frac{\beta_5 F}{RT}\,(E-E_{\mathrm{r}})\right] \end{aligned} \tag{5.37}$$

[33, 76]. The anodic current from FA is quenched at 1.0 V, corresponding to an oxide coverage of 0.3 assuming that PdO formation has a saturation charge of 420 μC cm^{-2} [47, 108]. It has been suggested that the low-coverage oxide layer ($<$0.25 ML) on palladium forms a (2$\times$2) structure with the oxo-species in a bridge site (one O(ads) per two Pd) [169]. Given the reasonable assumption that HCOO(ads) needs two or more adjacent sites to adsorb, there would exists less than a f fth of the surface available for FA adsorp-

tion. Palladium oxide is known to be nonreactive to organic oxidation [107, 128]. In perchloric acid, HCOO(ads) is detected in the oxide region, which suggests that the oxide is inhibiting HCOO(ads) oxidation [147]. This could be because the PdO surface holds little aff nity towards protons and so the proton transfer in Eq (5.29) must take place using non-adsorbed water. Anderson has calculated that deprotonation of formate occurs more favorably through an adsorbed oxo-intermediate than directly to near surface water [115]. Again, this can be modeled by an addition of a Frumkin term to Eq. (5.29).

The main features of formic acid oxidation on palladium can be reconstructed from the six reactions given in the previous section. We make the following simplif cations grounded by the experimental results: in sulfuric acid Eq. (5.30) can be considered fast and in perchloric acid it becomes rate determining; the electron transfers are irreversible; mass transfer is faster than the electrooxidation; and anion adsorption contributes no signif cant current. After the addition of the Frumkin terms, the rate equation for HCOO(ads) oxidation becomes

$$v_3 = k_3\theta_{\mathrm{HCOO}} \exp\left[\frac{(1-\beta_3)F}{RT}(E-E_{\mathrm{r}}) - g_{\mathrm{FA-SA}}\theta_{\mathrm{SA}} - g_{\mathrm{FA-O}}\theta_{\mathrm{O}}\right] \tag{5.38}$$

where the subscript **SA** corresponds to the supporting electrolyte anion. The rate expression for anion adorption is taken as

$$\begin{aligned} v_6 &= k_6\theta_{\mathrm{Pd}} \exp\left[\frac{(1-\beta_6)F}{RT}(E-E_{\mathrm{r}}) - g_6\theta_{\mathrm{A}}\right] \\ &\quad -k_{-6}\theta_{\mathrm{A}} \exp\left[-\frac{\beta_6 F}{RT}(E-E_{\mathrm{r}})\right] \end{aligned} \tag{5.39}$$

Maple was used to solve the system of six differential equations describing formic acid

oxidation in perchloric and sulfuric acids. Each differential equation was of the form

$$\Gamma_{\mathrm{m}} \frac{d\theta_i}{dt} = r_i \tag{5.40}$$

where r_i is the net rate of production of i, e.g. $r_{\mathrm{HCOO}} = v_2 - v_3$. Assuming that the adsorption of the anion contributes little to the current, the faradaic current is then def ned as

$$j = F r_{\mathrm{e}} = F\left(v_2 + v_3 + 2v_5\right) \tag{5.41}$$

The aim of the simulations was to provide qualitative support for the explanations given in the previous section and not necessarily to closely match the experimental data. The g values are repulsive and based on the value used to model the oxide growth, the physical meaning of which is unclear. The values used are provided in Table 5.1. The simulation, shown in Figs. 5.15 and 5.16, provides a similar voltammogram to that in Fig. 5.3 and the coverage plots are similar to the SEIRAS data [147]. That is, the coverage of formate increases when (bi)sulfate becomes prevalent on the surface. This in turn decreases the overall oxidation rate. In perchloric acid, the build up of $\mathrm{CO_3(ads)}$ on the surface creates the plateau in the current. Formate is only seen in the oxide region since the oxide adversely affects the H–C bond cleavage. This suggests that anion and oxide effects can account for the potential controlled passivation.

5.6 Conclusions

Palladium has great potential in its use in DFAFCs. Its ability to oxidize FA at low potentials (and therefore high cell potentials) along with its stability make it a candidate for

Table 5.1: Values used for the simulation of formic acid oxidation.

	H_2SO_4	$HClO_4$
E_r / V	0	0
[HCOOH] / mol cm^{-3}	10^{-5}	10^{-5}
Γ_m / mol cm^{-2}	2.18×10^{-9}	2.18×10^{-9}
k_1—k_{-1} / cm s^{-1}	8.72×10^{-5}—6.54×10^{-12}	2.18×10^{-2}—2.18×10^{-8}
k_2—k_{-2} / mol cm^{-2} s^{-1}	2.18×10^{-12}—2.18×10^{-11}	2.18×10^{-12}—0
β_2	0.5	0.5
k_3—k_{-3} / mol cm^{-2} s^{-1}	2.18×10^{-11}—0	2.18×10^{-11}—0
β_3	0.5	0.5
g_{FA-A}—g_{FA-O}	25.3—50.6	0—75.9
k_4—k_{-4} / mol cm^{-2} s^{-1}	2.18×10^{-7}—0	1.09×10^{-9}—0
k_5—k_{-5} / mol cm^{-2} s^{-1}	2.18×10^{-24}—6.54×10^{-3}	2.18×10^{-24}—6.54×10^{-3}
β_5—β_{-5}	1—0.5	1—0.5
g_5	25.3	25.3
k_6—k_{-6} / mol cm^{-2} s^{-1}	2.18×10^{-15}—2.18×10^{-4}	0—0
β_6	0.5	0—0
g_6—g_{-6}	12.7—25.3	0—0

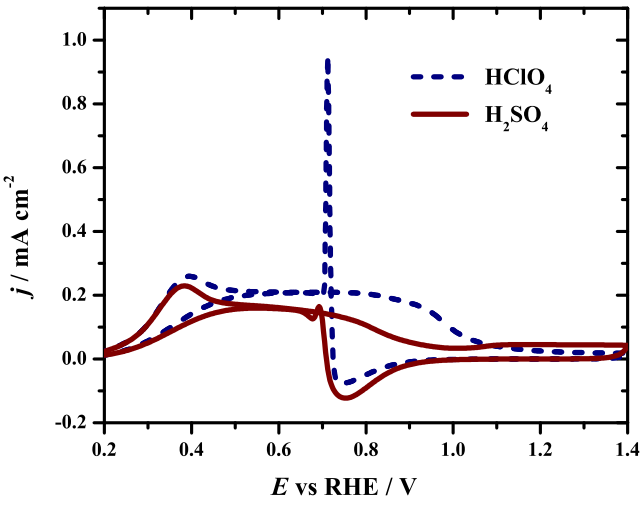

Figure 5.15: Voltammogram simulation of formic acid oxidation on palladium in (**red solid**) sulfuric acid and (**blue dash**) perchloric acid. Sweep rate of 100 mV s^{-1}.

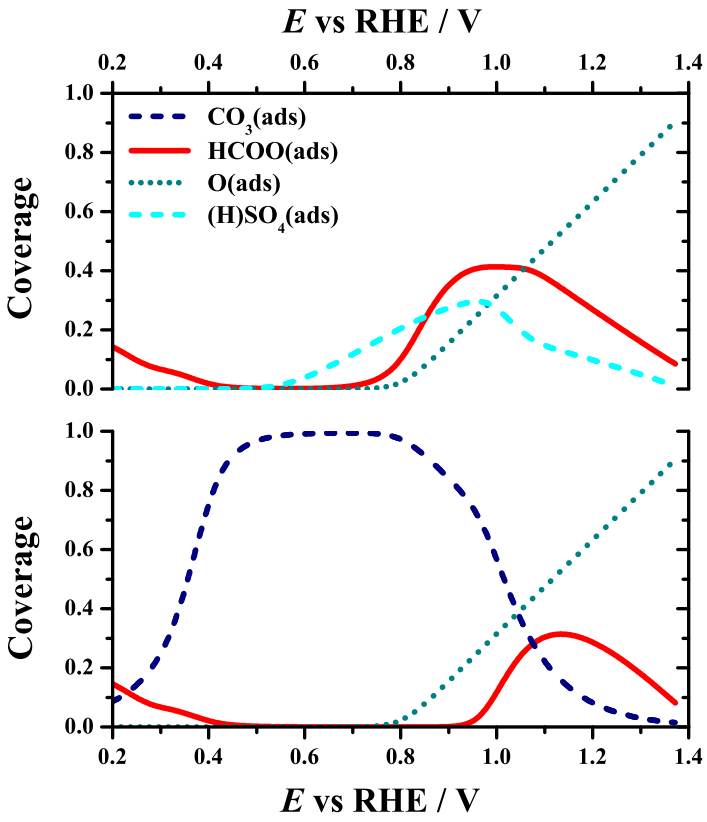

Figure 5.16: Coverage plots from the simulation of formic acid oxidation on palladium in (top) sulfuric acid and (bottom) perchloric acid. Sweep rate of 100 mV s^{-1}. Legend in plot.

future fuel cell systems. The mechanism of formic acid electrooxidation on polycrystalline palladium is complex and is affected by a multitude of variables. There is a strong interaction between formic acid and the surface condition of the Pd. Formic acid oxidation is best described as surface-promoted dehydrogenation followed by oxidation of H(ads). We conclude that FA oxidation is limited by the removal of adsorbed CO_2 near the anodic peak in perchloric acid. In sulfuric acid, anion effects play a stronger role and decrease the rate of HCOO(ads) oxidation, thereby lowering the current. After the peak the oxidation of HCOO(ads) is inhibited by the co-adsorption of $(H)SO_4$(ads) and the growth of the oxide inhibits the removal of the adsorbed formate. This interaction was modeled by the addition of a Frumkin term. Using the given mechanism and rate equations, the resulting simulation provided a good qualitative match to the experimental results.

Studying the poisoning of the surface by spiking the solution with various small organic compounds provided insights into the passivation pathway. Formaldehyde and CO completely passivate the surface, though they also delay the oxide growth and produce a large anodic peak near 0.95 V. No such delay in the oxide nor a large anodic peak at 0.95 V is detected in the poison stripping experiment. There is no evidence of poisoning due to methyl formate or methanol contamination. However, we suggest that they do in fact poison Pd *nanoparticles* given that methanol is able to adsorb at reactive sites of these surfaces. If methanol oxidation takes place then the rate of CO(ads) formation would inevitably increase, thus poisoning the surface and producing a CO-like peak during the poison stripping experiment.

We also present two possible ways to extend the activity of the palladium catalyst. We conf rm the conclusion of Yu and Pickup [153] that a brief potential sweep or jump to 1.2–1.5 V can reactivate the surface. The reactivation is caused by the oxidation and displacement of a byproduct which is adsorbed more strongly than formate but less strongly than oxide precursor(s). Charging the palladium with absorbed hydrogen causes the current

to increase at lower potentials. This would have a synergistic effect by allowing a DFAFC to operate at a higher cell potential while still maintaining acceptable current. This would be a relatively easy way to increase the power of a DFAFC with a palladium anode.

Chapter 6

Mechanistic study of HCOOH on Pd - Part 2: impedance

6.1 Abstract

The electrooxidation of formic acid on polycrystalline palladium electrodes in sulfuric acid is studied by dynamic electrochemical impedance spectroscopy. Impedance spectra with a frequency range of 5 decades with 10 points per decade, obtained from a FFT on a multi-sine waveform at various scan rates and concentrations are used to interpret the mechanism of the electrooxidation. The use of the dynamic impedance method allows for studying the active electrooxidation at varying potential and sweep rate. We fit the data to equivalent circuits, and relate the circuit elements to a previously proposed mechanism. We provide additional evidence against CO formation on Pd surface within the time-scale of our experiments.

6.2 Introduction

The need for alternative forms of energy continues to grow as portable devices use increasingly more electric power while decreasing in size. Under this backdrop, interest in direct formic acid fuel cells (DFAFC) has increased since the 90's [137]. Formic acid (FA) as a fuel has advantages over other single carbon organic compounds (e.g., methanol) in that there is a minimum of bond rearrangement. In fact, in alkaline environment only a single H–C bond must be broken and a C–O π-bond must be made to complete the oxidation of formate to CO_2.

The mechanism of FA oxidation has been classically described in terms of a dual pathway where one path involves direct oxidation

$$\mathrm{Pd(site) + HCOOH(aq) \rightarrow PdHCOO(ads) + H^+(aq) + e^-} \tag{6.1}$$

$$\mathrm{PdHCOO(ads) \rightarrow Pd(site) + CO_2(aq) + H^+(aq) + e^-} \tag{6.2}$$

but the other goes through a CO(ads) intermediate and is referred to as the indirect path [128].

$$\mathrm{Pd(site) + HCOOH(aq) \rightarrow PdCO(ads) + H_2O(l)} \tag{6.3}$$

$$\mathrm{Pd(site) + H_2O(l) \rightarrow PdOH(ads) + H^+(aq) + e^-} \tag{6.4}$$

$$\mathrm{PdCO(ads) + PdOH(ads) \rightarrow 2\,Pd(site) + CO_2(aq) + H^+(aq) + e^-} \tag{6.5}$$

Palladium has been shown to be an ideal surface for FA oxidation as the indirect path-

way is signif cantly slower than on Pt [128]. Kinetic and mechanistic studies of FA oxidation on Pd surfaces have been conducted using spectroscopy (SEIRS [144, 145] and SERAS [147]) and potentiostatic methods on single crystal [144–146, 170], polycrystalline, see Chapter 5 and [107, 128], and nanoparticle surfaces [142, 153, 168, 171–174]. We previously used an array of potentiostatic methods along with deliberate additions of organic contaminants to study the passivisation process in Chapter 5. We proposed a mechanism where the coverage of an adsorbed intermediate, viz HCOO(ads) or CO_3(ads), increased, which then caused a decrease in the active surface area. That is, the mechanism linked the decrease in the anodic current to an increase in the coverage of a surface species. We then suggested that the increase in the coverage of, say, HCOO(ads) was due to the decrease in the H–C bond cleavage caused by the adsorption of (bi)sulfate anion, which deactivates the surface.

Electrochemical impedance spectroscopy (EIS) has been used to study organic oxidation reactions. In a simple analysis, the number of time constants–seen in the Nyquist plot as semi-circles–can be related to the number of surface species present [175, 176]. This is because a reaction that introduces the adsorbate will introduce an additional relaxation time. Dynamic EIS (dEIS) uses a multi-sine waveform to acquire impedance spectra on-the-f y as the potential is swept or time is elapsed. Our group have used this technique in the study of oxide growth at Pt and Pd, [21], Chapter 3. We have also used a similar method to study methanol and FA oxidation on Pt [106, 133]. In the latter two studies, the impedance suggested that there exists competition between the CO(ads) intermediate and coadsorbed oxo-species, e.g., OH(ads), near the potential region where the surface oxide begins to form. This was seen in the impedance as a Hopf bifurcation where the impedance crosses the negative Re(Z) axis at a particular frequency. Thus, potentiostatic oscillations could be induced at the onset of oxide growth for the FA-Pt system. While galvanostatic and potentiostatic oscillations are known to occur at Pt for various organic compounds

(methanol [177–179], formic acid [133, 180, 181], CO [182–184], and glycol [185]), they are not common for Pd.

Herein we use dEIS to study FA oxidation on polycrystalline Pd. We show that strongly bound organics do not reach high surface coverages. We present evidence that absorbed hydrogen has an important effect on the oxidation. It is shown that adsorbed oxo-species on Pd do not behave has they do on Pt nor does CO form on the surface. We also discuss the nature of the negative resistances in terms of the mechanism we previously presented in Chapter 5.

6.3 Experimental

6.3.1 dEIS setup

The instrumentation details and the experimental setup has been described previously [7] and only a brief description is given here. The "dc" voltammetry sweeps and the multi-sine waveform were synthesized by separate function generators. The signals were added together before being applied to the cell *via* a potentiostat. The potential and current were continuously digitized by an acquisition module and recorded to a data f le. After an experiment, the raw data was Fourier transformed and converted into impedance spectra at chosen intervals (here 5 mV) and ac voltammograms. The multi-sine ac waveform consisted of 45 frequencies from 13 kHz to 1 Hz and followed the rules as developed by Popkirov [9], Roy [12], and Sacci [7]: 1) each frequency in the waveform had an integer number of periods in the waveform period, $T = 1/f_{\text{min}}$; 2) the rms amplitude for the individual sine waves decreased by a factor of two for every decade increase in the frequency; 3) the phases of the individual sine waves were randomized; 4) the maximum peak-to-peak amplitude of the ac waveform was 30–35 mV which corresponded to a maximum amplitude of 4.5 mV rms for the lowest frequency and a minimum of 0.5 mV rms for the highest frequency. The

sampling was done by a Keithley-3116 module with a sampling speed of 40 kHz.

6.3.2 Electrochemistry

Formic acid electrooxidation in sulfuric acid was studied at a polycrystalline palladium wire (Johnson-Matthey, 99.998 %) spot welded to a copper wire with the joint covered by PTFE heat-shrink (Zeus, Inc.). The reference and the counter electrodes were polycrystalline platinum and palladium wires, respectively, (Johnson-Matthey, 99.998 %) sealed in glass or PTFE heat-shrink tubing. All potentials were measured and are quoted against the reversible hydrogen reference electrode, RHE, in the same electrolyte separated from the main cell by a Vycor® (1/8" dia., BAS) or ground glass joint. All experiments were carried out at ambient temperature, 21 °C. There was negligible phase shift throughout the frequency range due to the instrumentation and cell setup.

All glassware was thoroughly cleaned by soaking in fresh piranha solution (two parts concentrated H_2SO_4 and one part 30% w/w H_2O_2 by volume) for 10 min. It was then placed in hot concentrated H_2SO_4 overnight to remove remaining contaminants and to decompose any remaining peroxide. The glass was rinsed with Millipore water (18 MΩ cm), and then the cell was assembled. The electrolyte was added immediately after wards. The 0.5 M H_2SO_4 electrolyte was prepared using the Millipore water and concentrated sulfuric acid (Fluka, puriss).

Slow changes in electroactivity have been observed in similar reactions on Pt [106] and Pd [107], and so we were careful to standardize the conditions before conducting a dEIS experiment at a particular formic acid concentration and sweep rate. The working electrode was conditioned by cycling between 0.2 and 1.5 V at 200 mV s^{-1} for 30 min, and then from 0.25 to 1.4 V at 50 mV s^{-1} until the representative voltammogram was obtained in sulfuric acid. The double-layer capacitance at 0.6 V was measured prior to the addition of formic acid using impedance, and was used to obtain the true surface area for palladium,

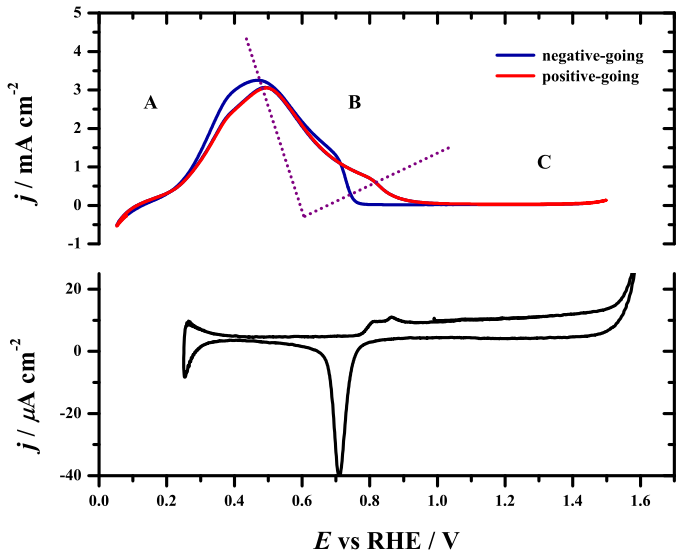

Figure 6.1: Voltammograms of 0.5 M HCOOH in 0.5 M H_2SO_4 (top) and in bare electrolyte (bottom) on Pd.

assuming 25 μF cm^{-2} for an ideally smooth surface [47]. Concentrated formic acid (98% Fluka, puriss) was then added to the electrolyte to obtain the desired concentration. Unless otherwise noted, the potential was cycled at the conditions given in the f gures at least three times before the dEIS recording began. All voltammograms were carried out with a sweep rate of 5 mV s^{-1} unless noted otherwise and were obtained by FFT of the raw data obtained during a dEIS sweep.

6.4 Results

6.4.1 Voltammograms

The voltammogram of formic acid oxidation on Pd can be divided into three basic regions, Fig. 6.1: **A**) positive Tafel region ($E < 0.48$ V); **B**, passivisation–negative Tafel slope region (0.48–0.9 V); and **C**, oxide region ($E > 0.9$ V). In region **A**, hydrogen absorption/desorption occurs and increasing the potential increases the current, as expected for an anodic process.

Region **B** contains the current maximum (0.49 V) and a negative j-E sloped region. In the absence of FA, this potential region shows no features and is generally considered the double layer region where the small current is due to charging the double layer of the surface|electrolyte interface. Partial charge transfer from the network of adsorbed anions has also be shown to be present here [186]. In region **C** oxide growth occurs by the oxidation of adsorbed water in the positive-going sweep. As discussed in Chapter 3, the rate for oxide growth on Pd typically assumes the direct logarithmic rate law which appears as a plateau in the voltammogram.

$$v_{\text{ox}} = k_{\text{ox}} \exp\left(\frac{\alpha_{\text{ox}} F}{RT} E\right) \exp(-b\sigma_{\text{ox}}) \tag{6.6}$$

It is clearly shown in Fig. 6.1 that the electrosorption of oxygen passivates the surface against FA oxidation, i.e., the current drops signif cantly. The reduction of the oxide gives the cathodic peak at 0.725 V in the negative-going sweep (black curve in Fig. 6.1a). In the presence of FA, the reduction leads to a reactivation of the surface, causing a rapid increase in the anodic current in the negative-going sweep.

The ac voltammograms obtained from dEIS provides supporting information to that in Chapter 5 since sweep rate can be used as a variable. The admittance plots can be divided into the same regions as the dc voltammograms. The real admittance in region B at low frequencies is negative, which matches the sign of the j-E slope, Fig 6.2. The only regions where the real admittance does not match that of the j-E slope is at the onset of oxide growth and near the reduction of the oxide. This suggests that the impedance prof le will likely not be missing any slower processes that occur along the time-scale of the positive-going potential sweep between 0–0.9 V. The admittance in the oxide region provides a close match to that of Pd in FA-free electrolyte (Chapter 3) at most frequencies regardless of sweep rate, which further suggests that oxide is an effective inhibitor.

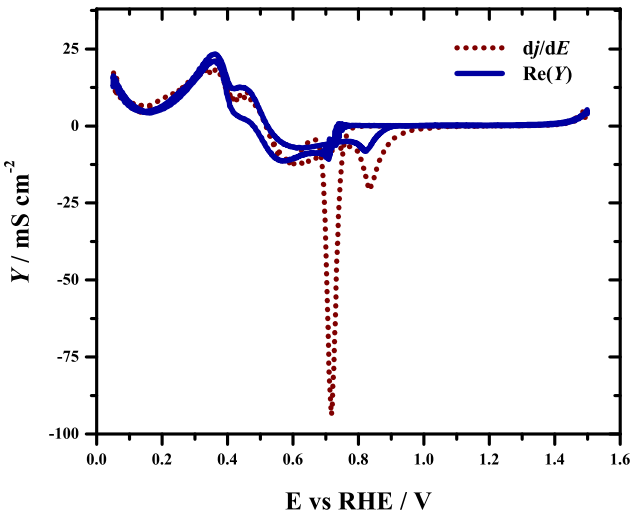

Figure 6.2: Comparison between the real part of the low frequency (5 Hz) admittance and the derivative of the dc voltammogram.

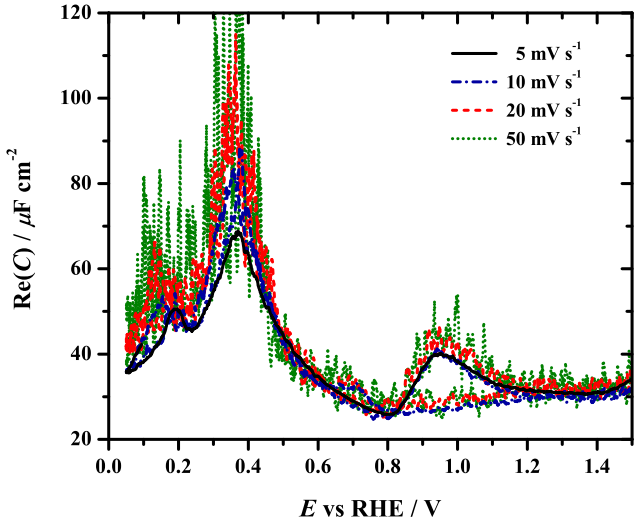

Figure 6.3: High frequency imaginary admittance normalized by frequency at varying sweep rates of 0.25 M FA. Frequency: 13 kHz.

The high frequencies in the waveform are used to probe the charging of the double layer and the solution resistance. The high frequency imaginary admittance (related to the double layer capacitance by $\mathrm{Im}(Y_{\omega\to\infty}) = \omega C_{\mathrm{dl}}$) shows no dependence on sweep rate, Fig. 6.3. This suggests that the coverages of adsorbed species, e.g. CO, FA, and formate, remain small. At lower frequencies, the peaks in the real admittance plot are affected by sweep rate, Fig. 6.4. The peak height increases with an increase in sweep rate. The imaginary plot is unaffected by sweep rate except in the oxide region where the peak at 0.85 V increases with sweep rate. The sweep rate dependence of this peak is as seen in bare electrolyte.

Concentration shows some effects on the high frequency admittance plots, Fig. 6.5. The peak maximum near 0.3 V increases and shifts to more positive potentials. Since in base electrolyte this high-frequency peak is correlated with the absorption of hydrogen, it may relate to the ability of FA to facilitate hydrogen absorption in palladium. At the onset of oxide growth the capacitance decreases with an increase in concentration and the oxide peak is delayed. This suggests that the coverage of intermediates in FA oxidation becomes

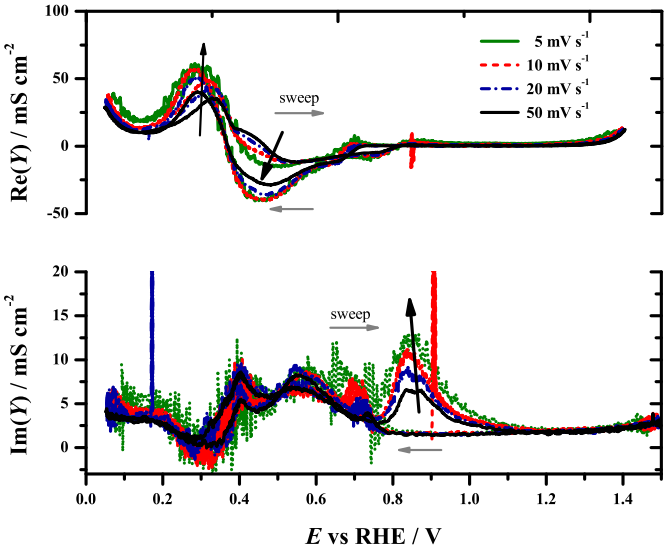

Figure 6.4: Admittance plots of the 5 Hz component of the dEIS sweep at different sweep rates. Arrows in direction of increasing sweep rate. FA concentration: 0.25 M.

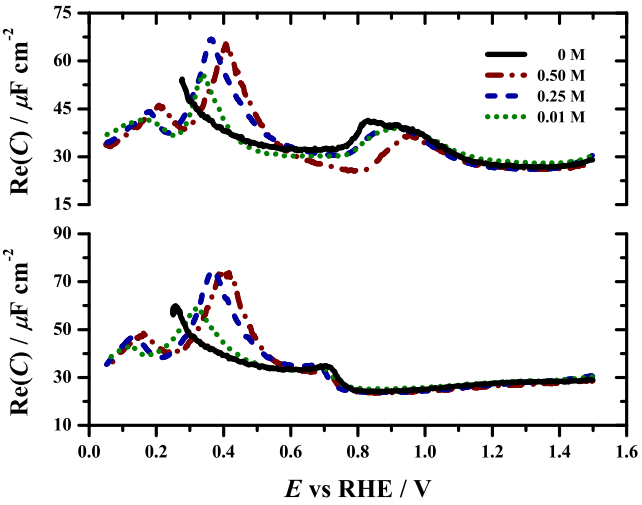

Figure 6.5: High-frequency (13 kHz) capacitance plot at varying concentration. Sweep rate: 5 mV s^{-1}.

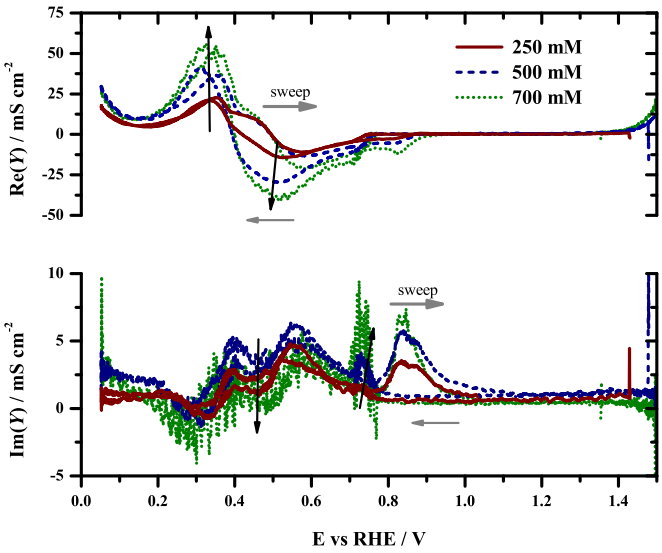

Figure 6.6: Admittance plots of the 5 Hz component of the dEIS sweep at different sweep rates. Arrows in direction of sweep rate. Sweep rate: 5 mV s^{-1}, FA concentration: 0.25 M.

high enough to delay the growth of the oxide only at high FA concentrations (> 0.25 M). The magnitude of the low frequency Re(Y) plots increase linearly with concentration, but there is little change in Im(Y), Fig. 6.6.

6.4.2 Impedance

This section is organized by potential regions, **A**, **B**, and **C** as def ned before. Only region **C** will be divided into positive-going and negative-going sweeps as the ac voltammograms showed little differences with the sweep direction in the other regions.

By combining the ac admittance values from all frequencies measured at a particular E value, an impedance spectrum is obtained. The general shape of the impedance plots change signif cantly along the voltammogram, Fig 6.7. At potentials below 0.3 V the impedance is a semicircle with the low frequencies appearing to form the start a second small semicircle. At 0.3 V the low frequencies cross into the fourth quadrant (Re(Z) > 0, -Im(Z) < 0). This is short lived as the low frequencies return to the f rst quadrant and form

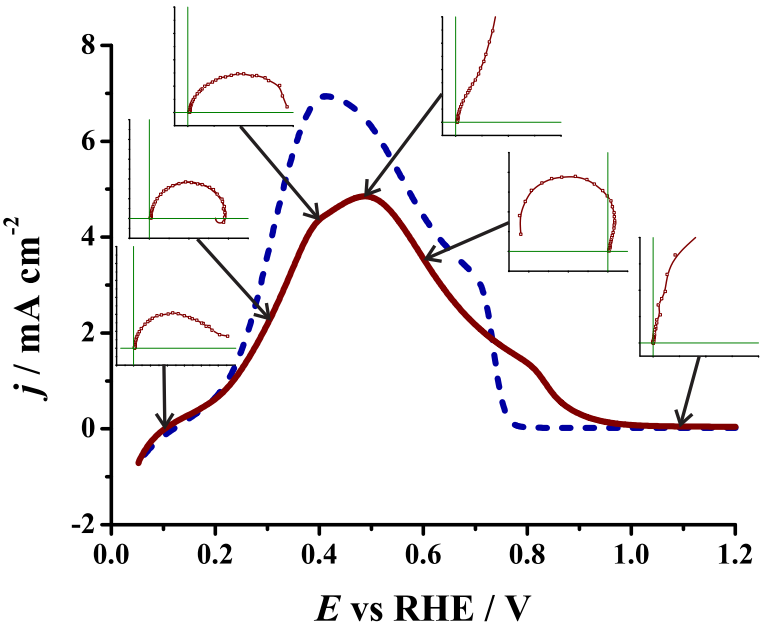

Figure 6.7: Representative dEIS voltammogram showing select impedance plots obtained during the positive-going (**red solid**) and negative-going (**blue dash**) sweeps in 0.5 M HCOOH and 0.5 M H_2SO_4. The impedance snapshots were taken at 0.10, 0.25, 0.40, 0.49, 0.60, and 1.10 V. Green lines in insets show the axes.

a large second semicircle that slowly turns into a vertical line at the current peak (0.49 V). It then bends into the second Nyquist quadrant (Re(Z) < 0, -Im(Z) > 0). In the negative j-E slope region, **B**, the low frequency impedance values are clearly in the second quadrant. This behavior persists well into the oxide region (ca. 0.95 V), where the impedance flips back to the first quadrant resulting in a single large semi-circle. The reverse sweep gives the same impedance as the forward one, except in the oxide reduction region. Here, the impedance drastically changes within a 50 mV region, which will be discussed later. These general results occur at all sweep rates and at all concentrations.

The impedance in the hydrogen adsorption region (0.05–0.35 V) changes as expected from the dc and ac voltammograms, Fig. 6.8. Increasing either the potential or FA concentration generally decreases the diameter. At concentrations greater than 0.25 M, the low-frequency impedance curls towards the origin as it approaches the Re(Z)-axis. At 0.7 M the impedance curve crosses into the fourth quadrant. At potentials greater than 0.4 V, the curl recedes and a second semicircle appears at all concentrations. This time the size of the semicircle increases with potential. This matches the dc voltammogram where the j-E slope begins to decrease. The rate of growth for the second semicircle is inversely dependent upon concentration, that is, in 0.01 M FA the impedance increases more rapidly than in 0.5 M FA.

After the current maximum, the j-E slope is negative and the impedance flips into the second quadrant to give a negative Re(Z) low-frequency limit. This occurs at all concentrations and sweep rates, Fig. 6.9. As in the previous region, the size of the impedance curve decreases as concentration increases. The flip into the second quadrant occurs at 0.48–0.49 V for all concentrations. This is expected to correlate with the peak potential. However, the voltammogram peak depends on concentration; it is at 0.4 V for 0.01 M and ca. 0.5 V at concentrations greater than 0.25 M. While the 1 Hz impedance datum (0.01 M) does not enter the second quadrant until 0.48 V, the curve does begin to bend in the di-

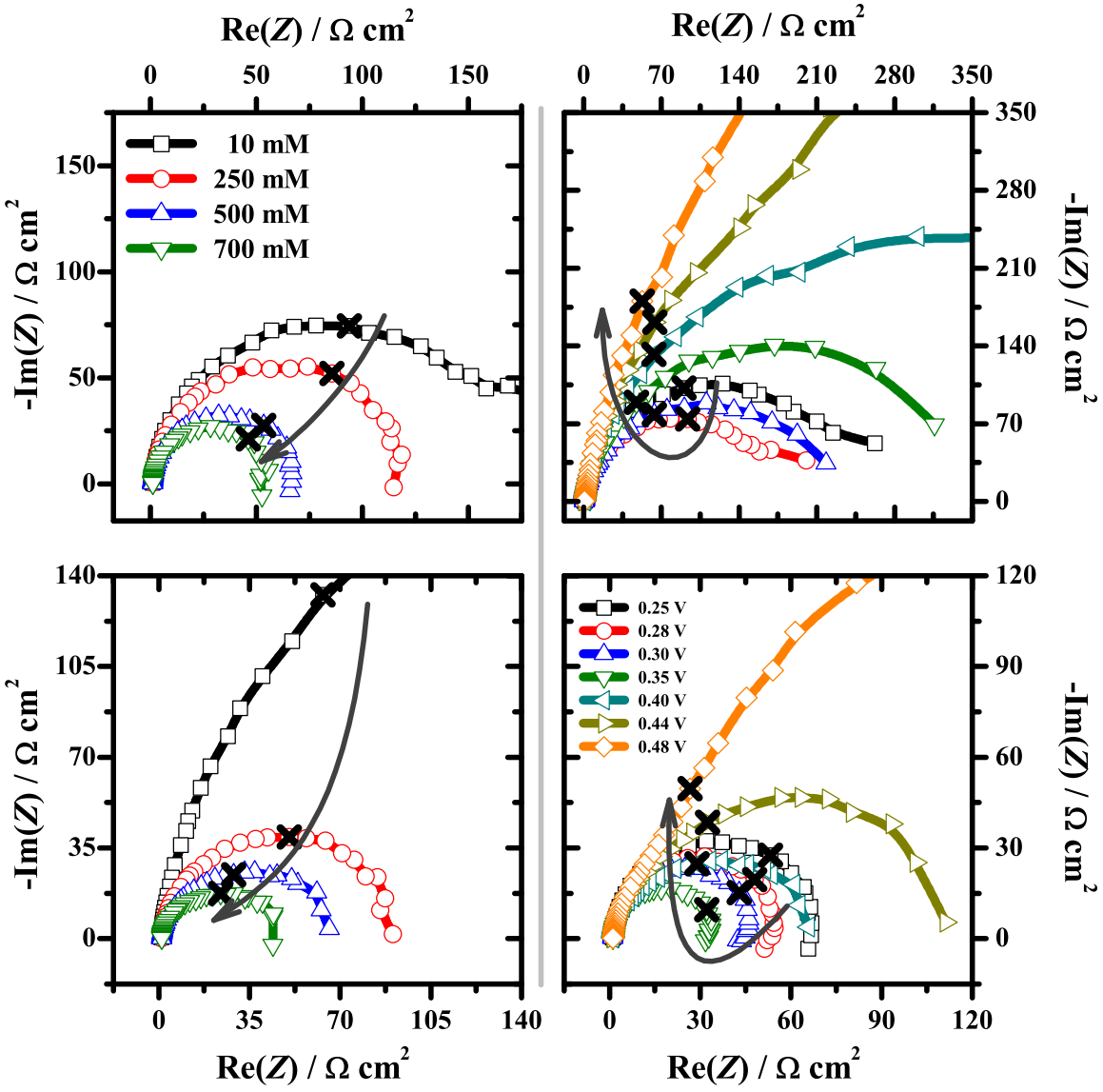

Figure 6.8: Nyquist plots of the impedance data acquired during the positive-going sweeps in region **A**. Left-most plots show the concentration effects at constant potentials: 0.25 V (top) and 0.45 V (bottom) with arrows in direction of increasing concentration. The right-most plots show the effects of potential at 0.01 M (top) and 0.5 M (bottom) with arrows in direction of increasing potential.

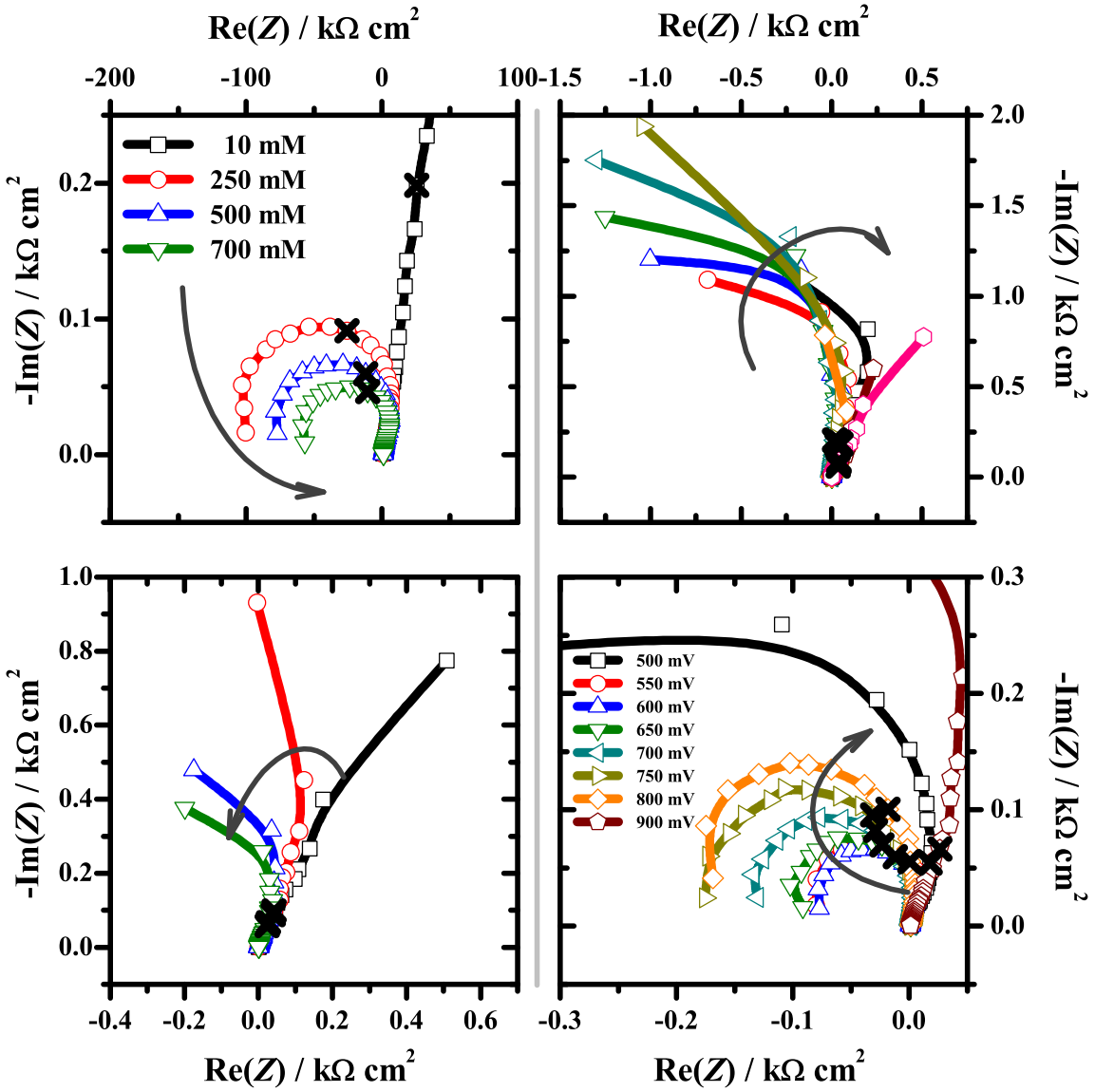

Figure 6.9: Nyquist plots of the impedance data acquired during the positive-going sweeps in region **B**. Left-most plots show the concentration effects at constant potentials: 0.6 V (top) and 0.8 V (bottom), with arrows in direction of increasing concentration. The right-most plots show the effects of potential at 0.01 M (top) and 0.5 M (bottom), with arrows in direction of increasing potential (0.6–0.9 V).

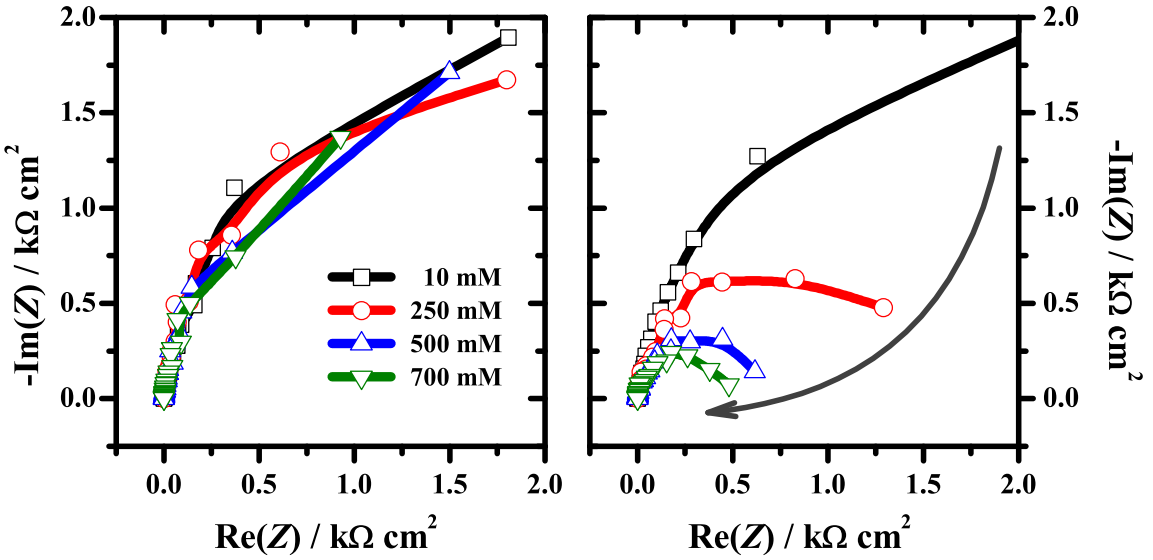

Figure 6.10: Nyquist plots of the impedance data acquired during the positive-going sweep in region **C** at varying concentrations. Left: 1.1 V, Right: 1.4 V.

rection of that quadrant at 0.44 V. This bend does not occur at higher concentrations until 0.48 V. The f ip back into the f rst quadrant—due to passivation of the oxide layer—occurs at higher potentials for higher concentrations. This suggests that either the adsorbed intermediates can inhibit oxide growth or that the impedance of FA oxidation is small and therefore it hides the parallel large impedance of oxide growth. The latter is reasonable given that before this region the total resistance due to FA oxidation is ca. -300 $\Omega\,\mathrm{cm}^2$, while that of the oxide growth in Chapter 3 was ca. 1000 $\Omega\,\mathrm{cm}^2$. This would give a parallel combination of -430 $\Omega\,\mathrm{cm}^2$ at $\theta_{\mathrm{O}} = 0.5$.

As stated previously, the growth of the oxide layer passivates the palladium surface toward FA oxidation. This is clearly seen in Fig 6.10, where the impedances are near identical for all concentrations at 1.1 V. However, in the extended oxide region ($E > 1.35$ V), FA oxidation resumes. Here, we see a dependence on concentration as the diameter of the semicircle decreases with increasing concentration.

The impedance during the oxide region shows sporadic behavior at low frequencies,

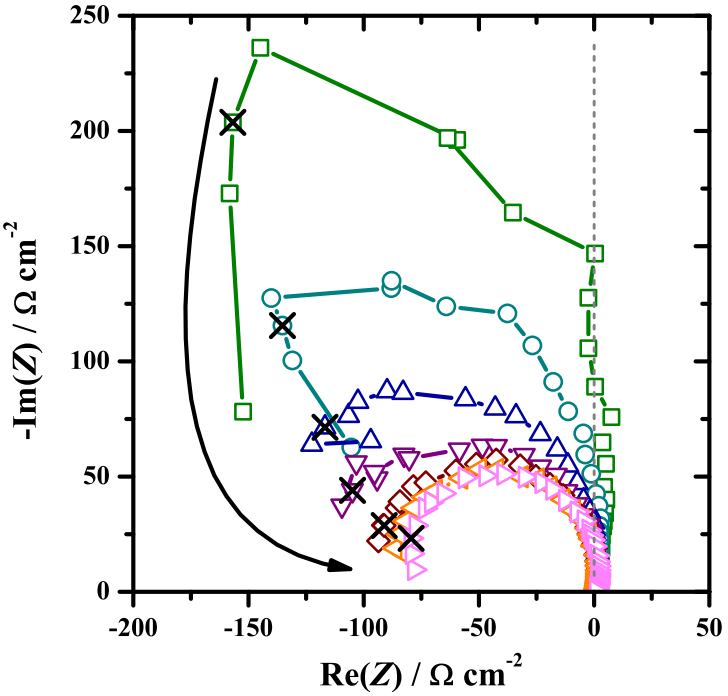

Figure 6.11: Nyquist plots of the impedance data acquired during the negative-going sweep in the oxide reduction region. Potential range: 0.75–0.69 V. Arrow in direction of decreasing potential.

Fig. 6.11. This is due to the fact that the surface is being rapidly reactivated upon the reduction and removal of the oxide layer. This causes the current to increase rapidly, which as mentioned in Chapters 2 and 4, interferes with the validity of FFT baseline correction. It is clear that the impedance flips into the second quadrant, however, whether or not it crosses into the third quadrant remains uncertain. If the impedance did cross into this quadrant it would imply the ability to potentiostatically oscillate. Given that fitting any sensible equivalent circuit to the data in this region produced χ^2 values greater than 0.01 and individual element values with large errors we refrain from a detailed analysis in this potential range.

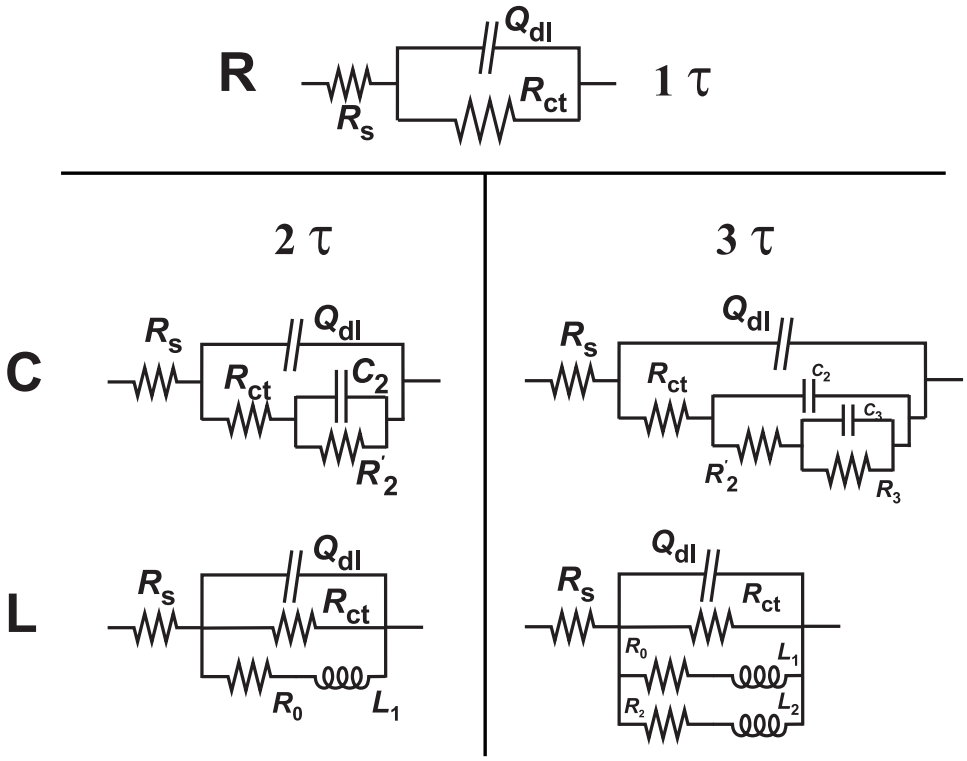

Figure 6.12: Equivalent circuits used to fit the impedance data arranged by number of time constants and type of elements. $Q_{\rm dl}$ is a CPE representing the double layer whose psuedocapacitance is of the form $C_{\rm dl} = (Q_{\rm dl} R_{||}^{1-\alpha})^{1/\alpha}$.

6.4.3 Circuits

In order to extract quantitative information about the reaction mechanism and kinetics, equivalent circuits were used to fit the data and to test for the presence of multiple time-constants. This is useful given that the number of time constants have been related to number of "kinetically important" intermediates [133, 175, 176, 187, 188]. We begin with a simple equivalent circuit modeling an electron-transfer where mass transport is fast, **R** in Fig. 6.12, as the most simple circuit. We have shown that this circuit, while overly simple, provides good fits to oxide growth and CO oxidation in Chapters 3 and 4, respectively. Given the nature of ECs there are multiple ways of incorporating additional time-constants depending on the physical nature of the system in question and the desired information [2]. We fit the data using the parallel *RL* combination style (**L** in Fig. 6.12) as opposed to the

nested *RC* form (**C** in Fig. 6.12) since it more simply related to kinetic parameters.

$$R_{\mathrm{ct}}^{-1} = F\left(\frac{\partial r_{\mathrm{e}}}{\partial E}\right)_{\theta} \tag{6.7}$$

$$C_2 = -\Gamma_{\mathrm{m}}\left(\frac{\partial r_{\mathrm{e}}}{\partial E}\right)_{\theta}^{2} \Big/ \left[\left(\frac{\partial r_{\mathrm{e}}}{\partial \theta}\right)_{E}\left(\frac{\partial r_{\theta}}{\partial E}\right)_{\theta}\right] \tag{6.8}$$

$$R_2' = -R_{\mathrm{ct}}^{-1} \Big/ \left[C_2\left(\frac{F}{\Gamma_{\mathrm{m}}}\left(\frac{\partial r_{\theta}}{\partial \theta}\right)_{E} R_{\mathrm{ct}}^{-1} + \frac{R_{\mathrm{ct}}^{-2}}{C_2}\right)\right] \tag{6.9}$$

$$L_1 = -\Gamma_{\mathrm{m}} \Big/ \left[F\left(\frac{\partial r_{\mathrm{e}}}{\partial \theta}\right)_{E}\left(\frac{\partial r_{\theta}}{\partial E}\right)_{\theta}\right] \tag{6.10}$$

$$R_0 = \left(\frac{\partial r_{\theta}}{\partial \theta}\right)_{E} \Big/ \left[F\left(\frac{\partial r_{\mathrm{e}}}{\partial \theta}\right)_{E}\left(\frac{\partial r_{\theta}}{\partial E}\right)_{\theta}\right] \tag{6.11}$$

where r_i refers to the net rate of production of species i and θ is the coverage of the adsorbed intermediate—in this chapter it refers to HCOO(ads) unless stated otherwise. The time constant of the *RL* circuit is obtained in a much simpler form than that of the *RC*

$$\tau_1^{-1} = \frac{R_0}{L_1} = \frac{R_{\mathrm{ct}} + R_2'}{C_2 R_{\mathrm{ct}} R_2'} = -\frac{1}{\Gamma_{\mathrm{m}}}\left(\frac{\partial r_{\theta}}{\partial \theta}\right)_{E} \tag{6.12}$$

$$B_1 = \frac{1}{L_1} = \frac{1}{C_2 R_{\mathrm{ct}}^2} = -\frac{F}{\Gamma_{\mathrm{m}}}\left(\frac{\partial r_{\mathrm{e}}}{\partial \theta}\right)_{E}\left(\frac{\partial r_{\theta}}{\partial E}\right)_{\theta} \tag{6.13}$$

From a statistical point of view, the propagation of error causes the values of τ_1^{-1} and B_1 to have larger uncertainty when calculated from the RC elements. Since **L2** produces the lowest error (Table 6.1) and could be used in a larger potential range we chose to use the *RL* circuits in our impedance analysis.

The F-test was used to determine the number of time constants present in the impedance data. The same procedure was followed as described in Chapter 3. The addition of element must cause a decrease in χ^2 of 1 % or more to be considered statistically valid. In addition to

Table 6.1: Percent errors of the individual circuit elements from f tting EC **C2** and **L2** to the impedance at 0.3 V and 0.6 V and the error propagation in calculating τ_1^{-1} and B_1.

	C2		**L2**	
E / V	0.3	0.6	0.3	0.6
R_s / %	0.2	1.4	0.2	1.4
Q_dl / %	0.7	4.6	0.7	5.4
α / %	0.1	0.6	0.1	0.6
R_ct / %	0.3	79.9	0.3	771
C_2 or L_2 / %	5.6	152.5	5.2	5.1
R_2 or R_0 / %	2.7	75.5	2.9	12.3
τ_1^{-1} / %	6.5	4900	5.8	31.6
B_1 / %	5.9	191	5.1	31.2

that, the values of the elements must 1) have individual errors of less than 50 %; 2) proceed logically from values at adjacent potentials; 3) have reasonable physical values. Fig. 6.13 summarized the equivalent circuits used at particular potential regions. The number of time constants and are also given.

$$F(a,\, v_{new}) \;=\; \frac{\chi^2_{old} - \chi^2_{new}}{\chi^2_{new}} \frac{v_{new}}{\alpha}$$

where v is the degrees of freedom given by $v = 2N_{freq} + N_{parameters} - 1$ [57], α is the number of parameters added between "old" and "new" models, and χ^2 is proportional to the sum of squares. Figure 6.13 provides an example of how increasing the number of time constants increases the f t. In each case presented circuit **R** deviated from the impedance data, especially at low frequencies. In the negative Tafel region, a third time constant was added which decreased the χ^2 by an order of magnitude (improved the f t). We used circuit **L2** throughout region **A**, **L3** though out region **B**, and **R** between 1.0 V and 1.5 V. As seen in the f gures below, the values for the individual elements follow logically from one another even when the equivalent circuit used to f t the data was changed.

6.4.4 Equivalent circuit f ts

The extracted element values behave as expected from the voltammograms. The double-layer capacitance is extracted from the CPE using the parallel combination of the resistors [56].

$$C_{\mathrm{dl}} \;=\; (Q_{\mathrm{dl}} R_{||}^{1-\alpha})^{1/\alpha}$$

The obtained plot is similar in shape and value as that of the high frequency admittance plot in Fig. 6.3. Like in Fig. 6.3 there is no change due to sweep rate. The α plot stays

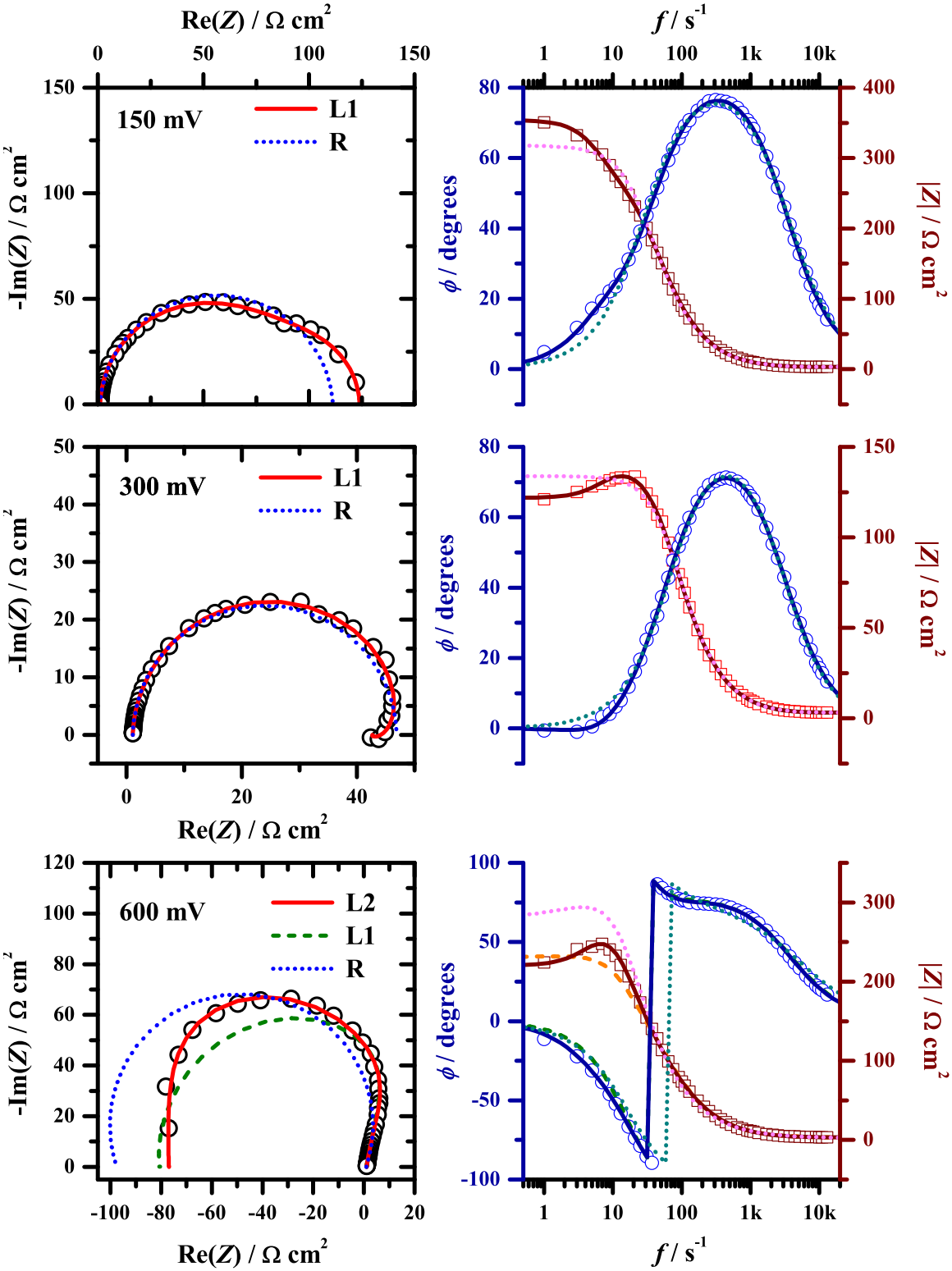

Figure 6.13: Impedance (left) and Bode (right) plots on the positive-going sweep, showing the quality of the f ts provided by the equivalent circuits given. Solid line: best f t and most time constants used; dotted line: worst f t and one time constant.

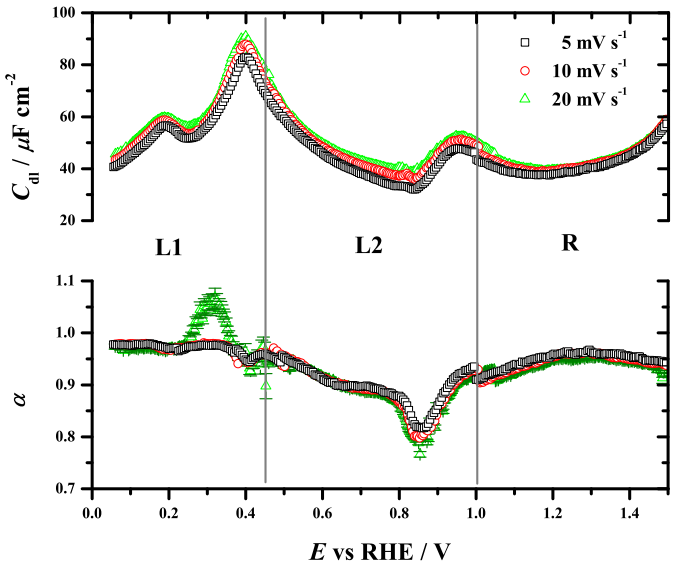

Figure 6.14: Double layer capacitance and CPE exponent α obtained from f ts to the circuits (given in f gure) in the forward sweep at varying sweep rate.

between the normal values of 0.98–0.80 except for 20 mV s^{-1}. Here, a small peak between 0.2 and 0.4 V is seen but no corresponding effect is shown in the capacitance plot. The peak reaches a maximum at 1.08. α values greater than 1 are not common, and thus may be an artifact of the f tting procedure. The plots of the faradaic elements also show no dependency on sweep rate throughout the potential, Fig 6.15. In the potential region 0.2–0.4 V the 20 mV s^{-1} sweep diverges from the others. Here is a large peak in the R_{ct}^{-1} plot, R_0 does not become positive, and L_1^{-1} approaches negative inf nity. Given these facts and the peak in the α plot, it is clear that the f tting procedure is not able to properly distinguish the elements at this sweep rate within the potential region of 0.2–0.4 V.

The R_{ct}^{-1} plot for FA oxidation on Pd is quite different from that on Pt, in that throughout most of the potential range it decreases as the potential increases. Between 0.15 and 0.35 V the Tafel slope of R_{ct}^{-1} is +330 mV dec^{-1}, after the peak the Tafel slope is -130 mV dec^{-1}. The Tafel slope of R_{ct}^{-1} on Pt is reported to be +111 mV dec^{-1} for the potential range of 0.50–0.65 V [133]. Early in the sweep, R_0 and L_1^{-1} are negative. Their magnitudes increase with potential at the same rate, resulting in τ_1^{-1} being constant (ca. 35 Hz). Afterward, both elements become positive (0.2–0.4 V), which correspond to the entrance into the fourth quadrant. Upon going negative again, the magnitude of the two elements sharply increase at 0.4 V. Afterward, R_0 slowly decreases until 0.54 V before slowly increasing with potential. L_1^{-1} increases more rapidly with potential and peaks at 0.54 V. A second peak in L_1^{-1} forms at 0.8 V. τ_1^{-1} is constant at 50 Hz between the potential region of 0.06–0.40 V. Afterward, it jumps to 200 Hz then increases exponentially between 0.6 and 0.8 V with a Tafel slope of +260 mV dec^{-1}. During the negative Tafel slope region (0.5–0.9 V), a second RL branch is added to the equivalent circuit (**L3**), Fig. 6.16. R_2 shows a negative peak ca. 0.75 V which is the onset of oxide growth. After the peak it goes through a minimum before increasing exponentially in magnitude with potential. L_2^{-1} increases linearly with potential until 0.75 V. Afterward it forms a negative peak then its magnitude decreases exponentially

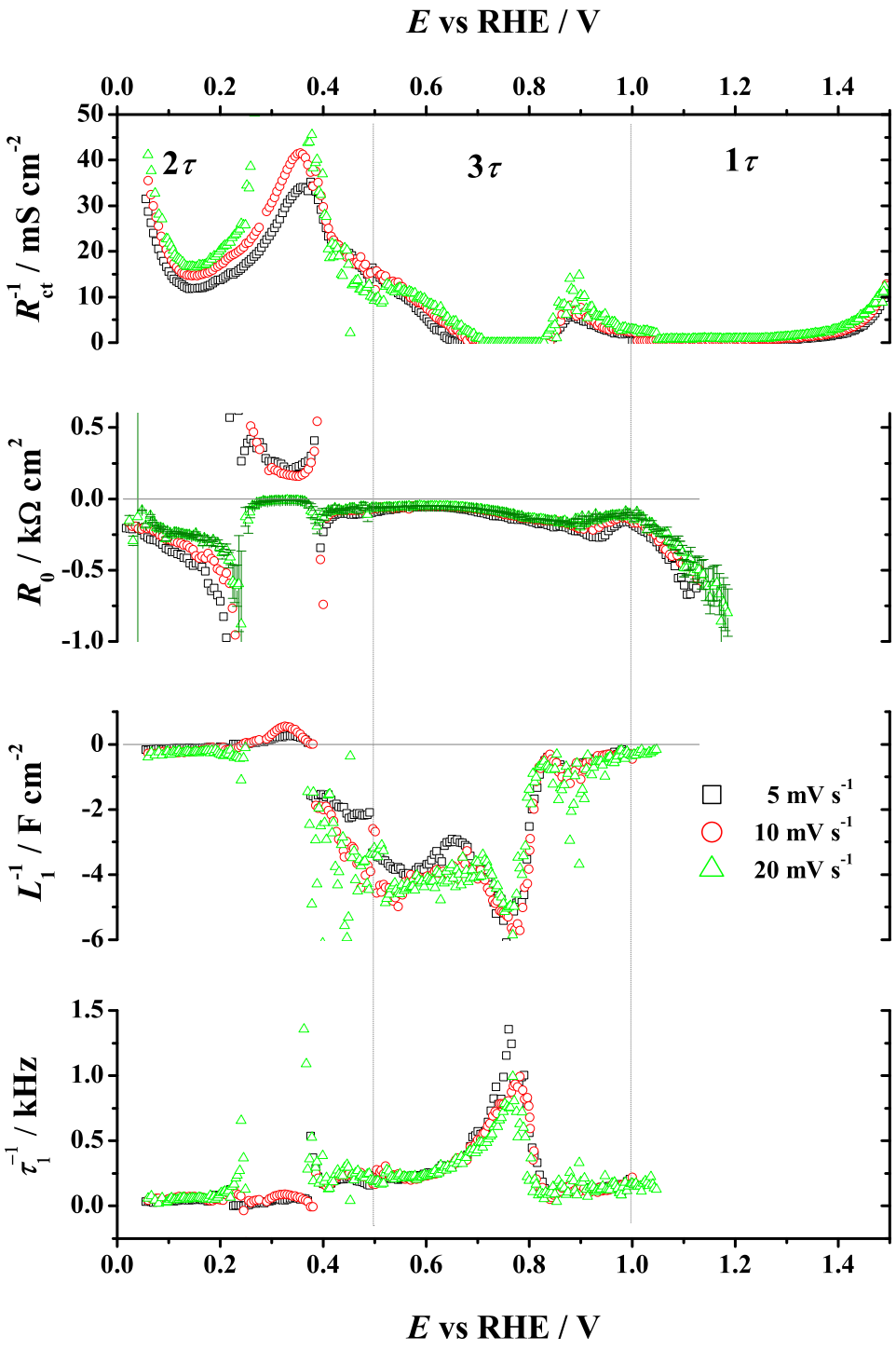

Figure 6.15: Circuit elements f tted during the positive going sweep at various sweep rates. FA concentration, 0.5 M.

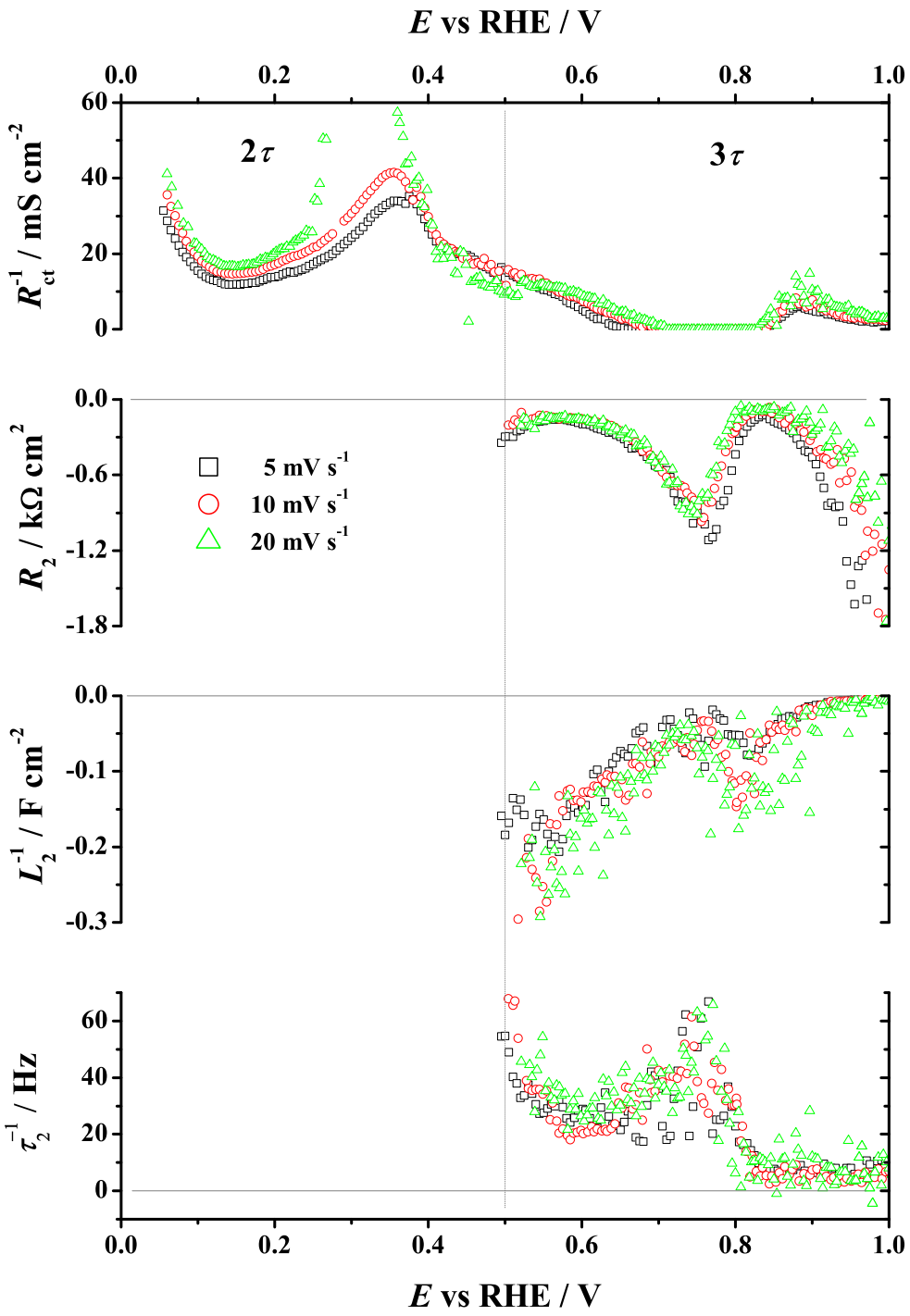

Figure 6.16: Circuit elements f tted during the positive going sweep at various sweep rates. FA concentration, 0.5 M.

with potential. The product of the two elements gives the time constant τ_2^{-1}, which is relatively constant at 35 Hz, between 0.55 and 0.7 V. Another plateau region ($\tau_2^{-1} = 7.5$ Hz) in the early oxide region 0.8–0.9 V. Only R_{ct}^{-1} showed subtle sweep rate dependence, suggesting that the surface state is unaffected by sweep rate, and that a non-electrochemical step is rate-determining.

Concentration showed to have some affect on the circuit elements, Fig. 6.17. R_{ct}^{-1} is proportional to concentration between 0.25 and 0.6 V. The Tafel slope of R_{ct}^{-1} is dependent on concentration, giving +130 mV dec^{-1} before the peak and -120 mV dec^{-1} after. R_0 and L_1^{-1} are linearly dependent on concentration at potentials greater than 0.25 V. However, R_0 shows an inverse relationship to concentration, which caused τ_1^{-1} to be independent of concentration throughout the entire potential range. The second RL branch is mostly independent of concentration, Fig. 6.18. R_2 shows a linear relationship with concentration between 0.70 and 0.76 V. The time constant of the branch shows no dependence on concentration.

6.5 Discussion

6.5.1 Stability

The number of time constants present in the impedance spectra relates to the number of adsorbed species. The high frequency time constant corresponds to the charge transfer resistance and the charging of the double layer. Each additional time constant relates to an adsorbed species, that is

$$n_\theta = n_\tau - 1$$

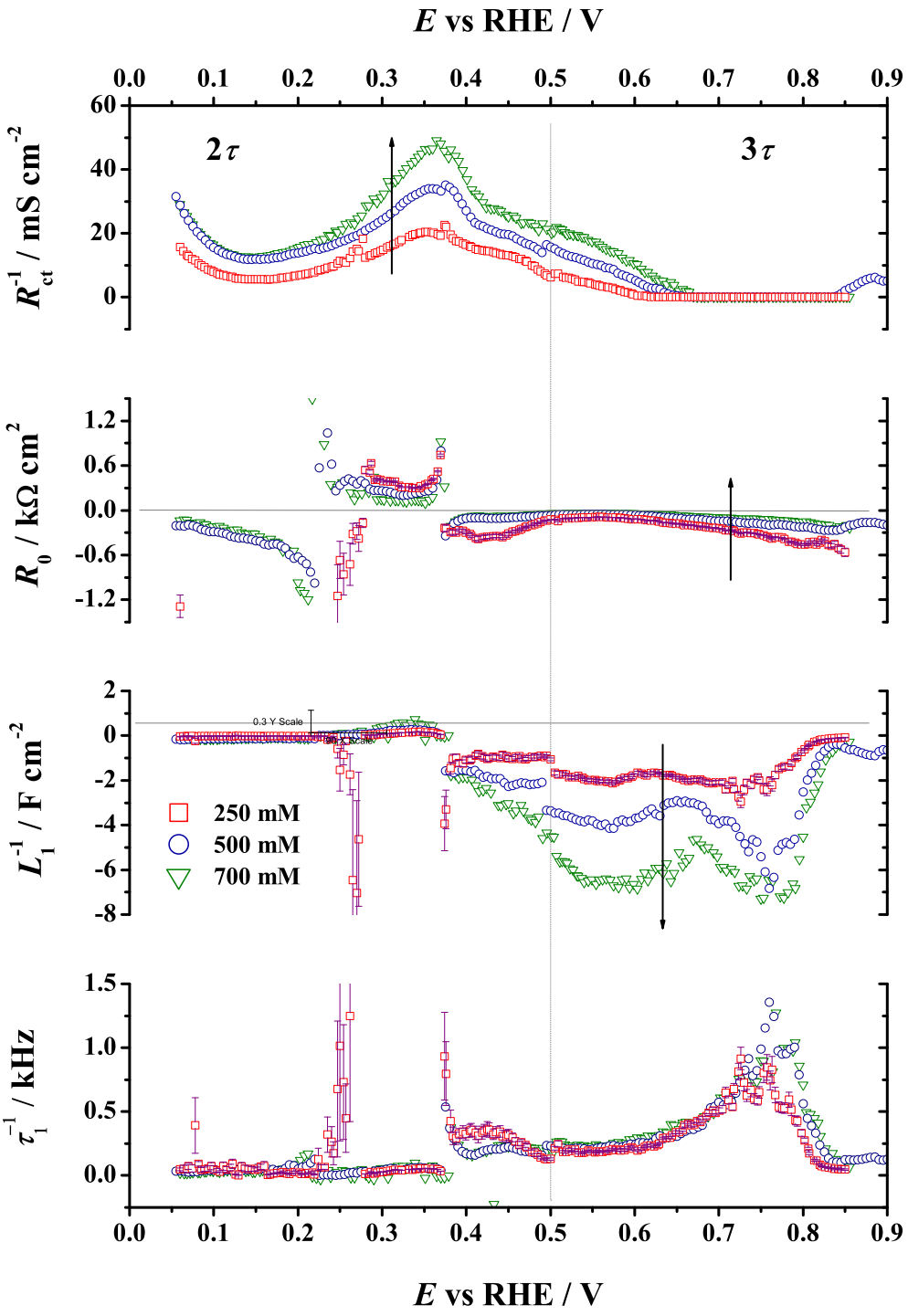

Figure 6.17: Circuit elements f tted during the positive going sweep at various FA concentrations. Sweep rate, 5 mV s^{-1}.

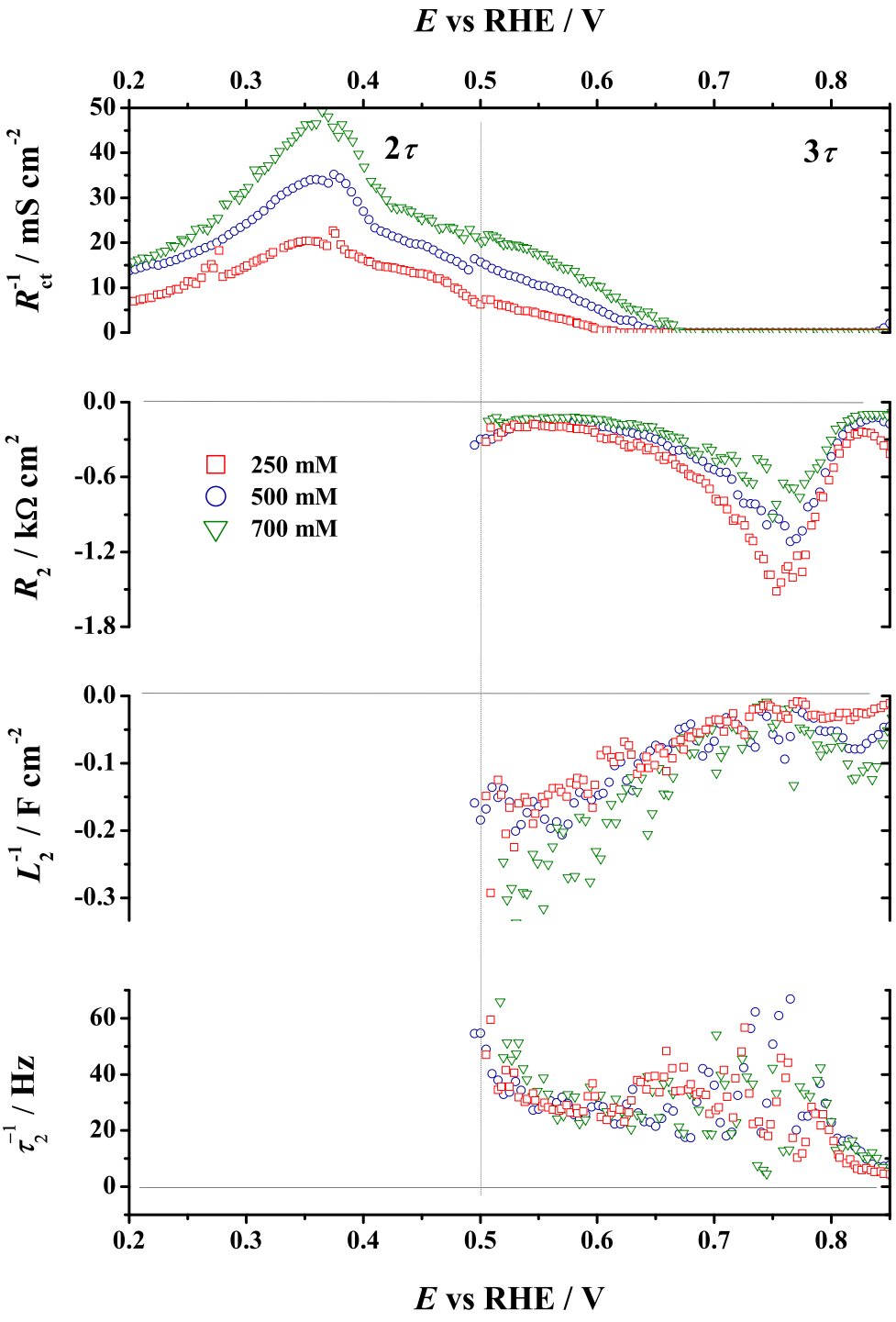

Figure 6.18: Circuit elements f tted during the positive going sweep at various FA concentrations. Sweep rate, 5 mV s^{-1}.

where n_θ and n_τ is the total number of adsorbed species and time constants. This does not mean that a particular time constant is related to a particular adsorbed species, as in $\tau_i^{-1} = f(\theta_i)$. This only occurs when there is a single adsorbed species. The expression for the time constants when there are multiple species are more complicated.

Electrooxidation of small organic molecules where CO forms on the surface seem to process regions where oscillations can be induced. This region typically occurs near the onset of surface oxidation. We have presented evidence that CO oxidation on palladium showed unstable behavior in Chapter 4. This has been seen on platinum with CO, methanol, and formic acid. The prevailing explanation is for these cases is that CO and OH(ads) (or O(ads)) compete for free surface sites that form during the oxidation. Incipient potentiostatic oscillations are signaled in the impedance by the crossing the negative Re(Z) axis, which corresponds to a negative time constant. That is, oscillations may be induced by adding a resistor whose value is equal to the point where the impedance crosses the negative Re(Z) axis to the working electrode circuit. The frequency at which this occurs is known as the Hopf frequency and has been related to the frequency of the oscillation.

All the elements used to f t the impedance data produced positive time constants. This suggests that the system is stable throughout the potential region measured. Sweep-hold experiments can also be used to test for instability in a system. In a stable system when the potential is held, the current response either remains constant or it decreases. If the system is unstable, the current continues to increase after the potential sweep is stopped. Chapter 5 showed that there was only one region that showed unstable behavior, the oxide reduction region. While the current increases when the potential sweep is held in this region, it quickly converges to the value of the positive-going sweep. The low frequency impedance in this region is sporadic due to the validity constraints of dEIS, that is the change in surface conditions along the order of the slow perturbations. Since the oxide reduction on palladium produces a sharp cathodic peak it is reasonable to assume that the rapid change

in surface reactivity due to the removal of the oxide is the cause for the inability to extract the low frequency impedance from the FFT. However, once the oxide is removed the low frequencies stabilize in the second quadrant and the double layer capacitance matches that of the positive-going sweep. Therefore, the instability is short lived and is not due to competition between CO and oxo-species. Since all the time constants are positive, and there is no competition between CO and oxo-species, the FA oxidation on Pd is not expected to possess regions of incipient potentiostatic oscillations as exist on Pt.

6.5.2 CO as poison

The formation of CO on the Pd surface is considered slow, which is the reason for the large broad peak beginning at 0.25 V [128]. Fuel cell performance experiments using commercial Pd black catalysts have been shown to be far less susceptible to passivation than Pt black catalysts for formic acid [137]. While it is typical to ascribe the passivisation process to the formation of CO, there is little evidence that CO actually reaches coverages where it can passivate the surface. Spectroscopic experiments have shown that CO only forms on the surface in small amounts and at potentials lower than 0.3 V [145, 147]. The disagreement between the spectroscopic results and the nanoparticle results lies in the difference in conditions. The spectroscopic results were conducted at much lower concentrations and on smoother surfaces than the nanoparticle. In Chapter 5, the series of passivisation experiments suggest that formation CO on the surface was much slower than the time scale of our experiments.

The double layer capacitance plots reaff rm the premise that the coverage of CO is negligible. C_{dl} is independent of sweep rate and increases with formic acid concentration between 0.25–0.5 V. At 0.5 V, the double layer capacitance of CO on Pd, methanol on Pt and formic acid on Pd are 9, 18, and 18 μF cm^{-2}, respectively. Comparing that with the capacitance value in bare electrolyte—30 μF cm^{-2} for Pd and 50 μF cm^{-2} for Pt—shows

that if CO adsorbs on the surface the capacitance decreases. In addition, no impedance feature was detected that could be ascribed to the formation and passivation of CO. Since the low frequency admittance closely matches that of the derivative of the j-E curve, there is no missing relaxation that occurs on the time scale of the sweep. That is, there is no slow CO passivation process that is detectable.

6.5.3 Mechanism

In light of the above discussion we will once again ignore the CO intermediate pathway and consider the mechanism presented in Chapter 5.

$$\mathrm{Pd(site) + HCOOH(aq) \rightleftarrows PdHCOOH(ads)} \tag{6.14}$$

$$\mathrm{PdHCOOH(ads) \rightleftarrows PdHCOO(ads) + H^{+}(aq) + e^{-}} \tag{6.15}$$

$$\mathrm{PdHCOO(ads) \rightleftarrows PdCO_2(ads) + H^{+}(aq) + e^{-}} \tag{6.16}$$

$$\mathrm{PdCO_2(ads) \rightleftarrows Pd(site) + CO_2(aq)} \tag{6.17}$$

We will also ignore region **C** as its impedance is dominated by oxide growth, which was discussed in Chapter 3. Our explanation of the passivation region, **B**, relies on adsorption of supporting anions and the oxide precursor. We assume that the adsorption of (bi)sulfate

takes up many Pd sites, Eq. (6.18).

$$x\mathrm{Pd(site)} + \mathrm{HSO_4^-(aq)} \quad \rightleftarrows \quad \mathrm{Pd}_x\mathrm{HSO_4(ads)} + \mathrm{e^-} \tag{6.18}$$

Differentiation between inhibition by (bi)sulfate adsorption or oxide precursor is not within the scope of this chapter and so Eq (6.18) can represent blocking by one or both species. Since there is one electron for many Pd atoms, the current due to anion adsorption is small, but it can have a strong effect on the other reaction steps as a site blocker or by affecting another reaction step. In Chapter 5 we incorporated into the mass action rate form of Eq. (6.16) a repulsive Frumkin effect to simulate the adverse effect that adsorbed (bi)sulfate has on the H–C bond cleavage.

In Chapter 5, we suggested that the electrooxidation was principally governed by the applied potential. The sweep rate was found to have little effect on the voltammogram, which suggested that a chemical step was rate limiting. The slight dependence of the real low frequency admittance and R_{ct}^{-1} on sweep rate is in agreement with the current being only slightly affected. Since the other circuit elements that depend on coverage (and the change thereof) show no dependence on sweep rate, a pseudo-equilibrium state is readily achieved. Therefore, the coverages are a unique function of the applied potential.

The peak in Re(C) near 0.4 V shifts to more positive potentials as FA increases, Fig. 6.5. This peak occurs in the absence of FA and occurs at the onset of hydrogen absorption (0.3 V). Since hydrogen absorption is prevalent at low potentials, this peak suggests that FA and H(abs) affect one another. This was discussed in detail in Chapter 5. It was proposed that FA undergoes sequential dehydrogenation since the equilibrium in this potential region is towards absorption and not desorption of the hydrogen. The decrease in R_{ct}^{-1} between 0.06 V and 0.15 V is due to the decrease in the rate of proton reduction—the current here is cathodic. The decrease in rate is caused by both the increase in potential and further

adsorption of FA. Both R_0 and L_1^{-1} are negative in this region thereby producing a second semi-circle in the f rst quadrant which increases as the potential increase. After the current becomes anodic at 0.15 V the signs of R_0 and L_1^{-1} become positive. Because FA oxidation occurs via dehydrogenation it follows that the equilibrium will also shift towards hydrogen oxidation, which may cause the inductive behavior.

Once the potential increases past 0.38 V, R_0 and L_1^{-1} become negative again and remain there until the oxide region. The elements form a smooth line even when a second *RL* branch is added to the equivalent circuit. Given that SEIRAS shows adsorbed formate is present on Pd in sulfuric acid, this branch may relate to the oxidation step in Eq. (6.16). If so, then the time constant relationship with FA concentration gives information on how in-solution concentration affects the surface coverage.

Figure 6.17 shows that the time constant is independent of FA concentration. However, the charge transfer resistance, which corresponds to the change in the net electron transfer rate with respects to E (Eq. (6.7)), is proportional to concentration. We assume that the net rates of production for electrons (r_e) and formate (r_θ) can be written as the product of individual functions of FA concentration (c^*), potential, and coverage, that is

$$r_{\mathrm{e}} = g_{\mathrm{e}}(\theta) f_{\mathrm{e}}(E) h_{\mathrm{e}}(c^*) \tag{6.19}$$

$$r_\theta = g_\theta(\theta) f_\theta(E) h_\theta(c^*) \tag{6.20}$$

Substituting these equations into Eqs. (6.7) and (6.12) gives

$$R_{\mathrm{ct}}^{-1} = \left(\frac{\partial r_{\mathrm{e}}}{\partial E}\right)_{\theta,c^*} = g_e(\theta) f_e'(E) h_e(c^*) \tag{6.21}$$

$$\tau_1^{-1} = \left(\frac{\partial r_\theta}{\partial \theta}\right)_{E,c^*} = g_\theta'(\theta) f_\theta(E) h_\theta(c^*) \tag{6.22}$$

This means that the dependence of R_{ct}^{-1} on concentration is the same for r_{e}, and likewise

τ_1^{-1} and r_θ have the same concentration dependence. The reaction order with respect to formic acid is one, Chapter 5, i.e., the current is proportional to c^*. Since the current is proportional to r_e, $r_\mathrm{e} \propto c^*$. This then requires that R_ct^{-1} be proportional to c^*, which it is. Therefore the assumption has consistency with experimental data, with $h_\mathrm{e} \propto c^*$. Further simulations of the mechanism presented in Chapter 5 show that θ becomes more independent of c^* as c^* increases. This agrees with τ_1^{-1} being independent of concentration, that is

$$r_\theta = g_\theta(\theta) f_\theta(E) \tag{6.23}$$

A second check for consistency is in how R_0 and L_1^{-1} are affected by concentration. Figure 6.17 shows that R_0 is inversely proportional to c^* while L_1^{-1} is directly proportional. The def nitions of R_0 and L_1^{-1} (Eqs. (6.11) and (6.13)) suggest that either $\left(\frac{\partial r_\mathrm{e}}{\partial \theta}\right)_{E,c^*}$ or $\left(\frac{\partial r_\theta}{\partial E}\right)_{\theta,c^*}$ is proportional to concentration. Using the same functional analysis as before, but using Eq. (6.23) for r_e, the two partial differentials, become

$$\left(\frac{\partial r_\mathrm{e}}{\partial \theta}\right)_{E,c^*} = g_e'(\theta) f_e(E) h_e(c^*) \tag{6.24}$$

$$\left(\frac{\partial r_\theta}{\partial E}\right)_{\theta,c^*} = g_\theta(\theta) f_\theta'(E) \tag{6.25}$$

Since $R_0 \propto 1/\left(\frac{\partial r_\mathrm{e}}{\partial \theta}\right)_{E,c^*}$ and $L_1^{-1} \propto \left(\frac{\partial r_\mathrm{e}}{\partial \theta}\right)_{E,c^*}$, their product ($\tau_1^{-1}$) will be concentration independent. Therefore, the net electron transfer rate can be written as

$$r_\mathrm{e} = v_2 + v_3 = k_\mathrm{e}(E) c^* \tag{6.26}$$

while the net rate of θ production is written as

$$r_\theta = v_2 - v_3 = k_\theta(E) \tag{6.27}$$

throughout most of the potential region ($E > 0.2$ V).

When $E > 0.65$ V, $R_{\rm ct}$ is not able to be fitted properly in that its fitted value was greater than $10^{20}\,\Omega\,{\rm cm}^2$. In similar experiments of methanol and formic acid electrooxidation on Pt [106, 133], $R_{\rm ct}$ was found to be difficult to fit with a positive value in regions where the impedance flipped into the second quadrant. It was explained that its value continued to decrease beyond the capability of the fitting procedure to detect properly and so it was fitted with a negative value. This fitted $R_{\rm ct}$ may only be an "apparent" $R_{\rm ct}$, since conceptually $R_{\rm ct}$ should always be positive [2]. In this case, the value of $R_{\rm ct}$ increased with an increase in potential until the fitting procedure produced the limiting value of $10^{20}\,\Omega\,{\rm cm}^2$ which corresponds to $R_{\rm ct}^{-1} = 0\,{\rm S\,cm}^{-2}$. These results are real, as the small high frequency semicircle in the Nyquist plots, do visually increase with potential, suggesting that it is not an artifact of the fitting procedure. Thus, the rate of electron production is inversely related to the potential in this region.

As stated before, the kinetic definitions of the circuit elements become more complicated when the number of time constants is greater than two. The impedance is a ratio of two determinants [2] with the two time constants coming from the solutions s_1 and s_2 of the numerator determinant:

$$\begin{vmatrix} \left(\frac{\partial r_\theta}{\partial \theta}\right)_{E,\theta_{\rm SA}} + \Gamma {\rm m} s & \left(\frac{\partial r_\theta}{\partial \theta_{\rm SA}}\right)_{E,\theta} \\ \left(\frac{\partial r_{\rm SA}}{\partial \theta}\right)_{E,\theta_{\rm SA}} & \left(\frac{\partial r_\theta}{\partial \theta_{\rm SA}}\right)_{E,\theta} + \Gamma {\rm m} s \end{vmatrix} = 0$$

which is a quadratic in s. Here the subscript SA denotes the (bi)sulfate anion; $s_1 = \tau_1^{-1}$ and $s_2 = \tau_2^{-1}$. The introduction of a third time constant at $E > 0.5$ did not signif cantly change the other two time constants' relationship to the sweep rate or concentration. That is, $R_{\rm ct}^{-1}$ remained proportional to concentration and slightly dependent on sweep rate, and τ_1^{-1} remained independent of both. Also, $R_{\rm ct}^{-1}$ continued to decrease with potential after 0.5 V. Spectroscopic results suggest that there are two adsorbed species within this region: formate and (bi)sulfate [147]. The introduction of τ_2 does correspond with the potential at which the (bi)sulfate signal appears. Also, the likelihood of the rate of (bi)sulfate adsorption being affected by HCOO(ads) is low given their relative adsorption strengths, that is

$$\left(\frac{\partial r_{\rm SA}}{\partial \theta}\right)_{E,\theta_{\rm SA}} \approx 0 \tag{6.28}$$

Therefore, $\left(\frac{\partial r_\theta}{\partial \theta}\right)_{E,\theta_{\rm SA}}$ is directly related to τ_1 and $\left(\frac{\partial r_\theta}{\partial \theta_{\rm SA}}\right)_{E,\theta}$ is related to τ_2^{-1}. Given these facts, we can relate τ_2 to (bi)sulfate adsorption and τ_1 to formate production as affected by (bi)sulfate adsorption, or more specif cally, (H)$\rm SO_4(ads)$ inf uences the H–C bond cleavage of adsorbed formate, Eq. (6.16). Because the two time constants are isolated from one another, Eqs. (6.7) and (6.12) are still valid for analyzing the kinetics.

Like τ_1^{-1}, τ_2^{-1} is independent of sweep rate and FA concentration. However, it is more or less constant with respect to potential, as opposed to τ_1^{-1} which increases exponentially. This means that $r_{\rm SA}$ is affected by E differently than how r_θ is. Since τ_2 is positive, the addition of (H)$\rm SO_4$(ads) would cause $r_{\rm SA}$ to decrease. It also decreases the rate at which HCOO(ads) oxidizes, i.e., $\left(\frac{\partial r_\theta}{\partial \theta}\right)_{E,\theta_{\rm SA}}$ becomes more negative.

(Bi)sulfate has a relatively high charge density and it is reasonable to assume that its adsorption isotherm is Frumkin since (H)$\rm SO_4$(ads) species would repel each other. If this repulsion is large, then the SA adsorption rate may be approximately independent of po-

tential (similar to oxide growth). Therefore, its coverage would be a function of potential which can be approximated by a linear relationship, $\theta_{\mathrm{SA}} = b_{\mathrm{SA}}(E - E_{\mathrm{SA}})$ when $E \geq E_{\mathrm{SA}}$, otherwise $\theta_{\mathrm{SA}} = 0$. The rate expressions for v_2 and v_3 are similar in form to these given in Chapter 5, i.e.,

$$v_2 = k_2 \exp\left(\frac{(1-\beta_2)F}{RT}(E - E_r)\right) = k_{2,\mathrm{e}}(E) \tag{6.29}$$

$$v_3 = k_3\theta \exp\left(\frac{(1-\beta_3)F}{RT}(E - E_r) - g_{\mathrm{SA}}\theta_{\mathrm{SA}}\right) = k_{3,\mathrm{e}}(E) \tag{6.30}$$

The charge transfer resistance is given as

$$R_{\mathrm{ct}}^{-1} = F\left[\left(\frac{\partial v_2}{\partial E}\right)_{\theta,\theta_{\mathrm{SA}}} + \left(\frac{\partial v_3}{\partial E}\right)_{\theta,\theta_{\mathrm{SA}}}\right] \tag{6.31}$$

$$= F\left[\frac{(1-\beta_2)F}{RT}k_{2,\mathrm{e}}(E) + \frac{(1-\beta_3)F}{RT}k_{3,\mathrm{e}}(E)\right] \tag{6.32}$$

The perturbation of θ_{SA} is slow at the frequency we are measuring R_{ct}^{-1} and so we can substitute the linear approximation, so $g\theta_{\mathrm{SA}}$ can be recast in terms of E. Therefore, v_3 becomes

$$v_3 = k_3\theta \exp\left(\frac{(1-\beta_3)F}{RT}(E - E_r) - G_{\mathrm{SA}}(E - E_{\mathrm{SA}})\right) \tag{6.33}$$

If the inhibition factor G_{SA} is greater than the charge transfer factor, increasing the potential will cause an exponential decrease in v_3. R_{ct}^{-1} will then decrease exponentially as it is more dependent on v_3 as v_3 is thought to be rate-limiting.

Likewise, τ_1 will have the form

$$\tau_1^{-1} = \frac{1}{\Gamma_\mathrm{m}}\left[\left(\frac{\partial v_3}{\partial\theta}\right)_{E,\theta_\mathrm{SA}} - \left(\frac{\partial v_2}{\partial\theta}\right)_{E,\theta_\mathrm{SA}}\right] \tag{6.34}$$

$$= \frac{1}{\Gamma_\mathrm{m}}\left[\frac{(1-\beta_3)F}{RT}k_{3,\mathrm{e}}(E) - \frac{(1-\beta_2)F}{RT}k_{2,\mathrm{e}}(E)\right] \tag{6.35}$$

throughout the potential region where FA oxidation is at pseudo-steady state. Again, $k_{3,\mathrm{e}}(E)$ will decrease exponentially since $\tau_1^{-1} \gg \tau_2^{-1}$, i.e., θ_SA is constant at these frequencies and can be approximated by the linear expression. The fact that τ_1^{-1} increases exponentially and $k_{3,\mathrm{e}}(E)$ decreases exponentially suggests that τ_1^{-1} is mostly determined by v_2, or $\tau_1^{-1} \approx -\frac{1}{\Gamma_\mathrm{m}}\left(\frac{\partial v_2}{\partial\theta}\right)_{E,\theta_\mathrm{SA}}$. The Tafel slope of τ_1^{-1} may be related to $\frac{RT}{(1-\beta_2)F}$; assuming $\beta_2 = 0.5$ the slope would be ca. $120\,\mathrm{mV\,s^{-1}}$. The experimental value of $130\,\mathrm{mV\,s^{-1}}$ agrees with this qualitatively predicted value though more modeling is required to correlate the Tafel slope with a particular reaction step.

6.6 Conclusions

Dynamic electrochemical impedance spectroscopy allows for the measurement of impedance spectra simultaneously with dc voltammetry. The technique can be used to provide supplemental information to an electrochemical experiment. It also allows for varying time-dependent variables, such as sweep rate, to obtain different surface conditions at particular potentials. Three equivalent circuits were used throughout the potential region which provided information on the number of adsorption and charge transfer relaxations. Sweep rate did not affect the adsorption time constants nor the double-layer capacitance, which provides support for dc voltammogram in Chapter 5. The positive time constants in the negative Tafel region correspond to the potential dependent passivisation process.

The potential dependence of the R_ct^{-1} gives a Tafel slope similar to that of the dc voltam-

mogram. Like the current, the R_{ct}^{-1}-E slope is negative between 0.5 and 0.8 V and was interpreted as deactivation due to adsorption of (bi)sulfate and oxide precursor species. After the peak, a third positive time constant is observed which corresponds to the negative R_{ct}^{-1} and current slope. The value of this time constant is an order of magnitude less than the first. The second quadrant impedance behavior in this region is closely related to the potential-driven changes of the electrode interface, particularly the adsorption of (bi)sulfate. The first *RL* is then related to the net formation of adsorbed formate, which increases as the amount of (bi)sulfate increases. This agrees well with the model presented in Chapter 5, where the coverage of formate followed that of (bi)sulfate.

Chapter 7

Conclusions

7.1 Conclusions

This work focused on the redox properties of polycrystalline palladium in acidic solutions. While the electrochemical literature on platinum is extensive for anion adsorptions, oxide growth and reduction, and organic electrooxidations, palladium has been relatively neglected. Pd shows properties that are useful in the DFAFC, one of which is resistance toward CO poisoning during formic acid oxidation. The aim of this work was to study and model Pd redox behavior in acids to elucidate the electrooxidation mechanisms of CO and formic acid.

A sub-theme throughout this work is the reactivity of the double layer region and the oxide region of palladium. We suggest that Pd facilitates stronger adsorption of water and supporting anions than Pt. We used this to explain the potential-driven passivation of formic acid oxidation.

Oxide growth is shown to passivate the electrode surface towards CO and formic acid oxidation. The oxide growth on palladium follows the same direct logarithmic rate law as Pt, which is zero-order with respect to free sites. The zero-order kinetics are explained by

fast place-exchange that occurs with oxygen electrosorption. This allows for the number of electrosorption sites to remain constant as the oxide continues to form. However, the double layer capacitance of Pt and Pd in the oxide region is drastically different, suggesting that the nature of the oxide or the interactions between the oxide and the electrolyte is different. This may explain the difference in reactivity of the two oxides.

CO adsorbs irreversibly on the Pd surface and oxidizes slowly at potentials less than 0.9 V. Therefore, if CO is an intermediate in FA oxidation on Pd, CO would build up on the surface and poison it. Within the time scale of our experiments there is no noticeable formation of CO. This is confirmed by others spectroscopic investigations and our passivation experiments. Methyl formate is not a poisoning contaminant on polycrystalline Pd surface as it is on highly active Pd nanoparticles. This is because methyl formate undergoes hydrolysis and the resulting methanol is unreactive on Pd(poly). On Pd(nano) the methanol oxidizes to CO which passivates the surface. The electrooxidation of formic acid undergoes sequential dehydrogenations. In the hydrogen adsorption region this means that FA oxidation produces absorbed hydrogen, and therefore FA can be used as a means of hydrogen storage. The oxidation of adsorbed hydrogen occurs in parallel with FA oxidation, and therefore the power output of a DFAFC can be increased by charging the Pd particles up with hydrogen.

The interactions between the electrode surface and the electrolyte cannot be disregarded in studying FA electrooxidation on Pd. The anodic current has a negative $j - E$ slope at potentials greater than 0.5 V. This decrease is explained by the coadorption of (bi)sulfate and oxide precursors, which act to slow down the rate determining step, H–C bond cleavage. The inverse dependence of reaction rate on (bi)sulfate coverage was modeled by a Frumkin interaction parameter. Without this interaction it is difficult to explain the negative $j - E$ slope without a reduction step in the mechanism.

The impedance results support the mechanism used to explain the dc experiments. The

impedance implies a single adsorbed species at potentials less than 0.5 V, which correspond to the positive $j - E$ slope region. However, the species is not the same throughout the region as the signs of R_0 and L_1 are positive in the hydrogen adsorption region and negative afterwards. A second RL banch was added to the equivalent circuit in the negative $j - E$ slope region and it did not strongly affect the value of R_{ct}, R_0 and L_1. The first time constant increases, suggesting a decrease in the rate of the reaction that corresponds to it. This agrees with the proposed mechanism of a coadsorbed species adversely affecting the rate determining step, HCOO(ads) oxidation. This is why HCOO(ads) is seen in surface IR spectroscopy experiments along with (bi)sulfate anion. Therefore, adjusting the electrolyte may allow for better anode performance in DFAFCs.

7.2 Future Work

The limitations and validity of this new technique need to be explored by applying it to some well-understood "calibration" systems. For example a near-ideal redox couple, $\mathrm{Fe(CN)}_6^{-3/-4}$, can be used to study the mass transport component of electrochemical impedance measurements. dEIS can be incorporated into potential-step, sweep-hold, and RDE experiments to measure the change in the surface flux of the solute with time and potential. This work presents the first studies using the multisine dEIS system. These have used it only with cyclic voltammetry. In addition dEIS allows for the measurement of harmonic and intermodulation frequencies. Harmonic and intermodulation impedances have the advantage of being insensitive to linear processes such as double layer charging. The technique allows for in depth study of harmonic impedance of surface processes such as hydrogen adsorption on platinum. Such studies further demonstrate the versatility of the technique.

Using dEIS in conjunction with sweep hold measurements would allow for the mea-

surement of the oxide-growth impedance as a function of oxide coverage at constant potential. This would give a ref ned rate expression to obtain more detailed information on the oxide growth kinetics. More information on the change in the double layer capacitance due to oxide growth would be useful to decide if the change in capacitance is due to the change in oxide coverage or potential. Such studies may lead to evidence that Pt and Pd interact differently with the electrolyte, which then affects their catalytic properties.

Our study on CO electrooxidation should be extended with a more thorough explanation of the impedance data. This requires incorporation of an accurate model of CO mass transport, which was outside the scope of this dissertation. There are a number of questions that need to be answered: 1) why does the low frequency impedance not match the sign of the $j - E$ slope? 2) does R_{ct} posses a similar Koutecky-Levich relationship to rotation rate as the current does? 3) how does the measured impedance compare to the impedance predicted by the mechanism given in Chapter 4? A combination of the proposed mechanism of oxide growth in Chapter 3, with the mechanism of CO oxidation is desirable in order to distinguish between NGC and MFT explanations.

dEIS allowed us to obtain a large amount of information on formic acid oxidation on Pd. There have been few thourogh impedance studies on formic acid oxidation that have explored anion effect. We want to test the model presented in Chapter 5 more thoroughly by changing the supporting anion to perchlorate. Likewise, adding small amounts of a strongly adsorbing anion, i.e. $H_2PO_4^-$, should increase the passivation rate.

Formaldehyde is a target for future studies. Since CO is a known intermediate in the oxidation of H_2CO and the surface coverage of CO is measurable using dEIS, we can follow the change in the oxidation rate as a function of CO coverage. This would be an interesting contrast to the FA oxidation that does not involve signif cant CO adsorption.

Bibliography

[1] E. Barsoukov, J. R. Macdonald, Impedance Spectroscopy Theory, Experiment, and Applications, Wiley-Interscience, 2nd edition, 2005.

[2] D. A. Harrington, P. van den Driessche, Electrochim. Acta 56 (2011) 8005–8015.

[3] D. E. Smith, Anal. Chem. 48 (1976) 517A–526A.

[4] D. E. Smith, Anal. Chem. 48 (1976) 221A–240A.

[5] A. M. Bond, R. J. O'Halloran, I. Ruzic, D. E. Smith, J. Electroanal. Chem. 90 (1978) 381–388.

[6] M. E. Orazem, B. Tribollet, Impedance Spectroscopy Theory, Experiment, and Applications, Wiley-Interscience, 2008.

[7] R. L. Sacci, D. A. Harrington, ECS Trans. 19 (2002) 31–42.

[8] C. Gabrielli, F. Huet, M. Kaddam, J. F. Lizee, J. Electroanal. Chem. 138 (1982) 201–208.

[9] G. S. Popkirov, R. N. Schindler, Rev. Sci. Instrum. 64 (1993) 3111–3115.

[10] K. Darowicki, J. Electroanal. Chem. 486 (2000) 101–105.

[11] J. Hazi, D. M. Elton, W. A. Czerwinski, J. Schiewe, V. A. Vincente-Beckett, A. M. Bond, J. Electroanal. Chem. 437 (1997) 1–15.

[12] M. J. Walters, J. E. Garland, C. M. Pettit, D. S. Zimmerman, D. R. Marr, D. Roy, J. Electroanal. Chem. 499 (2001) 48–60.

[13] K. Darowicki, P. Slepski, J. Electroanal. Chem. 547 (2003) 1–8.

[14] G. A. Ragoisha, A. S. Bondarenko, Electrochim. Acta 50 (2005) 1553–1563.

[15] S. C. Creason, J. W. Hayes, D. E. Smith, J. Electroanal. Chem. 47 (1973) 9–46.

[16] R. J. O'Halloran, J. C. Schaar, D. E. Smith, Anal. Chem. 50 (1978) 1073–1079.

[17] J. E. Garland, C. M. Pettit, D. Roy, Electrochim. Acta 49 (2004) 2623–2635.

[18] G. S. Popkirov, Electrochim. Acta 41 (1996) 1023–1027.

[19] D. A. Harrington, J. Electroanal. Chem. 355 (1993) 21–35.

[20] D. A. Harrington, J. Electroanal. Chem. 420 (1997) 101–109.

[21] M. E. van der Geest, N. J. Dangerf eld, D. A. Harrington, J. Electroanal. Chem. 420 (1997) 89–100.

[22] S. O. Englom, J. C. Myland, K. B. Oldham, J. Electroanal. Chem. 480 (2000) 120–132.

[23] S. O. Englom, J. C. Myland, K. B. Oldham, A. L. Taylor, Electroanal. 12 (2001) 626–630.

[24] C. M. Pettit, P. C. Goonetilleke, D. Roy, J. Electroanal. Chem. 589 (2006) 219–231.

[25] G. Ragoisha, N. Osipovich, A. Bondarenko, J. Zhang, S. Kocha, A. Iiyama, J. Solid State Electrochem. 14 (2010) 531–542.

[26] M. Rosvall, M. Sharp, Electrochem. Comm. 2 (2000) 338–343.

[27] J. Yoo, S. Park, Anal. Chem. 72 (2000) 2035–2041.

[28] L. Wang, X. Huang, Electroanal. 19 (2007) 1421–1428.

[29] D. A. Harrington, J. Electroanal. Chem. 355 (1993) 21–35.

[30] R. F. Probstein, Physicochemical Hydrodynamics: An Introduction, Wiley-Interscience, 2nd edition, 2003.

[31] V. G. Levich, Physicochemical Hydrodynamics, Prentice Hall, 1962.

[32] W. J. Albery, M. L. Hitchman, Ring-Disc Electrodes, Oxford: Clarendon Press, 1971.

[33] B. E. Conway, Prog. Surf. Sci. 49 (1995) 331–452.

[34] M. Grden, M. Lukaszewski, G. Jerkiewicz, A. Czerwinski, Electrochim. Acta 53 (2008) 7583–7598.

[35] B. S. Gilman, Electroanal. Chem. 2 (1967) 112–192.

[36] F. T. Wagner, P. N. Ross, Surf. Sci. 160 (1985) 305–330.

[37] K. Itaya, S. Sugawara, K. Sashikata, J. Vac. Sci. Technol. A8 (1990) 515.

[38] W. X. Li, E. K. Vestergaard, R. T. Vang, J. Matthiesen, T. M. Pedersen, E. Laegsgaard, B. Hammer, F. Besenbacher, Phys. Rev. Lett. 93 (2004) 146104.

[39] S. P. Devarajan, J. A. Hinojosa, J. F. Weaver, Surf. Sci. 602 (2008) 3116–3124.

[40] A. Sun, J. Franc, D. D. Macdonald, J. Electrochem. Soc. 153 (2006) B260–B277.

[41] G. Jerkiewicz, G. Vatankhah, J. Lessard, M. Soriaga, Y. Park, Electrochim. Acta 49 (2004) 1451–1459.

[42] V. I. Birss, M. Chang, J. Segal, J. Electroanal. Chem. 355 (1993) 181–191.

[43] W. Böld, M. Breiter, Electrochim. Acta 5 (1961) 145–160.

[44] K. J. Vetter, J. W. Schultze, J. Electroanal. Chem. 34 (1972) 131–140.

[45] K. J. Vetter, J. W. Schultze, J. Electroanal. Chem. 34 (1972) 141–150.

[46] A. Sun, D. D. Macdonald, ECS Trans. 2 (2007) 1–10.

[47] B. Losiewicz, L. Birry, A. Lasia, J. Power Sources 611 (2007) 26–34.

[48] V. Birss, V. Beck, A. Zhang, P. Vanýsek, J. Electroanal. Chem. 429 (1997) 175–184.

[49] B. S. Gilman, Electrochim. Acta 9 (1964) 1025–1046.

[50] W. Pell, A. Zolfaghari, B. Conway, J. Electroanal. Chem. 532 (2002) 13–23.

[51] T. Pajkossy, D. M. Kolb, Electrochim. Acta 53 (2008) 7403–7409.

[52] T. Pajkossy, Solid State Ionics 176 (2005) 1997–2003.

[53] T. Pajkossy, D. Kolb, Electrochem. Comm. 9 (2007) 1171–1174.

[54] E. Sibert, Electrochem. Comm. 3 (2001) 181–186.

[55] E. Sibert, R. Faure, R. Durand, J. Electroanal. Chem. 515 (2001) 71–81.

[56] G. J. Brugg, A. L. G. van den Eeden, M. Sluyters-Rehbach, J. H. Sluyters, J. Electroanal. Chem. 176 (1984) 275–295.

[57] P. R. Bevington, Data Reduction and Error Analysis for the Physical Sciences, McGraw-Hill, New York, 1972.

[58] T. Pajkossy, D. Kolb, Electrochim. Acta 46 (2001) 3063–3071.

[59] T. Pajkossy, D. Kolb, Electrochem. Comm. 5 (2003) 283–285.

[60] H. Angerstein-Kozlowska, B. Conway, W. B. A. Sharp, J. Electroanal. Chem. 43 (1973) 9–36.

[61] B. Conway, B. Barnett, H. Angerstein-Kozlowska, B. V. Tilak, J. Chem. Phys. 93 (1990) 8361–8373.

[62] B. Conway, G. Jerkiewicz, J. Electroanal. Chem. 339 (1992) 123–146.

[63] D. V. Heyd, D. A. Harrington, J. Electroanal. Chem. 335 (1992) 19–31.

[64] M. Alsabet, M. Grden, G. Jerkiewicz, J. Electroanal. Chem. 589 (2006) 120–127.

[65] M. E. van der Geest, N. J. Dangerf eld, D. A. Harrington, J. Electroanal. Chem. 420 (1997) 89–100.

[66] B. Conway, G. Tremiliosi-Filho, G. Jerkiewicz, J. Electroanal. Chem. 297 (1991) 435–443.

[67] M. Breiter, J. Electroanal. Chem. 7 (1964) 38–49.

[68] B. E. Conway, S. Gottesfeld, J. Chem. Soc. Faraday Trans. I 69 (1973) 1090–1100.

[69] W. Visscher, M. A. V. Devanathan, J. Electroanal. Chem. 8 (1964) 127–137.

[70] N. Cabrera, N. F. Mott, Rep. Prog. Phys. 12 (1949) 163–173.

[71] A. Damjanovic, A. T. Ward, M. O'Jea, J. Electrochem. Soc. 121 (1974) 1186–1196.

[72] A. K. N. Reddy, M. A. Genshaw, J. O. Bockris, J. Chem. Phys. 48 (1969) 671–681.

[73] D. Gilroy, J. Electroanal. Chem. 71 (1976) 257–277.

[74] L. Dall'Antonia, G. Tremiliosi-Filho, G. Jerkiewicz, J. Electroanal. Chem. 502 (2001) 72–81.

[75] M. Grden, Electrochim. Acta 54 (2009) 909–920.

[76] D. A. Harrington, J. Electroanal. Chem. 420 (1997) 101–109.

[77] P. G. Allen, S. D. Conradson, M. S. Wilson, S. Gottesfeld, I. D. Raistrick, J. Valerio, M. Lovato, J. Electroanal. Chem 384 (1995) 99–103.

[78] S. Helveg, H. T. Lorensen, S. Horch, L. Laegsgaard, I. Stensgaard, K. W. Jacobsen, J. K. Norskov, F. Besenbacher, Surf. Sci. 430 (1999) L533–L539.

[79] J. G. Wang, W. X. Li, M. Borg, J. Gustafson, A. Mikkelsen, T. M. Pedersen, E. lundgren, J. Weissenrieder, J. Klikovits, M. Schmid, B. Hammer, J. N. Andersenr, Phys. Rev. Lett. 95 (2005) 256102.

[80] D. Friebel, D. J. Miller, C. P. O'Grady, T. Amniyev, J. Bargar, U. Bergmann, H. Ogasawara, K. T. Wikfeldt, L. G. M. Pettersson, A. Nilsson, Phys. Chem. Chem. Phys. 13 (2011) 262–266.

[81] H. Imai, K. Izumi, M. Matsumoto, Y. Kubo, K. Kato, Y. Imai, J. Am. Chem. Soc. 131 (2009) 6293–6300.

[82] A. Capon, R. Parsons, J. Electroanal. Chem. 39 (1972) 275–286.

[83] J. A. Caram, C. Gutierrez, J. Electroanal. Chem. 344 (1993) 313–333.

[84] G. Macf e, A. Cooper, M. F. Cardosi, Electrochim. Acta in press (2011).

[85] K. J. J. Mayrhofer, M. Arenz, B. B. Blizanac, V. Stamenkovic, P. N. Ross, N. M. Markovic, Electrochim. Acta 50 (2005) 5144–5154.

[86] N. M. Markovic, P. N. Ross, Surf. Sci. Rep. 45 (2002) 117–229.

[87] F. Seland, R. Tunold, D. A. Harrington, Electrochim. Acta 52 (2006) 773–779.

[88] H. A. Gasteiger, N. Markovic, P. N. Ross, E. J. Cairns, J. Phys. Chem. 98 (1994) 617.

[89] B. Alvarez, V. Climent, A. Rodes, J. M. Feliu, J. Power Sources 497 (2001) 125–138.

[90] H. A. Gasteiger, N. M. Markovic, P. N. Ross, J. Phys. Chem. 99 (1995) 16757–16767.

[91] H. A. Gasteiger, N. M. Markovic, P. N. Ross, J. Phys. Chem. 99 (1995) 8290–8301.

[92] M. N. Markovic, B. N. Grgur, C. A. Lucas, P. N. Ross, J. Phys. Chem. B 103 (1999) 487–495.

[93] F. Gao, Y. Wang, D. W. Goodman, J. Am. Chem. Soc 131 (2009) 5734–5735.

[94] D. Radosavkic, N. Barrett, R. Belkhou, N. Marsot, C. Guillot, Surf. Sci. 516 (2002) 56–68.

[95] K. Nakao, O. Watanabe, T. Sasaki, S. Ito, K. Tomishige, K. Kunimori, Surf. Sci. 601 (2007) 3796–3800.

[96] S. Nagarajan, K. Thirunavukkarasu, C. S. Gopinath, J. Phys. Chem. C 113 (2009) 7385–7397.

[97] M. Arenz, V. Stamenkovic, P. N. Ross, N. M. Markovic, Electrochem. Comm. 5 (2003) 809–813.

[98] M. Arenz, V. Stamenkovic, T. J. Schmidt, K. Wandelt, P. N. Ross, N. M. Markovic, Surf. Sci. 523 (2003) 199–209.

[99] M. Arenz, V. Stamenkovic, T. J. Schmidt, K. Wandelt, P. N. Ross, N. M. Markovic, Surf. Sci. 506 (2002) 287–296.

[100] Y. Takasu, Z.-G. Zhang, S. Minoura, Y. Murakami, App. Surf. Sci. 121/122 (1997) 596–600.

[101] K. Kunimatsu, J. Phys. Chem. 88 (1984) 2195–220.

[102] L. W. H. Leung, M. J. Weaver, J. Power Sources 109 (1987) 5113–5119.

[103] H. Siwek, M. Lukaszewski, A. Czerwinski, Phys. Chem. Chem. Phys. 10 (2008) 3752–3765.

[104] J. A. Caram, C. Gutierrez, J. Electroanal. Chem. 344 (1992) 313–333.

[105] A. Lasia, Modern Aspects of Electrochemistry, volume 43, Springer, pp. 67–137.

[106] F. Seland, R. Tunold, D. A. Harrington, Electrochim. Acta 51 (2006) 3827–3840.

[107] S. Garbarino, L. D. Burke, Int. J. Electrochem. Sci. 5 (2010) 828–851.

[108] K. Gossner, E. Mizera, J. Electroanal. Chem. 125 (1981) 347–358.

[109] W. Akemann, K. A. Friedrich, U. Stimming, J. Chem. Phys. 113 (2000) 6864–6874.

[110] J. Narayanasamy, A. B. Anderson, J. Electroanal. Chem. 554-555 (2003) 35–40.

[111] N. P. Lebedeva, M. T. M. Koper, J. M. Feliu, R. A. van Santan, J. Phys. Chem. B 106 (2002) 12938–12947.

[112] F. Maillard, E. R. Savinova, U. Stimming, J. Electroanal. Chem. 559 (2007) 221–232.

[113] G. Garcia, M. T. M. Koper, Phys. Chem. Chem. Phys. 11 (2009) 11437–11446.

[114] G. Garcia, M. T. M. Koper, Phys. Chem. Chem. Phys. 10 (2008) 3802–3811.

[115] A. Anderson, N. M. Neshev, J. Electrochem. Soc. 149 (2002) E383–E388.

[116] B. Love, J. Lipkowski, ACS Symp. Ser. 378 (1988) 484–496.

[117] M. Metikos-Hukovic, S. Omanovic, J. Mol. Cat. A 136 (1998) 75–84.

[118] M. T. M. Koper, A. P. J. Jansen, R. A. van Santen, J. J. Lukkien, P. A. J. Hilbers, J. Chem. Phys. 109 (1998) 6051–6062.

[119] C. Korzeniewski, D. Kardash, J. Phys. Chem. B 105 (2001) 8663–8671.

[120] B. Andreaus, F. Maillard, J. Kocylo, E. R. Savinova, M. Eikerling, J. Phys. Chem B 110 (2006) 21028–21040.

[121] A. M. El-Aziz, L. A. Kibler, J. Power Sources 534 (2002) 107–114.

[122] N. P. Lebedeva, A. Rodes, J. M. Feliu, M. T. M. Koper, R. A. van Santan, J. Phys. Chem. B 106 (2002) 9863–9872.

[123] S. Gilman, J. Phys. Chem. 66 (1962) 2657–2664.

[124] M. Grden, M. Lukaszewski, G. Jerkiewicz, A. Czerwinski, Electrochim. Acta 53 (2008) 7583–7598.

[125] G. Jerkiewicz, G. Vatankhah, J. Lessard, M. P. Soriaga, Y.-S. Park, Electrochim. Acta 49 (2004) 1451–1459.

[126] J. D. Roth, M. J. Weaver, J. Electroanal. Chem. 307 (1991) 119–137.

[127] W. T. Napporn, J. M. Leger, C. Lamy, J. Electroanal. Chem. 408 (1996) 141–147.

[128] A. Capon, R. Parsons, J. Electroanal. Chem. 44 (1973) 239–254.

[129] D. Gilroy, B. E. Conway, J. Phys. Chem. 69 (1965) 1259–1267.

[130] H. Miyake, T. Okada, G. Samjeske, M. Osawa, Phys. Chem. Chem. Phys. 10 (2008) 3662–3669.

[131] J. A. Keith, G. Jerkiewicz, T. Jacob, ChemPhysChem 11 (2010) 2779–2794.

[132] D. A. Harrington, B. E. Conway, Electrochim. Acta 32 (1987) 1703–1712.

[133] F. Seland, R. Tunold, D. A. Harrington, Electrochim. Acta 53 (2008) 6851–6864.

[134] L. D. Burke, F. A. Lewis, C. Kemball, J. Catal. 5 (1966) 539–542.

[135] N. Tian, Z. Y. Zhou, S. G. Sun, Y. Ding, Z. L. Wang, Science 316 (2007) 732–735.

[136] I. A. Kibler, A. M. El-Aziz, R. Hoyer, D. M. Kolb, Angew. Chem., Int. Ed. 44 (2005) 2080–2084.

[137] X. Yu, P. G. Pickup, J. Power Sources 182 (2008) 124–132.

[138] W. Zhou, J. Y. Lee, J. Phys. Chem. C 112 (2008) 3789–3793.

[139] A. Lasia, J. Electroanal. Chem. 593 (2006) 159–166.

[140] X. Yu, P. G. Pickup, Electrochem. Comm. 11 (2009) 2012–2014.

[141] X.-G. Zhang, T. Arikawa, Y. Murakami, K. Yahikozawa, Y. Takasu, Electrochim. Acta 40 (1995) 1889–1897.

[142] W. Xu, Y. Gao, T. Lu, Y. Tang, B. Wu, Catal Lett 130 (2009) 312–317.

[143] M. Baldauf, D. M. Kolb, J. Phys. Chem. 100 (1996) 11375–11381.

[144] N. Hoshi, M. Nakamura, K. Kida, Electrochem. Comm. 9 (2007) 279–282.

[145] N. Hoshi, K. Kida, M. Nakamura, M. Nakada, K. Osada, J. Phys. Chem. B 110 (2006) 12480–12484.

[146] N. Hoshi, M. Kuroda, T. Ogawa, O. Koga, Y. Hori, Langmuir 20 (2004) 5066–5070.

[147] H. Miyake, T. Okada, G. Samjeské, M. Osawa, Phys. Chem. Chem. Phys. 10 (2008) 3662–3669.

[148] K. Nishimura, K. Kunimatsu, K.-I. Machida, M. Enyo, J. Electroanal. Chem. 260 (1989) 181–192.

[149] S. A. Kuliev, V. N. Andreev, N. V. Osetrova, V. S. Bagotskii, Y. B. Vasil'ev, Elektrokhim. 18 (1982) 787–791.

[150] O. Yepez, B. R. Scharifker, Int. J. Hydrogen Energy. 27 (2002) 99–105.

[151] L. Birry, A. Lasia, Electrochim. Acta 51 (2006) 3356–3364.

[152] B. D. A. andA Chen, Mater Today 14 (2011) 283–289.

[153] X. Yu, P. G. Pickup, Electrochem. Comm. 11 (2009) 2012–2014.

[154] C. Xu, L. Cheng, P. Shen, Y. Liu, Electrochem. Comm. 9 (2007) 997–1001.

[155] A. V. Smolin, B. Podlovchenko, Elektrokhimiya 34 (1998) 281–295.

[156] K. Gossner, E. Mizera, J Electroanal. Chem. 98 (1979) 37–48.

[157] W. L. Law, A. M. Platt, P. D. C. Wimalaratne, S. L. Blair, J. Electrochem. Soc. 156 (2009) B553–B557.

[158] S. Gilman, J. Phys. Chem. 68 (1964) 70–80.

[159] V. S. Bagotzky, Y. B. Vassilyev, Electrochim. Acta 12 (1967) 1323–1343.

[160] J. L. Haan, R. I. Masel, Electrochim. Acta 54 (2009) 4073–4078.

[161] B. Andreaus, M. Eikerling, J Electroanal. Chem. 607 (2007) 121–132.

[162] J.-Y. Wang, H.-X. Zhang, K. Jiang, W.-B. Cai, J. Am. Chem. Soc. 133 (2011) 14876–14879.

[163] N. Hoshi, K. Kagaya, Y. Hori, J. Electroanal. Chem. 485 (2000) 55–60.

[164] B. E. K. Swamy, J. Maye, C. Vannoy, M. Schell, J. Phys. Chem. B 108 (2004) 16488–16494.

[165] A. V. Smolin, B. I. Podlovchenko, Y. M. Maksimov, Russ. J. Electrochem. 33 (1997) 477–484.

[166] M. Zhao, C. Rice, R. I. Masel, P. Waszezuk, A. Wieckowski, J. Electrochem. Soc. 151 (2004) A131–A136.

[167] Y. Wang, B. Wu, Y. Gao, Y. Tang, T. Lu, W. Xing, C. Liu, J. Power Sources 192 (2009) 372–375.

[168] Y. Liu, L. Wang, G. Wang, C. Deng, B. Wu, Y. Gao, J. Phys. Chem. C 114 (2010) 21417–21422.

[169] E. H. Voogt, A. J. M. Mens, O. L. J. Gijzeman, J. W. Geus, Surf. Sci. 373 (1997) 210–220.

[170] M. Baldauf, D. M. Kolb, J. Phys. Chem 100 (1996) 11375–11381.

[171] W. Xu, Y. Gao, T. Lu, Y. Tang, B. Wu, Catal. Lett. 130 (2009) 312–317.

[172] Q. Yi, W. Huang, X. Liu, G. Xu, Z. Zhou, A. Chen, J. Electroanal. Chem. 619 (2008) 197–205.

[173] X. Yu, P. G. Pickup, J. Power Sources 192 (2009) 279–284.

[174] G.-Q. Lu, A. Crown, A. Wieckowski, J. Phys. Chem. B 103 (1999) 9700–9711.

[175] C. Gabrielli, M. Keddam, Electrochim. Acta. 41 (1996) 957.

[176] D. Schuhmann, Electrochim. Acta. 35 (1990) 1527.

[177] E. A. Carbonio, R. Nagao, E. R. Gonzalez, H. Varela, Phys. Chem. Chem. Phys. 11 (2009) 665–670.

[178] J. Lee, C. Eickes, M. Eiswirth, G. Ertl, Electrochim. Acta 47 (2002) 2297–2301.

[179] L.-L. Li, Z.-D. Wei, X.-Q. Qi, C.-X. Sun, G.-Z. Yin, Sci. China Ser. B: Chem. 51 (2008) 322–332.

[180] G. Samjeske, A. Miki, S. Ye, A. Yamakata, Y. Mukouyama, H. Okamoto, M. Osawa, J. Phys. Chem. B 109 (2005) 23509–23516.

[181] I. Z. Kiss, N. Munjal, R. S. Martin, Electrochim. Acta. 55 (2009) 395–403.

[182] R. Imbihl, M. P. Cox, G. Ertl, H. Muller, W. Brenig, J. Chem. Phys. 83 (1985) 1578–1587.

[183] D. C. Azevedo, A. L. N. Pinheiro, E. R. Gonzalez, Electrochem. Solid-State Let. 5 (2002) A51–A54.

[184] S. Malkhandi, A. Bonnefont, K. Krischer, Electrochem. Solid-State Let. 7 (2005) 710–716.

[185] E. Sitta, H. Varela, Electrocatal. 1 (2010) 19–21.

[186] M. J. Walters, J. E. Garland, C. M. Pettit, D. S. Zimmerman, D. R. Marr, D. Roy, J. Electroanal. chem. 499 (2001) 48–60.

[187] D. Schuhmann, J. Chim. Phys. 60 (1963) 359.

[188] P. Zoltowski, J. Electroanal. Chem. 375 (1994) 45.

Appendix A

Maple Calculations

The following is the Maple worksheet used to simulate the coverages and current of formic acid electrooxidation on palladium in Chapter 5. Note that the relationship between the change in coverage of species i to the net rate of production of the same is written as

$$\frac{d\theta_i}{dt} = \frac{r_i}{\Gamma_{\mathrm{m}}} \tag{A.1}$$

for ease of programming. Reaction 6 in the worksheet is given in terms of X^-(aq) adsorbing to give X(ads). Here "X" corresponds to either the perchlorate or (bi)sulfate anion depending on what is being modelled.

Formic Acid Electrooxidation

Robert L. Sacci and David A. Harrington

Department of Chemistry, University of Victoria

This worksheet attempts to simulate the current and coverage of formic acid oxidation on palladium. The first section is in perchloric acid which has little interaction with adsorbed formate. The second section is in sulfuric acid which has been shown to drastically affect the current response.

Variables

F -- Faraday's constant, C / mol
R -- ideal gas constant, J / mol K
T -- temperature, K
C -- concentration, mol / cm3
Γ_m -- surface concentration of Pd atoms, mol / cm2
v -- sweep rate, V / s

$k\_\#$ -- rate constant, mol / cm2 s or cm / s
$v\_\#$ -- reaction rate expression, mol / cm2 s
$r\_\#$ -- the net rate of production of a species, mol / cm2 s

Reaction scheme

1) HCOOH(aq) + Pd = PdHCOOH(ads)
2) HCOOH(ads) = HCOO(ads) + H+ + e-
3) HCOO(ads) = CO2(ads) + H+ + e-
4) CO2(ads) = CO2(aq) + Pd

5) H2O + Pd = PdO(ads) + H+ + e-
6) X- + Pd = PdX(ads) + e-

Perchloric acid

The following simulates HCOOH oxidation in perchloric acid. ***NO MASS TRANSPORT.***

Definitions

Steady State

Current

$E := Einit;$

$$Einit \qquad \textbf{(3.2.1.1)}$$

$v1 := k1 \cdot C[HCOOH, bulk] \cdot \text{theta}[Pd] - k1m \cdot \text{theta}[HCOOH]:$
$v2 := k2 \cdot \text{theta}[HCOOH] \cdot \exp(c2 \cdot E) - k2m \cdot \text{theta}[HCOO] * \exp(-c2 \cdot E):$
$v3 := k3 \cdot \text{theta}[HCOO] \cdot \exp(c3 \cdot E) \cdot \exp(-3 \cdot b5 \cdot \text{theta}[O]) - k3m \cdot \text{theta}[CO2] \cdot \exp(-c3 \cdot E):$
$v4 := k4 \cdot \text{theta}[CO2] - k4m \cdot \text{theta}[Pd]:$

$v5 := k5 \cdot \exp(c5 \cdot E) \cdot \exp(-b5 \cdot \text{theta}[O]) - k5m \cdot \text{theta}[O] \cdot \exp(-c5m \cdot E):$
$v6 := k6 \cdot \text{theta}[Pd] \cdot \exp(c6 \cdot E - k6m \cdot \text{theta}[X]) \cdot \exp(-c6 \cdot E):$
$rate\_HCOOH := v1 - v2:$
$rate\_HCOO := v2 - v3:$
$rate\_CO2 := v3 - v4:$
$rate\_Pd := v4 - v1 - v5:$
$rate\_O := v5:$
$\#rate\_X := v6:$

$j := F \cdot (v2 + v3 + 2 \cdot v5):$

Can we find another expression for the current?

$F \cdot (v2 + v3 + 2 \cdot v5) - j;$

$$0 \qquad \textbf{(3.2.1.2)}$$

Here we check to make sure we start off at equilibrium at the particular E value we chose.

$allparamsss := params;$
$ans := fsolve(subs(allparamsss, \{rate\_HCOOH = 0, rate\_HCOO = 0, rate\_CO2 = 0, rate\_O = 0, \text{theta}[Pd] + \text{theta}[O] + \text{theta}[HCOOH] + \text{theta}[HCOO] + \text{theta}[CO2] = 1\}), \{\text{theta}[Pd] = 0..1, \text{theta}[O] = 0..1, \text{theta}[HCOOH] = 0..1, \text{theta}[HCOO] = 0..1, \text{theta}[CO2] = 0..1\});$

$$\{Cd = 0.000020, Eup = 1.4, F = 96485, R = 8.3145, T = 298.15, b5 = 25.3, c2 = 20, c3 = 20, c5 = 40, c5m = 20, c6 = 20, k1 = 0.0218, k1m = 2.18\ 10^{-8}, k2 = 2.18\ 10^{-12}, k2m = 0, k3 = 2.18\ 10^{-11}, k3m = 0, k4 = 1.09\ 10^{-9}, k4m = 0, k5 = 2.18\ 10^{-24}, k5m = 0.00654, k6 = 0, k6m = 0, v = 0.05, Einit = 0, C_{HCOOH,\ bulk} = 0.00001, \Gamma_m = 2.176504120\ 10^{-9}\}$$

$$\{\theta_{CO2} = 0.001663879668, \theta_O = 3.333333333\ 10^{-22}, \theta_{Pd} = 0.08320230281, \theta_{HCOO} = 0.08319398341, \theta_{HCOOH} = 0.8319398341\} \qquad \textbf{(3.2.1.3)}$$

$eval(v1, allparamsss \textbf{ union } ans);$
$eval(v2, allparamsss \textbf{ union } ans);$
$eval(v3, allparamsss \textbf{ union } ans);$

$$1.81363\ 10^{-12}$$

$$1.813628838\ 10^{-12}$$

$$1.813628838\ 10^{-12} \qquad \textbf{(3.2.1.4)}$$

Solve the steady state *j-E* plot.

```
oldDigits := Digits :
Digits := 20 :
ss := NULL :
for Ess from 0 to 1.2 by 0.05 do
allparamsss := params minus {Einit = 0} union {Einit = Ess} :
ans := fsolve(subs(allparamsss, { rate_HCOOH = 0, rate_HCOO = 0, rate_CO2 = 0, rate_O
    = 0, theta[Pd] + theta[O] + theta[HCOOH] + theta[HCOO] + theta[CO2] = 1}),
     {theta[Pd] = 0..1, theta[O] = 0..1, theta[HCOOH] = 0..1, theta[HCOO] = 0..1,
    theta[CO2] = 0..1});
ss := ss, [Ess, eval(j·1000, allparamsss union ans), ans] :
od:
ss := [ss] :
Digits := oldDigits :
ssj := ListTools:-Transpose(ListTools:-Transpose(ss)[1..2]) :
pointplot(ssj, labels = ["E vs RHE / V", "j / mA cm-2"]);
```

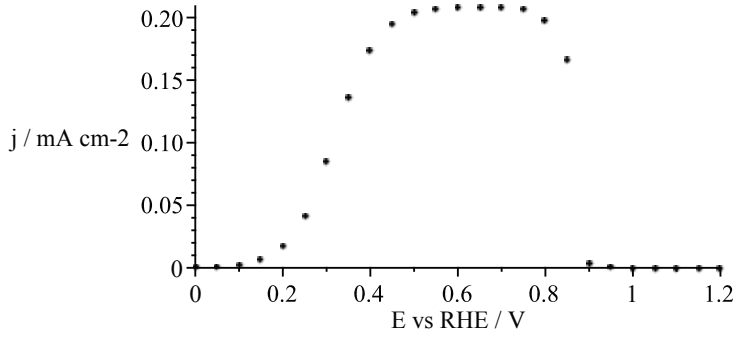

Impedance

```
vars := [E, species[3..-2][]];
rates := subs(theta[Pd] = 1 - theta[O] - theta[HCOOH] - theta[HCOO] - theta[CO2], [
    -j/Cd, rate_O/Γm, rate_HCOOH/Γm, rate_HCOO/Γm, rate_CO2/Γm]) :
```

$$[Einit, \theta_O, \theta_{HCOOH}, \theta_{HCOO}, \theta_{CO2}] \qquad \textbf{(3.2.2.1)}$$

```
Q := Jacobian(rates, vars) - DiagonalMatrix([I·omega, I·omega, I·omega, I·omega, I
    ·omega]) :
```

```
Z := -Determinant(Q[2..-1, 2..-1]) / Cd / Determinant(Q) :
Znum := simplify(expand(eval(Z, params))) :
```

Which then gives the steady-state impedance plot:

```
m := 7 : ssans := {E = ss[m][1]} union ss[m][3];
```

$$\{Einit = 0.30,\ \theta_{CO2} = 0.40124364569195242779,\ \theta_{O} = 2.18866563790980510 30 \times 10^{-14},\ \theta_{Pd} = 0.051735396235083371592,\ \theta_{HCOO} = 0.049729178006706219426,\ \theta_{HCOOH} = 0.49729178006623609454\} \quad \textbf{(3.2.2.2)}$$

```
Zss := eval(Znum, {omega = 10^logomega} union ssans) :
complexplot(conjugate(Zss), logomega = -3..6, scaling = constrained);
```

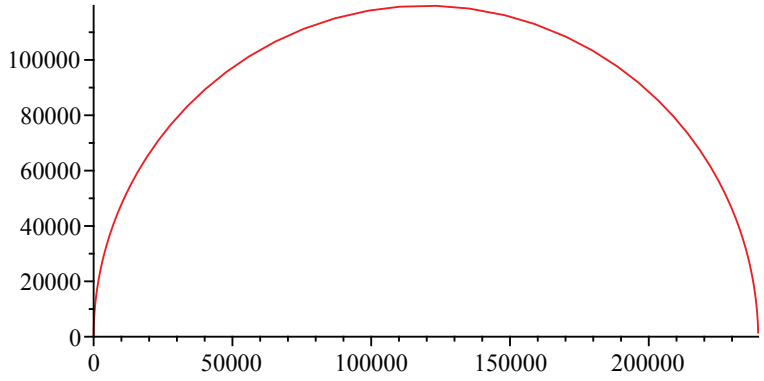

To do

Create loop that exports the impedance data and solves for each potential in the SS curve.

ss contains the solutions for the current + all the converages at that potential. Its format is

```
ss[4]
```

$$[0.15,\ 0.0072814439240615054243,\ \{\theta_{CO2} = 0.00017308969745407746092,\ \theta_{O} = 2.7010279758584611514 \times 10^{-18},\ \theta_{Pd} = 0.049751666538610525352,\ \theta_{X} = 2.0071254653040952629 \times 10^{-10},\ \theta_{HCOO} = 0.086176286884401498383,\ \theta_{HCOOH} = 0.86389895667882134957\}] \quad \textbf{(3.2.3.1)}$$

******** The Following Code writes results to a file for processing in Origin **********

```
out := "C:\\Users\\Robert\\Desktop\\FAoxClO4_ss.txt" :
#fopen(out, WRITE, TEXT);
writedata(out, [["k1", "k2", "k3", "k4", "k5", "k6"]], string);
writedata[APPEND](out, [[1, 0.01, 0.1, 100, 1e−15, 1e−6]]);
writedata[APPEND](out, [["k1m", "k2m", "k3m", "k4m", "k5m", "k6m"]], string);
writedata[APPEND](out, [["0.01", "0", "0", "0", "3e6", "1e5"]], string);
writedata[APPEND](out, [["c2", "c3", "c5", "c5m", "c6", "b5"]], string);
writedata[APPEND](out, [["20", "20", "40", "20", "20", "25.3"]], string);
writedata[APPEND](out, [" ", " ", " ", " ", " ", ], string);
writedata[APPEND](out, [["E", "j", "covCO2", "covO", "covPd",
    "covHCOO" "covHCOOH"]], string);
writedata[APPEND](out, ll);
fclose(out) :
```

****

Dynamic Sweep

Current

```
Ed := t→piecewise(t < (Eup-Einit) / v, Einit + v·t, Eup − v·(t-(Eup − Einit) / v)) :
v1d := k1·C[HCOOH, bulk]·theta[Pd] − k1m·theta[HCOOH] :
v2d := k2·theta[HCOOH]·exp(c2·Ed(t)) − k2m·theta[HCOO]*exp(-c2·Ed(t)) :
v3d := k3·theta[HCOO]·exp(c3·Ed(t))·exp(-3· b5·theta[O]) − k3m·theta[CO2]·exp(-c3
    ·Ed(t)) :
v4d := k4·theta[CO2] − k4m·theta[Pd] :
v5d := k5·exp(c5·Ed(t))·exp(-b5·theta[O]) − k5m·theta[O]·exp(-c5m·Ed(t)) :
v6d := k6·theta[Pd]·exp(c6·Ed(t) − k6m·theta[X])·exp(-c6·Ed(t)) :
rate_HCOOHd := v1d − v2d :
rate_HCOOd := v2d − v3d :
rate_CO2d := v3d − v4d :
rate_Pdd := v4d − v1d − v5d − v6d :
rate_Od := v5d :
rate_Xd := v6d :

mbsurface := {theta[Pd] + theta[O] + theta[HCOOH] + theta[HCOO] + theta[CO2]
    + theta[X] = 1} :
jd := F·(v2d + v3d + 2· v5d) :

timedepvar := {theta[Pd], theta[O], theta[CO2], theta[HCOOH], theta[HCOO],
    theta[HSO4], theta[X]};
funcoft := map(x → x = x(t), {op(timedepvar)});

d_HCOOHd := diff(theta[HCOOH](t), t) = subs(funcoft, rate_HCOOHd / Γm) :
```

```
d_HCOOd := diff(theta[HCOO](t), t) = subs(funcoft, rate_HCOOd/Γ_m):
d_CO2d := diff(theta[CO2](t), t) = subs(funcoft, rate_CO2d/Γ_m):
d_Pdd := diff(theta[Pd](t), t) = subs(funcoft, rate_Pdd/Γ_m):
d_Od := diff(theta[O](t), t) = subs(funcoft, rate_Od/Γ_m):
d_Xd := diff(theta[X](t), t) = subs(funcoft, rate_Xd/Γ_m):
mbsurface_t := subs(funcoft, mbsurface):
j_t := subs(funcoft, j):
```

$$\{\theta_{CO2}, \theta_O, \theta_{Pd}, \theta_X, \theta_{HCOO}, \theta_{HCOOH}, \theta_{HSO4}\}$$

$$\{\theta_{CO2} = \theta_{CO2}(t), \theta_O = \theta_O(t), \theta_{Pd} = \theta_{Pd}(t), \theta_X = \theta_X(t), \theta_{HCOO} = \theta_{HCOO}(t), \theta_{HCOOH} = \theta_{HCOOH}(t), \theta_{HSO4} = \theta_{HSO4}(t)\} \quad \textbf{(3.3.1.1)}$$

```
voltrange := 2·(Eup − Einit);
trange := eval(voltrange/v, params);
diffsys := {d_HCOOHd, d_HCOOd, d_CO2d, d_Pdd, d_Od, d_Xd, } :
initcond := {theta[Pd](0) = 0.4, theta[O](0) = 0, theta[HCOOH](0) = 0.2,
    theta[HCOO](0) = 0.2, theta[CO2](0) = 0.2, theta[X](0) = 0};
ansd := dsolve(subs(params, diffsys) union initcond), numeric, method = rosenbrock_dae,
    range = 0..trange);
```

$$2\,Eup - 2\,Einit$$

$$56.00000000$$

$$\{\theta_{CO2}(0) = 0.2, \theta_O(0) = 0, \theta_{Pd}(0) = 0.4, \theta_X(0) = 0, \theta_{HCOO}(0) = 0.2, \theta_{HCOOH}(0) = 0.2\}$$

proc(*x_rosenbrock_dae*) ... **end proc** **(3.3.1.2)**

```
plt := odeplot(ansd, subs(params, [Ed(t), subs(funcoft, 2·v5d·F·1000)]), 0..trange, refine
    = 2, labels = ["E vs RHE / V", "j[oxide] / mA cm-2"]) : display(%);
plt2 := odeplot(ansd, subs(params, [Ed(t), subs(funcoft, jd·1000)]), 0..trange, refine = 2,
    labels = ["E vs RHE / V", "j / mA cm-2"]) : display(%);
#plt3:=odeplot(ansd, subs(params, [[Ed(t), subs(funcoft, theta[HCOO])], [E(t),
    subs(funcoft, theta[CO2])]]), 0..trange, refine = 2, labels = [E, coverage]) :
    display(%);
odeplot(ansd, subs(params, [[t, theta[Pd](t)], [t, theta[HCOOH](t)], [t,
    theta[HCOO](t)], [t, theta[CO2](t)], [t, theta[O](t)], [t, theta[X](t)]]), 0..trange,
    refine = 2, labels = ["t / s", "Coverage"], legend = ["Pd", "HCOOH", "HCOO", "CO2",
    "O", "X"]);
```

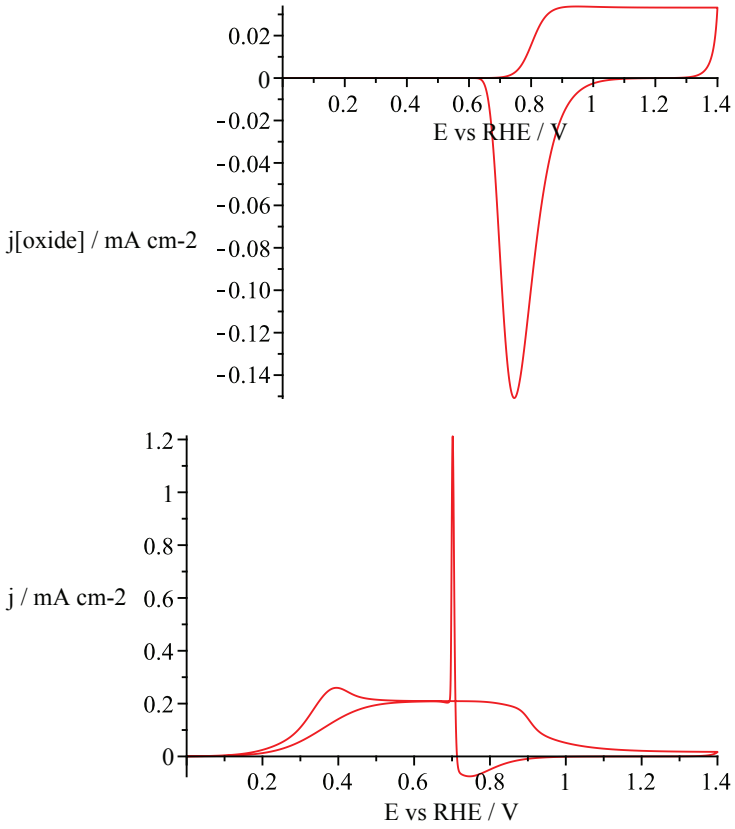
0.02
0
-0.02
-0.04
-0.06
-0.08
-0.10
-0.12
-0.14
j[oxide] / mA cm-2
0.2
0.4
0.6
0.8
1
1.2
1.4
E vs RHE / V
1.2
1
0.8
0.6
0.4
0.2
0
j / mA cm-2
0.2
0.4
0.6
0.8
1
1.2
1.4
E vs RHE / V

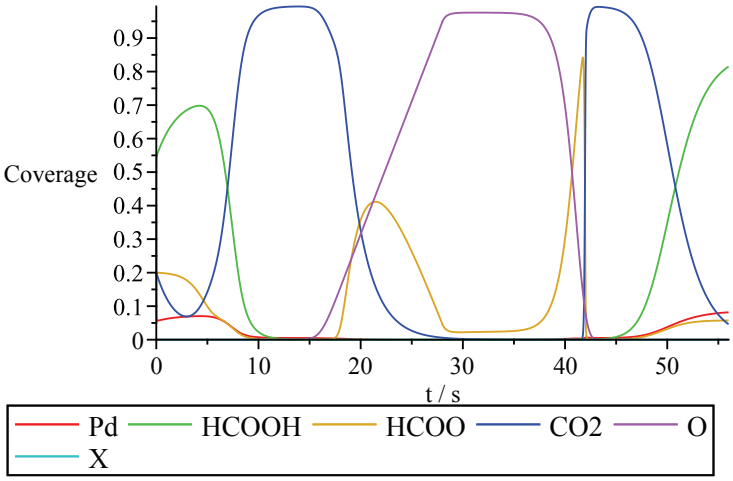

******** The Following Code writes results to a file for processing in Origin **********

```
ll := NULL :
for tim from 0 to 56 by 0.05 do:
eval(subs(funcoft, subs(params, [t, E(t), j, theta[Pd](t), theta[HCOO](t), theta[CO2](t),
    theta[O](t), theta[HSO4](t)])), ans(tim)) :
ll := ll, evalf(%) :
od:
ll := [ll] :

 out := "C:\\Users\\Robert\\Desktop\\FAoxSO4_50.txt" :
 #fopen(out, WRITE, TEXT);
writedata(out, [["k1", "k2", "k3", "k4", "k5", "k6"]], string);
writedata[APPEND](out, [[1, 0.01, 0.1, 100, 1e−15, 1e−6]]);
writedata[APPEND](out, [["k1m", "k2m", "k3m", "k4m", "k5m", "k6m"]], string);
writedata[APPEND](out, [["0.01", "0", "0", "0", "3e6", "1e5"]], string);
writedata[APPEND](out, [["c2", "c3", "c5", "c5m", "c6", "b5"]], string);
writedata[APPEND](out, [["20", "20", "40", "20", "20", "25.3"]], string);
writedata[APPEND](out, [" ", " ", " ", " ", " ", ], string);
writedata[APPEND](out, [["Time", "E", "i", "covPd", "covHCOO", "covCO2",
    "covO" "covHSO4"]], string);
 writedata[APPEND](out, ll);
 fclose(out) :
```

****

Impedance

```
vars := [E, species[3 .. -2][ ]];
```

```
rates := subs( theta[Pd] = 1 - theta[O] - theta[HCOOH] - theta[HCOO] - theta[CO2], [
    -j/Cd, rate_O/Γ_m, rate_HCOOH/Γ_m, rate_HCOO/Γ_m, rate_CO2/Γ_m ]) :
                    [Einit, θ_O, θ_HCOOH, θ_HCOO, θ_CO2]                    (3.3.2.1)
Q := Jacobian(rates, vars) - DiagonalMatrix([I·omega, I·omega, I·omega, I·omega, I
    ·omega]) :
Z := -Determinant(Q[2..-1, 2..-1]) / Cd / Determinant(Q) :
Znumd := simplify(expand(eval(Z, params))) :
Zcvd := simplify(expand(subs(Einit = subs(cvparam, piecewise(t < (Eup)/v, v·t, Eup - v·(t
    -(Eup)/v)), subs(map(x → x = x(t), species[3..-1]), Znumd)))) :
Vdc := 0.17;
tdc := eval((Einit + Vdc)/v, cvparam); eval(Ed(tdc), cvparam);
ansd(tdc);
Zcvnumd := subs(omega = 10^logomega, subs(%, Zcvd)) :
complexplot(conjugate(Zcvnumd), logomega = -4..6, scaling = constrained);
                                  0.17
                              3.400000000
                             0.1700000000
[t = 3.400000000, θ_CO2(t) = 0.0720688560231589, θ_HCOO(t) = 0.166547561483836,
    θ_HCOOH(t) = 0.691852622195097, θ_O(t) = 8.98275229053822 10^-18, θ_Pd(t)
    = 0.0695309602979090, θ_X(t) = 0.]
```

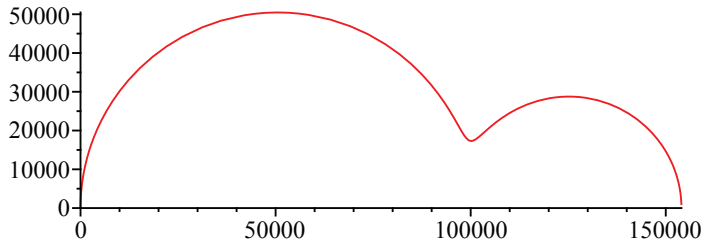

Sulfuric acid

The following is the same system as above except this simulates the sulfate anion effects.

Definitions

```
restart : with(plots) : with(LinearAlgebra) : with(VectorCalculus) :
species := [e, theta[Pd], theta[O], theta[HCOOH], theta[HCOO], theta[CO2], theta[X]];
```

$$\left[e, \theta_{Pd}, \theta_{O}, \theta_{HCOOH}, \theta_{HCOO}, \theta_{CO2}, \theta_{X}\right] \tag{4.1.1}$$

```
param := {C[HCOOH, bulk] = 1e-5, Γ[m] = 210e-6/96485, R = 8.3145, T = 298.15, F = 96485,
    Cd = 20e-6} :
rateparamFOR := {k1 = 8.72e-5, k2 = 2.18e-12, k3 = 2.18e-11, k4 = 2.18e-7, k5
    = 2.18e-24, k6 = 2.18e-15} :
rateparamBACK := {k1m = 6.54e-12, k2m = 2.18e-11, k3m = 0, k4m = 0, k5m = 6.54e-3,
    k6m = 2.18e-4} :
Transfer := {c2 = 20, c3 = 20, c5 = 40, c5m = 20, b5 = 25.3, c6 = 20} :

cvparam := {v = 0.05, Einit = 0, Eup = 1.4} :
params := rateparamFOR union rateparamBACK union Transfer union param union cvparam :
```

Steady State

Current

```
E := Einit;
```

$$Einit \tag{4.2.1.1}$$

```
timedepvar := {theta[Pd], theta[O], theta[CO2], theta[HCOOH], theta[HCOO], theta[X]};
funcoft := map(x → x = x(t), {op(timedepvar)});
```

$$\left\{\theta_{CO2}, \theta_{O}, \theta_{Pd}, \theta_{X}, \theta_{HCOO}, \theta_{HCOOH}\right\}$$

$$\left\{\theta_{CO2} = \theta_{CO2}(t), \theta_{O} = \theta_{O}(t), \theta_{Pd} = \theta_{Pd}(t), \theta_{X} = \theta_{X}(t), \theta_{HCOO} = \theta_{HCOO}(t), \theta_{HCOOH} = \theta_{HCOOH}(t)\right\} \tag{4.2.1.2}$$

```
v1 := k1·C[HCOOH, bulk]·theta[Pd] − k1m·theta[HCOOH] :
v2 := k2·theta[HCOOH]·exp(c2·E) − k2m·theta[HCOO]·exp(−c2·E) :
v3 := k3·theta[HCOO]·exp(c3·E)·exp(− b5·theta[O] − b5·2·theta[X]) − k3m
    ·theta[CO2]·exp(−c3·E) :
v4 := k4·theta[CO2] − k4m·theta[Pd] :
v5 := k5·exp(c5·E)·exp(−b5·theta[O]) − k5m·theta[O]·exp(−c5m·E) :
v6 := k6·theta[Pd]·exp(c6·E − (b5/2)·theta[X]) − k6m·theta[X]·exp(−c6·E + b5
    ·theta[X]) :

rate_HCOOH := v1 − v2 :
rate_HCOO := v2 − v3 :
rate_CO2 := v3 − v4 :
rate_Pd := v4 − v1 − v5 − v6 :
rate_O := v5 :
rate_X := v6;
j := F·(v2 + v3 + 2·v5) :
```

$$k6\,\theta_{Pd}\,e^{c6\,Einit-\frac{1}{2}\,b5\,\theta_X}-k6m\,\theta_X\,e^{-c6\,Einit+b5\,\theta_X} \qquad \textbf{(4.2.1.3)}$$

Can we find another expression for the current?

```
F·(v2 + v3 + 2·v5) − j;
```

$$0 \qquad \textbf{(4.2.1.4)}$$

```
allparamsss := params;
ans := fsolve(subs(allparamsss, { rate_HCOOH = 0, rate_HCOO = 0, rate_CO2 = 0, rate_O
    = 0, rate_X = 0, theta[Pd] + theta[O] + theta[HCOOH] + theta[HCOO] + theta[CO2]
     + theta[X] = 1}), {theta[Pd] = 0..1, theta[O] = 0..1, theta[HCOOH] = 0..1,
    theta[HCOO] = 0..1, theta[CO2] = 0..1, theta[X] = 0..1});
```

$$\{Cd = 0.000020,\ Eup = 1.4,\ F = 96485,\ R = 8.3145,\ T = 298.15,\ b5 = 25.3,\ c2 = 20,\ c3 = 20,\ c5 = 40,\ c5m = 20,\ c6 = 20,\ k1 = 0.0000872,\ k1m = 6.54\ 10^{-12},\ k2 = 2.18\ 10^{-12},\ k2m = 2.18\ 10^{-11},\ k3 = 2.18\ 10^{-11},\ k3m = 0,\ k4 = 2.18\ 10^{-7},\ k4m = 0,\ k5 = 2.18\ 10^{-24},\ k5m = 0.00654,\ k6 = 2.18\ 10^{-15},\ k6m = 0.000218,\ v = 0.05,\ Einit = 0,\ C_{HCOOH,\,bulk} = 0.00001,\ \Gamma_m = 2.176504120\ 10^{-9}\}$$

$$\{\theta_{CO2} = 0.000004722527875,\ \theta_O = 3.333333333\ 10^{-22},\ \theta_{Pd} = 0.008264423781,\ \theta_X = 8.264423781\ 10^{-14},\ \theta_{HCOO} = 0.04722527875,\ \theta_{HCOOH} = 0.9445055749\} \qquad \textbf{(4.2.1.5)}$$

```
eval(v1, allparamsss union ans);
eval(v2, allparamsss union ans);
eval(v3, allparamsss union ans);
```

$$1.029511077\ 10^{-12}$$

$$1.029511076\ 10^{-12}$$

$$1.029511077\ 10^{-12} \qquad \textbf{(4.2.1.6)}$$

```
oldDigits := Digits :
Digits := 20 :
ss := NULL :
 for Ess from 0 to 1.2 by 0.05 do
 allparamsss := params minus {Einit = 0} union {Einit = Ess} :
 ans := fsolve(subs(allparamsss, { rate_HCOOH = 0, rate_HCOO = 0, rate_CO2 = 0, rate_O
    = 0, rate_X = 0, theta[Pd] + theta[O] + theta[HCOOH] + theta[HCOO] + theta[CO2]
     + theta[X] = 1}), {theta[Pd] = 0..1, theta[O] = 0..1, theta[HCOOH] = 0..1,
    theta[HCOO] = 0..1, theta[CO2] = 0..1, theta[X] = 0..1});
ss := ss, [Ess, eval(j·1000, allparamsss union ans), ans] :
od:
ss := [ss] :
 Digits := oldDigits :
 ssj := ListTools:-Transpose(ListTools:-Transpose(ss)[1..2]) :
 pointplot(ssj, labels = ["E vs RHE / V", "j / mA cm-2"]);
```

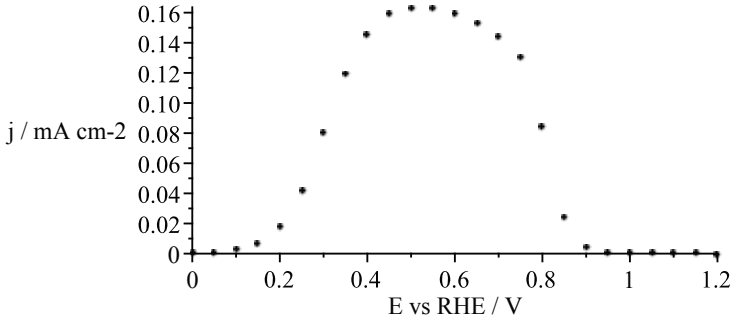

Impedance

```
vars := [E, species[3..-1][ ]];
rates := subs( {theta[Pd] = 1 - theta[O] - theta[HCOOH] - theta[HCOO] - theta[CO2]
    - theta[X]}, [ -j·1000/Cd, rate_O/Γ_m, rate_HCOOH/Γ_m, rate_HCOO/Γ_m, rate_CO2/Γ_m,
    rate_X/Γ_m ] ) :
```

$$[Einit, \theta_O, \theta_{HCOOH}, \theta_{HCOO}, \theta_{CO2}, \theta_X] \qquad \textbf{(4.2.2.1)}$$

```
Q := Jacobian(rates, vars) - DiagonalMatrix( [I·omega, I·omega, I·omega, I·omega, I
    ·omega, I·omega]) :
Z := -Determinant(Q[2..-1, 2..-1]) / Cd / Determinant(Q) :
Znum := simplify(expand(eval(Z, params))) :
```

Which then gives the steady-state impedance plot:

```
l := 17 : ssans := {E = ss[l][1]} union ss[l][3];
```

$$\{Einit = 0.80, \theta_{CO2} = 0.0020195323863682704778, \theta_O \qquad \textbf{(4.2.2.2)}$$
$$= 0.056294693852549149137, \theta_{Pd} = 0.50488326704339030755, \theta_X$$
$$= 0.20017635034267017235, \theta_{HCOO} = 0.23660342953199702107, \theta_{HCOOH}$$
$$= 0.00002272684302507941223 6\}$$

```
Zss := eval(Znum, {omega = 10^logomega} union ssans) :
complexplot(conjugate(Zss), logomega = -9..6, scaling = constrained);
```

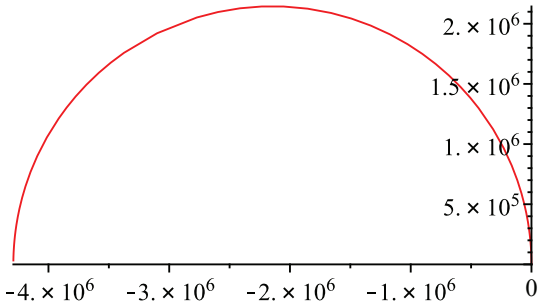

Dynamic Sweep

Current

$$Ed := t \to piecewise(t < (Eup - Einit)/v, Einit + v\cdot t, Eup - v\cdot(t - (Eup - Einit)/v));$$
$$v1d := k1\cdot C[HCOOH, bulk]\cdot theta[Pd] - k1m\cdot theta[HCOOH]:$$
$$v2d := k2\cdot theta[HCOOH]\cdot \exp(c2\cdot Ed(t)) - k2m\cdot theta[HCOO]*\exp(-c2\cdot Ed(t)):$$
$$v3d := k3*theta[HCOO]*\exp(c3\cdot Ed(t))\cdot\exp(-\ b5\cdot\ theta[O] - \ b5\cdot 2\cdot\ theta[X]) - k3m * theta[CO2]*\exp(-c3\cdot Ed(t)):$$
$$v4d := k4\cdot theta[CO2] - k4m\cdot theta[Pd]:$$

$$v5d := k5\cdot\exp(c5\cdot Ed(t))\cdot\exp(-b5\cdot theta[O]) - k5m\cdot theta[O]\cdot\exp(-c5m\cdot Ed(t)):$$
$$v6d := k6\cdot theta[Pd]\cdot\exp\left(c6\cdot Ed(t) - \frac{b5}{2}\cdot theta[X]\right) - k6m*theta[X]*\exp(-c6\cdot Ed(t) + b5\cdot theta[X]):$$
$$t \to piecewise\left(t < (Eup + VectorCalculus{:}\text{-}`\text{-}`(Einit))\ \frac{1}{v}, Einit + v\,t, Eup + VectorCalculus{:}\text{-}`\text{-}`\left(v\left(t + VectorCalculus{:}\text{-}`\text{-}`\left((Eup + VectorCalculus{:}\text{-}`\text{-}`(Einit))\ \frac{1}{v}\right)\right)\right)\right) \qquad \textbf{(4.3.1.1)}$$
$$rate\_HCOOHd := v1d - v2d:$$
$$rate\_HCOOd := v2d - v3d:$$
$$rate\_CO2d := v3d - v4d:$$
$$rate\_Pdd := v4d - v1d - v5d - v6d:$$
$$rate\_Od := v5d:$$
$$rate\_Xd := v6d:$$

$$mbsurface := \{theta[Pd] + theta[O] + theta[HCOOH] + theta[HCOO] + theta[CO2] + theta[X] = 1\}:$$
$$jd := F\cdot(v2d + v3d + 2\cdot v5d):$$
$$timedepvar := \{theta[Pd], theta[O], theta[CO2], theta[HCOOH], theta[HCOO],$$

```
    theta[HSO4], theta[X]};
funcoft := map(x → x = x(t), {op(timedepvar)});
```

$$\{\theta_{CO2}, \theta_O, \theta_{Pd}, \theta_X, \theta_{HCOO}, \theta_{HCOOH}, \theta_{HSO4}\}$$

$$\{\theta_{CO2} = \theta_{CO2}(t), \theta_O = \theta_O(t), \theta_{Pd} = \theta_{Pd}(t), \theta_X = \theta_X(t), \theta_{HCOO} = \theta_{HCOO}(t), \theta_{HCOOH} = \theta_{HCOOH}(t), \theta_{HSO4} = \theta_{HSO4}(t)\} \quad \textbf{(4.3.1.2)}$$

```
d_HCOOHd := diff(theta[HCOOH](t), t) = subs(funcoft, rate_HCOOHd/Γm):
d_HCOOd := diff(theta[HCOO](t), t) = subs(funcoft, rate_HCOOd/Γm):
d_CO2d := diff(theta[CO2](t), t) = subs(funcoft, rate_CO2d/Γm):
d_Pdd := diff(theta[Pd](t), t) = subs(funcoft, rate_Pdd/Γm):
d_Od := diff(theta[O](t), t) = subs(funcoft, rate_Od/Γm):
d_Xd := diff(theta[X](t), t) = subs(funcoft, rate_Xd/Γm):
mbsurface_t := subs(funcoft, mbsurface):
j_t := subs(funcoft, j):

voltrange := 2·(Eup − Einit);
trange := eval(voltrange/v, params);
diffsys := {d_HCOOHd, d_HCOOd, d_CO2d, d_Pdd, d_Od, d_Xd, }:
initcond := {theta[Pd](0) = 0.4, theta[O](0) = 0, theta[HCOOH](0) = 0.2,
    theta[HCOO](0) = 0.2, theta[CO2](0) = 0.2, theta[X](0) = 0};
ansd := dsolve(subs(params, diffsys) union initcond), numeric, method = rosenbrock_dae,
    range = 0..trange);
```

$$2\,Eup - 2\,Einit$$

$$56.00000000$$

$$\{\theta_{CO2}(0) = 0.2, \theta_O(0) = 0, \theta_{Pd}(0) = 0.4, \theta_X(0) = 0, \theta_{HCOO}(0) = 0.2, \theta_{HCOOH}(0) = 0.2\}$$

proc(*x_rosenbrock_dae*) ... **end proc** **(4.3.1.3)**

```
plt := odeplot(ansd, subs(params, [Ed(t), subs(funcoft, 2·v5d·F·1000)]), 0..trange, refine
    = 2, labels = ["E vs RHE / V", "j[oxide] / mA cm-2"]):display(%);
plt2 := odeplot(ansd, subs(params, [Ed(t), subs(funcoft, jd·1000)]), 0..trange, refine = 2,
    labels = ["E vs RHE / V", "j / mA cm-2"]):display(%);
#plt3:=odeplot(ansd, subs(params, [[Ed(t), subs(funcoft, theta[HCOO])], [Ed(t),
    subs(funcoft, theta[CO2])]]), 0..trange, refine = 2, labels = [E, coverage]):
    display(%);
odeplot(ansd, subs(params, [[t, theta[HCOO](t)], [t, theta[O](t)], [t, theta[X](t)]]), 0
    ..30, refine = 2, labels = ["t / s", "Coverage"], legend = ["HCOO", "O", "X"]);
```

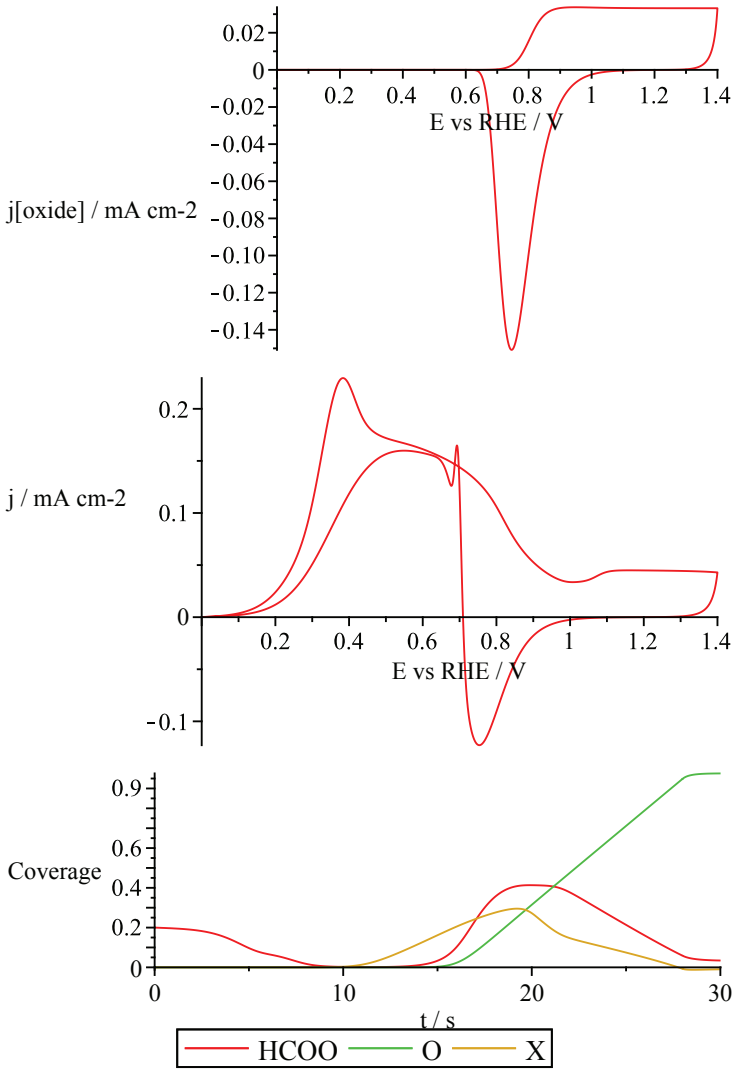

Impedance

vars := [*E*, *species*[3 .. -1][ ]];

$$rates := subs\left(\text{theta}[Pd] = 1 - \text{theta}[O] - \text{theta}[HCOOH] - \text{theta}[HCOO] - \text{theta}[CO2],\ \left[-\frac{jd}{Cd},\ \frac{rate\_Od}{\Gamma_m},\ \frac{rate\_HCOOHd}{\Gamma_m},\ \frac{rate\_HCOOd}{\Gamma_m},\ \frac{rate\_CO2d}{\Gamma_m},\ \frac{rate\_Xd}{\Gamma_m} \right]\right):$$

$$\left[Einit, \theta_O, \theta_{HCOOH}, \theta_{HCOO}, \theta_{CO2}, \theta_X\right] \quad \textbf{(4.3.2.1)}$$

$$Q := Jacobian(rates, vars) - DiagonalMatrix([I\cdot omega, I\cdot omega, I\cdot omega, I\cdot omega, I\cdot omega, I\cdot omega]):$$

$$Z := -Determinant(Q[2..-1, 2..-1]) / Cd / Determinant(Q):$$

$$Znumd := simplify(expand(eval(Z, params))):$$

$$Zcvd := simplify(expand(subs(Einit = subs(cvparam, piecewise(t < (Eup)/v, v\cdot t, Eup - v\cdot(t - (Eup)/v)), subs(map(x \to x = x(t), species[3..-1]), Znumd)))):$$

$$Vdc := 0.4;$$

$$tdc := eval((Einit + Vdc)/v, cvparam); eval(E, cvparam);$$

$$ansd(tdc);$$

$$Zcvnumd := subs(\text{omega} = 10\text{^}logomega, subs(\%, Zcvd)):$$

$$complexplot(conjugate(Zcvnumd), logomega = -1..6, scaling = constrained);$$

$$0.4$$

$$8.000000000$$

$$0$$

$$\left[t = 8.000000000, \theta_{CO2}(t) = 0.00541906560636391, \theta_{HCOO}(t) = 0.0182096466282829, \theta_{HCOOH}(t) = 0.174369311870685, \theta_O(t) = 8.80410684746185\ 10^{-12}, \theta_{Pd}(t) = 0.801935290705570, \theta_X(t) = 0.0000666851802944770\right]$$

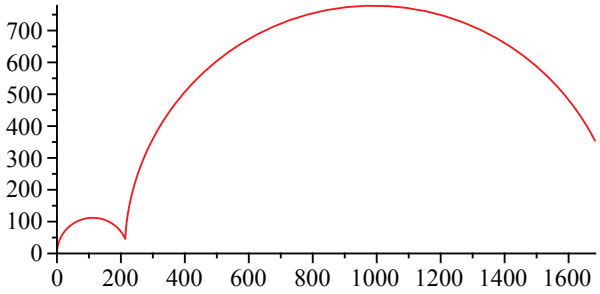
700
600
500
400
300
200
100
0
0
200
400
600
800
1000
1200
1400
1600